Dissertation
submitted to the
Combined Faculty of Natural Sciences and Mathematics
of the Ruperto Carola University Heidelberg, Germany

for the degree of
Doctor of Natural Sciences

Presented by

M.Sc. Aileen Berger

Born in Mainz
Oral examination: 21.07.2020

NY-BR-1 specific CAR$^+$ T cells engineered by S/MAR vectors prove effectiveness in pre-clinical models of breast cancer

Referees: Prof. Dr. rer. nat. Viktor Umansky
Prof. Dr. med. Dirk Jäger

Abstract

Breast cancer is the most frequent cause of death among cancer diseases in women despite improved treatment options, which makes new and further development of additional therapeutic approaches urgently necessary. Immunotherapy, in particular CAR - based T cell therapy, became an increasingly important therapeutic tool in recent decades due to great success in the treatment of hematological diseases. However, this approach proved to be very challenging in the treatment of solid tumors due to the lack of tumor specific antigens and inefficient persistence and infiltration of CAR^+ T cells into these tumors. The breast cancer antigen NY-BR-1, which is overexpressed in more than 70 % of breast cancer tumors and metastases, might serve as a target antigen for CAR - based immunotherapy. The feasibility of this hypothesis was investigated in this study using three different CAR candidates varying in their binding sites within the NY-BR-1 protein. During this process, the efficacy and safety of the individual CAR candidates was evaluated using various *in vitro* and *in vivo* experiments. At the beginning of this work, human and murine NY-BR-1 - expressing cell lines were successfully generated by lentiviral transduction. However, surface expression of the NY-BR-1 protein decreased over time, mainly due to the dependency of NY-BR-1 expression on the G1 cell cycle phase and degradation by proteasomes. For the generation of murine CAR^+ T cells, a novel transfection strategy based on S/MAR DNA vectors (pS/MARter, NanoCMARter) was established. This innovative technology enabled a cost-efficient, fast and very effective generation of CAR - expressing murine T cells and was also successfully applied to human (CAR^+) T cells. Indeed, all three CAR candidates, expressed in lentivirally transduced or (S/MAR vector) electroporated T cells, proved to be very effective in eliminating NY-BR-1 - expressing cell lines and primary pleural effusion cells isolated from breast cancer patients. Additional cross-reactivity analyses with the NY-BR-1.1 protein, which exhibits a high homology to NY-BR-1 and is expressed in the breast tissue and brain, revealed a high safety risk for the application of one particular CAR candidate in clinical trials. The same CAR additionally caused strongly increased blood cytokine levels in NY-BR-$1^{tg/-}$ mice displaying low NY-BR-1 expression levels in the organs. In C57BL/6 wild-type mice, however, all CAR candidates proved to be safe. The CAR^+ T cell treatment of tumor bearing mice resulted in significantly delayed tumor growth and prolonged overall survival, but the CAR^+ T cells differed in their infiltration efficiency depending on the CAR type. This work demonstrated that NY-BR-1 is an attractive target antigen for CAR - based immunotherapy in breast cancer patients. A direct comparison of the CAR candidates presented here revealed that one of these three candidates is particularly suitable for use in clinical trials due to its safety profile and high effectiveness.

Zusammenfassung

Brustkrebs stellt trotz verbesserter Therapiemöglichkeiten die häufigste Todesursache unter den Krebserkrankungen bei Frauen dar, was die Weiter- und Neuentwicklung zusätzlicher Therapieansätze notwendig macht. Die Immuntherapie, insbesondere die CAR$^+$ T Zelltherapie, gewann in den letzten Jahrzehnten aufgrund der großen Erfolge bei der Behandlung hämatologischer Erkrankungen zunehmend an Bedeutung. Jedoch erwies sich dieser Ansatz bei der Behandlung von soliden Tumoren wegen mangelnder tumorspezifischer Antigene und ineffizienter Infiltration der CAR$^+$ T Zellen in das Tumorgewebe als sehr schwierig. Das Brustkrebsantigen NY-BR-1, das in über 70 % der Brustkrebstumore und Metastasen überexprimiert wird, könnte als Zielantigen für eine CAR basierte Immuntherapie dienen. Die Umsetzbarkeit dieser Hypothese wurde in der vorliegenden Arbeit anhand drei verschiedener CAR Kandidaten, die sich in ihren Binderegionen innerhalb des NY-BR-1 Proteins unterscheiden, untersucht. Während dieses Prozesses sollte vor allem die Effektivität und Sicherheit der CARs unter Einsatz verschiedener *in vitro* und *in vivo* Versuche evaluiert werden. Zu Beginn dieser Arbeit wurden mittels lentiviraler Transduktion humane und murine NY-BR-1 exprimierende Zelllinien generiert. Die Oberflächenexpression des NY-BR-1 Proteins verringerte sich jedoch mit der Zeit, was vor allem auf einer Abhängigkeit der NY-BR-1 Expression von der G1 Zellzyklusphase und dem Abbau durch Proteasome beruhte. Für die Generierung von murinen CAR$^+$ T Zellen wurde eine neuartige Transfektionsstrategie, die auf S/MAR DNA Vektoren (pS/MARter, NanoCMARter) basiert, etabliert. Diese Technologie ermöglichte eine kostengünstige, schnelle und effektive Generierung von murinen CAR exprimierenden T Zellen, die auch erfolgreich auf humane (CAR$^+$) T Zellen angewandt wurde. Tatsächlich erwiesen sich alle drei CAR Kandidaten, die in lentiviral transduzierten oder (S/MAR Vektor) elektroporierten T Zellen exprimiert wurden, als sehr effektiv bei der Eliminierung von NY-BR-1 exprimierenden Zelllinien und primären Pleurazellen, die aus Brustkrebspatienten isoliert wurden. Zusätzliche Analysen zur Kreuzreakivität gegenüber des NY-BR-1.1 Proteins, das eine hohe Homologie zu NY-BR-1 aufweist und neben dem Brustgewebe auch im Gehirn exprimiert wird, offenbarten ein hohes Sicherheitsrisiko für den Einsatz eines bestimmten CAR Kandidaten in klinischen Studien. Dieser CAR führte zudem zu stark erhöhten Cytokinkonzentrationen in NY-BR-1$^{tg/-}$ Mäusen, die geringe NY-BR-1 Expressionslevel in den Organen aufweisen. In C57BL/6 Wildtyp Mäusen erwiesen sich jedoch alle CAR Kandidaten als sicher. Die CAR$^+$ T Zellbehandlung von tumortragenden Mäusen führte zu einem signifikant verzögerten Tumorwachstum und einem verlängerten Gesamtüberleben, wobei sich die CAR$^+$ T Zellen in ihrer Infiltrationseffizienz unterschieden. Die Ergebnisse der vorliegenden Arbeit zeigten, dass NY-BR-1 ein attraktives Zielantigen für CAR basierte Immuntherapien bei Brustkrebspatienten darstellt. Beim direkten Vergleich der hier vorgestellten CAR Kandidaten wurde ersichtlich, dass sich vor allem einer der drei Kandidaten aufgrund seines Sicherheitsprofils und hoher Effektivität für einen Einsatz in klinischen Studien eignet.

Table of contents

1 Introduction

Despite improved therapies and prevention strategies, cancer incidence and mortality are growing worldwide. 17.0 million new cancer cases and 9.5 million cancer deaths were reported worldwide in 2018 [1]. Moreover, it is expected that there will be a worldwide increase to over 27.5 million new cancer cases and 16.3 million cancer deaths by 2040, predicting cancer might become the leading cause of death worldwide. The reasons are manifold and include not only aging and growth of population but also the failure of established treatments for cancer recurrence, which necessitates the development of new treatment approaches [1-3].

1.1 Breast cancer

Breast cancer is the second most common cause of cancer death (after lung cancer) worldwide and is the most commonly diagnosed cancer in women, accounting for over 25 % of all cancers [1,4]. Next to family and genetic predispositions (e.g. *BRCA1/2*, *p53*, or *PTEN* mutations) [5] or general lifestyle factors such as excessive alcohol consumption, smoking or overweight, age is one important risk factor for breast cancer, which is reflected in higher incidence rates with increasing age [5,6]. Most breast cancer diagnoses are made in women after the age of 45. In addition, an increased “hormonal load”, influenced by different factors such as hormone treatments, pregnancy, long nursing periods, early menarche or later menopause, belongs to the main risk factors for developing breast cancer [5-8]. However, different studies demonstrated that risk factors, especially genetic factors, vary depending on the molecular subtype of breast cancer [9].

Due to the heterogeneity of this malignancy, breast cancer is divided into different types on the basis of tumor grade as well as histological and molecular biological analysis [10-13]. A basic distinction is made between non-invasive and invasive breast carcinoma. The latter, representing over 80 % of all breast cancer diagnoses [11], means that tumor cells infiltrate surrounding breast tissue. These types are further classified into a wide range of subtypes according to the cells of origin, whereby breast duct – derived cancers, so-called ductal carcinoma, represent the majority of both non-invasive (83 %) [11] and invasive (80 %) breast cancers [13] (see Figure 1.1.1). The second most common type of invasive breast cancer (15 %) arises from lobules of the breast and is known as lobular carcinoma [13].

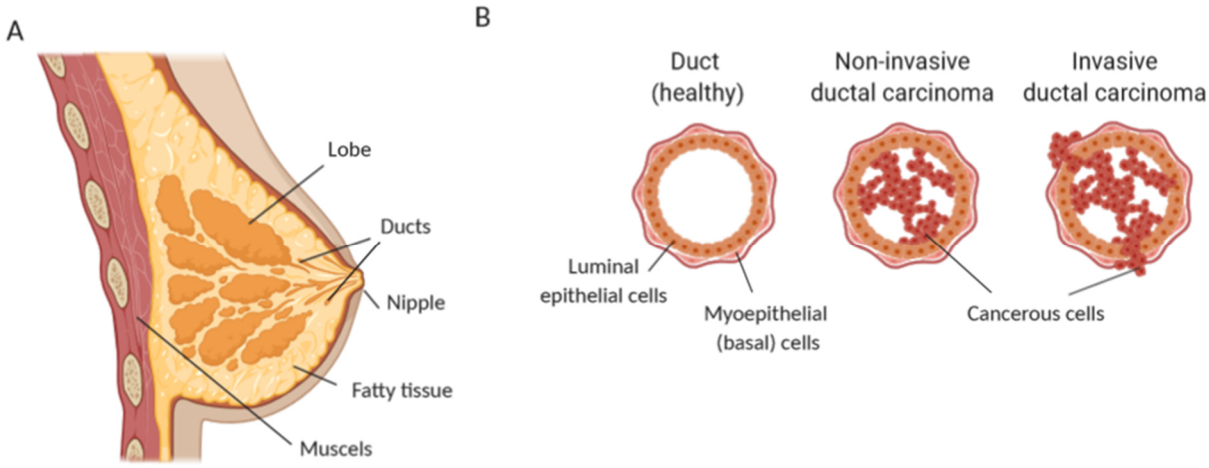

Figure 1.1.1: Anatomy of the female breast including ductal structures
[A] Each female breast exhibits lobes, which are further divided into smaller milk-producing glands (lobules), and ducts to carry milk from the lobules to the nipple. [B] Ducts and lobules compose of (inner) luminal epithelial and (outer) myoepihelial (basal) cells. Both cell types can serve as cells of origin for breast cancer. Non-invasive ductal carcinoma, also known as ductal carcinoma *in situ*, means that cancerous cells remain inside the milk ducts, whereas invasive ductal carcinoma is defined by spreading of cancerous cells into surrounding breast tissue.

Based on molecular analysis and expression profiles of hormone and proliferation-related genes, for example, breast cancers are further classified into five intrinsic subtypes: luminal A, luminal B, HER2-enriched, triple negative, and basal-like [14,15]. These in turn differ in their histological features, responses to chemotherapies, clinical outcomes and relapse rates. The most commonly diagnosed (40 – 60 %) subtype, luminal A, is defined as estrogen receptor positive (ER^+), human epidermal growth factor receptor 2 negative ($HER2^-$) and / or progesterone receptor positive (PR^+) and exhibits low expression rates of the proliferation marker Ki-67 [16,17]. In general, patients suffering from luminal A tumors have a low recurrence risk and a good prognosis compared to other subtypes [14-17].

In contrast, 10 to 20 % of breast cancers belong to the luminal B subtype, which is divided into two groups depending on the HER2 expression profile [18,19]. While the $HER2^-$ luminal B subset is defined as ER^+, $HER2^-$, $Ki\text{-}67^{high}$ and / or PR^+ with Ki-67 expression levels of over 14 %, the $HER2^+$ type displays an ER^+ and / or PR^+ phenotype [18,19]. Besides, luminal B tumors have a higher mutational burden and worse prognosis with higher recurrence rates compared to luminal A [14,19]

In contrast to the luminal subtypes, HER2 - enriched tumors are negative for both hormone receptors ER and PR, have lower expression of luminal genes and exhibit very high expression rates of HER2 [14]. In addition, these tumors are characterized by high mutational burden, high risk of recurrence and lead to metastasis in brain and visceral organs [14,20-22].

Triple negative breast cancer (TNBC), which is characterized by the absence of ER, PR and HER2 expression, is much less common (10 – 17 % of breast cancer cases), but represents a very heterogeneous and aggressive subgroup with early age of outcome [23,24]. The heterogeneity of this subclass is reflected in distinct patterns of molecular alterations, somatic mutations and copy-number variations leading to seven different clusters: basal-like 1 (BL1), basal-like 2 (BL2), immunomodulatory

(IM), mesenchymal (M), mesenchymal-stem-like (MSL), luminal androgen receptor (LAR), and an unstable cluster within TNBC [24]. The majority (71 %) of TNBC tumors have a basal-like phenotype [25], which means that these tumors express basal markers such as cytokeratin 5 (CK5), CK6, CK14, CK17 and / or the epidermal growth factor receptor (EGFR) [25,26] . However, TNBC and basal-like breast cancer cannot be used as synonyms because not all basal-like tumors are triple negative and vice versa [25]. In fact, various studies showed that only 70 – 90 % of molecular basal-like tumors are triple-negative, whereas the rest shows high expression of ER or HER2 [23,25,27]. Nevertheless, in addition to the expression of basal markers, basal-like and TNBC show further similarities such as high frequency of *BRCA1* mutations, distant metastasis and poor prognosis [23-26,28].

Table 1.1: Gene expression profiles in breast cancer subtypes

Subtypes	ER	PR	HER2	Ki-67	Luminal marker	Basal marker
Luminal A	+	+ / -	-	Low (< 14 %)	CK8, CK18	
Luminal B ($HER2^-$)	+	+ / -	-	High (> 14 %)	CK8, CK18	
Luminal B ($HER2^+$)	+	+ / -	+	Any	CK8, CK18	
HER2-enriched	- or low level	-	+	Any	CK7, CK8, CK18	
Triple-negative (TNBC)	-	-	-	Any		~ 71 % basal-like: CK5, CK6, CK17 and / or EGFR
Basal-like	- or low level	- or low level	- or low level	Any		CK5, CK6, CK17 and / or EGFR

There are diverse hypothetical models for the development of different breast cancer subtypes, so that the general question arises whether certain breast cancer phenotypes are already present in the originally transforming tumor cell or if different phenotypes develop during tumorigenesis [29]. In general, the cancer stem cell concept proposes that a small subpopulation of cancer cells has the ability to renew and differentiate, and to exhibit clonal and tumorigenic potentials [30]. Indeed, Al Hajj *et al.*(2003)[31] identified a subpopulation of breast cancer cells with a stem cell-like $CD44^+CD24^{-/low}$ ESA^+ (epithelial surface antigen) phenotype, which was capable to reconstituting tumors on serial

transplantation in immunodeficient NOD SCID mice with a phenotypic heterogeneity found in the initial tumor. This breast cancer stem cell theory was confirmed by further studies. For example, breast cancer stem cells were identified and isolated from breast cancer lesions as well as established breast cancer cell lines and showed the ability to renew, to extensively proliferate as clonal non-adherent spherical clusters and to differentiate along different mammary epithelial lineages (ductal and myoepithelial) *in vitro* [31,32].

The findings from several studies on the development of various breast cancer subtypes led to two hypothetical models summarized in Figure 1.1.2. According to the "one cell of origin" theory (Figure 1.1.2 A), all breast cancer subtypes derive from the same breast cancer stem cells by subset specific genetic and epigenetic mutations of the same mammary epithelial or progenitor stem cell [8,29,33]. However, the other and most accepted hypothesis implies that each tumor subtype arises from distinct cell types (stem cell, progenitor cell or differentiated cell) (Figure 1.1.2 B) [8,29,33,34]. Here, gradual accumulation of random mutations might result in transformation into tumor cells when sufficient mutations have accumulated [8]. While both luminal A and B breast cancers show gene expression profiles similar to differentiated inner luminal epithelium [35], triple-negative and basal-like tumors are suspected to be derived from basal or luminal progenitor cells [33,36,37], whereby the latter seem to express basal-specific genes [36]. The precursor population for HER2-enriched cancer might be late luminal progenitor cells [35].

There are several hypotheses about the roles of cancer stem cells, stromal microenvironment and genetic profiles in the formation of breast cancer metastases. All of the following have been suggested by traditional models of breast cancer metastasis: (1) only a small subset of tumors cells acquires the metastatic capacity during late tumorigenesis, (2) all tumor cells can form metastasis through spontaneous metastasis spread, or (3) metastatic variants or subclones arise within the primary tumor [10,38]. According to the model from Weigelt *et al.* (2005) [10], metastatic "poor prognosis" breast tumors might develop when oncogenic mutations occur in breast stem cells, whereas non-metastatic "good prognosis" breast cancers might arise from mutations in differentiated progenitor cells. Moreover, different studies indicate that tissue-specific genetic profiles differ between various breast cancer stem cells, which might explain the tissue selectivity for metastasis (e.g. lung, liver, bone, pancreas, adrenal glands, skin, gastrointestinal) [10]. At the site of metastasis, required stromal responses and formation of blood vessels are again initiated by disseminated breast cancer stem cells [10].

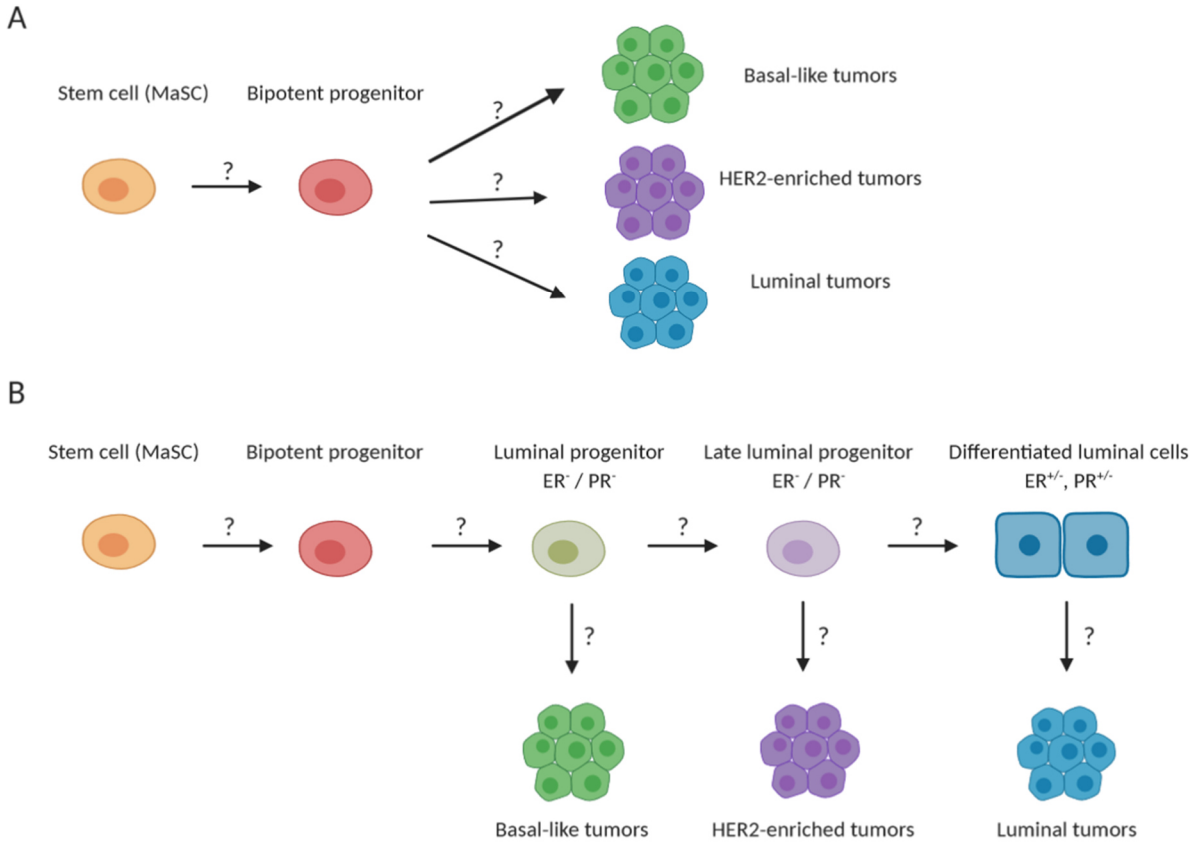

Figure 1.1.2: Hypothetical models for the development of different breast cancer subtypes
[A] The cancer stem cell theory proposes that all breast cancer subsets derive from the same mammary epithelial or progenitor stem cell by subtype-specific genetic or epigenetic mutations. [B] The tumor subtype specific hypothesis suggests that each tumor subset derives from a different cell type (single stem or progenitor cells) by gradually accumulation of random mutations, whereby the exact intermediate transforming steps are unknown so far.

Various studies have focused on determining the risk of developing metastases by using prognostic markers. In general, lymph-node metastasis, large-size tumors and loss of histopathological differentiation enhance the risk of metastasis formation [10]. In addition to molecular prognostic marker such as over-expression of HER2 or increased levels of PAI1 / uPA [10], 70 genes were identified in order to classify patients into good and poor prognosis groups [39,40]. Depending on breast cancer subtype and prognosis, different treatment options are applied (see chapter 1.1.1).

1.1.1 Treatment options for breast cancer

The primary therapy for breast cancer consists of surgical procedures that include removal of the primary tumor (along with a rim of normal tissue in order to decrease the risk of local recurrence) and axillary lymph nodes, followed by radio therapy [41]. Additional systematic therapy such as chemotherapy might be applied preoperative (neoadjuvant), postoperative (adjuvant) or both [42].

Depending on the breast cancer subtype, stage and prognosis, different systemic therapies are utilized. Hormone-receptor positive breast cancers (luminal A and B) are treated with endocrine therapies by taking advantage of the fact that estrogen plays a key role for tumor growth [43,44]. Tamoxifen and Toremefine are selective estrogen receptor modulators (SERMs), which competitively inhibit estrogen's binding to ER and, thus, act anti-estrogenic in breast tissue but estrogenic in other tissues such as liver, uterus or bone [43,45,46]. Using Tamoxifen, the cancer recurrence rate was decreased by 50 % in the first five years post diagnosis compared to control group without endocrine therapy [44]. However, resistance to Tamoxifen was observed in 30 % of women after prolonged exposure to the drug [43,47]. Various causes for resistance development have been hypothesized and include, among others, loss of ER expression, *ER* gene mutation, abnormal splicing, abnormal expression of co-regulatory proteins such as "amplified in breast cancer 1" AIB1 or interaction with growth factor signaling pathways [43,44,48]. Therefore, inhibition of the aromatase (AI), which converts androgens to estrogens, is applied in case of Tamoxifen resistant tumors in women after menopause [49,50] . Another alternative treatment approach for Tamoxifen-resistance cancer in postmenopausal women is the selective degradation of estrogen receptors with Fulvestrant, which induces degradation and downregulation of ER at protein level as well as depletion of *ER* transcriptional activation [51,52]. In addition to endocrine therapies, CDK4/6 inhibitors were proved to be beneficial for patients with ER^+ $HER2^-$ advanced (metastatic) breast cancer. The blockage of CDK4/6, whose activity is increased in cancer cells, results in a cell cycle block in mid-G1 phase, which in turn impedes proliferation of breast cancer cells [53].

In contrast, HER2 (also known as ERBB2) enriched breast tumors are treated with drugs targeting the HER2 molecule. Common therapies include Trastuzumab or Pertuzumab in combination with chemotherapy (or hormone therapy for ER^+ $HER2^+$ tumors) [54,55]. Trastuzumab, a humanized monoclonal antibody directed against the juxtamembrane region HER2, might act by the induction of an antibody dependent cellular cytotoxicity (ADCC) [56]. However, several studies also proposed that Trastuzumab inhibits dimerization and activation / phosphorylation of HER2 [55,56]. By comparison, Pertuzumab is a recombinant humanized antibody that binds to the extracellular dimerization domain II of HER2, which in turn provokes ADCC as well as inhibition of HER2 heterodimerization. Preclinical studies suggest that a combination therapy of Pertuzumab and Trastuzumab is more potent than either monotherapy [54].

Due to the lack of hormone receptors in triple negative breast cancers (TNBC), therapeutic approaches are limited and primarily include Anthracycline- and / or taxane-based chemotherapies [57,58]. However, immune checkpoint blockade therapy represents an additional treatment option for a variety of cancers, including hormone receptor positive and triple negative breast cancers [59,60]. Immune checkpoints are generally important to prevent autoimmunity and excessive immune

reactions but they often impede efficient anti-tumor immune responses [61,62]. For example, CTLA-4 is upregulated on activated T cells and attenuates TCR signaling by rivalising with the co-stimulatory molecule CD28 for the B7 ligands B7-1 (CD80) and B7-2 (CD86) [63]. The combination of Tremelimumab, a CTLA-4 antibody, and Exemestane led to an increase in peripheral ICOS (inducible costimulator) expressing $CD4^+$ and $CD8^+$ T cells relative to regulatory T cells (T_{reg} cells) in patients suffering from ER^+ metastatic breast cancer [64]. In addition, stable disease (SD) (for at least 3 months) was observed in 42 % of patients [64]. Further ongoing trials evaluate PD-1 / PD-L1 inhibitors (in combination with anti-CTLA-4 antibodies) for ER^+, $HER2^+$ and triple negative breast cancers [60,65]. PD-1 is upregulated on activated T cells and acts as a negative costimulatory signal upon binding to its ligand PD-L1, which is widely expressed in tumor-infiltrating immune cells and nonlymphoid tissues including breast cancer cells [66,67]. In fact, the FDA and EMA approved a checkpoint-inhibitor, Atezolizumab, in combination with Nab-paclitaxel, a novel formulation of Paclitaxel, for the treatment of PD-L1 positive TNBC. Phase III clinical trial (NCT02425891) demonstrated median progression-free survival of 7.4 months and complete response in 9 % vs. 4.8 months and 1 % in the control group [57,58]. Moreover, clinical trials are investigating combinations of the anti-HER2 therapy with checkpoint inhibitors using Trastuzumab and Pembrolizumab (NCT03747120, NCT02901301).

Nevertheless, the problem of many standard therapies is that they act on rapidly dividing cells and usually fail in complete eradication of breast cancer stem cells, which often remain in a quiescent state [68-70]. In fact, chemotherapies lead to increased frequencies of tumorigenic $CD44^+/CD24^{-/low}$ cells [69]. Moreover, different trials indicate that breast cancer stem cells might play a key role or rather be the origin for resistance to endocrine therapies [68-71]. Therefore, many trials are focusing on the treatment of breast cancer stem cells. Possible therapeutic approaches, among others, include the application of nanoparticles encapsulating chemotherapeutic agents or DNA hypermethylation inhibitors [72,73] and the use of anti-CD44 [73,74] or anti-CD133 antibodies [73]. Safety and effectiveness of both nanoparticle (NCT03749850, NCT02425891) [73,75] and antibody based therapies (NCT02254005) [76] are evaluated in clinical trials.

Other therapeutical approaches, which are focusing on the improvement of T cell mediated anti-tumor immune responses by vaccinations, such as tumor cell or lysate, recombinant viral vectors, heat shock proteins, tumor peptides, DNA, RNA or DC-based vaccines, are under development [77,78]. For example, treatment of hormone receptor positive breast cancer patients with NeuVax, a breast cancer vaccine that recognizes the HER2 - derived peptide E75 (nelipepimut-S) combined with the immune adjuvant granulocyte macrophage colony stimulating factor (GM-CSF), provoked improved overall survival and was well tolerated in clinical trials [77]. Peptide-based vaccines with Muc1, a protein that is overexpressed in the majority of breast cancers, or Muc1 tumor-associated antigens are tested in clinical trials [78]. Both HER2 and Muc1 are also widely used for DC-based vaccine strategies [78]. In

addition, several studies are ongoing for personalized RNA vaccinations, especially for triple-negative breast cancer patients [78,79].

Next to vaccinations, different preclinical and clinical trials with *ex vivo* expanded tumor-infiltrating T cells or CAR^+ T cells directed against HER2, Muc1, Mesothelin or cMet are ongoing and will be further explained in chapter 1.2.1.1. [80,81].

1.1.2 The breast cancer associated antigen NY-BR-1

Tumor associated antigens (TAAs) are proteins, glycoproteins, glycolipids or carbohydrates, which represent attractive targets for diagnostic and therapeutic approaches [82-84]. However, in contrast to tumor specific antigens, TAAs are not selectively expressed in tumor tissues and are classified according to their expression patterns [82,83]. For example, differentiation antigens are defined by the expression in tumors in a lineage-associated pattern and in normal healthy tissues (or at differentiation stages of special cell types) of the same origin. In contrast, tumor germline ("tumor-testis") antigens can only be found in cancers, gametes and trophoblasts but not in normal healthy tissues [83]. Antigens which are overexpressed in tumors compared with normal cells or tissues represent another class of TAAs and might be useful vaccine targets [82-84].

The breast cancer associated antigen NY-BR-1 (New York Breast 1), also known as Ankyrin repeat domain-containing protein 30A, was identified by applying the strategy of "serological identification of antigens by recombinant expression cloning" (SEREX) [85]. This technology was developed by Sahin *et al.* (1995)[86] and is based on tumor cDNA expression libraries, which are cloned into λ phage expression vectors for subsequent transfection of *E.coli*. Afterwards, diluted autologous sera from breast cancer patients are screened using phage plaques containing nitrocellulose membranes. Positive clones, which are usually detected by secondary anti-human IgG antibodies, are isolated and sequenced [86,87].

Different SEREX and computational analysis revealed that the *NY-BR-1* gene is located on chromosome 10p11-p12, has an open reading frame of 4.2 kb and consists of 37 exons, whereby multiple repetitive sequences were found [85]. In addition, the NY-BR-1 protein exhibits a bipartite nuclear localization signal, five tandem ankyrin repeats and a bZIP site (DNA-binding site followed by leucine zipper motif) [85]. Moreover, four estrogen receptor response elements (EREs) nearby the promoter region of *NY-BR-1* were identified [88]. Additionally, a 54% amino acid homology to a protein (NY-BR-1.1) expressed in brain, breast and testis was found [85]. However, the exact function of NY-BR-1 could not be defined so far

Specific feature of this protein is its restricted expression to epithelium of normal healthy breast, testis and prostates as well as its over-expression in over 70 % of primary breast tumors (non-invasive

and invasive ductal / lobular carcinoma) and metastasis [89-91]. RNA microarray - based studies, performed by Radvanyi *et al.* (2005)[92], compared gene expression profiles of 54 breast cancers with 289 normal tissue samples and even demonstrated an average overexpression of *NY-BR-1* by a factor of 52 fold over normal tissues [92]. Further immunohistochemistry and bioinformatic analyses showed that this 158 kDa protein is located in both the membrane and cytoplasm [91,93]. In fact, bioinformatic analyses suggest that the membrane-bound NY-BR-1 protein has two transmembrane domains close to the N terminus site but extracellular N and C terminal sites [93]. Nevertheless, breast cancer cell lines seem to be negative for NY-BR-1 (surface) expression [89,93] .

Diverse expression analyses of breast tumors suggest the presence of alternative splice variants. Theurillat *et al.* (2008)[88] demonstrated that *NY-BR-1* expression was significantly stronger and more frequently detected by probes binding within exons 30 – 33 than by exons 4 – 7 by using *in situ* hybridization experiments. Moreover, NY-BR-1 protein expression directly correlates with the grade (grade 1: 82 %, grade 2: 69 %, grade 3: 46) [94], estrogen receptor [88,94] and HLA class I expression [94]. In fact, 70 % of ER positive tumors exhibit NY-BR-1 expression and tumors showed reduced NY-BR-1 expression levels after tamoxifen treatment expression [88,94]. In contrast, *HER2*-gene and EGFR status inversely correlate with NY-BR-1 expression [94].

Another important aspect of this differentiation TAA is its immunogenicity, since NY-BR-1 induces both humoral and cellular immune responses. 7 % out of 43 tested patients with NY-BR-1$^+$ breast cancers exhibited NY-BR-1 specific antibodies [95]. Furthermore, diverse NY-BR-1 specific CD8$^+$ and CD4$^+$ T cell restricted epitopes were found by co-cultivation of patient derived T cells with NY-BR-1 proteins [96,97] or NY-BR-1 specific DNA immunization of HLA transgenic mice [98] .

Thus, the overexpression of NY-BR-1, with its simultaneously limited expression pattern and immunogenic properties, make this protein a promising target for antibody or T cell - based immunotherapies.

1.2 Cancer immunotherapy

Immunotherapy is defined as the “fifth pillar” of cancer therapy along with surgery, chemotherapy, radiation and targeted therapy. Basis for cancer immunotherapy is the capability of the immune system to detect and kill nascent transformed cells, as depicted in the “immune surveillance” theory (first described from Paul Ehrlich) [99]. However, due to new findings, such as the fact that the immune system exerts both host-protecting and tumor-sculpting effects, the “immune surveillance” theory was replaced with the term “cancer immunoediting” [99]. Cancer immunoediting includes three processes: elimination / immune surveillance, equilibrium and escape [99,100]. During the elimination process, both the innate and adaptive immune system recognize transformed cells due to the expression of tumor-specific or stress induced antigens [99,100]. However, surviving tumor cells enter the equilibrium phase, in which remaining tumor cells are under selection pressure leading to tumor cell variants with greater capacity for immune evasion. The following escape phase is characterized by the induction of immune tolerance and survival or rather outgrowth of tumors [99-101]. The underlying mechanisms are very diverse and include, among others, decreased expression levels of human leukocyte antigens (HLA) class I [100,101], adhesion and costimulatory molecules [101] or the loss of antigens [99-101]. Moreover, an immunosuppressive tumor microenvironment occurs because of increased expression of immunosuppressive components (e.g. PD-L1) or release of immunosuppressive cytokines and metabolites [99-101]. Therefore, cancer immunotherapies are aiming to activate immune cells or to affect the tumor itself or its microenvironment by monoclonal antibodies, oncolytic viruses, vaccines, immune checkpoint inhibitors, cytokines or adoptive cell therapies, many of which are currently applied in breast cancer treatment (see chapter 1.1.1) [102].

1.2.1 Adoptive cellular therapy

Although targeted therapy or checkpoint blockade achieved great results for different cancer types, a large proportion of patients develop disease progression. Therefore, the adoptive immunotherapy is a promising approach for cancer treatment in which naturally occurring or gene-engineered antigen-specific lymphocytes, especially T cells, are expanded *ex vivo* and transferred back to the patient [103-105]. Adoptive cell therapy (ACT) is classified into three different types: tumor-infiltrating lymphocytes (TILs), T cell receptor (TCR) – engineered and chimeric antigen receptor (CAR) modified T cells [104]. Adoptive TIL therapy was originally developed for patients with metastatic melanoma and is based on the *ex vivo* expansion of TILs with subsequent adoptive transfer into the patient [103,106]. Indeed, clinical trials demonstrated that 50 % of those melanoma patients treated with TILs and high doses of IL-2

after lymphodepleting chemotherapy exhibited objective response rates and 24 % showed complete remission [106-109]. Moreover, TILs can be isolated from solid tumors such as breast, renal, non-small cell lung or cervical cancers and represent a promising source for ACT [104]. Nevertheless, the therapeutic use of TILs is limited due to usually low cell yield and weak cytolytic activity of the obtained T cells [110,111]. Therefore, the real impact on solid tumors is investigated in many pre- and clinical trials [104]. A disadvantage of TIL based immunotherapies is the heterogeneity of the administered TIL population, which contains both non-tumor and tumor reactive T cells of unknown specificities, so that an expansion and reinfusion into the patient lead to auto reactivities or weakened anti-tumor responses [112]. The identification of tumor-reactive populations by using different markers (e.g. PD-1, LAG-3, TIM-3, CD137) improve this therapeutic approach but the problem of unknown specificity remains [112-114]. Single cell sequencing or RT-PCR analysis helps to identify the TCR clonotypes, which allows the generation of gene-engineered TCR^+ T cells [113-115].

In general, TCR based gene therapies had great success in the treatment of various types of cancers such as metastatic melanoma, synovial sarcoma or colorectal cancers [116]. However, the HLA restricted antigen recognition by TCRs represents a fundamental problem since HLA presentation is often deregulated in tumors due to defects in antigen processing or the downregulation of HLA molecules [117-119]. Furthermore, HLA molecules are highly polygenic and polymorphic. In fact, the HLA family consists of more than 200 genes, which are characterized by extraordinary polymorphism with >1,980 unique known alleles, leading to a high diversity of HLA molecules and HLA-peptide complexes between individuals [120,121]. As a consequence, TCR therapies have to be individualized to ensure recognition of epitopes presented by HLA complexes and to prevent cross- and allo-reactivities [122]. Moreover, numerous tumor specific carbohydrates or glycolipid structures are not presented via HLA molecules. In addition, TCR mispairing, which can occur between endogenous and exogenous TCR heterodimers following viral transfer of TCR genes, represents an appreciable risk of autoreactivity and reduced therapeutic efficacy [123-125]. Various strategies are being worked on to minimize this risk of TCR mispairing. These include genomic knockout of the endogenous TCR [124], murinized TCRs (mouse constant domains) [126], fusion of TCR chains to CD3ζ transmembrane and signaling subunits [127] or addition of interchain disulfide bonds within the constant domain of the introduced TCR [123,128].

1.2.1.1 Chimeric antigen receptor therapy: design, strategy and challenges

Chimeric antigen receptors are synthetic immune receptor composed of distinct modules derived from antibodies, TCRs and T cell derived co-stimulatory domains. Such antibody based recombinant receptors consist of the antigen binding domain, which is linked to an extracellular spacer, and

transmembrane and intracellular signaling domains (see Figure 1.2.1) [129-131]. For the generation of HLA independent antigen recognizing receptors, TAA specific single chain variable fragments, derived from the variable portions of both the light and heavy chains of a monoclonal antibody, are fused via a flexible linker (e.g. Gly4Ser3) and enable the recognition of a wide range of antigens, including carbohydrates, proteins, gangliosides and HLA presented antigens [129-131]. However, CARs are not limited by available antibodies. Alternative binding domains derive from ligands [132], adnectins [132], nanobodies[133] or extracellular parts of a receptor, such as the NKp-30 CAR, which was developed by Zhang et al. (2012) [134]. The antigen binding region is usually bound to an IgG-(CH2/CH3) derived spacer domain [130]. Alternatively, hinge regions derived from the extracellular domains of CD8 and CD28, lacking FcγR binding activity, have been used [135]. The spacer domain provides flexibility and stability for efficient CAR expression, whereby the length is very crucial for optimal formation of immunological synapses [130]. Moreover, the spacer domain can be used for the detection of CARs on T cells' surfaces. The transmembrane (TM) region consists of a hydrophobic α helix, mainly derived from CD3, CD4, CD8 or CD28, and affects surface CAR expression levels and receptor aggregation [129-131]. The intracellular domains of the earliest CARs just consisted of cytoplasmic tails derived from TCRs [136]. The incorporation of a single CD3ζ endodomain was an important improvement for CAR functionality [137] but these first generation CARs led to T cell anergy and low proliferation rates [138]. Further development of CARs resulted in second and third generation CARs with one or two additional co-stimulatory domains, which provide the required, additional activation signals and led to enhanced clinical responses and persistence (see Figure 1.2.1) [129,130]. Latest developments have led to TRUCKs (T cells redirected for universal cytokine killing), which were engineered in order to produce and release special, mostly pro-inflammatory cytokines upon CAR activation, and represent CARs of the fourth generation [139].

The choice of co-stimulatory domains is a very important consideration for the functional and metabolic properties of CAR - expressing T cells [131,140,141]. A wide variety of co-stimulatory molecules such as CD27, CD28, CD134 (OX40), CD137 (4-1BB) or CD154 (CD40L) have been successfully tested, whereby most studies to date are being conducted with CD28 and 4-1BB based CARs [141]. Various studies demonstrated that CD28 co-stimulation promotes the development of a short lived, effector memory phenotype with enhanced glycolysis and IL-2 secretion, whereas 4-1BB bearing CAR^+ T cells show characteristics of a central memory phenotype, increased oxidative metabolism and decreased exhaustion [141,142].

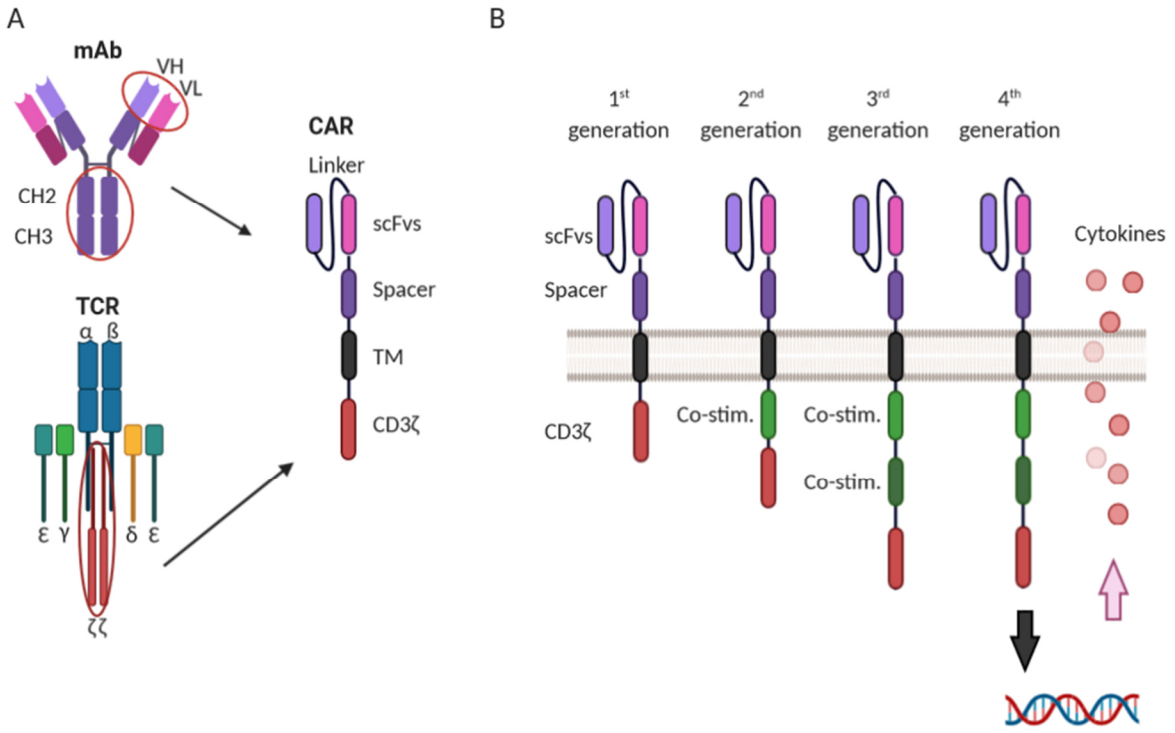

Figure 1.2.1: Architecture of chimeric antigen receptors of different generations
[A] Chimeric antigen receptors consist of linked scFvs derived from variable regions of both the light and heavy chains of a mAb, a spacer domain often derived from the IgG CH2/CH3 domain, a transmembrane region mainly derived from CD3, CD4, CD8 or CD28 and the intracellular CD3ζ endodomain. [B] CARs of the first generation exhibited one intracellular signaling domain (CD3ζ). The addition of one or two co-stimulatory domains (e.g. CD28, 4-1BB, OX40) led to CARs of second and third generations. The fourth generation of CARs can induce the production and release of cytokines in T cells following antigen binding via activation of downstream transcription factors.

In general, activation of CAR$^+$ T cells occurs upon ligation of scFvs to antigen, which provokes aggregation of CAR polypeptides [143]. Due to the integration of the CD3ζ endodomain, which contains three immunoreceptor tyrosine-based activation motifs (ITAMs), the intracellular activation pathway proceeds via the classical ZAP70 mediated pathway [144]. First, ITAMs are phosphorylated by src-kinases (Lck and Fyn). ZAP70/Syk protein tyrosine kinases then bind to the phosphorylated ITAMs, which in turn leads to full activation of ZAP70. Afterwards, the adapter proteins LAT and SLP-67 are phosphorylated, which provokes recruitment and activation of further kinase families and enzymes. One of the most important signaling pathways is the phospholipase C-IP3 pathway, which finally ends in activation of different transcription factors such as NF-κB [145,146]. The co-stimulatory domains support the activation of T cells by initiating different signaling pathways such as the PI3/Akt pathway (in case of CD28), which results in expansion and high IL-2 production, or the TRAF/Erk or MAPK/Erk (in case of 4-1BB) pathways leading to T cell activation and differentiation [145,147].

In order to eliminate cancer cells upon formation of the immunological synapse, CAR$^+$ T cells mainly use the exocytosis of cytotoxic granules containing perforin and granzymes without the need for death

receptor molecules on the target surface [148,149]. Perforin is a glycoprotein that forms pores with a size of 5 to 20 nm in target cells by polymerization in a Ca^{2+} dependent manner, facilitating the entry of pro-apoptotic granzymes [148]. Furthermore, different studies revealed the existence of an antigen-independent bystander killing mechanism that is based on the Fas/FasL pathway [149]. FasL is upregulated upon CAR$^+$ T cell activation and can lead to the trimerization of Fas receptors, which in turn results in the activation of caspase 8 and final cell death [149].

Generation of the first CARs was reported over 30 years ago [136,137]. Since then, there has been a continuous development until first successful clinical trials with CAR$^+$ T cells were reported. The treatment options for hematological diseases especially have been revolutionized by CAR$^+$ T cell therapy [150,151]. Here, the best investigated target is CD19 as it is expressed on the surface of B cells at most stages of their development as well as on most B cell malignancies including acute lymphoblastic leukemia (B-ALL), chronic lymphocytic leukemia (B-CLL), diffuse large B-cell lymphoma (DLBCL) and B-cell non-Hodgkin lymphoma (NHL) [150-152]. Different clinical trials for B-ALL demonstrated impressive outcomes with response rates of up to 60 - 90 % and complete remission rates of 70 – 90%, depending on the different therapeutic processes, patients' age and usage of various co-stimulatory domains [150,151,153,154]. In 2017, the FDA approved the first CAR$^+$ T cell therapy for children and young adults with refractory B-ALL. However, despite high response rates, many patients suffer from relapses (30 to 60 % of ALL patients) because of antigen loss (10 to 20 % of ALL patients develop CD19 negative relapse), T cell exhaustion or limited persistence of CAR$^+$ T cells [155]. Therefore, strategies such as the expression of several CARs (CD19, CD20, CD22) in one T cell, the use of CAR$^+$ T cells with central memory / stem cell like memory phenotypes or a combination therapy with checkpoint inhibition are pursued [155].

Nevertheless, critical point and challenge of CAR$^+$ T cell therapy is the balance between efficiency and risk. It is important to prevent unwanted or excessive CAR$^+$ T cell responses, as these can contribute to dangerous side effects. In general, the most common side effect of CAR$^+$ T cell therapy is cytokine release syndrome (CRS) [156,157]. This toxicity occurs in almost 70 - 90 % of patients treated with anti-CD19$^+$ CAR-T cells and is associated with fever, fatigue, headache, arthralgia, myalgia and malaise [156,157]. The release of high levels of inflammatory cytokines such as IFNγ and GM-CSF by CAR$^+$ T cells and IL-6 by macrophages, monocytes and endothelial cells leads to systemic inflammatory responses [156,158,159], which can be treated with Tocilizumab (a humanized anti-human IL-6R monoclonal antibody) or immunosuppressive agents (e.g. corticosteroids) [159].

Despite the success of CAR - based T cell therapies for hematological malignancies, prevention of toxic side effects is also one of the major challenges in translating CAR$^+$ T cell therapies for treatment of solid tumors. Here, the major obstacles are the heterogeneity of solid tumors and lack of tumor specific antigens, since the expression of the target antigen in healthy tissue increases the risk of on-target/off-tumor toxicity [160]. B cell aplasia can be accepted in the case of CD19 CAR$^+$ T cell therapy [161],

whereas targeting of many other non-tumor specific antigens can be fatal in the treatment of solid tumors. For example, a patient suffering from malignant colon carcinoma died after treatment with anti-HER2 CAR$^+$ T cells, as HER2 was also expressed at low levels in epithelial cells of the lung [162]. Furthermore, CAR$^+$ T cell trafficking and infiltration into the tumor are often impeded by tumor-associated fibroblasts, myeloid cells forming extracellular matrix (ECM) and an immunosuppressive tumor microenvironment [160].

There is currently no approved CAR$^+$ T cell therapy for the treatment of breast cancer, but many clinical studies are ongoing. In fact, one promising clinical trial evaluates the functionality and safety of the huMNC2-CAR44, which binds to the cleaved form of Muc1 (called Muc1*). Muc1* acts as a growth factor receptor and is associated with a high percentage of solid tumors, including breast cancer (NCT04020575). Further promising clinical studies have been conducted or are currently ongoing with anti-EGFRVIII CARs (NCT01454596, NCT03726515). EGFRVIII is an oncogenic variant of EGFRV [163], which has been particularly identified in a high proportion of glioblastoma multiforme (GBM) brain tumors [164]. Several studies suggest that EGFRVIII is also involved in tumorigenicity, invasiveness, and metastasis in breast cancer [165,166], so that anti-EGFRVIII CAR therapy could possibly be applied to breast cancer patients.

1.2.1.2 Three different anti-NY-BR-1 CAR candidates

Overexpression of the NY-BR-1 protein in more than 70 % of breast cancer tumors [95] makes NY-BR-1 an interesting target for CAR - based immunotherapy (see chapter 1.1.2). Three different CAR candidates were designed on the basis of the mAbs clone2, 10D11 and clone3 in our group. The mAbs clone2 and clone3 were generated by NY-BR-1 peptide (aa 851-928) immunization of BALB/c mice [167], whereas the 10D11 antibody was identified by NY-BR-1 full length immunization (unpublished). All three mAbs recognize different epitopes within the NY-BR-1 protein, which were identified by PEPperPRINT or group internal analyses (unpublished data; see Figure 1.2.2).

Figure 1.2.2: Binding sites of the anti-NY-BR-1 mAbs clone2, 10D11 and clone3
The 10D11 antibody binds close to the N-terminus (aa 51 – 60) of NY-BR-1 protein, whereas the epitopes of clone3 (aa 748 – 764) and clone2 (aa 989 -909) antibodies are located in the middle or next to the C-terminus. The two predicted transmembrane (TM) regions are displayed at aa 147 – 167 and aa 208 – 228.

Furthermore, BLAST analyses demonstrated high similarities between the NY-BR-1 and NY-BR-1.1 proteins within the CAR / antibody epitopes (see Figure 1.2.3). In fact, the two proteins differ only in one amino acid within the clone2 epitope and in three or more than 10 aa within the epitope sequences of the 10D11 and clone3 CARs.

These preliminary results suggested that this thesis should focus on both efficiency and safety analyses of all three anti-NY-BR-1 CARs, especially with regard to cross-reactivity.

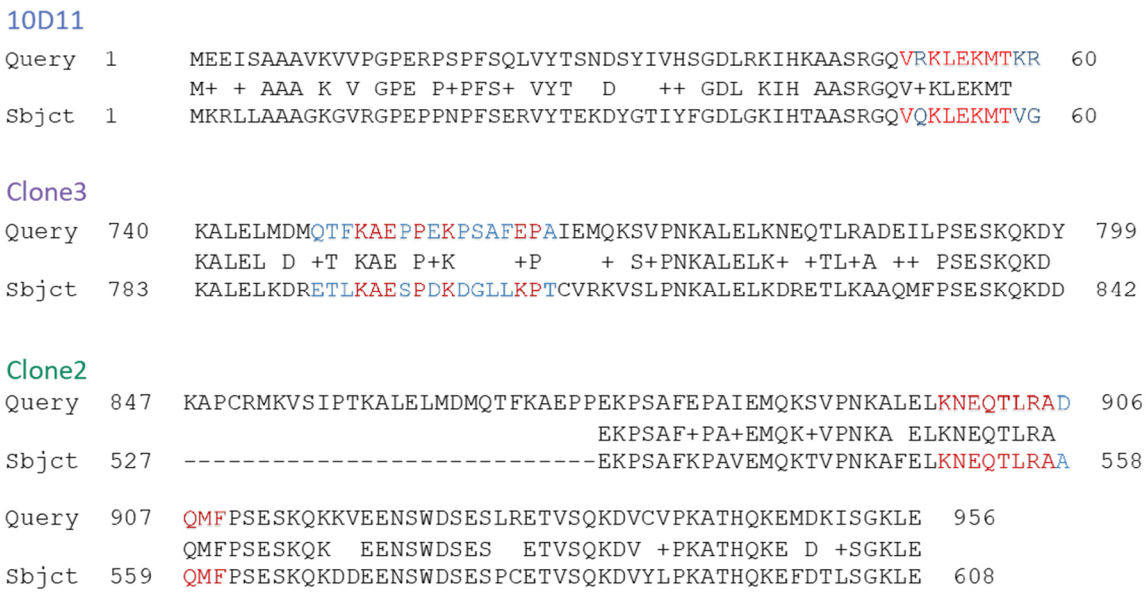

Figure 1.2.3: Similarities of the NY-BR-1 and NY-BR-1.1 proteins within the epitopes of the mAbs clone2, 10D11 and clone3 BLAST analysis of the NY-BR-1 and NY-BR-1.1 proteins. The epitopes of the mAbs 10D11, clone3 and clone2 are given. Matching amino acids are colored red, while different amino acids are marked blue within the epitope sequences.

1.2.2 Current methods for the generation of genetically modified mammalian cells

Genetic modification is an important technique for the generation of stably protein expressing cells. In particular, genetically modified immune cells expressing, for example, TCRs or CARs are already successfully applied in adoptive cellular therapies. The most widespread technologies for genetic modifications are based on viral (retro- or lentiviral) transduction systems [168] (see chapter 1.2.2.1). However, due to the oncogenic potential of viral vectors, non-viral approaches such as the CRISPR/Cas9 genome editing system [169,170], Sleeping Beauty transposons [171] or electroporation with innovative S/MAR based vector systems [172](see chapter 1.2.2.2) moved more and more into the focus for the generation of genetically modified mammalian cells.

1.2.2.1 Lentiviral transduction system

Lentiviruses belong to the family of *Retroviridae*, group VI, single-stranded RNA. Their genome consists of at least three basic genes *gag*, *pol* and *env* for survival, replication and functionality [168,173]. In fact, g*ag* encodes for capsid proteins, *pol* for replication enzymes such as the reverse transcriptase and integrase and *env* for envelope glycoproteins [168,173]. Human immunodeficiency virus (HIV) also has two regulatory genes (*tat*, *rev*) for initiation of viral replication and four accessory genes (*vif*, *vpr*, *vpu*, *nef*) that are crucial for *in vivo* replication, virus budding and pathogenesis [174]. On the basis of lentiviruses (primarily HIV), lentiviral gene delivery DNA vectors were developed in order to produce non-replicating, transducing particles [173]. Production of these lentiviral vector particles is usually performed by co-transfection of a lentivirus producer cell line (e.g. HEK 293T) with a minimum of three plasmids: transfer (harbouring the LTR flanked gene of interest), envelope (harbouring *env*) and packaging vector (harbouring *gag* and *pol*) [173,175]. According to the natural lentivirus life cycle, the lentivirus-like particle binds to its target cell and viral proteins such as the reverse transcriptase and integrase as well as viral RNA encoding for the gene of interest are released into the cytoplasm of the target cell (see Figure 1.2.4). Subsequently, viral RNA is reversely transcribed to pro-viral DNA, imported into the nucleus and randomly integrated into the genome using viral proteins [173,175]. To minimize the risk of self-replication, genes encoding for viral packaging and transduction machineries are expressed from separate plasmids in 2nd and 3rd generation lentiviral systems (see above). Furthermore, so-called self-inactivating vectors (SIVs) were designed by deletion of 3'-LTR elements (including TATA-box) [175-178]. The abolished LTR promoter activity reduces the risk of spontaneously

produced replication-competent viruses but does not impair viral titers [176,177] or lentiviral transduction efficiency [175-177].

Lentiviral transduction generally offers many advantages such as the infection of both non-dividing and dividing cells [175,179,180], long term gene expression and capability to transduce a broad range of cell types [173,175,181,182]. Although lentiviruses, in contrast to other retroviruses, favor active transcriptional units for integration [175,183], the integration site is random and uncontrolled to a certain extent, which might affect the clinical outcomes and implies a certain risk of integration-mediated oncogenesis [175,184,185].

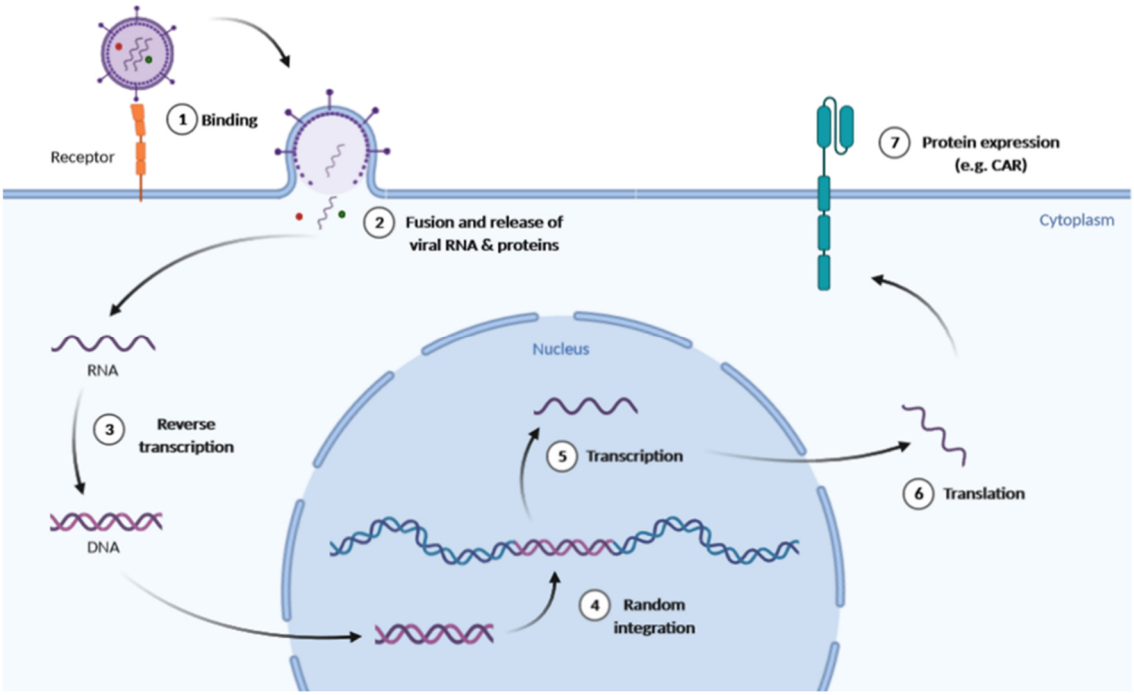

Figure 1.2.4: Schematic representation of lentiviral transduction
Lentiviral vector particle binds to the target cell via interactions between its viral envelope glycoprotein and the specific target antigen. Upon membrane fusion of the lentivirus-like particle with the host cell, viral RNA and proteins are released into the cytoplasm of the target cell. The RNA is reversely transcribed to cDNA that is in turn transported into the nucleus and randomly integrated into the host genome. Finally, the gene of interest is transcribed and translated with the host machinery leading, for example, to surface expression of chimeric antigen receptors.

1.2.2.2 DNA vector technologies

Transfection of mammalian cells with plasmid DNA (pDNA) is transient and transgene expression is often lost after a few days, since the gene of interest is not stably integrated into the host genome and therefore diluted by cell division [186,187]. Moreover, the co-occurrence of epigenetic events and immune responses against bacterial sequences might impair gene expression or even contribute to gene

silencing [187]. Therefore, stable episomal vectors are required. The attempt to generate such vectors by integrating genetic elements of viral plasmid replicons such as the Similian virus 40 (SV40) or Epstein-Barr virus (EBV) was successful to a certain extent [186,187]. Those vectors are transfected as naked DNA and contain a viral origin of replication and viral early genes. However, SV40 derived episomal vectors often led to cell death due to high replication rates and associated increasing copy numbers per cell [186,188]. In addition, they require viral proteins such as the large T antigen for initiation of replication, which represents a safety problem [187,189]. By comparison, EBV based vectors led to the greatest progress in the development of virus-based episomal vectors. They demonstrated retention and replication in different cell types such as human epithelial [190] and lymphoma cells [190-192] via interactions of the origin of replication (oriP) and trans-acting factor EBNA1 (EBV nuclear antigen-1) (see Figure 1.2.5) [186,187]. Nevertheless, EBV-based episomes do not have a retention rate of 100 % in the absence of antibiotic selection, whereas integration of the plasmid into the host genome can be provoked by continuous selection [187]. Furthermore, safety concerns remain due the need of viral proteins (EBNA1) [193,194].

Due to risks associated with virus-based episomal vectors, other approaches focused on finding chromosomal DNA elements that might support episomal existence and replication of pDNA. One of these chromosomal DNA elements are scaffold matrix attachment regions (S/MARs), which are responsible for the attachment of chromatin to nuclear matrix proteins during interphase [195]. The exact effect of AT rich S/MAR domains on gene expression is not clear but looped domains, which are formed by binding of S/MARs to the nuclear matrix, play a key role in many cellular processes, including DNA replication, transcription, DNA repair, RNA processing and signal transduction [187,196]. Indeed, different studies suggest that S/MARs might act as insulators and augment transcription by insulating coding regions from methylation effects [197-199], enabling access of transcriptions factors to promoters and enhancers [187,200], interacting with chromatin remodeling proteins (such as Bright, SAF-A and p300) [201,202] or nuclear matrix proteins such as SAF-B and SATB1 [187].

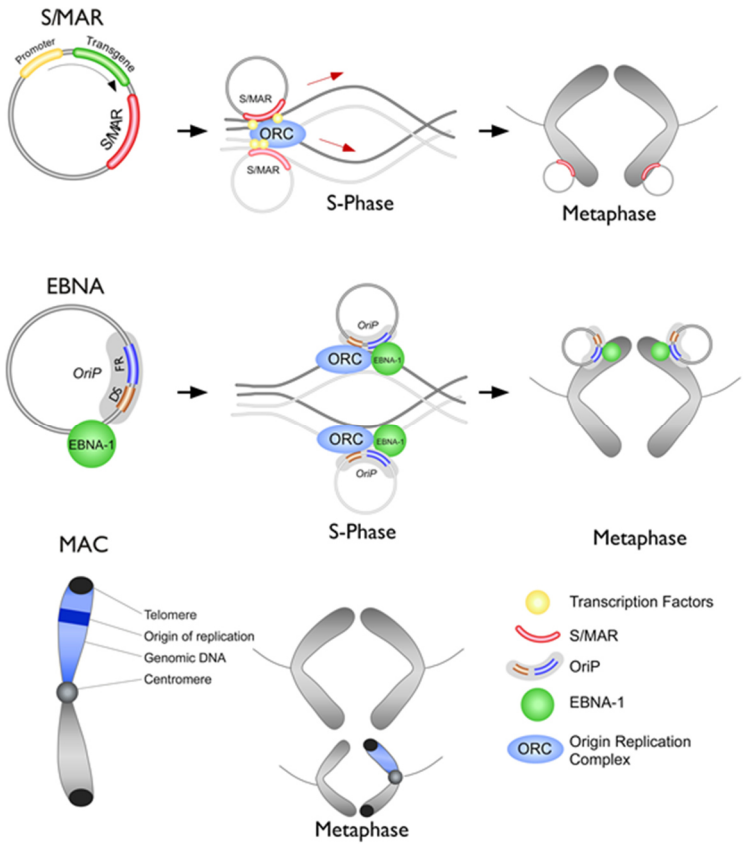

Figure 1.2.5: Schematic representation of episomal retention and replication of S/MAR and EBV based vectors
In contrast to EBV, S/MAR derived vectors do not need viral proteins for episomal retention and replication. It is suggested that S/MAR binds to mitotic chromosomes via interactions with the nuclear scaffold attachment factor A (SAF-A) and recruiting of nuclear components, which results in helix destabilization and opening of chromatin domains at the origin of replication. EBV based vectors are replicated via a "piggy back" mechanism initiated by association between EBNA1, the viral origin of replication (oriP), and the host ORC. Figure derived from Wong et al. (2015)[187].

The first episomal maintaining S/MAR vector (pEPI) containing only mammalian sequences for its replication was described in 1999 [203]. This vector provided long term gene expression in different cell lines such as CHO [204], HeLa [205], pluripotent p19 embryonic carcinoma [206] and human hematopoietic stem cells [207] *in vitro*. Further development of this vector type by, for example, replacing lentiviral with tissue-specific promoters [208] or integration of insulators led to more stable and longer-lasting expression of transgenes *in vitro* and *in vivo* [187]. However, several studies demonstrated that transgene expressions were very low in pEPI transfected cells [172,187,209].

Removal of fI Ori, use of Kanamycin resistance gene, and decoupling of S/MAR functionality from transgene expression and linkage to Puromycin resistance gene expression led to the so-called pS/MART vectors, which, indeed, resulted in enhanced transgene expression levels compared to appropriate pEPI vectors[172] (see Figure 1.2.6). To further optimize the pS/MART vector system, genomic insulators (e.g. anti-repressive element 40) were introduced before the mammalian promoter and the ß-globulin derived S/MAR domain was replaced with the Apolipoprotein L (ApoL) MAR motif [172]. These pS/MARter vectors were much more efficient than their predecessors [172].

As bacterial sequences in plasmids can be responsible for triggering inflammation or gene silencing by *de novo* methylation at CpG sites [187,210] , minimally sized DNA vectors, so-called minicircles, were designed. In fact, several groups demonstrated that minicircles provoke higher and prolonged levels of gene expression [187,211,212]. Based on this technology, NanoCMARter vectors were designed (unpublished; patent WO2019/060253Al). In contrast to pS/MARter vectors, NanoCMARter vectors no longer contain bacterial antibiotic resistance genes and have a minimally sized bacterial backbone (see Figure 1.2.6).

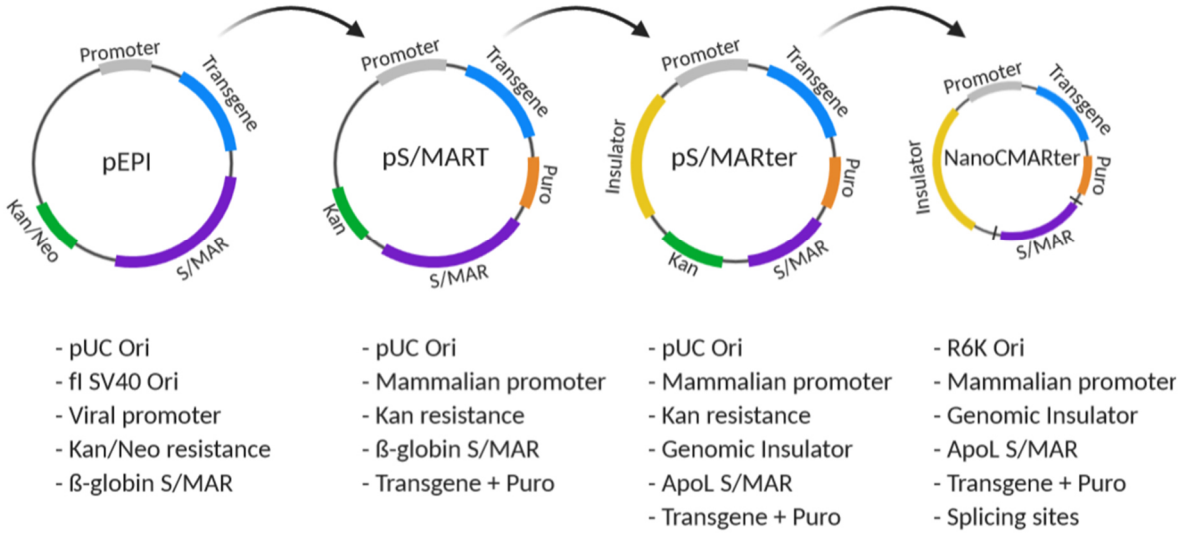

Figure 1.2.6: Schematic representation of the “next generation” S/MAR based vector systems

1.2.3 Mouse models for preclinical studies

In order to evaluate the effectiveness and safety of new cancer therapies, preclinical studies in appropriate animal models are still indispensable. In particular, the mouse has proven to be suitable for preclinical cancer research as this low cost and easy-to-handle model exhibits many similar anatomical, cellular and molecular characteristics to humans [213]. However, it is difficult to emulate the whole process of tumorigenesis in mice. Therefore, the critical point is the examination of the most suitable mouse model. Since chronic exposure of carcinogens is a time intensive and expensive approach, which is not suitable for all cancer types, syngeneic, xenograft and genetically engineered mouse models represent the most common models [213,214]. Implanting of mouse cells into immunocompetent mice of the same genetic background describes the syngeneic model (allotransplantation), whereas implanting of human derived cells into immunodeficient or humanized mice defines the xenograft model. In both cases, tumor cells are injected ectopically (most subcutaneously), which means that the transplantation site is not the origin of the tumor cells, or orthotopically to induce tumor progression at the same site / organ of origin [214].

Genetically engineered mouse (GEM) models represent the second most common type of mouse model in oncology research and offer opportunities, among others, to study the role of a specific gene or cooperation of individual mutations in tumor development, to model familial cancer predisposition syndromes, and to image molecular, cellular or anatomical changes using reporters [214]. Another benefit of GEM modeling, with respect to immunotherapy, is that fully immunocompetent mice can be used. GEM models are generated by using different strategies: retroviral vector infection of mouse embryos, microinjection of DNA into the pronuclei of fertilized mouse oocytes and genetic manipulation of embryonic stem cells [215]. Several mutation techniques, including site-specific recombinase (SSR) (e.g. Cre-loxP, Flp-FRT) and transposon systems, gene silencing by short hairpin RNA, genome editing with programmable endonucleases (CRISPR/CAS9, Zinc-finger nucleases) and random integration of oncogenes under the control of a tissue-specific promoter, are currently available to generate the required knock-in, knock-out or transgenic mouse models [214,215].

1.2.3.1 NY-BR-1 transgenic mouse model

The NY-BR-1$^{tg/-}$ mouse model was generated by microinjection of NY-BR-1 - encoding DNA into fertilized oocytes from C57BL/6 mice via cooperation between the IBF Heidelberg and our group (see Figure 1.2.7). Random integration of this transgene into the mouse genome resulted in transgenic offsprings that were heterozygous for *NY-BR-1* (unpublished). A homozygous transgenic mouse line

could only be generated to a limited extent by crossing the offspring. The mouse mammary tumor virus long terminal repeat (MMTV-LTR) promoter was originally chosen for its tissue specificity, which was demonstrated in several transgenic mouse models such as the MMTV-PyMT mouse. In this model the polyomavirus middle T antigen (PyMT) is selectively expressed in the mammary glands leading to transformation of the mammary epithelium and development of metastatic lesions in lymph nodes and lungs [216,217]. However, NY-BR-1$^{tg/-}$ mice do not show development of mammary adenocarcinomas or metastatic lesions and, additionally, the expression of NY-BR-1 is not restricted to mammary glands. Different RNA based analyses revealed *NY-BR-1* expression in various organs, especially in mammary and salivary glands as well as in the uterus, thymus, lung and colon (unpublished). Nevertheless, the presence of *NY-BR-1* expression in various organs makes this mouse model suitable for safety and efficiency analyses of the three anti-NY-BR-1 CAR candidates.

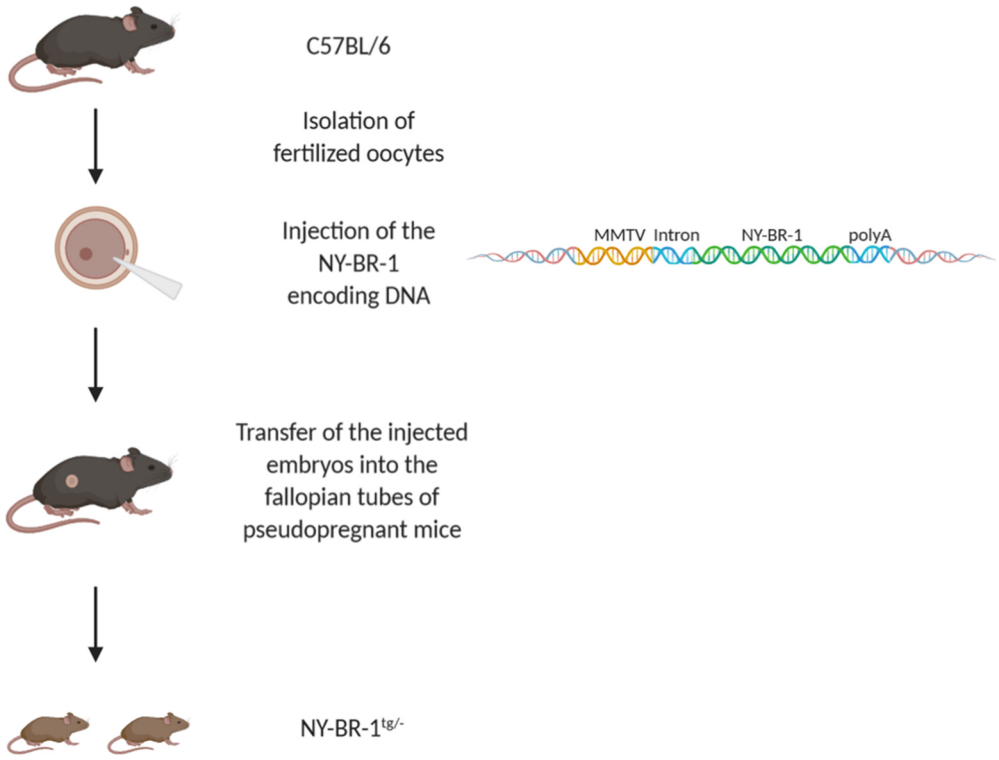

Figure 1.2.7: Generation strategy of the NY-BR-1$^{tg/-}$ mouse model
MMTV-NY-BR-1 encoding DNA (MMTV-LTR_NY-BR-1full_SV40polyA) was injected into fertilized oocytes from C57BL/6 mice leading to randomly integration of the transgene into the mouse genome. The injected embryos were transferred into pseudopregnant C57BL/6 mice. Transgenic offsprings were heterozygous for *NY-BR-1*.

1.3 Aim of the study

Breast cancer is the most common cancer in women and is expected to account for 30 % of all new cancer diagnoses in women. Despite improved prevention and treatment options, patients suffering from advanced or metastatic breast cancer currently have low chances of recovery. While immunotherapies, especially CAR^+ T cell - based therapies, are playing an increasingly important role in the treatment of cancer and had already achieved great success in the treatment of hematological malignancies, translating this treatment option to solid tumors still remains challenging. The main reasons include the lack of tumor specific antigens, weak trafficking to the tumor site and hampered tumor infiltration. However, the breast cancer associated antigen NY-BR-1 might be a useful target for CAR - based immunotherapies due its over-expression in over 70 % of primary breast tumors and its restricted expression patterns to normal healthy breast, testis and prostates.

Therefore, the principle aim is to evaluate NY-BR-1 as a target molecule for CAR – based immunotherapies using three different CAR candidates (clone2, 10D11, clone3) varying in their scFvs. In this process, the optimal anti-NY-BR-1 scFv and CAR backbone shall be examined with respect to efficiency and safety in both human and murine T cells using different *in vitro* and *in vivo* assays. With regard to a possible clinical application of these immune receptors, the investigations shall be carried out with both NY-BR-1 expressing cell lines and primary material from breast cancer patients. Since no NY-BR-1 expressing breast cancer cell lines are available, the goal will be the generation of stable NY-BR-1 expressing cell lines. Furthermore, possible cross-reactivities with the homolog protein NY-BR-1.1, which is expressed in the brain, shall be studied. In the later portion of this thesis, the already existing NY-BR-$1^{tg/-}$ mouse model will be utilized to test both effectivity and safety of the three anti-NY-BR-1 CAR candidates. Moreover, subcutaneous tumor mouse models shall be established in order to assess anti-tumor reactivities in an appropriate *in vivo* setting.

Aside from the anti-NY-BR-1 CAR constructs themselves, a new principle of CAR^+ T cell generation, the electroporation with a S/MAR based vector system, shall be evaluated against lentiviral transduction.

In addition, as with any target antigen, the question of its biological function arises. Therefore, this project will also focus on the expression pattern of NY-BR-1 in more detail.

Thus, these investigations are intended to contribute to the therapeutic questioning of NY-BR-1 as a possible target for CAR – based immunotherapies and to evaluate a possible CAR candidate for clinical studies.

2 Material

2.1 Instruments and equipment

Equipment	Manufactured/ distributed by
BioPhotometer plus	Eppendorf
Bond-MAX	Leica
CryoStarNX70	ThermoScientific
FACSanto™ II	BD Biosciences
GentleMACS Dissociater	Miltenyi Biotec
Heraeus Multifuge X1R Centrifuge	Thermo Scientific
Light Cycler © 480 II	Roche
Microm EC 350-2	ThermoScientific
Microm STP420D	ThermoScientific
Neon™ pipette	Invitrogen
Neon™ Transfection system	Invitrogen
Photometer	BioTek
T3000 Thermocycle	Biometra
xCELLigence Real Time Cell Analysis Instrument	ACEA Biosciences Inc.

2.2 Consumables

Item	Manufactured/ distributed by
0.45 µm membrane filter	Millipore
100 µm cell strainer (EASYstrainer)	Greiner
12 well plate	Greiner
14 mL round buttom polypropylene tubes	Greiner
15 mL Falcon™ tubes	Greiner
24 well plate	Greiner
250 mL polycarbonate bottles	Beranek
45 µm cell strainer	Greiner
50 mL Falcon™ tubes	Greiner
6 well plate	Greiner

96 well electronic microtiter plates (E-Plate 96)	ACEA Biosciences Inc.
96 well ELISA plate (half well)	Greiner
96 well plate	Greiner
96 well plate (round buttom)	Greiner
Cell culture flask (50 mL, 250 mL, 550 mL)	Greiner
Centricon Plus-70 30kDa	Millipore
PCR Plate for LC480	Steinbrenner Laborsysteme

2.3 Kits

Item	**Manufactured/ distributed by**
Bond Polymer Refine Detection Kit	Leica
CellTrace CFSE Cell Proliferation Kit	ThermoScientific
DNeasy Blood and Tissue Kit	QIAGEN
EndoFree NucleoBond Xtra Maxi Kit	Macherey-Nagel
Human 11 Plex Cytokine Kit	Ayoxxa
In-Fusion HD cloning	Takara
Maxima H Minus First Strand cDNA Synthesis Kit	QIAGEN
Mouse 12 Plex Cytokine Kit	Ayoxxa
Neon™ Transfection 100 µL Kit	Invitrogen
NucleoBond® Xtra Maxi Plus Kit	Macherey-Nagel
Pan T cell Isolation Kit human	Miltenyi Biotec
Pan T cell Isolation Kit II mouse	Miltenyi Biotec
QIAprep ® Spin Miniprep Kit	QIAGEN
QIAquick ® Gel Extraction Kit	QIAGEN
QIAquick® PCR Purification Kit	QIAGEN
RNeasy Mini Kit	QIAGEN
Bond Polymer Refine Detection Kit (DS9800)	Leica Biosystems

2.4 Chemicals and additives

2.4.1 Molecular biology

Item	Manufactured/ distributed by
Agarose	Peqlab Biotechnologie
Bacto ™ Agar	BD Biosciences
Bacto-Tryptone	Carl Roth
Bacto-Yeast	Carl Roth
BD OpEIA ™ TMB Substrate Reagent Set	BD Biosciences
Dithiothreitol (DTT)	Gerbu Biotechnik
DNase	Invitrogen
DNase I	Qiagen
EDTA	Sigma
Ethidium bromide solution 1%	Carl Roth
Gel loading Dye, purple 6x	New England BioLabs
Glycerol 87% BioChemica	PanReac AppliChem
NaCl	Carl Roth
SYBR-Green master mix	BioSystems

2.4.2 Cell culture

Item	Order Nr.	Manufactured/ distributed by
Activation cocktail	423301	BioLegend
Aphidicolin	A4487	Sigma
Brefeldin A	420601	BioLegend
EDTA	E5134	Sigma
FCS	P40-47500	PAN Biotech
Ficoll	17-1440-03	Thermo Fisher Scientific
Human IL-15	130-095-760	Miltenyi Biotec
Human IL-2		Pharmacy

Human IL-7	130-095-367	Miltenyi Biotec
Lactacystin	ab141411	Abcam
L-glutamine	P04-80050	PAN Biotech
L-mimosine	M0253	Sigma
Monensin	420701	BioLegend
Mouse IL-15	130-094-072	Miltenyi Biotec
NaCl		Carl Roth
Nocodazole	SML1665	Sigma
Non-essential amino acids	M11-003	Sigma
PBS (Phosphate Buffered Saline)		Sigma
Pen Strep (Penicillin Streptomycin)	P4333	Thermo Fisher Scientific
PhenolRed Solution	P0290	Sigma
Polybrene	107689	Sigma
Polyethyleneimine, linear (PEI)	23966-2	Polysciences, Inc.
Puromycin	Anti-pr-1	InvivoGen
Retronectin	T100A	Lonza
ß-mercaptoethanol	31350010	ThermoScientific
T cell Trans Act™ human	130-111-160	Miltenyi Biotec
Thymidine	T1895	Sigma
Trypan blue	T8154	Sigma®
Trypsin-EDTA (1X) 0.05 %	25300-054	Thermo Fisher Scientific

2.5 Buffers and media

2.5.1 Molecular biology

Restriction enzyme and ligation buffers

CutSmart ® Buffer 10 x	B7204S	New England BioLabs
NEBuffer 1		New England BioLabs
NEBuffer 2	B7002S	New England BioLabs
NEBuffer 3.1	B7203S	New England BioLabs
T4 DNA Ligase buffer 10x	B0202S	New England BioLabs

TAE – Buffer (50x)

Tris base	242 g
Glacial acetic acid	57.1 mL
EDTA 0.5 M (pH 8.3)	100 mL

Filled up to 1 L with dH_2O.

Buffer TFB 1

Glycerine	75 mL
KAC	30 mM
$MnCl_2$	50 mM
RbCl	100 mM
$CaCl_2$	10 mM

Filled up to 500 mL with dH_2O, pH 5.8

LB medium

Bacto-Tryptone	10 g
Bacto-Yeast	5 g
NaCl	10 g
H_2O	900 mL
Adjust the pH to 7.0 with 10 M NaOH	

Adjust volume to 1 L with H_2O, sterilize by autoclaving

LB-Agar

LB medium	1 L
Bacto-Agar	15 g

Sterilize by autoclaving

Antibiotic selection of transfected bacteria

Antibiotic	Final concentration	Manufactured / distributed by
Kanamycin	100 µg mL^{-1}	Roth
Carbenicillin	100 µg mL^{-1}	Roth

Heat-labile antibiotics were sterile filtered and added to the autoclaved media.

2.5.2 Cell culture

Cultivation media

Medium	Manufactured / distributed by
RPMI-1640	ThermoFisher Scientific
DMEM (+GlutaMAX)	ThermoFisher Scientific
RPMI-1640 (w / o phenol red)	ThermoFisher Scientific
X-Vivo 20	Lonza
TexMACS GMP	Miltenyi Biotec
DMEM (w / o phenol red)	Invitrogen
Opti-MEM (1X) + GlutaMAX	ThermoFisher Scientific

Freezing medium

FCS	90 %
DMSO	10 %

Erythrocyte lysis buffer

NH_4C	155 mM
$KHCO_3$	10 mM
EDTA	0.1 mM

Filled up to 1 L with dH_2O.

Coating buffer (NY-BR-1 / NY-BR-1.1 peptide coating and human, mouse IFNγ ELISA)

Na_2CO_3	0.1 M
$NaHCO_3$	7.13 g
Na_2CO_3	1.59 g

Filled up to 1 L with dH_2O, pH 9.5

Washing buffer (NY-BR-1 / NY-BR-1.1 peptide coating and human, mouse IFNγ ELISA)

PBS	
Tween-20	0.05 %

Blocking buffer (NY-BR-1 / NY-BR-1.1 peptide coating)

PBS	
Tween-20	0.05 %
Casein	0.2 %

Blocking buffer (Human, mouse IFNγ ELISA)

PBS	
FCS	10 %

2.5.3 Flow cytometry

FACS buffer (Surface staining)

PBS	
FCS	1 %
EDTA	2 mM

FACS buffer (Intracellular staining)

PBS	
FCS	1 %
NaN_3	0.1 %

Fixation and permeabilization solutions

Solution	Manufactured / distributed by
Cytofix / Cytoperm	BD Biosciences
Perm / Wash	BD Biosciences
PFA (working solution 4 %PFA in PBS)	

Nicoletti buffer

dH_2O	
Propidium iodide	50 µg / mL
Sodium citrate	0.1 % (w/v)
Triton X-100	0.1 % (v/v)

2.6 Antibodies

2.6.1 Flow cytometry

Name	Order Nr.	Manufactured / distributed by
Clone2		Inhouse
10D11 (humanized)		Inhouse
Clone3 (humanized)		Inhouse
PE - conjugated anti-human IgG (Fcγ fragment specific)	109-116-098	Jackson Immuno Research
APC - conjugated anti-human IgG (Fcγ fragment specific)	109-135-098	Jackson Immuno Research
PE - conjugated anti-mouse IgG (Fcγ subclass I specific)	115-115-205	Jackson Immuno Research
APC - conjugated anti-mouse IgG (Fcγ subclass I specific)	115-135-205	Jackson Immuno Research
APC - conjugated anti-human CD3	555335; clone: UCHT1	BD Biosciences
APC - conjugated anti-mouse CD3	565643; clone: 17A2	BD Biosciences
PerCP-Cy5.5- conjugated anti-mouse CD69	104522	BioLegend
FITC - conjugated anti-mouse CD4	100406	BioLegend
PerCp-Cy5.5 - conjugated anti-mouse CD8	100734	BioLegend
APC - conjugated anti-mouse IFNγ	505810	BioLegend
PE-Cy7 - conjugated anti-mouse TNFα	506324	BioLegend

Pacificblue - conjugated anti-GranzymeB	515408	BioLegend

2.6.2 Stimulation of murine T cells

Name	Order Nr.	Manufactured / distributed by
Anti-mouse CD28	130-093-183	Miltenyi Biotec
Anti-mouse CD3ε	130-092-973	Miltenyi Biotec

2.6.3 Anti-NY-BR-1 antibody ELISA

Name	Order Nr.	Manufactured / distributed by
HRP - conjugated anti-mouse IgG antibody	115-035-003	Dianova

2.6.4 Immunohistochemistry

Name	Order Nr.	Manufactured / distributed by
Rabbit anti-human / mouse CD3	16669	Abcam
HRP-conjugated anti-rabbit	DS9800	Leica

2.7 Vectors

2.7.1 Gateway cloning vectors

Name	Properties
#35 (pENTR_attL1_clone2scFv_hFc_ hCD28_h4-1BB_CD3z_attL2)	Gateway entry vector, encoding the NY-BR-1 specific CAR clone2scFv_hFc_ hCD28_h4-1BB_CD3z
#142 (pENTR_attL1_10D11cFv_hFc_ hCD28_h4-1BB_CD3z_attL2)	Gateway entry vector encoding the NY-BR-1 specific CAR 10D11cFv_hFc_hCD28_h4-1BB_CD3z
#143 (pENTR_attL1_clone3cFv_hFc_ hCD28_h4-1BB_CD3z_attL2)	Gateway entry vector, encoding the NY-BR-1 specific CAR clone3cFv_hFc_hCD28_h4-1BB_CD3z

#187 (pENTR_attL1_RFB4scFv_mFcΔ_ mCD28Δ_m4-1BB_CD3z_attL2)	Gateway entry vector, encoding the CD22 specific CAR RFB4scFv_mFcΔ_mCD28Δ_m4-1BB_CD3z
#200 (pENTR_attL1_clone2scFv_mFcΔ_ mCD28Δ_m4-1BB_CD3z_attL2)	Gateway entry vector, encoding the NY-BR-1 specific CAR clone2scFv_mFcΔ_mCD28Δ_ m4-1BB_CD3z
#205 (pENTR_attL1_10D11scFv_mFcΔ_ mCD28Δ_m4-1BB_CD3z_attL2)	Gateway entry vector, encoding the NY-BR-1 specific CAR 10D11scFv_mFcΔ_mCD28Δ_ m4-1BB_CD3z
#206 (pENTR_attL1_clone3scFv_mFcΔ_ mCD28Δ_m4-1BB_CD3z_attL2)	Gateway entry vector, encoding the NY-BR-1 specific CAR clone3scFv_mFcΔ_mCD28Δ_ m4-1BB_CD3z
#511 (pENTR_attL1_clone2scFv_ hFcΔ_hCD28Δ_h4-1BB_CD3z_attL2)	Gateway entry vector, encoding the NY-BR-1 specific CAR clone2scFv_hFcΔ_hCD28Δ_ h4-1BB_CD3z
#512 (pENTR_attL1_10D11cFv_hFcΔ_ hCD28Δ_h4-1BB_CD3z_attL2)	Gateway entry vector, encoding the NY-BR-1 specific CAR 10D11cFv_hFcΔ_hCD28Δ_h4-1BB_CD3z
#513 (pENTR_attL1_clone3cFv_hFcΔ_ hCD28Δ_h4-1BB_CD3z_attL2)	Gateway entry vector, encoding the NY-BR-1 specific CAR clone3cFv_hFcΔ_hCD28Δ_ h4-1BB_CD3z

2.7.2 Lentiviral vectors

Name	**Properties**
#1 (pCMV VSV-G)	Lentiviral helper plasmid, encoding the envelope protein VSV-G
#2 (pCMV dR8.74)	Lentiviral helper plasmid, encoding the proteins HIV-gag and HIV-pol
#44 (pRRL_hPGK_NY-BR-1_IRES_ Puromycin_WPRE)	Lentivirus transfer vector, encoding the NY-BR-1 full length protein
#85 (pRRL_hPGK_attB1_clone2scFv_hFc _hCD28_h4-1BB_CD3z _attB2)	Lentivirus transfer vector, encoding the NY-BR-1 specific CAR NY-BR1scFv_hFc_hCD28_h4-1BB_hCD3
#126 (pRRL_CMV_attR1_CmR_*ccdB*_ attR2_hPGK_DsRed2_WPRE)	Lentivirus transfer vector, containing the ccdB, chloramphenicol-resistance and DsRed2 genes
#216 (pRRL_CMV_attB1_clone2scFv_ mFcΔ_mCD28Δ_m4-1BB_CD3z_attB2_ hPGK_DsRed2_WPRE)	Lentivirus transfer vector, encoding the NY-BR-1 specific CAR clone2scFv_mFcΔ_mCD28Δ_ m4-1BB_CD3z and red fluorescent protein DsRed2
#217 (pRRL_CMV_attB1_10D11scFv_ mFcΔ_mCD28Δ_m4-1BB_CD3z_attB2_ hPGK_DsRed2_WPRE)	Lentivirus transfer vector, encoding the NY-BR-1 specific CAR 10D11scFv_mFcΔ_mCD28Δ_ m4-1BB_CD3z and the red fluorescent protein DsRed2

#218 (pRRL_CMV_attB1_clone3scFv_ mFcΔ_mCD28Δ_m4-1BB_CD3z_attB2_ hPGK_DsRed2_WPRE)	Lentivirus transfer vector, encoding the NY-BR-1 specific CAR clone3scFv_mFcΔ_mCD28Δ_ m4-1BB_CD3z and the red fluorescent protein DsRed2
#240 (pRRL_mPGK_attB1_NY-BR-1(full)_att B2_WPRE)	Lentivirus transfer vector, encoding the NY-BR-1 full length protein
#241 (pRRL_mPGK_attB1_clone2scFv_ mFcΔ_mCD28Δ_m4-1BB_CD3z_attB2_ WPRE)	Lentivirus transfer vector, encoding the NY-BR-1 specific CAR clone2scFv_mFcΔ_mCD28Δ_ m4-1BB_CD3z
#268 (pRRL_CMV_attB1_10D11scFv_ mFc_mCD28_m4-1BB_CD3z_attB2_IR ES_eGFP_WPRE)	Lentivirus transfer vector, encoding the NY-BR-1 specific CAR 10D11scFv_mFc_mCD28_ m4-1BB_CD3z
#269 (pRRL_CMV_attB1_clone3scFv_ mFc_mCD28_m4-1BB_CD3z_attB2_IR ES_eGFP_WPRE)	Lentivirus transfer vector, encoding the NY-BR-1 specific CAR clone3scFv_mFc_mCD28_ m4-1BB_CD3z
#514 (pRRL_hPGK_clone2scFv_hFcΔ_ hCD28Δ_h4-1BB_CD3z_WPRE)	Lentivirus transfer vector, encoding the NY-BR-1 specific CAR clone2scFv_hFcΔ_hCD28Δ_ h4-1BB_CD3z
#515 (pRRL_hPGK_10D11scFv_hFcΔ_ hCD28Δ_h4-1BB_CD3z_WPRE)	Lentivirus transfer vector, encoding the NY-BR-1 specific CAR 10D11scFv_hFcΔ_hCD28Δ_ h4-1BB_CD3z
#516 (pRRL_hPGK_clone3scFv_hFcΔ_ hCD28Δ_h4-1BB_CD3z_WPRE)	Lentivirus transfer vector, encoding the NY-BR-1 specific CAR clone3scFv_hFcΔ_hCD28Δ_h 4-1BB_CD3z
#537 (pRRL_hPGK_clone2scFv_hFc_ hCD28_CD3z_hOX40_WPRE)	Lentivirus transfer vector, encoding the NY-BR-1 specific CAR clone2scFv_hFc_hCD28_CD3z_hOX40
#538 (pRRL_hPGK_10D11scFv_hFc_ hCD28_CD3z_hOX40_WPRE)	Lentivirus transfer vector, encoding the NY-BR-1 specific CAR 10D11scFv_hFc_hCD28_CD3z_hOX40
#539 (pRRL_hPGK_clone3scFv_hFc_ hCD28_CD3z_hOX40_WPRE)	Lentivirus transfer vector, encoding the NY-BR-1 specific CAR clone3scFv_hFc_hCD28_CD3z_hOX40

2.7.3 pS/MARter vectors

Name	Properties
#272 (pS/MARter_hPGK_CEAscFv_hFc_ hCD28_CD3z_hOX40_S/MAR)*	pS/MARter electroporation vector encoding the CEA specific CAR CEAscFv_hFc_hCD28_ CD3z_hOX40
#273 pS/MARter_hPGK_clone2scFv_hFc _hCD28_h4-1BB_CD3z_S/MAR)*	pS/MARter electroporation vector, encoding the NY-BR-1 specific CAR clone2scFv_hFc_hCD28_ h4-1BB_CD3z
#277 (pS/MARter_mPGK_clone2scFv_	pS/MARter electroporation vector, encoding the NY-BR-1 specific CAR clone2scFv_mFcΔ_mCD28Δ

mFcΔ_mCD28Δ_m4-1BB_CD3z_S/MAR)*	_m4-1BB_CD3z
#295 (pS/MARter_mPGK_10D11scFv_mFcΔ_mCD28Δ_m4-1BB_CD3z_S/MAR)*	pS/MARter electroporation vector, encoding the NY-BR-1 specific CAR 10D11scFv_mFcΔ_mCD28Δ_m4-1BB_CD3z
#296 (pS/MARter_mPGK_clone3scFv_mFcΔ_mCD28Δ_m4-1BB_CD3z_S/MAR)*	pS/MARter electroporation vector, encoding the NY-BR-1 specific CAR clone3scFv_mFcΔ_mCD28Δ_m4-1BB_CD3z
#302 (pS/MARter_hPGK_10D11scFv_hFc_hCD28_h4-1BB_CD3z_S/MAR)*	pS/MARter electroporation vector, encoding the NY-BR-1 specific CAR 10D11scFv_hFc_hCD28_h4-1BB_CD3z
#303 (pS/MARter_hPGK_clone3scFv_hFc_hCD28_h4-1BB_CD3z_S/MAR)*	pS/MARter electroporation vector, encoding the NY-BR-1 specific CAR clone3scFv_hFc_hCD28_h4-1BB_CD3z
#432 (pS/MARter_hPGK_clone2scFv_hFc_hCD28_CD3z_hOX40_S/MAR)*	pS/MARter electroporation vector, encoding the NY-BR-1 specific CAR clone2scFv_hFc_hCD28_CD3z_hOX40
#433 (pS/MARter_hPGK_10D11scFv_hFc_hCD28_CD3z_hOX40_S/MAR)*	pS/MARter electroporation vector, encoding the NY-BR-1 specific CAR 10D11scFv_hFc_hCD28_CD3z_hOX40
#434 (pS/MARter_hPGK_clone3scFv_hFc_hCD28_CD3z_hOX40_S/MAR)*	pS/MARter electroporation vector, encoding the NY-BR-1 specific CAR clone3scFv_hFc_hCD28_CD3z_hOX40
#517 (pS/MARter_hPGK_clone2scFv_hFcΔ_hCD28Δ_h4-1BB_CD3z_S/MAR)*	pS/MARter electroporation vector, encoding the NY-BR-1 specific CAR clone2scFv_hFcΔ_hCD28Δ_h4-1BB_CD3z
#518 (pS/MARter_hPGK_10D11scFv_hFcΔ_hCD28Δ_h4-1BB_CD3z_S/MAR)*	pS/MARter electroporation vector, encoding the NY-BR-1 specific CAR 10D11scFv_hFcΔ_hCD28Δ_h4-1BB_CD3z
#519 (pS/MARter_hPGK_clone3scFv_hFcΔ_hCD28Δ_h4-1BB_CD3z_S/MAR)	pS/MARter electroporation vector, encoding the NY-BR-1 specific CAR clone3scFv_hFcΔ_hCD28Δ_h4-1BB_CD3z

*pS/MARter backbone was kindly provided by Dr. Richard Harbottle's laboratory (DKFZ, DNA Vector Research Group)

2.7.4 NanoCMARter vectors

Name	Properties
#418 (CMARter_hPGK_clone2scFv_hFc_hCD28_h4-1BB_CD3z_S/MAR)*	NanoCMARter electroporation vector, encoding the NY-BR-1 specific CAR clone2scFv_hFc_hCD28_h4-1BB_CD3z
#419 (CMARter_hPGK_10D11scFv_hFc_hCD28_h4-1BB_CD3z_S/MAR)*	NanoCMARter electroporation vector, encoding the NY-BR-1 specific CAR 10D11scFv_hFc_hCD28_h4-1BB_CD3z

#419 (CMARter_hPGK_clone3scFv_ hFc_hCD28_h4-1BB_CD3z_S/MAR)*	NanoCMARter electroporation vector, encoding the NY-BR-1 specific CAR clone3scFv_hFc_hCD28 _h4-1BB_CD3z
#531 (CMARter_hPGK_clone2scFv_ hFc_hCD28_CD3z_hOX40_S/MAR)*	NanoCMARter electroporation vector, encoding the NY-BR-1 specific CAR clone2scFv_hFc_hCD28 _CD3z_hOX40
#532 (CMARter_hPGK_10D11scFv_ hFc_hCD28_CD3z_hOX40_S/MAR)*	NanoCMARter electroporation vector, encoding the NY-BR-1 specific CAR 10D11scFv_hFc_hCD28 _CD3z_hOX40
#533 (CMARter_hPGK_clone3scFv_ hFc_hCD28_CD3z_hOX40_S/MAR)*	NanoCMARter electroporation vector, encoding the NY-BR-1 specific clone3scFv_hFc_hCD28 _CD3z_hOX40

*NanoCMARter vectors were cloned and provided by Dr. Richard Harbottle's laboratory (DKFZ, DNA Vector Research Group)

2.8 Oligonucleotides

Name	Sequence 5' - 3'	Description
#5	GATTTTGAGACACGGGCCAGA	Rev primer for cloning of murine CAR backbone (#187) into vector #35, resulting in vector #200
#22	CCTATGCTGCTCTTCGATTCTTCC	qPCR primer specific for the *NY-BR-1* gene and RNA transcript
#60	CAAGAGCTCTGCAGTGTGAGATTG	qPCR primer specific for the *NY-BR-1* gene and RNA transcript
#85	ATGCGGCCGCTGTGCCAAGAGATGGCGGC	Fwd primer for cloning of murine CAR backbone (#187) into vector #35, resulting in vector #200
#150	TTGATTATTGACTAGTCCACTATGATATCAA TTCTACCGGGTAGG	In-Fusion fwd primer for cloning of *mPGK* (#240) into vector #272; resulting in vector #277
#151	TTTAAACGCTTCCCGAAAGGCCCGGAGATG AGG	In-Fusion rev primer for cloning of *mPGK* (#240) into vector #272; resulting in vector #277
#152	CCTTTCGGGAAGCGTTTAAACTTAAGCTTG CCG	In-Fusion fwd primer for cloning of murine CAR gene cassette (#241) into vector #272; resulting in vector #277
#153	GGCTCTCCGGTAGGCCTCGAGAGATTATCT AGGGGCCAGTGTCTG	In-Fusion rev primer for cloning of murine CAR gene cassette (#241) into vector #272; resulting in vector #277
#370	ACTTGTTTATTGCAGCTTATAATGG	qPCR primer for the SV40 poly A - encoding gene

#371	CAAACCACAACTAGAATGCAGTG	qPCR primer for the SV40 poly A - encoding gene
#531	ACTGGAAATCAAACGTGC	Fwd primer for cloning of human CAR backbone (#68) into vectors #273 and #303, resulting in vectors #517, #519
#532	ATATACTCGAGTTAGCGAGGGGGCA	Rev primer for cloning of human CAR backbone (#68) into vectors #273 and #303, resulting in vectors #517, #519
#534	CTCCCCAGGGGGATCCAGCGTTTAAACTTAAGCTTGCCG	In-Fusion fwd primer for cloning of human CAR gene cassette (#511) into vector #85; resulting in vector #514
#535	GAGGTTGATTGTCGACTCTAGATTAGCGAGGGGGC	In-Fusion rev primer for cloning of human CAR gene cassette (#511) into vector #85; resulting in vector #514
#552	ATATGGATCCAGCGTTTAAACTTAAGCTTGCC	Fwd primer for cloning of human CAR gene cassette (#512, 513) into vector #514, resulting in vectors #515 and #516
#553	ATATGTCGACTCTAGATTAGCGAGGGGGCA	Rev primer for cloning of human CAR gene cassette (#512, 513) into vector #514, resulting in vectors #515 and #516
#562	CTCCCCAGGGGGATCCGGCTAGCGCCACCATGGTTC	In-Fusion fwd primer for cloning of human CAR gene cassette (#432) into vector #514; resulting in vector #537
#563	GAGGTTGATTGTCGACCTCGAGCTAGATTTTAGCCAGGG	In-Fusion rev primer for cloning of human CAR gene cassette (#432, #433, #434) into vector #514; resulting in vectors #537, #538 and #539
#564	CTCCCCAGGGGGATCCGCCGAAGCCGCTAGCCGC	In-Fusion fwd primer for cloning of human CAR gene cassette (#433, #434) into vector #514; resulting in vectors #538 and #539

2.9 Size standards

In order to size and quantify DNA fragments by agarose gel electrophoresis, the 100 bp DNA Ladder (NEB; N3231S) and 1 kB DNA Ladder (NEB; N3232L) were applied (see Figure 2.9.1).

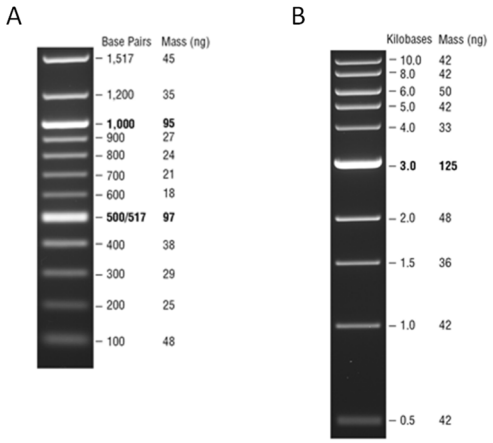

Figure 2.9.1: Applied DNA ladders for gel electrophoresis
Banding patterns of the applied 100 bp DNA Ladder [A] and 1 kB DNA Ladder [B] (source: https://international.neb.com).

2.10 Enzymes

2.10.1 Restriction enzymes

Name	Manufactured/ distributed by
AvrII	NEB
BamHI	NEB
BstEII	NEB
EcoRI	NEB
HindIII	NEB
NcoI	NEB
NheI	NEB
NotI	NEB
Pme I	NEB
SacI	NEB
SalI	NEB
ScaI	NEB
SmaI	NEB
SpeI	NEB

SphI	NEB
XbaI	NEB
XcmI	NEB
XhoI	NEB
XmaI	NEB

2.10.2 Other enzymes for DNA manipulation

Name	Manufactured/ distributed by
T4 DNA Ligase	NEB
Gateway cloning LR clonase enzyme mix	ThermoScientific

2.11 Cell lines and primary cells

HEK 293T

The human embryonic kidney (HEK) 293T cell line is derived from HEK 293 cells and constitutively expresses the simian virus 40 (SV 40) large T antigen, conferring the capacity to amplificate vectors containing the SV 40 ori with high efficiency [218,219].

Bosc23

The Bosc23 cell line is derived from HEK 293T cells by stable transfection with two retroviral (M-MuLV derived) packaging plasmids: pCRIPenv$^-$ (expressing gag, pol) and pCRIPgag-2 (expressing env)[220]

Jurkat

The Jurkat cell line is an human immortalized T lymphocyte cell line, originally derived from a child suffering from T cell leukemia [221].

EO771

Murine breast cancer (adenocarcinoma) cell line originally isolated from a spontaneous tumor in C57BL/6 mouse [222].

NIH/3T3

The NIH/3T3 cells were originally established from mouse embryonic fibroblast cells [223]

Pleural effusion cells

Pleural effusion cells were isolated from breast cancer patients (informed consent: Ethics vote S-207/2005) in cooperation with the Department of Obstetrics and Gynecology at Medical Faculty Heidelberg and the Department for Diagnostic and interventional Radiology with Nuclear Medicine of the Thoraxklinik Heidelberg.

Pleural effusion cells	Provided by
HD-A-185	Prof. Dr. Claus Peter Heußel, Thoraxklink Heidelberg
HD-A-213	Prof. Dr. Claus Peter Heußel, Thoraxllinik Heidelberg

The protocol is described in chapter 3.2.3.

Human T cells

Peripheral blood T cells were isolated from healthy donors according to the protocol described in chapter 3.2.8.1.

Murine T cells

Murine T cells were isolated from mouse spleens according to the protocol described in chapter 3.2.8.2.

3 Methods

3.1 Molecular biology

3.1.1 Bacterial culture

3.1.1.1 Generation of chemically competent *E.coli* bacteria

E.coli bacteria (*Stbl3*, *ccdB*, XL-1) were subcultured in 5 mL LB-medium in 14 mL round buttom polypropylene tubes (Greiner) overnight. Two 1.5 mL subcultures were transferred to 200 mL LB-medium and shaken until an optical density of 0.4 to 0.6 measured at a wavelength of 600 nm (Eppendorf, BioPhotometer plus) was achieved. Then, bacterial cultures were transferred to 250 mL polycarbonate bottles (Beranek) and left on ice for 10 min. After one centrifugation step at 4500 rpm for 10 min, pellets were resuspended in 30 mL of sterile filtered buffer TFB 1 (75 mL glycerine, 30 mM KAC, 50 mM $MnCl_2$, 100 mM RbCl, 10 mM $CaCl_2$, add to 500 mL dH20, ph 5.8). Following incubation on ice for 10 min, bacterial suspension was pelleted (4500 rpm, 10 min) and resuspended in 5 mL of sterile filtered TFB 2 (30 mL glycerine, 10mM MOPS-Na, 75 mM $CaCl_2$, 10 mM RbCl, add to 200 mL dH_2O, pH 7). Finally, bacterial suspension was aliquoted (100 µL / tube) and stored at -80 °C.

3.1.1.2 Growth and storage of chemically competent *E.coli* bacteria

Liquid cultures of *XL1*, *Stbl3* or *ccdB* chemically competent *E.coli* bacteria were grown in *Lysogeny broth* (*LB*) medium with the appropriate antibiotic at 37° C in a shaking incubator. Culture volumes varied between 5 mL for small scale (Miniprep) and 400 mL for large scale (Maxiprep) production (see chapters 3.1.5.1 and 3.1.5.2). Bacteria were stored at -80° C following addition of 240 µL glycerol (87 %) to 420 µL of bacterial culture.

3.1.1.3 Transformation of chemically competent *E.coli* bacteria

In order to replicate the plasmids of interest, a transformation of *XL1*, *Stbl3* or *ccdB* chemically competent *E.coli* bacteria was performed. The chemically competent *E.coli* bacteria, stored at - 80 °C, were thawed on ice and mixed with 100 ng to 200 ng of plasmid DNA. The bacteria / plasmid mixture

was placed on ice for 30 min. To improve the uptake of plasmid DNA, a heat shock was performed for 90 sec at 42 °C. Next, bacteria were incubated on ice for 2 min, mixed with 500 µL LB-medium and shaked at 37°C for 1.5 h. Finally, transformed bacterial clones were plated and selected on a 10 cm LB agar plate containing the appropriate antibiotic. Next day, single clones were selected to inoculate liquid bacterial cultures followed by plasmid purification via miniprep (see chapter 3.1.5.1).

3.1.2 Agarose gel electrophoresis

Gel electrophoresis was performed with 0.5, 1 or 2 % agarose gel, which allows the separation of DNA fragments of different sizes due to their migration in a given time. The agarose solution was prepared from Ethidium bromide and TAE buffer (1x) at a ratio of 1:10,000. DNA samples (6 volumes) were mixed with 1 volume of 6 x loading dye and loaded into the wells of the dried gel. Depending on gel size, a voltage of 90 or 130 V was applied for 30 to 40 min. The 1 kb DNA Ladder (NEB, N3232) or 100 bp DNA Ladder (NEB N3231) were used as size standard. DNA fragments were visualized by a UV-transilluminator (Quantum-ST4, peqlab Biotechnologie GmbH).

3.1.3 Polymerase chain reaction

Polymerase chain reaction (PCR) was used to amplify relevant CAR and NY-BR-1 encoding DNA sequences. PCRs were carried out in the thermocycler (Biometra, T3000). For the design of oligonucleotide primers, the software SnapGene was used. The amplification reaction had a final volume of 25 µL containing 12µL master mix (GoTaq long PCR master mix, Promega), 10 µM primers and 1 to 25 ng template.

For PCR reaction, the annealing (Ta) and melting temperatures (Tm) directly correlate with length and composition of the applied primer pair.

$$Tm = 2\,^{\circ}C * (A + T) + \ 4\,^{\circ}C * (C + G)$$

A: adenine
T: thymine
C: cytosine
G: guanine

Table 3.1: Conditions of the PCR reactions

PCR step	Temperature [°C]	Time [sec]	Cycles
Initial denaturation	95	300	1
Denaturation	95	30	35
Annealing	Tm - 2 to 5 °C	30	
Elongation	72	60 sec for 1kbp	
Final elongation	72	300	1
Cooling	4	∞	1

PCR products were analyzed by gel electrophoresis (see chapter 3.1.2). The purification of DNA fragments was performed by using the QIAquick Gel extraction Kit (QIAGEN, see chapter 3.1.5.3) or QIAquick PCR Purification Kit (QIAGEN; see chapter 3.1.5.4).

3.1.4 Real-time quantitative polymerase chain reaction

Real-time quantitative polymerase chain reaction (real-time qPCR) was used for the detection and quantification of DNA copy number and gene expression. By using the fluorescent reporter SYBR-green and primer pairs specific for the gene of interest, DNA / cDNA amplification was monitored at each cycle of PCR. PCRs were carried out in the LightCycler 480 (Roche). The amplification reaction had a final volume of 10 µL containing 5 µL master mix (SYBR-Green master mix, BioSystems), 0.2 µL of each primer [100 µM], 2 µl gDNA/cDNA and 2.5µl dH_2O. The quantitative analysis of DNA copy number was performed using a standard curve of plasmid dilutions of known copy number and analysis type "quantification/2nd derivative max". For quantification of gene expression, relative changes in target gene expression were calculated relative to control cells and a reference gene (ß-actin) using the $2^{-\Delta\Delta Ct}$ method.

Table 3.2: Conditions of the qPCR reactions

PCR step	Temperature [°C]	Time [sec]	Cycles
Initial denaturation	95	300	1
Denaturation	95	30	40
Annealing	Tm - 2 to 5 °C	20	
Elongation	72	60 sec for 1kbp	
Melting curve step 1	95	15	1
Melting curve step 2	55	15	1
Melting curve step 3	95	∞	1
Cooling	15	∞	1

3.1.5 DNA isolation

3.1.5.1 Small scale isolation of plasmids via Miniprep

Following transformation of *ccdB*, *Stbl3* or *XL1* competent *E.coli* bacteria with the plasmid of interest (see chapter 3.1.1.3), bacteria were grown in 5 mL liquid LB-medium with the appropriate antibiotic. Plasmid DNA was isolated using the QIAprep Spin Miniprep Kit from Qiagen. After one centrifugation step (12,000 rpm for 5 min), bacterial pellet was resuspended in 250 µL of resuspension buffer (+RNAse A) enabling the degradation of RNA. Thereafter, 250 µL of lysis buffer were added and the solution was inverted for four to six times. In order to neutralize and precipitate proteins and DNA of lysed bacterial cells, 350 µL of neutralization buffer were added and the mixture was inverted immediately. To isolate plasmid DNA, the mixture was centrifuged (13,000 rpm for 10 min) and the supernatant was transferred to spin columns. Following two washing steps, DNA was eluted in 20 µL elution buffer or dH_2O.The spectrophotometer (BioTek Epoch), was used to determine the concentration of purified DNA. The presence of the correct plasmid has been validated by analytical digestions (see chapter 3.1.9.1).

3.1.5.2 Large scale isolation of plasmids via Maxiprep

For isolation of larger quantities of DNA, the NucleoBond Xtra Maxi kit from Machery-Nagel was used. In case of pS/MARter vectors, the EndoFree NucleoBond Xtra Maxi kit (Machery-Nagel) was applied according to the manufacturer's instructions. Mini- and Maxipreps differ basically in the upscaling of volumes. Bacteria were grown in 400 mL liquid LB-medium with the appropriate antibiotic. After that, bacteria were pelleted by centrifugation at 4500 rpm for 15 min and resuspended in RNase A containing resuspension buffer. After 5 min incubation with lysis buffer, neutralization buffer was added and the lysate was loaded onto the equilibrated column with an ion-exchange resin. Following several washing steps, elution was carried out at pH 9 and under high salt conditions allowing the charge neutralization of resin and release of plasmid DNA. For precipitation of plasmid DNA, 0.7 volumes room temperature isopropanol were added, immediately mixed by vortexing and pelleted at 4500 g for 30 min. After an ethanolic washing step, plasmid DNA was air-dried and resuspended in dH_2O or endotoxin-free elution buffer. The spectrophotometer (BioTek Epoch) was used to determine the concentration of isolated plasmid DNA (see chapter 3.1.8). The presence of the correct plasmid has been validated by analytical digestions (see chapter 3.1.9.1).

3.1.5.3 Agarose gel purification

After separation of DNA fragments by agarose gel electrophoresis, the desired DNA bands were cut out under UV light and isolated with the QIAquick Gel extraction Kit from Qiagen according to the manufacturer's instructions. Briefly, 3 volumes pH indicator containing buffer QG were added to 1 volume gel and incubated at 50°C for 10 min. The tube was vortexed every 2 to 3 minutes until the gel slice had dissolved completely. Since pH ≤7 is required for optimal DNA adsorption, 1 to 10 µL of 3 M sodium acetate (pH 5) were added in case of basic pH values. DNA was precipitated with 1 gel volume room temperature isopropanol and applied to the column. Afterwards, columns were washed with buffers QG and PE. Finally, DNA was eluted in 10 to 20 µL dH_20 or buffer EB. The spectrophotometer (BioTek Epoch), was used to determine the concentration of isolated DNA (see chapter 3.1.8).

3.1.5.4 Purification of PCR products

PCR products with a size of 100 bp to 10 kbp were purified with the QIAquick PCR Purification Kit (QIAGEN) according to the manufacturer's instructions. Briefly, 5 volumes buffer PB were added to 1 volume PCR mixture. The loading mixture should have a pH ≤ 7 for optimal DNA adsorption indicated by a yellow color. Otherwise, 1 to 10 µL of 3 M sodium acetate (pH 5) were added to the solution. DNA was bound by columns, washed with buffer PE and eluted in 10 to 20 µL dH_20 or buffer EB. If the purified PCR products had to be analyzed on an agarose gel, 1 volume of 6 x loading dye was added to 6 volumes of PCR samples (see chapter 3.1.2). The spectrophotometer (BioTek Epoch) was used to determine the concentration of isolated DNA (see chapter 3.1.8).

3.1.5.5 DNA isolation from mouse tissues

For the isolation of DNA from mouse tissue the DNeasy Blood and Tissue Kit (QIAGEN) was used according to the manufacturer's instructions. Briefly, small pieces (up to 10 mg) of the thawed tissues were transferred to 1.5 mL tubes and incubated with the provided buffer ATL (180 µL) and proteinase K at 56 °C until lysis was completed. Following addition of the provided buffer AL (200 µL) and 200 µL ethanol (96 - 100 %), the mixture was loaded into a DNeasy column and centrifuged at 8000 rpm for 1 min. Diverse washing steps were performed and, finally, DNA was eluted with 50 to 200 µL of dH_2O. The concentration of isolated DNA was determined with the spectrophotometer (BioTek Epoch), as described in chapter 3.1.8.

3.1.6 RNA isolation

The purification of RNA from cells was performed with the RNeasy Mini Kit (QIAGEN) according to the manufacturer's instructions. Here, a minimum of $1x10^6$ cells was pelleted (1500 rpm, 5 min) and resuspended in the appropriate amount of RLT buffer, which was supplemented with dithiothreitol (DTT) (20 µL of 2 M DTT to 1 mL RLT buffer). Following adding one volume of 70 % EtOH, the lysate was transferred to an RNeasy Mini spin column and centrifuged at 8000 rpm for 1 min. After several washing steps, 80 µL of DNase I (Qiagen, 79254) mixture (10 µL DNase I mixed with 70 µL buffer RDD) were added to the column and incubated for 15 min at room temperature in order to minimize the residual risk of DNA contaminations. After additional washing steps with the buffers RW1 and RPE, RNA was eluted with 20 µL of dH_2O. Finally, a second DNAse digestion step was performed by adding 7 µL of DNAse (Invitrogen, 18068-015) mixture (5 µL 10xDNase buffer mixed with 2 µL DNase) for 15 min at room temperature. The reaction was stopped by adding 5 µL of 5 mM EDTA solution. After an incubation period of 10 min at 65 °C, RNA concentration was measured with the spectrophotometer (BioTek Epoch), as described in chapter 3.1.8. RNA was stored at - 80°C until reverse transcription was performed (see chapter 3.1.7).

3.1.7 cDNA synthesis by reverse transcription

In order to synthesize cDNA from RNA templates, the Maxima H Minus First Strand cDNA Synthesis Kit (ThermoScientific) was applied according to the manufacturer's instructions. First strand cDNA was generated by adding primers (random hexamers, 100 pmol) and 1 µL of 10 mM dNTP mix to 50 - 100 ng RNA. Nuclease-free water was added to a final volume of 15 µL. Subsequently, 4 µL of 5 x RT buffer and 1 µL of Enzyme mix were added, gently mixed and centrifuged. Afterwads, samples were incubated for 10 min at 25°C followed by 30 min at 50 °C by using the thermocycler (Biometra, T3000). The reaction was terminated at 85 °C for 5 min. cDNA was stored at -80°C and used for real-time quantitative PCR (see chapter 3.1.4).

3.1.8 Photometric analysis of DNA and RNA concentration

To measure the concentration and purity of recovered DNA and RNA, the spectrophotometer (BioTek Epoch) was used. The concentration of dsDNA or ssRNA was determined my measuring the absorbance at OD 260. Here, 1.25 µL of purified DNA or RNA and dH_20 / buffer EB as blanks were

applied. The degree of purity was estimated by the absorbance ratio of A260 / A280. A ratio of ~ 1.8 is generally accepted as “pure” DNA, whereas a ratio of ~ 2.0 is generally valid as “pure” RNA.

3.1.9 Enzymatic reactions with double stranded DNA

3.1.9.1 Digestion with restriction enzymes

Restriction enzymes cleave DNA at defined recognition sites, which normally consist of four to eight base pairs, resulting in blunt or sticky ends. For optimal enzymatic conditions, 1 to 3 units of each appropriate restriction enzyme were used per µg DNA (plasmid DNA, PCR product), whereby one unit is defined as the required amount of enzyme to digest 1 µg of DNA in 1h (at usually 37°C). Moreover, 10 x digestion buffers supplied by the manufacturer and dH_2O were added to a final volume of 20 µL to create optimal conditions for various restrictions enzymes. Finally, the digested DNA was analyzed by gel electrophoresis (see chapter 3.1.2) and was used for further enzymatic reactions (see chapters 3.1.9.2 to 3.1.9.4).

3.1.9.2 Ligation with T4 DNA ligase

Ligation of inserts (e.g. digested PCR product) and linearized plasmid DNA was usually performed at a molar ratio of 3:1 or 5:1. Therefore, 30 to 50 µg of insert were mixed with the appropriate amount of linearized plasmid, 2 µL of T4 DNA Ligase reaction buffer and 1 µL of T4 DNA Ligase in a final volume of 20 µL. The reaction mixture was incubated at 16°C overnight or at room temperature for 2 h and was subsequently used for transformation of chemically competent *E.coli* bacteria (see chapter 3.1.1.3)

3.1.9.3 In-Fusion cloning strategy

The In-Fusion technology from Takara allows a fast, directional cloning of one or more fragments into one DNA vector via the In-Fusion enzyme that recognizes and fuses 15 bp overlaps at the end of DNA fragments (e.g. linearized vector and PCR fragments). Here, the In-Fusion HD cloning kit (Takara) was used according to the manufacturer’s instructions. Briefly, a linearized vector of interest was

generated by using restriction enzymes (see chapter 3.1.9.1) and was purified according chapters 3.1.2 and 3.1.5.3. The insert was usually generated by PCR (see chapters 3.1.3, 3.1.5.4). It should be noted that 15 bases at the 5' end of every primer must be homologous to 15 bases at one end of the linearized vector. In addition, the 3' end of every primer must be gene (insert) specific and should have a length of 18–25 bases. Depending on the length of the insert compared to the vector, molar ratios of 1:1, 3:1 or 5:1 were applied. The final cloning mixture consisted of 2 µL 5x In-Fusion Enzyme Premix, 30 to 50 µg of insert, the appropriate amount of linearized vector and dH_2O in a final volume of 10 µL. After a 15 minute incubation at 50°C and subsequent cooling on ice for 2 min, the mixture was used to transform chemically competent *E.coli* bacteria (see chapter 3.1.1.3).

3.1.9.4 Gateway cloning strategy

The Gateway cloning technology (Invitrogen) allows the transfer of DNA fragments by recombination reactions. The so-called entry vector encodes the gene of interest that is flanked by attL sites, whereas the destination vector harbours the *ccdB* gene flanked by attR sites. LR reaction performed with the LR clonase enzyme results in two plasmids: the expression vector containing the gene of interest that is now flanked by attB sites and the toxic byproduct harbouring the *ccdB* gene. In order to perform LR gateway cloning 200 ng of entry vector DNA, 200 ng of destination vector DNA and 1 µL LR clonase enzyme mix were mixed and incubated at 25 °C for 1 h. Finally, the reaction was stopped by addition of 0.5 µL proteinase K [2mg / mL] and an incubation period of 10 min at 37°C. Finally, transformation of *Stbl3 E.coli* bacteria was performed (see chapter 3.1.1.3).

3.2 Cell culture

Cell culture work was carried out under sterile benches in laboratories of safety levels I or II. Cells were incubated at 37°C under 5 % CO_2 and 95 to 100 % humidity.

3.2.1 Growth and maintenance of mammalian cell lines

HEK 293T and Bosc23 cells were cultured in Dulbecco's Modified Eagle medium (DMEM) with the addition of 10 % FCS (fetal calf serum) and 1 % P / S (Penicillin/Streptomycin). These adherent cells

were split every three to four days in case of 70 - 80 % confluency (see chapter 3.2.5). The basic medium for Jurkat cells was RPMI-1640 medium supplemented with 10 % FCS and 1 % P /S. These suspension cells were split every 3 to 4 days.

3.2.2 Growth and maintenance of murine cell lines

Dulbecco's Modified Eagle medium (DMEM) supplemented with 10 % FCS (fetal calf serum) and 1 % P / S (Penicillin/Streptomycin) was used for the cultivation of NIH/3T3 cells. EO771 cells were cultured in RPMI-1640 supplemented with 10 % FCS (fetal calf serum) and 1 % P / S. In case of 70 - 80 % confluency, these adherent cell lines were split according to chapter 3.2.5.

3.2.3 Isolation and cultivation of patient cancer derived pleural effusion cells

The pleural effusion cell containing punctate was divided among 50 mL Falcon™ tubes and centrifuged at 1500 rpm for 10 min. Supernatants were collected and stored at room temperature until further processing, while pelleted cells were resuspended in erythrocyte lysis buffer and incubated for 10 min at room temperature. Afterwards, cells were resuspended in RPMI-1640 without supplements and transferred into T175 cell culture flasks. For the macrophage adherence step, cells had to be cultivated at 37 °C for 1.5 h. Afterwards, non-adherent cells were transferred to 50 mL Falcon™ tubes. After centrifugation at 1500 rpm for 10 min, cells were resuspended in "conditioned" medium (RPMI-1640 mixed with supernatant of punctate at a 1:1 ratio) and cultivated at 37 °C. On the next days, cells were tested for the presence of tumor cells by flow cytometric and microscopic analyses.

The stored supernatants of punctuates were transferred to 50 mL Falcon™ tubes and pelleted at 3500 rpm for 10 min. The supernatant was used for preparing the conditioned medium (see above). In addition, pelleted cells were also cultured in conditioned medium and tested for the presence of tumor cells by flow cytometric and microscopically analyses.

3.2.4 Determination of cell cumber

To determine cell concentration and absolute cell number, cells were detached (if necessary), harvested, centrifuged and resuspended in a known volume of cell culture medium. 20 µL of this cell suspension were mixed with 20 µL trypan blue, which passes through the membrane of dead cells. 10 µL of this dilution were transferred to a cell counting chamber (Neubauer) and viable cells of four large squares were counted using a light microscope. The cell concentration was calculated with following formula:

$$cells\ mL^{-1} = \frac{cell\ number\ in\ four\ squares}{4}\ x\ 2\ (dilution\ factor)\ x\ 10^4$$

3.2.5 Splitting of adherent cells

Adherent cells had to be split in case of high confluency (70 - 80 %). Therefore, growth medium was aspirated and the monolayer was washed with PBS. Cells were detached with Trypsin / EDTA solution at 37°C for 5 min. With the addition of fresh culture medium, the reaction was stopped and the cells were split at a ratio of 1:5 or 1:10 and transferred into a new culture dish.

3.2.6 Freezing and thawing

For long term storage, murine and human cell lines were detached with Trypsin / EDTA solution if necessary, pelleted at 1500 rpm for 5 min and resuspended in freezing medium consisting of 90 % FCS and 10 % DMSO. 500 µL to 1 mL volumes were aliquoted into cryotubes and frozen slowly at - 80 °C. After 24 to 48 h, vials were transferred into liquid nitrogen. In contrast, mouse tissues and isolated tumors (with the exception of spleens or blood) were shock frozen in liquid nitrogen and stored at -80°C. Isolated splenocytes were pelleted at 1500 rpm for 5 min, resuspended in medium consisting of 90 % FCS and 10 % DMSO and frozen slowly at – 80 °C. Murine blood and plasma were frozen without any additives at – 80 °C

For thawing of murine and human cells, cryotubes were warmed up in a 37°C water bath. Warm culture medium was quickly added and cells were centrifuged (1500 rpm for 5 min) immediately to remove toxic DMSO of the freezing medium. Following one additional washing, cells were resuspended in the appropriate culture medium and seeded in a cell culture flask.

3.2.7 Puromycin selection

As the lentiviral NY-BR-1 - encoding vector #44 (hPGK_NY-BR-1_IRES_Puromycin_WPRE) confers puromycin resistance to successfully transduced cell lines, the antibiotic puromycin was used for the selection and cultivation of positive cells. Therefore, the medium of NY-BR-1 transduced EO771, HEK293T and Bosc23 cells was supplemented with puromycin at a final concentration of 5µg mL^{-1}.

3.2.8 Isolation of human und murine T cells via magnetic cell separation

3.2.8.1 Isolation and cultivation of human T cells

For the isolation of human T cells, Peripheral Blood Mononuclear Cells (PBMCs) had to be isolated from human blood using density gradient centrifugation at first. This procedure is based on the different densities of the blood components. The blood is layered over a high molecular fluid (*Ficoll-Paque*), in which blood cells divide into different, density-dependent phases after centrifugation. The PBMCs are found at the interface between the plasma and *Ficoll-Paque* layer. For this purpose, blood (each 27 mL) was diluted with PBS (up to 35 mL) and thoroughly added to a 15 mL *Ficoll-Paque* layer. Next, tubes were centrifuged at 2200 rpm for 20 min at room temperature without break. In order to isolate lymphocytes from erythrocytes, monocytes, granulocytes and plasma constituents, the interphase, predominantly consisting of PBMCs, was transferred into a new 50 mL Falcon™ tube. The following washing step was performed by refilling the new tube with PBS to a final volume of 50 mL and a renewed centrifugation step (1800 rpm, 10 min, with break). In case of residual erythrocytes, the cell pellet was resuspended in 5 mL erythrocyte lysis buffer. After 10 min, a second washing step was performed and cells were counted, as described in 3.2.4, for the further isolation of human T cells with the *Pan T cell Isolation Kit* (Miltenyi) according to the manufacturer's instructions.

The principle of the *Pan T cell Isolation Kit* is based on a magnetically labeling of non-target cells e.g. monocytes, neutrophils, B cells, dendritic cells, NK cells, granulocytes by using a cocktail of biotin-conjugated antibodies against CD14, CD15, CD16, CD19, CD34, CD36, CD56, CD123 and CD235a. This negative selection enables the passing of the $CD3^+$ faction through the magnetic field without being stopped or activated. Finally, isolated T cells were transferred to TexMACS medium (max. $2x10^6$ cells per mL) supplemented with TransAct™ (diluted 1:100), IL-7 (5 ng / mL) and IL-15 (5 ng / mL).

3.2.8.2 Isolation and cultivation of murine T cells

For the isolation of murine T cells the *Pan T cell Isolation Kit II, mouse* (Miltenyi) was used according to the manufacturer's instructions. At first, spleens were taken from mice, squeezed through a 100 µm cell strainer and washed with PBS (1500 rpm, 5 min). The erythrocytes were successfully lysed by adding 5 mL of blood lysis buffer for 10 min. After an additional washing step, splenocytes were counted and subjected to T cell isolation using the *Pan T cell Isolation Kit II.* The procedure is based on the depletion of magnetically labeled non-target cells, as already described in chapter "isolation and cultivation of human T cells". Here, biotin-conjugated antibodies against CD11b, CD11c, CD19, CD45R (B220), CD49b (DX5), CD105, Anti-MHC-class II, and Ter-119 were applied.

For the optimization of the cultivation protocol different media supplemented with diverse and differently concentrated supplements were tested. According to the final, optimized protocol murine T cells were cultivated in 12 well plates ($5x10^6$ cells / well) with RPMI-1640 medium supplemented with 10 % FCS, 1 % P / S as well as anti-CD3 antibody (2 µg / mL), anti-CD28 antibody (1 µg / mL), IL-2 (100 IU / mL), L-glutamine (2mM), ß-mercaptoethanol (50 µM) and non-essential amino acids (1x).

3.2.9 Lentiviral transduction

3.2.9.1 Co-transfection of HEK 293T cells

Lentiviral particles were produced by co-transfecting HEK 293T cells with two helper plasmids (VSV-G – encoding envelope plasmid #1 (pCMV_VSV_G); HIV Gag-Pol - encoding packaging plasmid #2 (pCMVR8.74)), the lentiviral (transfer) plasmid and cell transfection reagent Polyethyleneimine (PEI). PEI, a cationic polymer, forms positively charged complexes with DNA that bind to negatively charged cell membranes of eukaryotic cells, which in turn facilitates the endocytic uptake of the DNA:PEI complex.

Two days prior to transfection, 6 x 10^6 HEK 293T cells were plated into 15 cm cell culture dishes in 22.5 mL DMEM supplemented with 10 % FCS and 1 % P / S. For transfection the appropriate amounts (see below) of the lentiviral transfer plasmid and two helper plasmids (#1, #2) were mixed in Opti-MEM and incubated for 5 min at room temperature. Next, the required amount of PEI was added to the DNA master mix. After an incubation time of 20 min at room temperature, the transfection mixture was added dropwise to HEK 293T cells (60 - 70 % confluent). The next day, the cell culture medium was replaced with 14 mL fresh DMEM (without phenol red) supplemented with 1 % P / S. After

additional 24 h, the lentiviral supernatant was harvested and concentrated by using centricon centrifugal filters (Merck). First, the supernatant was centrifuged at 1800 rpm for 5 min in order to pellet and remove detached HEK 293T cells. Afterwards, the supernatant was filtered by using membrane filters (0.45 µm pore size), transferred to centricon centrifugal filters and centrifuged at 3500 g for 30 min. An additional centrifugation step with inverted centricon centrifugal filters at 1000 g for 2 min followed. The concentrated lentiviral particles were transferred into 1.5 mL tubes. These centrifugation steps were repeated until the entire viral supernatant was concentrated. Finally, concentrated viral supernatants were stored at - 80 °C.

The titer of harvested and concentrated lentiviral particles was determined by transduction of HEK 293T cells. One day prior to transduction, HEK 293T cells (1 x 10^5 / well) were seeded in 24 well plates and incubated in 1 mL DMEM supplemented with 10 % FCS and 1 % P / S. For lentiviral transduction, different volumes of concentrated viral supernatant (e.g. 1, 3 or 10 µL) and Polybrene (cfinal 8 µg / mL) were added to seeded HEK 293T cells. The transduction efficiency was determined by flow cytometric analysis 72 h after transduction (see chapter 3.2.18). The lentiviral titer was calculated from the frequency of positive tested cells.

15 cm cell culture dish

Opti-MEM [µL]	1500
Transfer vector [µg]	22.5
Packaging vector (pCMV-MLV-g/p) [µg]	14.6
Envelope vector (pCMV VSV-G) [µg]	7.9
PEI [1 mg/ mL] [µL]	132

3.2.9.2 Lentiviral transduction of Bosc23, EO771, HEK 293T and NIH / 3T3 cells

For lentiviral transduction of the adherent cell lines Bosc23, EO771 and NIH / 3T3, lentiviral supernatants of co-transfected HEK 293T cells (see chapter 3.2.9.1) were used. First, adherent cells were detached with Trypsin / EDTA, pelleted at 1500 rpm for 5 min, counted (see chapters 3.2.4, 3.2.5) and seeded (1 x 10^5 cells / well) in 12 well plates with fresh DMEM medium supplemented with 10 % FCS and 1 % P / S. The next day, cells were transduced at an MOI of 5 to 10 under the addition of Polybrene (cfinal 8 µg / mL). Polybrene, a positively charged polymer, increases infection efficiency by neutralizing the charge repulsion between virions and cell surfaces. 24 to 48 h post transduction, the medium was changed. Finally, the transduction efficiency was determined by flow cytometric analysis 48 to 72 h after transduction (see chapter 3.2.18)

3.2.9.3 Lentiviral transduction of Jurkat cells

For transduction of Jurkat cells, thawed lentiviral supernatants of co-transfected HEK 293T cells (see chapter 3.2.9.1) as well as Polybrene (cfinal 8 µg / mL) were added to 2 x 10^5 Jurkat cells (MOI 2 to 10) cultivated in a T25 cell culture flask with RPMI 1640 medium (with 10 % FCS and 1 % P / S). Due to possible cytotoxic effects of high polybrene concentration, medium was changed 24 h after transduction. The success of transduction was evaluated by flow cytometric analysis (see chapter 3.2.18).

3.2.9.4 Lentiviral transduction of human T cells

Prior to lentiviral transduction of human T cells, they had to be activated by cultivation in TexMACS medium supplemented with TransAct™ (diluted 1:100), IL-7 (5 ng / mL) and IL-15 (5 ng / mL) (see chapter 3.2.8.1) for a minimum of 48 h. Afterwards, activated T cells were washed, transferred to 12 well plates (2 – 3 x 10^6 cells / well in 1.5 mL TexMACS +IL7 +IL15) and transduced with the concentrated, lentiviral supernatants of co-transfected HEK 293T cells (see chapter 3.2.9.1) under the addition of Polybrene (8 µg/mL) at an MOI of 2 to 5. Two days after transduction, medium was changed and transduction efficiency was determined by flow cytometric analysis (see chapter 3.2.18).

3.2.9.5 Lentiviral transduction of murine T cells

An efficient activation of murine T cells is essential for successful transduction. Therefore, diverse protocols with different time points of transduction, various cell culture media and concentrations of activation cytokines were tested. Therefore, murine T cells were cultivated in X-Vivo 20 medium supplemented with anti-CD3 Ab (100 ng /mL), anti-CD28 Ab (100 ng / mL), human IL-2 (100 IU/ mL) and mouse IL-15 (5 ng /mL) for two days. In the same time, 24 well plates were coated with retronectin. Therefore, retronectin was diluted to 16 µg / mL (from a 1 mg / mL stock concentration, stored at -20°C) in PBS and added on non-tissue culture 24 well plates (350 µL / well). Following incubation at 37 °C for 2 h, retronectin was removed and activated T cells were seeded at a density of 5 x 10^5 cells / mL medium (X-Vivo20 supplemented with human IL-2 (50 IU / mL) and mouse IL-15 (2.5 ng / mL)) onto retronectin coated plates. The concentrated lentiviral supernatant (see chapter 3.2.9.1) was added at an MOI of 5. Finally, a spinoculation step at 2000 g and 32 °C was performed for 1.5 h. The frequency

of successfully transduced murine T cells was evaluated by flow cytometric analysis 48 h after transduction.

3.2.10 Electroporation of T cells

Electroporation of both human and murine T cells was performed with pS/MARter or NanoCMARter based systems, kindly provided by Dr. Richard Harbottle and Dr. Matthias Bozza from the DKFZ (DNA Vector Research Group), by using the Neon Transfection System from ThermoFisher Scientific. The advantage of this system is the generation of a uniform high electric field, less ion formation and minimal pH changes in the reaction chamber (Neon Tip), generated by two electrodes with minimized surface areas but maximized gap between both.

3.2.10.1 Electroporation of human T cells

Human T cells were activated by cultivation in TexMACS medium supplemented with TransAct™ (diluted 1:100), IL-7 (5 ng / mL) and IL-15 (5 ng / mL) (see chapter 3.2.8.1) for 24 to 48 h. On the day of electroporation, human T cells were washed twice with PBS (1500 rpm, 5 min). 5 x 10^6 T cells per transfection were resuspended in 100 µL buffer T (Neon Transfection Kit, ThermoFisher) and mixed with 10 µg of pS/MARter or NanoCMARter vectors. The DNA cell mixture was loaded into the Neon tip and plugged into the Neon Pipette Station by using the Neon Pipette. The cell / DNA mixture was shocked at 2200 V for 30 ms. Finally, transfected cells were transferred into 6 well plates with pre-warmed TexMACS medium without phenol red (1 x 10^7 T cells / 5 mL / well). After a recovery period of a few hours, the cytokines IL-7 (5 ng/ mL) and IL-15 (5 ng/ mL) were added. The frequency of successfully transduced human T cells was evaluated by flow cytometric analysis 24 to 48 h after electroporation (see chapter 3.2.18).

3.2.10.2 Electroporation of murine T cells

An electroporation protocol for murine T cells had to be established. Therefore, different activation protocols and all important electroporation parameters (e.g. voltage, duration, amount of pulses) had to be optimized. At the beginning, murine T cells were cultivated in RPMI-1640 medium supplemented

with 10 % FCS, IL-2 (100 IU / mL), L-glutamine (2 mM), non-essential amino acids (1x), anti-CD3 Ab (100 ng / mL) and anti-CD28 Ab (100 ng/ mL) for 24 h upon isolation. Afterwards, T cells were electroporated according to different protocols (protocol I: 1550 V, 10ms, 3 pulses; II: 1080 V, 50 ms, 1 pulse; III: 1550 V, 30 ms, 1 pulse; IV: 2000 V, 10 ms, 3 pulses) using the Neon Transfection System (Thermo Fisher) and cultivated in RPMI-1640 medium (w / o Phenol red) supplemented with 20 % FCS, IL-2 (100 IU / mL) and L-glutamine (2mM).

According to the final optimized protocol, murine T cells were cultivated / activated in 12 well plates (5 x 10^6 cells / well) with RPMI-1640 medium supplemented with 10 % FCS, 1 % P / S as well as anti-CD3 antibody (2 µg / mL), anti-CD28 antibody (1 µg / mL), IL-2 (100 IU / mL), L-glutamine (2mM), ß-mercaptoethanol (50 µM) and non-essential amino acids (1x) for one day. Prior to transfection, murine T cells had to be washed twice with PBS. Per transfection, 5 x 10^6 T cells were resuspended in 100 µL buffer T and mixed with 10 µg of pS/MARter or NanoCMARter vectors. The DNA / cell mixture was loaded into the Neon tip and plugged into the Neon Pipette Station by using the Neon Pipette. Different electroporation protocols with various voltages (e.g. 1550, 1800, 1900 or 2000 V) and amount of pulses (1, 2 or 3) were tested. Unless otherwise stated, T cells were electroporated according to the most optimized protocol (1900 V, 10 ms, 3 pulses). Finally, transfected cells were transferred into 24 well plates with pre-warmed RPMI-1640 medium (5 x 10^6 T cells / well) supplemented with 20 % FCS, IL-2 (100 IU / mL) and L-glutamine (2mM). The transfection efficiency was determined by flow cytometric analysis (see chapter 3.2.18).

3.2.11 Activation and cross-reactivity analysis with NY-BR-1 and NY-BR-1.1 full length proteins

3.2.11.1 Coating of 96 well plates with NY-BR-1 and NY-BR-1.1 full length proteins

NY-BR-1 / NY-BR.1.1 full length peptide containing protein lysates, extracted from GST-NY-BR-1 and GST-NY-BR-1.1 protein transfected HEK 293T cells (performed by Claudia Ziegelmeier), were coated on 96 well plates under sterile conditions. First, wells were coated with 50 µL / well glutathione casein (100 ng / well) diluted in sterilized coating buffer (0.1M Na_2Co_3, 7.13 g $NaHCO_3$, 1.59 g Na_2CO_3, ad 1 L dH_2O; pH to 9.5 with 10 N NaOH) overnight at 4 °C. The next day, the supernatant was discarded and wells were blocked with 50 µL / well of sterilized blocking buffer (PBS with 0.05 % Tween-20 and 0.2 % casein) for 1h at room temperature. Following three washing steps with 200 / well of sterilized washing

buffer (PBS with 0.05 % Tween-20), wells were coated with 30 µL of GST tagged NY-BR-1 or NY-BR-1.1 protein containing cell lysates (cfinal 3.75 µg / well in sterilized blocking buffer). Following centrifugation (2000 rpm, 1 min), the plate was shaken for 1 h at room temperature. Finally, wells were washed three times with 200 / well of sterilized washing buffer (PBS with 0.05 % Tween-20) and filled with 100 µL of sterilized washing buffer. The NY-BR-1 and NY-BR-1.1 coated plates were stored at 4 °C for several weeks.

3.2.11.2 Co-cultivation of CAR$^+$ T cells with NY-BR-1 and NY-BR-1.1 full length proteins

The specific activation of anti-NY-BR-1 CAR - expressing T cells was investigated by using NY-BR-1 full length proteins coated on a 96 well plate (see chapter 3.2.11.1). For this assay, 3 x 10^4 CAR$^+$ T cells were washed twice with PBS (1500 rpm, 5 min), resuspended in RPMI-1640 (10 % FCS, 1 % P / S) and transferred to NY-BR-1 coated wells. Following incubation period of 24 h, supernatants were analyzed for released IFNγ by using IFNγ ELISA (see chapter 3.2.12).

In order to estimate or rather investigate possible cross-reactivities of anti-NY-BR-1 CARs with the NY-BR-1.1 peptide, CAR$^+$ T cells were co-cultivated with NY-BR-1.1 full length proteins coated on 96 well plates. This assay was performed in the same way as the activation assay with NY-BR-1 proteins, described above. These assays were performed in triplicates.

3.2.12 Enzyme-linked Immunosorbent Assays (ELISAs)

3.2.12.1 Human and murine IFNγ ELISA

Enzyme-linked Immunosorbent Assays (ELISAs) were mainly utilized for the detection and quantification of human or murine IFNγ in cell culture supernatants by using the Human or Mouse IFNγ ELISA Sets from BD Pharmingen. Briefly, 96 well plates were coated with 30 µL of human or murine capture antibody (purified anti-human or anti-mouse IFNγ antibody) diluted 1:250 in coating buffer (0.1M sodium carbonate, 7.13 g NaHCO3, 1.59 g Na2CO3, ad 1 L dH_2O; pH to 9.5 with 10 N NaOH) at 37 °C for 2 h or overnight at 4 °C. Following five washing steps with washing buffer (PBS with 0.05 % Tween-20; 200 µL / well), free binding sites were saturated by the addition of 150 µL of assay diluent (PBS with 10 % FCS) per well at room temperature for 1 h. Next, the wells were washed five times with

washing buffer and 30 µL / well of the cell culture supernatants to be tested were added. Moreover, a known concentration series of IFNγ, provided by BD, was prepared according to the manufacturer's instructions. After an incubation period of 2 h at 37 °C, within which cytokines secreted in the supernatants were bound to the solid phase, wells were washed five times with washing buffer and 30 µL / well of working detector (Biotinylated detection antibody against human or mouse IFNγ plus SAv-HRP reagent; diluted 1:250 in assay diluent) were added and incubated for 1 h at room temperature. Now, wells were washed seven times with washing buffer (with 1 min soaks) and samples were incubated with 50 µL / well of the TMB substrate solution (BD OptEIA) for 30 min at room temperature in the dark. Finally, 25 µL of stop solution (2 N H_2SO_4) were pipetted per well and the absorbance was determined at 450 nm within 30 min with a reference wavelength of 570 nm by using the spectrophotometer (BioTek Epoch). The quantitative evaluation was carried out by a regression line created from cytokine standards.

3.2.12.2 Anti-NY-BR-1 antibody ELISA

For the detection of anti-NY-BR-1 antibodies in murine plasma, a specially designed ELISA was performed. Therefore, 96 well plates were coated with glutathione casein and 30 µL of GST-NY-BR-1 containing cell lysates (cfinal 3.75 µg / well in sterilized blocking buffer), as described in chapter 3.2.11.1. Following last washing step with washing buffer (PBS with 0.05 % Tween-20), 30 µL of undiluted murine plasma were added per well. The monoclonal antibody clone2 served as a positive control. After an incubation period of two hours, wells were washed with 150 µL of washing buffers three times. Afterwards, 30 µL of the secondary HRP - conjugated anti-mouse IgG antibody (Dianova, 115-035-003, pre-diluted 1:10000 in blocking buffer) were added and incubated for 1 h. After washing the wells with 150 µL of washing buffers three times, 50 µL / well of the TMB substrate solution (BD OptEIA) were added. Following short incubation for 15 min at room temperature in the dark, the reaction was terminated with 25 µL / well of stop solution (2N H_2SO_4). The absorbance was measured at 450 nm with a reference wavelength of 570 nm by using the spectrophotometer (BioTek Epoch).

3.2.13 xCELLigence killing assay

Cytolysis assays were mainly done with the xCELLigence RTCA instrument (ACEA Biosciences), enabling a noninvasive monitoring of cell proliferation, attachment and morphology change. The principle is based on the real-time measurement of cellular impedance which is measured by gold

microelectrodes on the bottom surface of the used 96 well electronic microtiter plates (E-Plate 96, ACEA Biosciences). Since the current flows through the bulk solution (e.g. culture medium, PBS), the flow of electrons is affected by adherent cells which in turn can be determined by the change of impedance. Consequently, the destruction and killing of adherent cells by CAR^+ T cells can be easily monitored and calculated.

Adherent target cells were resuspended in RPMI-1640, supplemented with 10 % FCS and 1 % P / S, and seeded into 96 well electronic microtiter plates (30.000 cells / well) 6 to 24 h prior to the addition of mock or CAR^+ T cells. Once target cells were adherent, CAR^+ T cells were added at a ratio of 1:1. Real-time monitoring occurred for at least 40 h. The killing capacity was calculated on the basis of a unit less parameter called Cell Index (CI), which describes the impedance at time point n (impedance in the absence of cells / nominal impendence value). In order to calculate the proportion of viable cells, cell indices were normalized to the time point of effector cell addition and, subsequently, the normalized CIs of mock and CAR^+ T cell - treated target cells were considered in relation to normalized CIs of untreated target cells. Moreover, surface expression levels of the target protein (NY-BR-1) were analyzed by flow cytometry (see chapter 3.2.18.1) and the concentration of IFNγ in cell culture supernatants was determined by IFNγ ELISAs (see chapter 3.2.12).

3.2.14 CFSE based killing assay of EO771 cells

Prior to cytolysis assays of EO771 cells, cells were labeled with CFSE by using the CellTrace CFSE Cell Proliferation Kit (ThermoFisher Scientific). Both EO771 and Lactacystin-treated NY-BR-1^+ EO771 cells (see chapter 3.2.17) were seeded into 6 well plates (1.5 x 10^5 cells / well) and cultivated as described in chapter 3.2.2. The next day, cells were detached with Trypsin / EDTA, washed and resuspended in PBS (2 mL PBS / well). 1 µL of DMSO / CellTrace CFSE staining solution (18 µL DMSO mixed with 1 µL Cell Trace) was added per mL PBS. Following incubation at 37 °C for 30 min, cells were washed twice with fresh medium and incubated for one additional day at 37 °C. Six hours after seeding 20,000 to 30,000 CFSE labeled cells per well (96 well plate), CAR^+ T cells (and the appropriate amount of mock T cells) or splenocytes, isolated from CAR^+ T cell - treated C57BL/6 and NY-BR-$1^{tg/-}$ mice, were added at a ratio of 1:1 and co-cultivated in RPMI-1640 (10 % FCS, 1 % P / S) for 24 h. The proportion of living CFSE labeled cells was determined by DAPI staining and flow cytometric analysis (see chapter 3.2.18). Moreover, the concentration of IFNγ in cell culture supernatants was determined by IFNγ ELISAs (see chapter 3.2.12).

3.2.15 Functional analysis of mouse persisting CAR$^+$ T cells

In order to determine the remaining activation and efficiency potential of murine CAR$^+$ T cells which persisted in C57BL/6 and NY-BR-1$^{tg/-}$ mice over a period of two weeks (see chapter 3.2.19.2), spleens were isolated, dissociated by using the gentleMACS Dissociater (Miltenyi) and pressed through the 100 µm cell strainer (Greiner). A washing step with PBS (1500 rpm, 5 min) followed and the erythrocytes were successfully lysed by adding 5 mL of blood lysis buffer for 10 min. Following analysis of persisting CAR$^+$ T cells by flow cytometry (see chapters 3.2.19.2 and 3.2.18.1), 3 x 10^4 splenocytes were co-cultivated with (NY-BR-1$^+$) EO771 cells in RPMI-1640 supplemented with 10 % FCS and 1 % P / S at a ratio of 1:1 (96 well format) for 24 h. Afterwards, the activation of splenocytes or rather persisted T cells was analyzed by intracellular staining for different activation-associated cytokines (see chapter 3.2.18.2) and, additionally, the concentration of released IFNγ was calculated by using IFNγ ELISA (see chapter 3.2.12). The proportion of killed (NY-BR-1$^+$) EO771 cells was determined by flow cytometric analysis using DAPI staining (see chapter 3.2.18.1). Splenocytes from C57BL/6 wt and NY-BR-1$^{tg/-}$ mice treated with untransfected (mock) T cells, originally derived from C57BL/6 wt mice, served as controls.

3.2.16 Ayoxxa Lunaris multiplex cytokine assay

The Lunaris technology from Ayoxxa enables the simultaneous detection of several cytokines in small volumes by using antibody-coated beads attached to micro-cavities on the planar *Lunaris BioChip*. The spatial separation of these beads facilitates an image-based readout. Therefore, the Lunaris technology was used for the quantification of over eleven human (Human 11-Plex Cytokine Kit) and twelve murine (Mouse 12-Plex Cytokine Kit) cytokines in the plasma of CAR$^+$ T cell - treated mice (see chapter 3.2.19).

Both the human and murine multiplex assays were performed according to the manufacturer's instructions. Briefly, 5 µL of prepared standards and samples (undiluted mouse plasma) were added to each prewashed well of the *Lunaris BioChip*. Loaded plates were incubated for 3 h at room temperature. After washing the wells three times, 10 µL of provided detection antibody solution (Streptavidin-Phycioerythrin mix) were added and incubated for 1 h at room temperature. In subsequent steps, wells were washed several times and 10 µL of provided SA-PE solution were added. Following incubation for 30 min at room temperature, wells were washed and air-dried for at least 1.5 h. Finally, imaging was performed with the *Lunaris reader* and analyzed by using *Lunaris analysis suite* and Microsoft *excel*.

3.2.17 Cell synchronization and proteasome inhibition for NY-BR-1 expression analysis

Synchronization of (NY-BR-1$^+$) EO771 and (NY-BR-1$^+$) Bosc cells was achieved by using different cell cycle blockers such as Thymidine, L-mimosine, Lactacystin or Nocodazole. Prior to the addition of cell cycle blockers, 1.5 x 10^5 (NY-BR-1$^+$) EO771 or 2.5 x 10^5 (NY-BR-1$^+$) Bosc cells per well (in a 6 well plate format) were incubated for a few hours, as described in chapters 3.2.1and 3.2.2. In addition, the cell culture medium of NY-BR-1 expressing cells was enriched with puromycin (5 µg / mL) during the analysis period (see chapter 3.2.7).

As high concentrations of Thymidine interrupt the deoxynucleotide metabolism pathway, a double Thymidine block was used to synchronize cells at the G1 / S boundary. Therefore, Thymidine (2 mM) was added a few hours after cells were seeded. Medium was changed approximately 18 h after the first Thymidine treatment. After an additional 8 to 10 h, Thymidine treatment was repeated. Expression and cell cycle analysis were performed the next day.

Lactacystin is a proteasome inhibitor (irreversible alkylation of subunit X of the 20S proteasome) and blocks cell cycle progression in both the G0 / G1 and G2 / M phases. Treatment with Lactacystin (5 µM) was carried out for at least 18 h prior to expression and cell cycle analysis.

L-mimosine is a plant amino acid and can be used as a G1 cell cycle blocker by preventing the binding of Ctf4 to chromatin. Hence, cells were treated with L-mimosine (400 µM) alone for at least 18 h or in combination with Thymidine double block.

Aphidicolin inhibits DNA synthesis by specific inhibition of the DNA polymerase α, which in turn leads to cell cycle arrest at G1/S boundary. Therefore, Aphidicolin (5 µg / mL) was applied in combination with Thymidine double block.

The interfering with microtubules in cells by the synthetic drug Nocodazole leads to the inhibition of microtubule dynamics and enables a cell cycle block at the G2 / M phase. (NY-BR-1$^+$) EO771 were treated with final Nocodazole concentrations of 0.2 to 0.4 µg/mL, while (NY-BR-1$^+$) Bosc cells received an increased concentration of up to 0.8 µg / mL.

The NY-BR-1 surface expression levels as well as the cell cycle profile were studied by flow cytometric analysis. Cells were stained with the monoclonal antibody clone2, which is directed against NY-BR-1, and propidium iodide (PI) (see chapters 3.2.18.1 and 3.2.18.2).

3.2.18 Flow cytometric analysis

Flow cytometry is a laser-based technology system, which provides rapid analysis of multiple characteristics of a cell. This is allowed by a laser system measuring the relative size (forward scatter) and granularity (side scatter) of passing cells, which are hydrodynamically focused with sheath fluid. In addition, the system is able to measure fluorescence characteristics of single cells, which result from labeled cell surface markers or labeled intracellular proteins using mAbs conjugated to fluorescent dyes. The information obtained is both qualitative and quantitative. The evaluation of flow cytometry based experiments was done with the FACS Canto II device (BD) and *FlowJo* software.

3.2.18.1 Surface staining

For staining of extracellular cell markers, cells were trypsinized if needed (or detached with cell scraper in case of NY-BR-1$^+$ EO771 and Bosc cells), harvested and counted. Approximately 2 x 10^5 cells were transferred into flow cytometry tubes, spun at 1500 rpm for 5 min and washed with 500 to 1000 µL of FACS buffer (PBS with 1 % FCS and 2mM EDTA). The supernatant was discarded and cells were stained with fluorochrome-conjugated mAbs (with the manufacturer's concentration specifications) in 100 µL FACS buffer for 30 min at 4 °C in the dark. In case of staining with non-conjugated primary antibodies such as the anti-NY-BR-1 mAbs (clone2 (cfinal 3µg/mL), 10D11 (cfinal 5 µg/mL), clone3 (cfinal 5 µg/mL)), the incubation period was prolonged to 60 min. In order to remove unbound mAbs, cells were washed twice with 2 mL FACS buffer. If the addition of secondary fluorochrome-conjugated mAbs was necessary, a second staining step was performed with the appropriate secondary antibodies (APC / PE – conjugated anti-human or anti-mouse IgG, and the manufacturer's concentration specifications) in 100 µL FACS buffer for 30 min at 4 °C in the dark, followed by two washing steps. Finally, cells were resuspended in 200 µL FACS buffer. For the distinction between living and dead cells, 1 µl of DAPI solution (cfinal 3 µM) was added. Since several fluorescent dyes have overlapping emission spectra, controls stained with one fluorescent-conjugated mAb were applied for compensation. Moreover, isotype controls were used to evaluate the intensity of non-specific binding events and unstained samples were utilized as negative controls.

For the flow-cytometry based CFSE cytolysis assay or functional analysis of mouse persisting CAR$^+$ T cells (see chapters 3.2.14 and 3.2.15), co-cultivated CAR$^+$ T cells / splenocytes and target cells were transferred into flow cytometry tubes and washed (see above). In some cases, cells were additional stained for CD3 – as described above – to differentiate between T cells and target cells in an even better way. The frequency of living target cells was determined by the addition of DAPI. For the final

evaluation, the proportion of survived T cell / splenocyte treated target cells, identified by CFSE or / and CD3 negative and DAPI labeling, was calculated in relation to the proportion of survived untreated target cells (control).

The flow-cytometry based analysis of cell cycle and proteasome dependent NY-BR-1 expression (see chapter 3.2.17) was performed with two different kinds of staining. Therefore, cells from the same well were transferred to two different flow cytometry tubes (one for surface expression analysis of NY-BR-1, one for cell cycle analysis with PI staining). The analysis of NY-BR-1 expression was performed with anti-NY-BR-1 mAbs as described above. In contrast, the cell cycle profile was examined by PI staining. Here, cells were washed (as described above) and resuspended in 300 µL of Nicoletti buffer (50 µg/ mL PI, 0.1 % (w/v) $Na_3C_6H_5O_7$, 0.1 % (v/v) Triton X-100). Following incubation for at least 15 min at room temperature, cells were vortexed and analyzed with the FACS Canto II device (BD).

3.2.18.2 Intracellular staining

Next to the analysis of surface markers, the detection of intracellular proteins plays a key role for the assessment of T cell activation or (intracellular) protein expression levels. For intracellular stainings, positive controls were treated with an activation cocktail (Biologend, #423301; diluted 1:500 in RPMI medium) for 1 h at 37 °C. Subsequently, all cells were treated with the Golgi stops Brefeldin A (cfinal 5 µg / mL) and Monensin (cfinal 2 mM) for 5 h at 37 °C. If cells were tested for both surface markers and intracellular proteins, surface staining was done as described in chapter 3.2.18.1. Afterwards, cells were transferred to a 96 well plate and centrifuged at 2000 rpm for 3 min. Next, pellets were resuspended in 200 µL of FACS buffer (PBS with 1 % FCS and 0.1 % NaN3) and centrifuged at 2000 rpm for 3 min. This washing step was done two times, followed by a fixation step with 100 µL of Cytofix / Cytoperm solution (BD). After an incubation period of 15 min at 4 °C, 200 µL of Perm / Wash solution (BD) were added to each well and plate was spun at 2000 rpm for 3 min. Following one additional washing step with Perm / Wash solution, the appropriate mAbs were diluted in Perm / Wash buffer (according to the manufacturer's instructions) and added to each well (50 µL / well). The staining was incubated for 20 min at 4 °C. Thereafter, the cells were washed two times with Perm / Wash solution (2000 rpm, 3 min) and finally resuspended in 200 µL of FACS buffer and stored at 4 °C.

3.2.19 Mouse experiments and preparation

For all mouse experiments, C67BL/6 wild-type (Taconic or IBF Heidelberg), NOD.CB17-Prkdc^{scid} (Taconic), NSG (Taconic or DKFZ animal house) or NY-BR-1$^{tg/-}$ (IBF Heidelberg) mice of different ages were used. Mice were kept in the animal house of the IBF Heidelberg at room temperature (22-23 ° C) and an artificial day / night rhythm of 12 h.

3.2.19.1 CAR$^+$ T cell treatment of tumor-bearing mice

Tumor cells (2 x 10^6 NY-BR-1$^+$ EO771 or NY-BR-1$^+$ Bosc23 cells in 100 µL PBS per mouse) were injected subcutaneously into the flank of C57BL/6 wt, NY-BR-1$^{tg/-}$, NOD.CB17-Prkdc^{scid} or NSG mice. CAR - expressing human ($1x10^6$) or murine T cells ($5x10^5$) were injected intravenously in a final volume of 100 µL PBS per mouse eight days post tumor engraftment. Untreated mice and mice treated with the appropriate amount of mock T cells served as controls. Mice engrafted with subcutaneous tumors were sacrificed by carbon dioxide at a tumor diameter of 15 mm or tumor volumes of 200 mm³ (EO771 in C57BL/6), 450 mm³ (NY-BR-1$^+$ EO771 in NOD.CB17-Prkdc^{scid}) or 300 mm³ (NY-BR-1$^+$ Bosc23 in NSG), whatever occurred first. Tumor volumes were calculated with the ellipsoid formula (1/6*π* length x width x depth).

Tumors, spleens and blood were removed for further analyses. Tumors were divided by using a scalpel. One part was shock frozen in liquid nitrogen for subsequent cryosectioning (see chapter 3.2.19.3). The other part was dissociated by a gentleMACS Dissociator (Miltenyi) for flow cytometric analysis, whereby the tumor supernatants were frozen and used for further analysis with the Ayoxxa multiplex cytokine assays (see chapter 3.2.16). Due to remaining cell clumps in the dissociated tumor cell suspension, these cells were additionally filtered by using 100 µm cell strainer (Greiner). Afterwards, the dissociated tumor cells were transferred to flow cytometry tubes to stain for NY-BR-1 expressing tumor cells and tumor-infiltrated T cells, as described in chapter 3.2.18.1. Spleens were also dissociated by using the gentleMACS Dissociator (Miltenyi) and pressed through a 100 µm cell strainer (Greiner). A washing step with PBS (1500 rpm, 5 min) followed and the erythrocytes were lysed by adding 5 mL of blood lysis buffer for 10 min. After one additional washing step, one part of the splenocytes was cryoconserved (see chapter 3.2.6), whereas the other part was analyzed for persisting CD3$^+$ T cells by using flow cytometric analysis (see chapter 3.2.18.1). Blood was mixed with the anti-coagulant heparin. Next, approximately 10 µL of the isolated blood were transferred to flow cytometry tubes and stained for (CAR$^+$) CD3$^+$ cells (chapter 3.2.18.1). The rest was cryoconserved, as described in chapter 3.2.6, or used for the isolation of plasma. Here, blood was carefully added to flow

cytometry tubes which were already filled with 500 µL *Ficoll-Plaque.* As already explained in chapter 3.2.8.1, blood cells are divided into different, density-dependent phases by the high molecular fluid (*Ficoll-Plaque*) during centrifugation. Therefore, blood / Ficoll filled tubes were centrifuged at 2200 rpm for 15 min (without break) and mouse plasma was obtained from the top layer and cryoconserved without any additives. Finally, mouse plasma was used for further analysis such as the Ayoxxa multiplex cytokine assays (see chapter 3.2.16).

3.2.19.2 CAR T cell treatment of C57BL/6 and NY-BR-1$^{tg/-}$ mice

Safety analyses of murine CAR$^+$ T cells were performed by intravenous injection of 5 x 10^5 CAR$^+$ T cells (T cells originally derived from C57BL/6wt mice) in C57BL/6 wt and NY-BR-1$^{tg/-}$ mice. Mice were examined daily for visible side effects such as weight loss. Two weeks after T cell engraftment, nearly all tissues (e.g. stomach, brain, kidney, lung, heart, liver, skin, spleen, blood and more) were isolated and examined for abnormalities or visible inflammation. Tissues were shock frozen in fluid nitrogen for subsequent cryosectioning and isolation of DNA according to chapters 3.2.19.3 and 3.1.5.5 or fixed in 4 % buffered formalin. In addition, isolated spleens and blood were analyzed for persistent CAR$^+$ T cells by flow cytometry, as also described in chapters 3.2.18.1 and 3.2.19.1. In order to detect changes in blood cytokine levels, plasma was isolated by using *Ficoll-Plaque*, as also described in chapter 3.2.19.1., and analyzed with the Ayoxxa multiplex cytokine assays (see chapter 3.2.16). Moreover, isolated spleens were used for co-cultivation with NY-BR-1 expressing target cells (see chapter 3.2.15).

3.2.19.3 Cryosectioning of tumors and organs

Cyopreserved tumors and organs were embedded in Tissue-Tek OTC-Mounting medium and sectioned in slices of 3 to 5 µm using the cryomicrotome (CryoStarNX70, ThermoScientific). These sections were stored at -80 °C and used for immunohistochemical staining (see chapter 3.2.19.5).

3.2.19.4 Sectioning of paraffin-embedded tissues

Formalin-fixed tissues were embedded in paraffin with the modular paraffin embedding center (Microm ES 350-2, Thermo Scientific) and sectioned in slices of 4 to 6 µm using a freezing microtome.

Subsequently, formalin-fixed paraffin embedded (FFPE) tissues were analyzed for infiltrated T cells by immunohistochemical staining (IHC) (see chapter 3.2.19.6).

3.2.19.5 Immunohistochemistry staining (IHC) of cryosectioned tissues

Cyrosectioned tissues were analyzed for T cell infiltration by using immunohistochemical stainings (IHC). First, tissues were fixed with 4 % PFA for 20 min and subsequently washed twice with PBS. IHC stainings were performed by Rosa Eurich (DKFZ, AG Halama/Jäger) according to the full automated protocol (Bond Polymer Refine Detection Kit (Leica); Microm STP420D, Thermo Scientific):

Step	Solution / Program	Time [min]	Repeats	Temperature
1	BOND Wash Solution	3	1	RT
2	Peroxide Block	20	1	RT
3	BOND Wash Solution		3	RT
4	Serum block (PBS with 10 % goat serum)	15	1	RT
5	BOND Wash Solution		3	RT
6	Primary antibody (anti-CD3 (ab16669 Abcam) in TBS / 10%FCS)	30		RT
7	BOND Wash Solution		3	RT
8	Secondary antibody (poly-HRP-anti-rabbit IgG)	8	1	RT
9	BOND Wash Solution	2	2	RT
10	Deionized water		1	RT
11	Mixed DAB Refine		1	RT
12	Mixed DAB Refine	10	1	RT
13	Deionized water		3	RT
14	Hematoxylin	10	1	RT
15	Deionized water		3	RT
16	BOND Wash Solution	5	1	RT
17	Deionized water	~	1	RT

3.2.19.6 Immunohistochemistry staining (IHC) of sectioned FFPE tissues

The immunohistochemical stainings of sectioned FFPE tissues were performed by Rosa Eurich (DKFZ, AG Halama/Jäger) according to the full automated protocol (Bond Polymer Refine Detection Kit (Leica); Microm STP420D, Thermo Scientific):

Step	Solution / Program	Time [min]	Repeats	Temperature
1	BOND Dewax Solution	0.5		72 °C
2	BOND Dewax Solution	0.5		72 °C
3	BOND Dewax Solution	0.5		RT
4	99 % Ethanol		3	RT
5	BOND Wash Solution		2	RT
6	BOND Wash Solution	5		
7	BOND ER Solution 1		2	RT
8	BOND ER Solution 1	20		100 ° C
9	BOND ER Solution 1	12		RT
10	BOND Wash Solution		3	37 °C
11	BOND Wash Solution	3	1	RT
12	Peroxide Block	20	1	RT
13	BOND Wash Solution		3	RT
14	Serum block (PBS with 10 % goat serum)	15	1	RT
15	BOND Wash Solution		3	RT
16	Primary antibody (anti-CD3 (ab16669 Abcam) in TBS / 10%FCS)	30		RT
17	BOND Wash Solution		3	RT
18	Secondary antibody (poly-HRP-anti-rabbit IgG)	8	1	RT
19	BOND Wash Solution	2	2	RT
20	Deionized water		1	RT
21	Mixed DAB Refine		1	RT
22	Mixed DAB Refine	10	1	RT
23	Deionized water		3	RT
24	Hematoxylin	10	1	RT
25	Deionized water		3	RT

26	BOND Wash Solution	5	1	RT
27	Deionized water	~	1	RT

4 Results

4.1 Generation of NY-BR-1 expressing human and murine cell lines

As this thesis focuses primarily on the investigation of the efficacy and pre-clinical safety of both human and murine anti-NY-BR-1 CARs, NY-BR-1 expressing cell lines were required. Due to the facts that no NY-BR-1 expressing breast cancer cell line was available and that previous experiments demonstrated that NY-BR-1 transduced breast cancer cell lines stop growing and lose NY-BR-1 surface expression (unpublished data) [93,96,224] , first challenge was the generation of NY-BR-1 expressing target cell lines. To address this issue, different cell lines such as the human Bosc23 and HEK 293T cell lines as well as the murine medullary breast adenocarcinoma cell line EO771, originally isolated from a spontaneous tumor in C57BL/6 mouse [222], were engineered to express the NY-BR-1 full length protein and evaluated for possible cell cycle - dependent NY-BR-1 expression profiles.

4.1.1 Lentiviral transduction of Bosc23 and HEK 293T cells

The human Bosc23 and HEK 293T cell lines have been examined for the ability to express the breast cancer associated protein NY-BR-1 on the cell surface. Both cell lines were lentivirally transduced with the NY-BR-1 - encoding expression vector #44 (hPGK_NY-BR-1_IRES_Puromycin_WPRE) at an MOI of 5, as described in chapter 3.2.9.2 (see also Supplementary Figure 6.1). Surface expression levels of NY-BR-1, determined by flow cytometric analysis with the monoclonal anti-NY-BR-1 clone2 and secondary APC or PE - conjugated anti-mouse IgG antibodies, differed widely between transduced Bosc23 and HEK 293T cells 72 h post transduction (see Figure 4.1.1). Over 40 % of transduced Bosc23 cells tested positive for NY-BR-1, whereas only 20 % of HEK 293T cells exhibited surface NY-BR-1 expression. These different expression rates were confirmed by further analyses on the following days. Although transduced cells were cultivated under puromycin pressure in order to select positive clones, the surface NY-BR-1 expression rates of selected cells remained low. In fact, the proportion of NY-BR-1$^+$ HEK 293T cells even decreased to less than 10 % after four weeks (see Figure 4.1.1). In contrast, over 40 % of transduced Bosc23 were still positive for NY-BR-1. In addition, it should be noted that a strong variation in the expression rates of NY-BR-1 was observed over several days in both transduced Bosc23 and HEK293T cells (see Figure 4.1.1; see Figure 4.1.2 B). Therefore, the role of cell density and different cell cycle phases for NY-BR-1 expression was further investigated (see chapter 4.1.1.1).

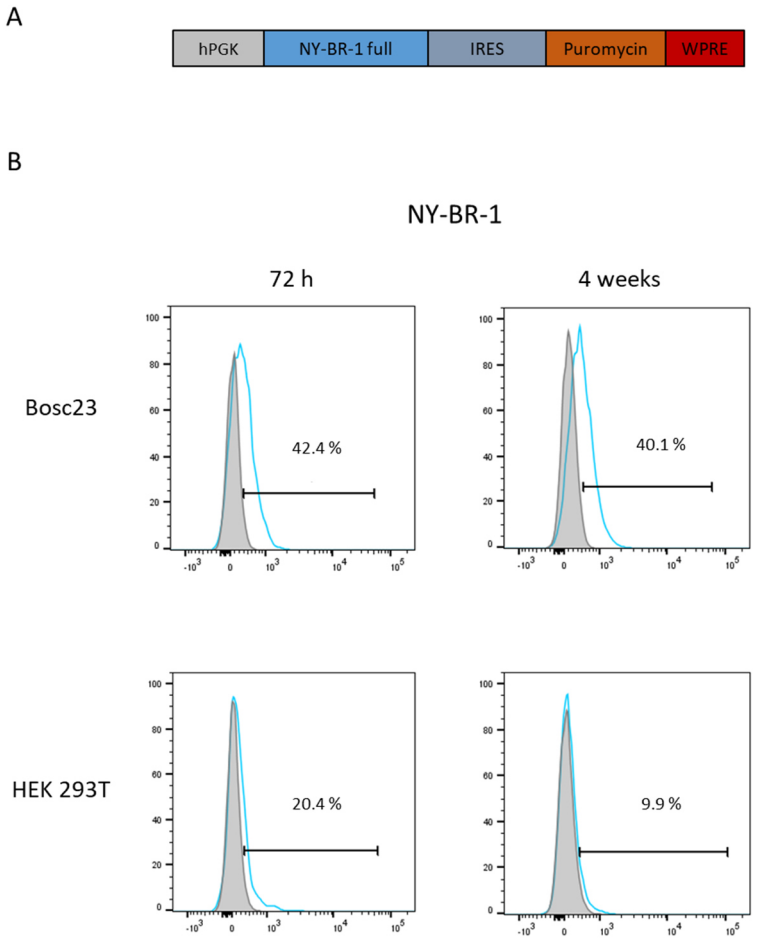

Figure 4.1.1: Surface expression levels of NY-BR-1 in lentivirally transduced Bosc23 and HEK 293T cells
Both Bosc23 and HEK 293T cells were engineered to express the full length NY-BR-1 protein. [A] Schematic representation of the expression vector #44 (hPGK_NY-BR-1_IRES_Puromycin_WPRE) encoding the NY-BR-1 full length protein and puromycin N-acetyltranferase under the control of the human phosphoglycerate kinase 1 promoter (hPGK). [B] 72 h post lentiviral transduction of Bosc23 and HEK 293T cells with vector #44, NY-BR-1 expression was examined by using flow cytometric analysis. Following four week cultivation under puromycin pressure, cells were analyzed again for the surface expression of NY-BR-1. Stainings were performed with the primary monoclonal antibody (mAb) clone2, directed against NY-BR-1, in combination with the secondary APC or PE - conjugated anti-mouse IgG antibody. Transduced Bosc23 and HEK 293T cells stained only with the anti-mouse IgG antibody (grey) were used as controls.

4.1.1.1 NY-BR-1 expression analysis depending on cell cycle and cell density

Since it was shown that NY-BR-1 expression does not reach high expression rates despite selection pressure and also varies greatly from day to day, the next approach was used to examine more closely whether different cell cycle phases as well as cell density affect NY-BR-1 expression.

Different cell cycle blockers (e.g. Thymidine, Nocodazole) were applied to synchronize transduced Bosc23 cells. Hence, Bosc23 cells (2.5 x 10^5 cells / well) were cultivated in 6 well plates and treated with Thymidine double block for G1 arrest or Nocodazole for G2 / M blockage (see chapter 3.2.17). The different cell cycle profiles were examined using propidium iodide (PI) and flow cytometric analysis as follows: After treatment with a cell cycle blocker, the contents of each well were divided into two

samples which were independently stained, one for NY-BR-1 and the other with propidium iodide. The resulting relationship between cell cycle and NY-BR-1 expression rate was then mapped (see Figure 4.1.2 A).

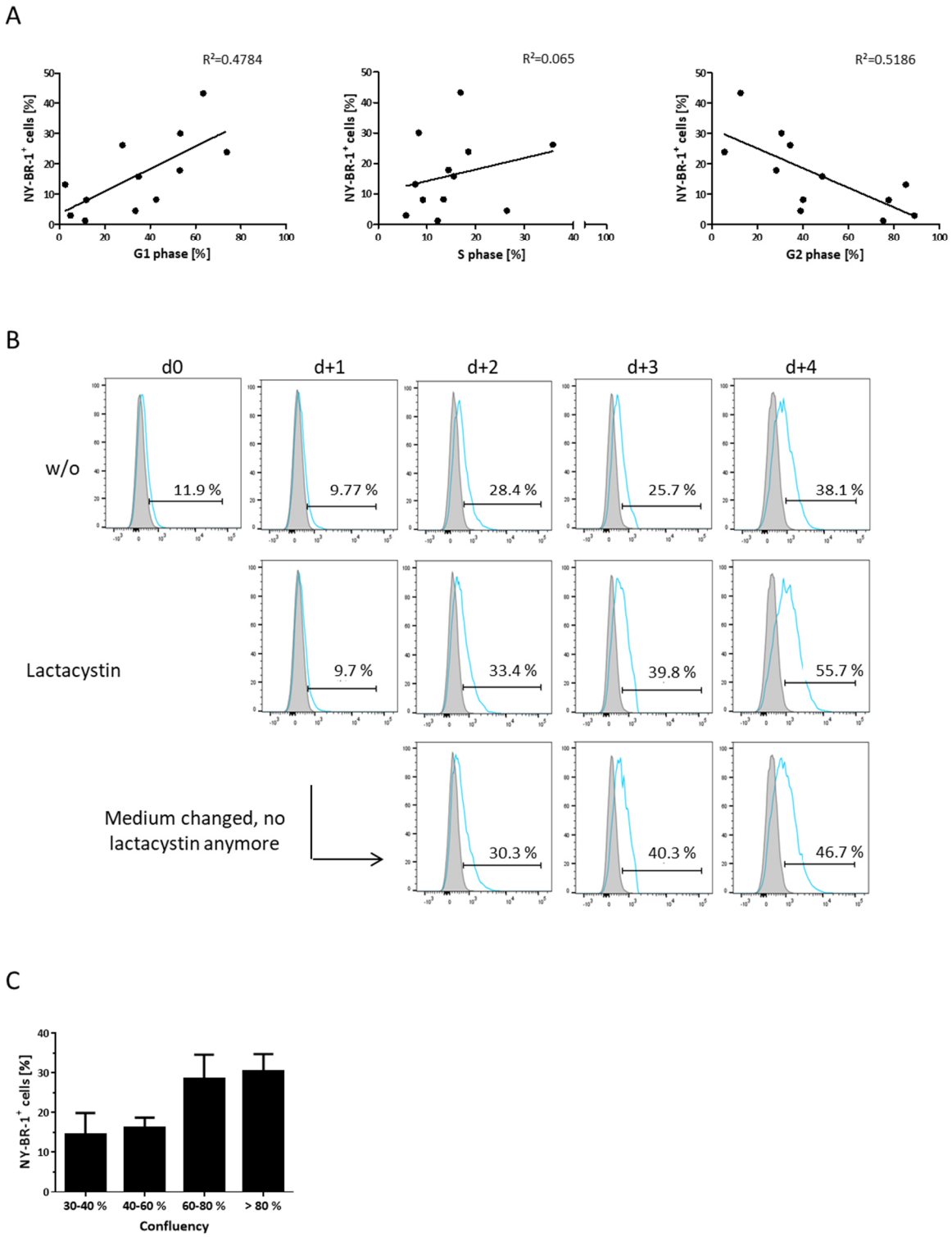

Figure 4.1.2: NY-BR-1 expression levels in transduced Bosc23 cells depending on cell cycle profile, proteasome activity and cell density

[A] NY-BR-1 transduced Bosc23 cells were synchronized with different cell cycle blockers (e.g. Thymidine, Nocodazole) over a few days. Afterwards, cells were analyzed for NY-BR-1 expression by the mAb clone2, directed against NY-BR-1, and secondary APC or PE labeled anti-mouse IgG antibody. Cell cycle profiles were determined by PI staining. Cell debris were

gated out using the FSC / PI channels (n = 12). Lines indicate the linear regression curves. The corresponding R^2 values are given. [B] NY-BR-1 expression profile of transduced, Lactacystin treated Bosc23 cells was compared with non-treated and Lactacystin treated cells (with exchanged medium upon d+1) over a period of five days. Expression levels of NY-BR-1 were determined, as described in [A]. Transduced cells only stained with the secondary antibody served as controls (grey). [C] Different amounts of transduced Bosc23 cells ($5x10^4$, $1x10^5$, $2x10^5$, $4x10^5$ cells / well) were seeded in 6 well plates to achieve varied cell densities between 30 and 80 % after several days. Expression levels of NY-BR-1 were determined as described in [A]. No statistically significant differences according to one-way ANOVA.

Indeed, different cell cycle blockages exhibited different effects on surface expression levels of NY-BR-1. With rising numbers of G1 arresting cells, the proportion of NY-BR-1 - expressing cells increased (see Figure 4.1.2 A). The opposite effect was observed for G2 arrest, which provoked decreasing NY-BR-1 expression levels. However, no clear statement can be made about the effects of S Phase on NY-BR-1 expression.

In addition to the cell cycle, degradation of the NY-BR-1 protein via proteasome may also play an important role in the modulation of NY-BR-1 surface expression, and should therefore be investigated in more detail with the use of Lactacystin as a proteasome inhibitor. To address this issue, NY-BR-1 expression was examined daily under Lactacystin treatment by using flow cytometric analysis. As the blockage of the proteasome is irreversible, NY-BR-1 surface expression was additionally investigated in Lactacystin treated cells with exchanged medium (see Figure 4.1.2 B). An initial important observation was the fluctuating surface expression of NY-BR-1 in untreated, transduced Bosc23 cells. Here, expression levels increased from 9 % on day d+1 to over 38 % on day d+4. Similar effects were observed in transduced Bosc23 cells under Lactacystin treatment. While the NY-BR-1 expression rate in Lactacystin-treated cells was around 9 % on day d+1, it had risen to over 33 % by day d+2 and 55 % by day d+4. In fact, Lactacystin treated cells always demonstrated higher NY-BR-1 expression levels than untreated or Lactacystin treated cells with exchanged medium. All these data indicate important roles of both the cell cycle profile and proteasome activity for surface expression of NY-BR-1.

Since longer cultivation periods of transduced Bosc23 cells led to increasing NY-BR-1 expression levels, as shown in Figure 4.1.2 B, the impact of cell density on NY-BR-1 expression was examined more closely. Hence, different cell densities of transduced Bosc23 cells were seeded in 6 well plates in order to achieve confluence rates between 30 and 80 % after several days. The average NY-BR-1 expression rates, calculated from several independently performed experiments with the use of flow cytometric analysis, are shown as bar charts in Figure 4.1.2 C and illustrate differences in the frequencies of NY-BR-1 expressing cells depending on cell density. While an average NY-BR-1 expression rate of 14 % was achieved at low cell densities, high cell densities led to elevated expression levels of approximately 30 %. Strikingly, among all tested cell densities, the largest increase of NY-BR-1 expression levels was observed from a cell density of 60 %, which, however, did not rise significantly with further increases in cell density.

4.1.2 Lentiviral transduction of the murine breast cancer cell line EO771

Due to immunological compatibility, the murine NY-BR-1 expressing tumor cell line needed to fulfil the requirement of being a murine breast cancer cell line with a C57BL/6 background. The medullary breast adenocarcinoma cell line EO771, derived from a spontaneous tumor of C57BL/6 mice, has already proved to be adapted for immune-based therapies [225-227]. Hence, the EO771 cell line was lentivirally transduced with the NY-BR-1 - encoding expression vector #44 (hPGK_NY-BR-1_IRES_Puromycin_WPRE) at an MOI of 5 (see also Supplementary Figure 6.1). Puromycin selection gave rise to one single cell clone which tested positive for both intracellular and surface expression of NY-BR-1 four weeks post transduction with the use of all three primary anti-NY-BR-1 antibodies (murine clone2, humanized 10D11 and humanized clone3) followed by secondary APC - conjugated anti-mouse or anti-human IgG antibodies (see Figure 4.1.2). Especially striking were the significantly elevated intracellular NY-BR-1 expression levels of up 90 %, compared to surface expression levels of only 27 % to 30 %. It was equally surprising that the mAb clone2 detected significantly higher intracellular NY-BR-1 expression levels than the mAb clone3. However, this effect was not observed on the cell surface. Eight weeks post transduction, transduced EO771 cells no longer showed any detectable surface expression of NY-BR-1. Intracellular NY-BR-1 expression levels were also significantly reduced compared to four weeks before and differed again depending on the detection antibodies used (clone2: 54.5 %; 10D11: 38.3 %; clone3: 6.83 %).

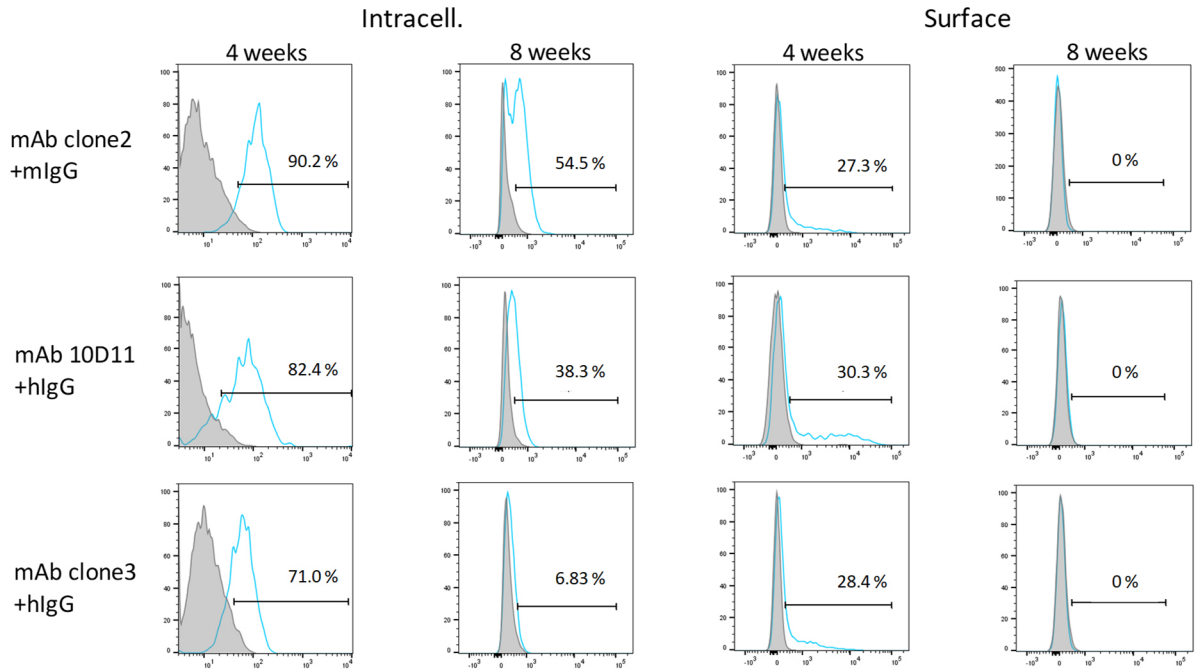

Figure 4.1.3: Intracellular and surface expression levels of NY-BR-1 in lentivirally transduced EO771 cells
The murine medullary breast adenocarcinoma cell line EO771 was lentivirally transduced with expression vector #44 (hPGK_NY-BR-1_IRES_Puromycin_WPRE) encoding the NY-BR-1 full length protein and puromycin N-acetyltranferase under the control of the human phosphoglycerate kinase 1 promoter (hPGK). NY-BR-1 was detected both intracellularly and on the

cell surface using three different primary monoclonal anti-NY-BR-1 antibodies (murine clone2, humanized 10D11, humanized clone3) and the corresponding secondary antibodies (APC-conjugated anti-mouse IgG or anti-human IgG). Untransduced EO771 cells were used as controls (grey). Percentages indicate the proportion of NY-BR-1 expressing cells of the total number of lentivirally transduced EO771 cells four and eight weeks post transduction and puromycin selection.

4.1.2.1 NY-BR-1 expression analysis in transduced EO771 cells depending on proteasome activity and cell cycle profiles

Having observed that NY-BR-1 transduced EO771 cells exhibit decreasing NY-BR-1 expression levels, especially on cell surface, a possible degradation of this protein as well as the role of different cell cycle phases were explored in more detail.

NY-BR-1 transduced EO771 cells were synchronized by different cell cycle blockers (e.g. Thymidine, L-mimosine, Aphidicoline, Nocodazole). The addition of Thymidine, L-mimosine and Aphidicoline to (NY-BR-1$^+$) EO771 cells cultivated in 6 well plates (1.5 x 10^5 / well) induces a G1 arrest, whereas Nocodazole leads to a G2 / M blockage, as described in chapter 3.2.17. The resulting cell cycle and NY-BR-1 expression profiles of the differently treated cells were examined by flow cytometric analysis using propidium iodide (PI) as well as the mAb clone2 in combination with secondary APC or PE labeled anti-mouse IgG antibodies (see Figure 4.1.4).

Indeed, G1 arrest had a positive effect on NY-BR-1 expression rates (see Figure 4.1.4 A). Similar observations were made with cells arresting between late G1 and early S phase. However, cell populations indicating low frequencies of S phase-arrested cells showed both high and low amounts of NY-BR-1-expressing cells in independently performed experiments. In contrast, an increasing proportion of G2 arrested cells resulted in greatly reduced amounts of NY-BR-1 expressing cells.

To explore the possible role of NY-BR-1 degradation by proteasomes, (NY-BR-1$^+$) EO771 cells were treated with the proteasome inhibitor, Lactacystin, and were examined regarding their surface expression levels of NY-BR-1 by flow cytometric analysis over a period of five days. Untreated cells were used as controls and exhibited almost no detectable surface expression levels of NY-BR-1 in this representative example in Figure 4.1.4 B. In contrast, Lactacystin treated cells displayed increasing NY-BR-1 surface expression levels of over 18 %, particularly in the first two days after treatment. Strikingly, a medium change 24 h after Lactacystin treatment, had a positive impact on NY-BR-1 expression. However, these surface expression levels did not remain constant even in treated cells. On day 3, almost no NY-BR-1 proteins were detectable on Lactacystin and untreated EO771 cells' surfaces via flow cytometry. Surprisingly, on day 4, the levels increased again up to 19 or 15 % in Lactacystin treated cells with or without exchanged medium. However, it was generally observed that the fluorescence intensities were very weak (see Figure 4.1.3), suggesting a low protein density.

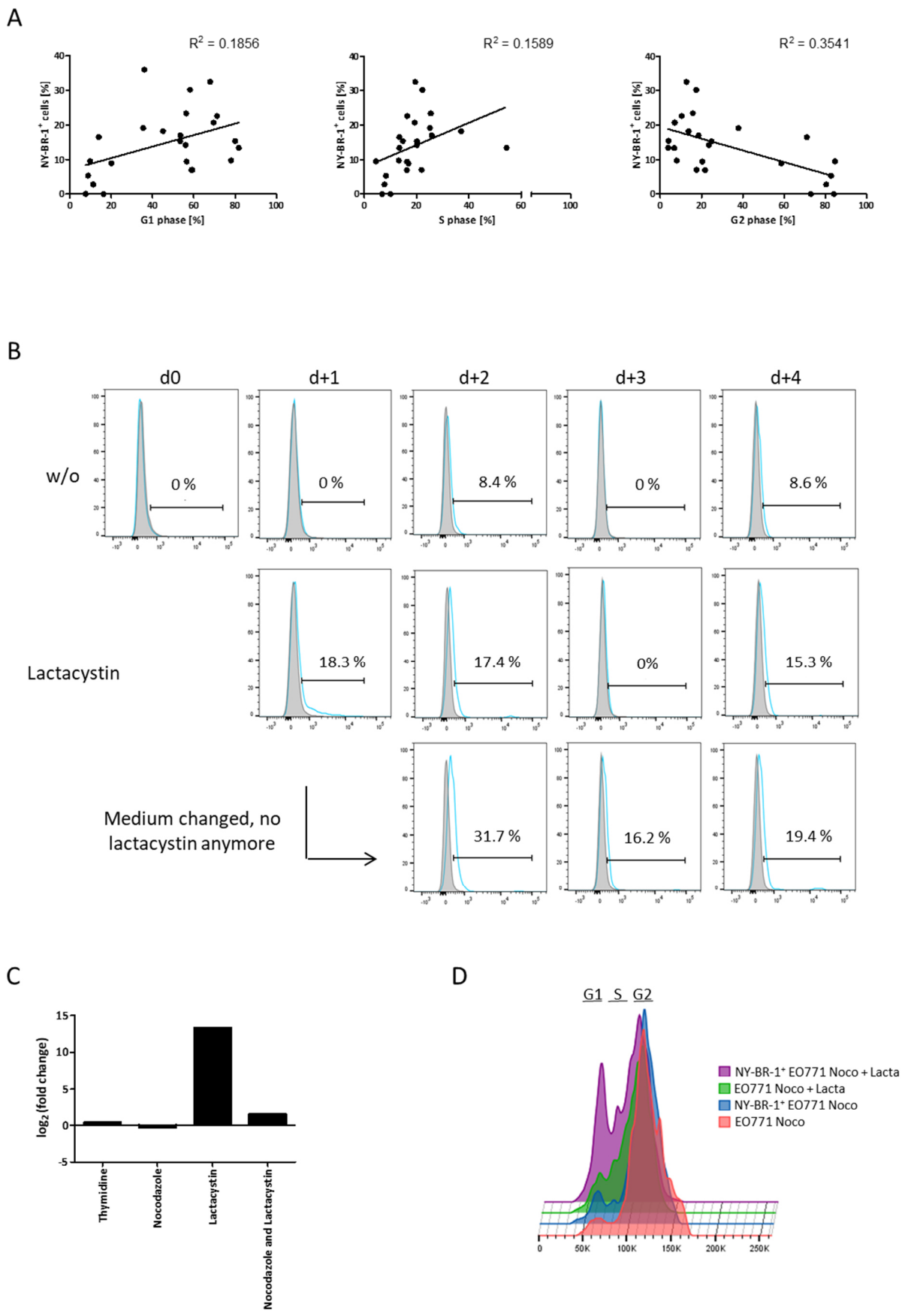

Figure 4.1.4: Analysis of NY-BR-1 expression levels in transduced EO771 cells treated with a proteasome inhibitor and different cell cycle blockers

[A] NY-BR-1 transduced EO771 cells were treated with different cell cycle blockers (e.g. Thymidine, Nocodazole, L-mimosine, Aphidicolin) over a few days. Cell cycle profiles and NY-BR-1 expression levels of synchronized cells were determined by flow

cytometric analysis. Therefore, cells were stained with PI or the mAb clone2 in combination with PE / APC labeled anti-mouse IgG antibodies. Cell debris were gated out using the FSC / PI channels (n = 24). Lines indicate the linear regression curves. The corresponding R^2 values are given. [B] NY-BR-1 expression profile of transduced, Lactacystin treated (NY-BR-1$^+$) EO771 cells was compared with non-treated and Lactacystin treated cells (with exchanged medium upon d+1) over a period of five days. NY-BR-1 was detected by using flow cytometric analyses, as described in [A]. Untransduced cells served as controls (grey). [C] *NY-BR-1* expression analysis at RNA level. Following RNA isolation of synchronized NY-BR-1 transduced EO771 cells, cDNA was synthesized via reverse transcription and analyzed for *NY-BR-1* expression by using real-time quantitative polymerase chain reaction (qPCR) with the primers #22 and #60, which generate an amplicon of 117 bps within the *NY-BR-1* RNA/cDNA transcript. The $\log_2$ based fold change of *NY-BR-1* expression was calculated relative to untreated transduced EO771 cells using the $2^{-\Delta\Delta Ct}$ method. ß-actin was used as the reference gene. [D] Overlayed cell cycle profiles of Nocodazole and Lactacystin treated (NY-BR-1$^+$) EO771 cells generated by PI staining and flow cytometric analysis, as described in [A]. The identified cell cycle phases are given.

In addition to the flow cytometric analysis of synchronized cells, *NY-BR-1* expression levels were also investigated at RNA level by using relative quantification of real-time qPCR. The $\log_2$ based fold changes in *NY-BR-1* expression, shown in Figure 4.1.4 C, were calculated relative to untreated transduced EO771 cells and indicated increasing expression levels under Thymidine and decreasing levels under Nocodazole treatment.

The combined effect of Lactacystin, as a proteasome inhibitor and cell cycle blocker (G0/G1 and G2/M), and Nocodazole was further evaluated with flow cytometric and RNA analyses. Here, cells were treated with Lactacystin for 24 h followed by the addition of Nocodazole, as described in chapter 3.2.17. Particularly noteworthy are the high *NY-BR-1* expression levels in Lactacystin treated transduced EO771 cells, which were increased by a factor of 13 compared to Thymidine treatment. A combined treatment of Nocodazole and Lactacystin resulted in higher *NY-BR-1* expression levels compared to a single treatment with Nocodazole (see Figure 4.1.4 C). In fact, the sole treatment with Nocodazole resulted in a G2 arrest in both wild-type EO771 and NY-BR-1 transduced EO771 cells (see Figure 4.1.4 D). However, the combined treatment led to different cell cycle profiles. Both cell lines (wild-type and transduced EO771) showed increased proportions of G1 arrested cells under double treatment compared to Nocodazole alone, but this effect was much more pronounced in transduced than in wild-type EO771 cells, indicating again a correlation between G1 phase and *NY-BR-1* expression.

Overall, these data show that the G1 phase plays a key role for the expression of NY-BR-1 in transduced EO771 cells. Moreover, Lactacystin treatment improves NY-BR-1 expression at both the protein and RNA level.

4.2 Generation of anti-NY-BR-1 chimeric antigen receptors

4.2.1 Cloning of murine lentiviral vectors

To generate murine anti-NY-BR-1 chimeric antigen receptor (CAR) expressing T cells, different lentiviral vectors encoding the three different anti-NY-BR-1 CARs (clone2, 10D11, clone3) consisting of anti-NY-BR-1 single chain variable fragments (scFvs), which were derived from the mAbs clone2, 10D11 and clone3, as well as the murine Fc, transmembrane, co-stimulatory domains and CD3z were required. Since at the beginning of this work only human anti-NY-BR-1 CAR - encoding vectors were available, the human Fc (hIgG1), transmembrane and co-stimulatory domains had to be exchanged with murine counterparts. For this purpose, DNA encoding the mFcΔ_mCD28Δ_m4-1BB_CD3z fragment, which contained mutations in the Fc (mIgG1) (TVPEV → NILGG) and CD28 (TRKPYQPYAPARDF → TRKAYQAYAAARDF) domains, was amplified from vector #187 (pENTR_attL1_RFB4scFv_mFcΔ_mCD28Δ_m4-1BB_CD3z_attL2) by PCR with the primers #5 and #85. In this process, the restriction sites for the restriction endonucleases *NotI* and *XbaI* were attached to the ends of this fragment (see Figure 4.2.1). Subsequently, the amplified fragment was cut with the aforementioned enzymes to create overhanging cohesive ends. The human Fc, co-stimulatory domains and CD3z - encoding DNA segments were removed from plasmid #35 (pENTR_attL1_clone2scFv_hFc_hCD28_h4-1BB_CD3z_attL2) by using the restriction enzymes *NotI* and *XbaI*. Next, the linearized vector DNA was ligated with the digested PCR fragment by the T4 DNA ligase resulting in vector #200 (pENTR_attL1_clone2scFv_mFcΔ_mCD28Δ_m4-1BB_CD3z_attL2), which was checked for its accuracy by analytical digestion with restriction enzymes (*EcoRI* and *HindIII*). The subsequent electrophoretic separation resulted in two bands of the expected sizes of 3300 base pair (bp) and 1100 bp. Afterwards, clone2scFv - encoding DNA segments from vector #200 were exchanged with those encoding the 10D11scFv or clone3scFv. For this purpose, 10D11scFv and clone3scFv - encoding DNA sections were excised from pre-existing vectors #142 (pENTR_attL1_10D11cFv_hFc_hCD28_h4-1BB_CD3z_attL2) and #143 (pENTR_attL1_clone3cFv_hFc_hCD28_h4-1BB_CD3z_attL2) by using the restriction enzymes *NcoI* / *NotI* and were ligated to the *NcoI / NotI* sliced vector #200. The resulting ligation products #205 pENTR_attL1_10D11scFv_mFcΔ_mCD28Δ_m4-1BB_CD3z_attL2) and #206 pENTR_attL1_clone3scFv_mFcΔ_mCD28Δ_m4-1BB_CD3z_attL2) were verified by analytical digestion with the restriction enzyme *XbaI,* which in both cases led to the expected band sizes of 2100 bp and 2200 bp after electrophoretic separation.

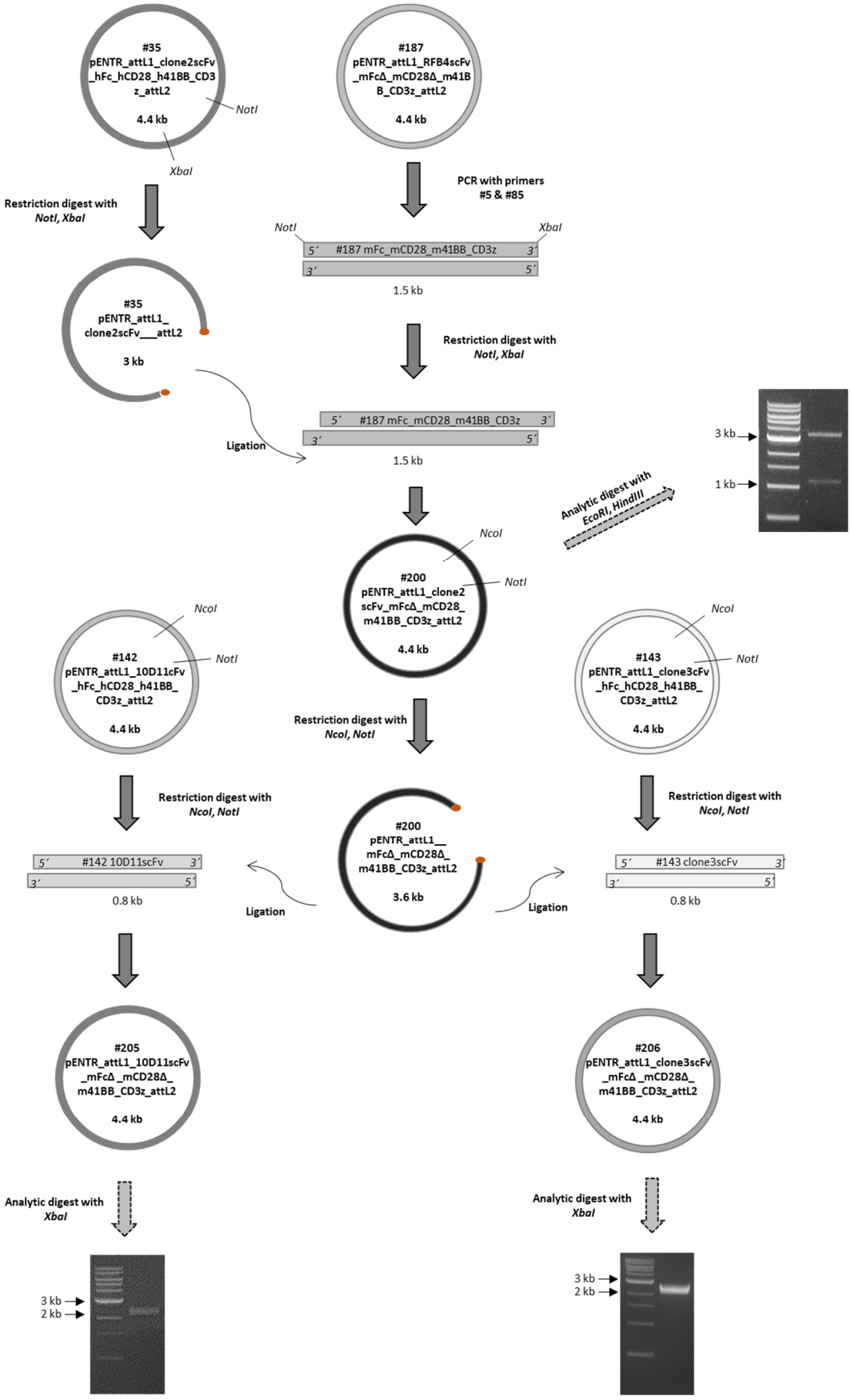

Figure 4.2.1: Cloning strategy of vectors #200, #205 and #206
The hFc_hCD28_h4-1BB_CD3z - encoding DNA fragment in vector #35 was exchanged with the mFcΔ_mCD28Δ_m4-1BB_CD3z encoding DNA segment from vector #187 with aid of PCR and restriction digestion, resulting in vector #200. Afterwards, clone2scFv - encoding DNA segments were exchanged with those encoding the 10D11scFv or clone3scFv. The final vectors #200, #205 and #206 were verified by analytical digestion.

The final lentiviral transfer vectors were generated by the gateway cloning technology, which allows the transfer of DNA fragments by recombination reactions. CAR - encoding segments, flanked by attL sites, were transferred from vectors #200, #205 and #206 into vector #126 (pRRL_CMV_attR1_CmR_*ccdB*_attR2_hPGK_DsRed2_WPRE) by the enzyme LR clonase, as described in chapter 3.1.9.4 (see Figure 4.2.2). The resulting lentiviral transfer vectors #216 (pRRL_CMV_attB1_clone2scFv_mFcΔ_mCD28Δ_m4-1BB_CD3z_attB2_hPGK_DsRed2_WPRE), #217 (pRRL_CMV_attB1_10D11scFv_mFcΔ_mCD28Δ_m4-1BB_CD3z_attB2_hPGK_DsRed2_WPRE) and #218 (pRRL_CMV_attB1_clone3scFv_mFcΔ_mCD28Δ_m4-1BB_CD3z_attB2_hPGK_DsRed2_WPRE) showed the expected band patterns after analytical digestion with the restriction enzyme *EcoRI* (#216/#217/#218: 1100 bp, 1800 bp, 7200 bp). The final lentiviral vectors encode the different murine anti-NY-BR-1 CARs (clone2, 10D11, clone3) under the control of the *cytomegalovirus* (CMV) promoter and allow the quantification of CAR expression by the DsRed2 protein.

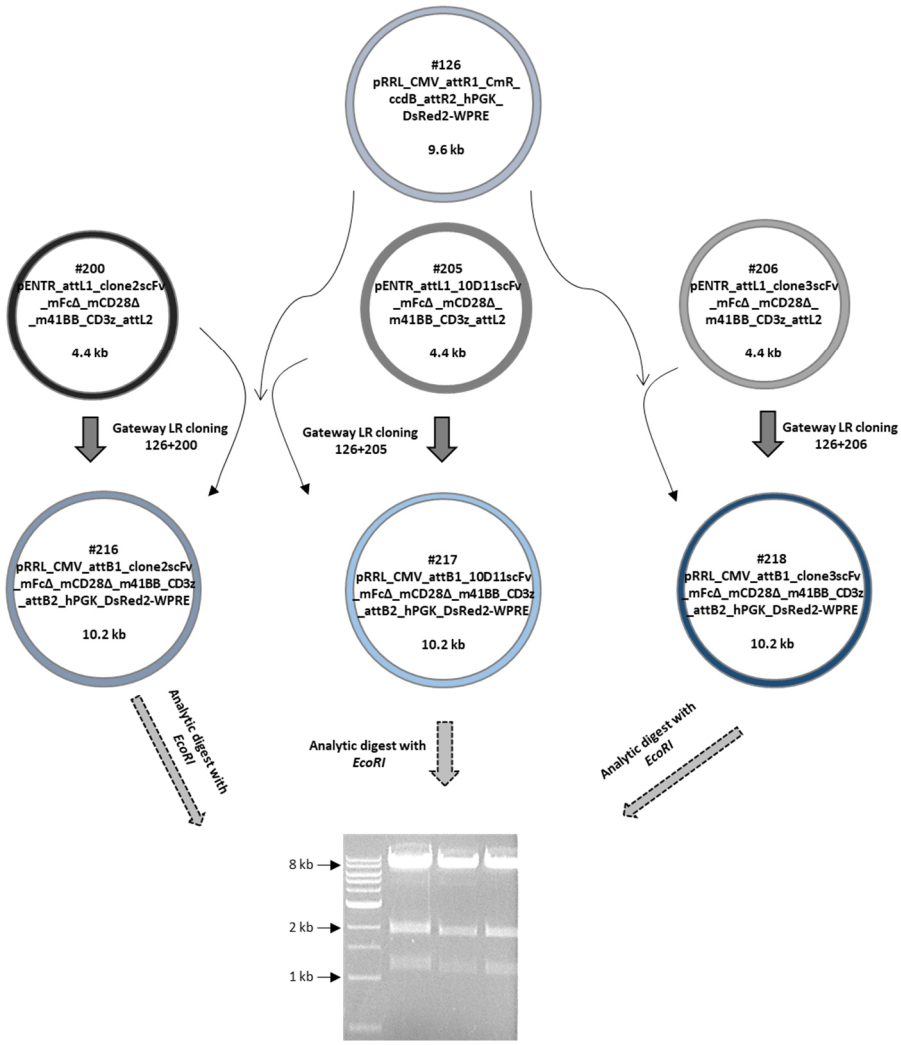

Figure 4.2.2: Cloning strategy of murine lentiviral transfer vectors #216, #217 and #218
The murine lentiviral transfer vectors #216, #217 and #218 were generated by the gateway cloning technology and were finally verified by analytical digest with the restriction enzyme *EcoRI.*

4.2.2 Cloning of murine pS/MARter vectors

Next to lentiviral transduction, a novel method for the generation of murine CAR$^+$ T cells was established in the further course of this work (see chapter 4.4.2). This technology is based on the electroporation of murine T cells with S/MAR derived vectors – so called pS/MARter vectors – which were kindly provided by Dr. Richard Harbottle and Dr. Matthias Bozza (DKFZ, DNA Vector Research Group).

Starting from the anti-CEA CAR - encoding pS/MARter vector #272 (pS/MARter_hPGK_CEAscFv_hFc_hCD28_CD3z_hOX40_S/MAR), provided by Dr. Richard Harbottle's laboratory, the murine anti-NY-BR-1 CAR - encoding pS/MARter vectors #277 (pS/MARter_mPGK_clone2scFv_mFcΔ_mCD28Δ_m4-1BB_CD3z_S/MAR), #295 (pS/MARter_mPGK_10D11scFv_mFcΔ_mCD28Δ_m4-1BB_CD3z_S/MAR) and #296 (pS/MARter_mPGK_clone3scFv_mFcΔ_mCD28Δ_m4-1BB_CD3z_S/MAR) were generated (see Figure 4.2.3). The required mPGK - encoding sequence was amplified from vector #240 (pRRL_mPGK_attB1_NY-BR-1(full)_attB2_WPRE) by PCR (primers 150 & 151). DNA segments encoding the murine clone2 CAR were amplified from plasmid #241 (pRRL_mPGK-attB1_clone2scFv_mFcΔ_mCD28Δ_m4-1BB_CD3z_attB2-WPRE) by PCR with primers #152 and #153. For both PCR reactions, special primers were created that meet the requirements for subsequent In-Fusion cloning, as described in chapter 3.1.9.3. By using the In-Fusion technology, both PCR amplicons were cloned into the pS/MARter backbone of the sliced (*BstXI* and *XhoI*) vector #272 in just one step. Thereafter, the clone2scFv - encoding DNA sequence of the resulting pS/MARter vector #277 was exchanged with 10D11scFv and clone3scFv - encoding DNA sequences from vectors #268 (pRRL_CMV_attB1_10D11scFv_mFc_mCD28_m4-1BB_CD3z_attB2_IRES_eGFP_WPRE) and #269 (pRRL_CMV_attB1_clone3scFv_mFc_mCD28_m4-1BB_CD3z_attB2_IRES_eGFP_WPRE) by restriction digest with the enzymes *PmeI* and *NotI* and subsequent ligation by T4 ligase. Finally, they were verified by analytical digestion with the restriction enzymes *EcoRI*, *SpeI, XcmI* or *XmaI,* which led to the expected band sizes of 200 bp, 1300 bp and 4900 bp for vector #277, of 600 bp and 6000 bp for vector #295 and of 1600 bp and 4900 bp for vector #296. The resulting pS/MARter vectors #277, #295 and #296 encode three different murine anti-NY-BR-1 CARs (clone2, 10D11, clone3) under the control of the murine phosphoglycerate kinase (mPGK) promoter.

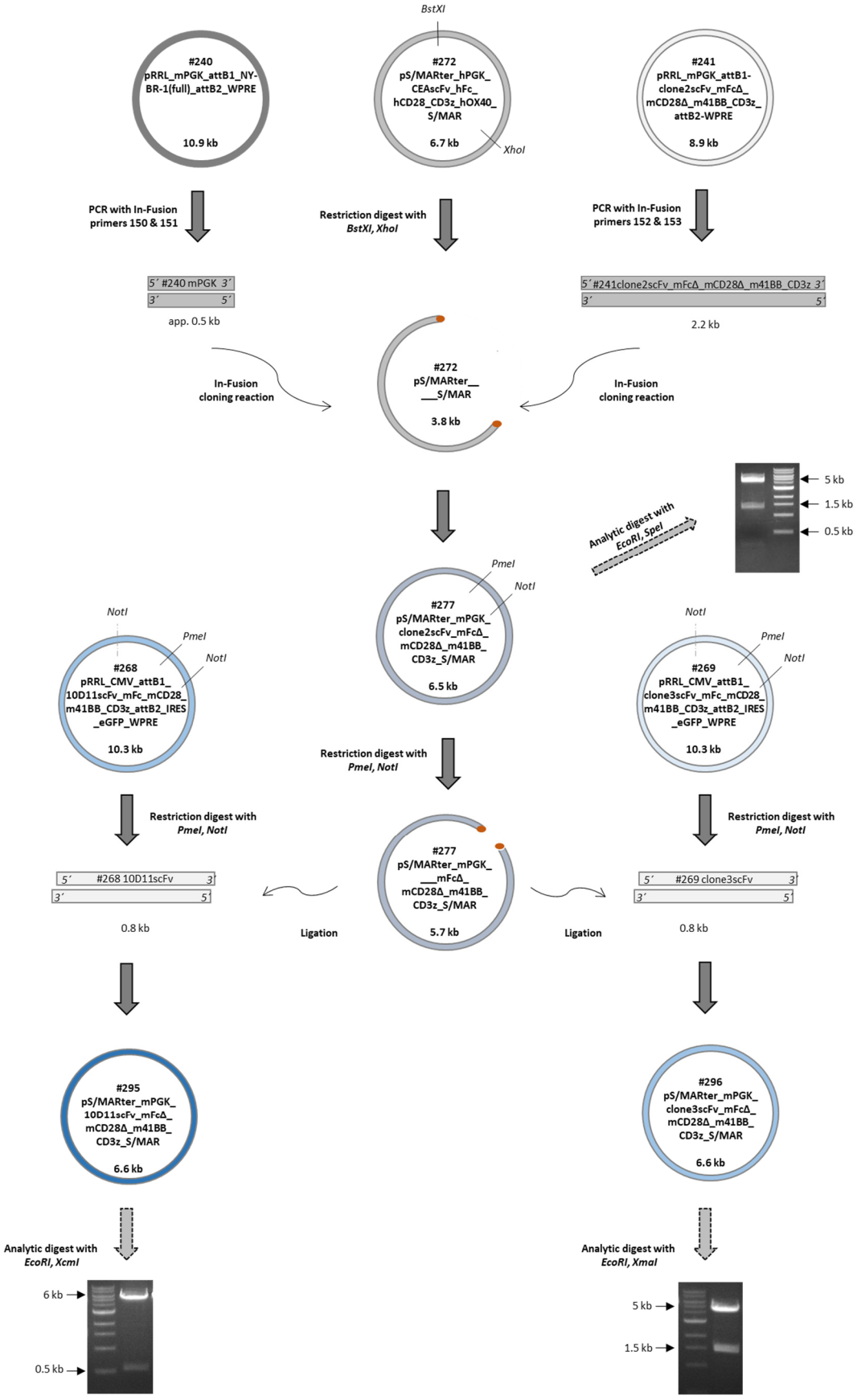

Figure 4.2.3: Cloning strategy of murine pS/MARter vectors #277, #295 and #296
The murine clone2CAR - encoding pS/MARter vector #277 was generated from vectors #240, #241 and #272 by using the In-Fusion technology. Thereafter, clone2scFv - encoding DNA segments in vector #277 were exchanged with those encoding 10D11 and clone3scFvs from vectors #268 and #269, resulting in the pS/MARter vectors #295 and #296, which were finally verified by analytical digest with the restriction enzymes *EcoRI*, *SpeI*, *XcmI* or *XmaI*.

4.2.3 Cloning of human pS/MARter vectors

At the beginning of this thesis, pS/MARter vectors encoding human anti-NY-BR-1 CARs of the 3rd generation were already available. However, in addition to the hCD28 and h4-1BB co-stimulatory domains, vectors encoding anti-NY-BR-1 CARs with incorporated hCD28_CD3z_hOX40 domains were still missing. Therefore, the required vectors were cloned from the pS/MARter vectors #272 (pS/MARter_hPGK_CEAscFv_hFc_hCD28_CD3z_hOX40_S/MAR), #273 (pS/MARter_hPGK_clone2scFv_hFc_hCD28_h4-1BB_CD3z_S/MAR) and #302 (pS/MARter_hPGK_10D11scFv_hFc_hCD28_h4-1BB_CD3z_S/MAR) (see Figure 4.2.4).

First, the hPGK and CEAscFv - encoding DNA sequences in vector #272 were removed by restriction digest with *HindIII* and *NotI*. The required hPGK, clone2scFv and 10D11scFc - encoding DNA sequences were cut from vectors #273 and #302 by enzymatic digest with *HindIII* and *NotI* and were subsequently ligated with the cut vector #272 by T4 ligase. The resulting vector #432 (pS/MARter_hPGK_clone2scFv_hFc_hCD28_CD3z_hOX40_S/MAR) was used to generate vector #434 (pS/MARter_hPGK_clone3scFv_hFc_hCD28_CD3z_hOX40_S/MAR) by replacing the clone2scFv - encoding sequence with the clone3scFv - encoding sequence from vector #303 (pS/MARter_hPGK_clone3scFv_hFc_hCD28_h4-1BB_CD3z_S/MAR) by enzymatic digest (*NheI*, *NotI*) and subsequent ligation by T4 ligase. The final analytic digest of all three resulting vectors #432, #433 (pS/MARter_hPGK_10D11scFv_hFc_hCD28_CD3z_hOX40_S/MAR) and #434 with the restriction enzymes *AvrII*, *NheI* or *BstEII* demonstrated the expected banding patterns of 2000 bp and 4700 bp (#432, #433) or 1500 bp and 5200 bp (#434).

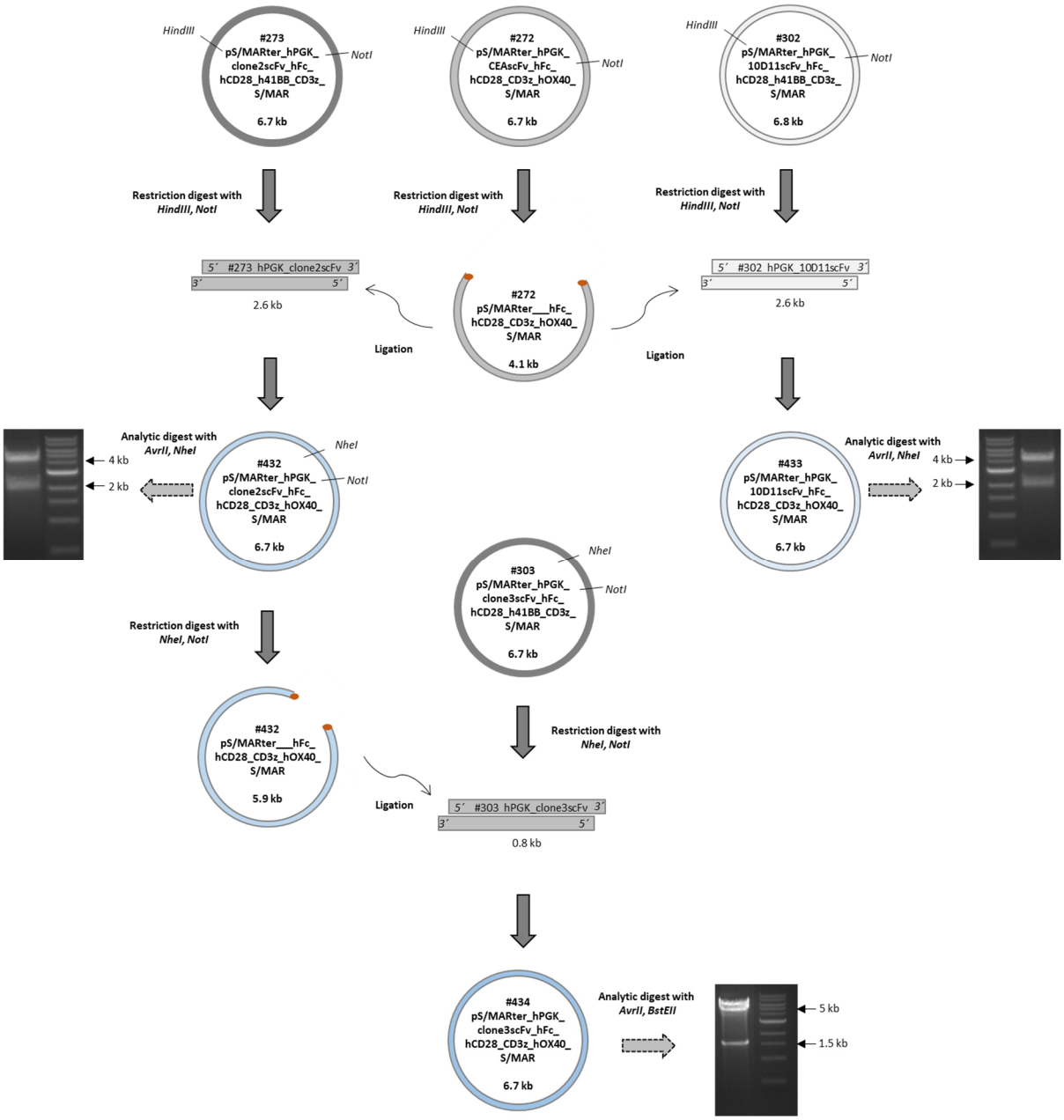

Figure 4.2.4: Cloning strategy of human pS/MARter vectors #432, #433 and #434
pS/MARter vectors encoding the three different human anti-NY-BR-1 CARs, incorporating both the hCD28 and hOX40 domains, were cloned from vectors #272, #273, #302 and #303 by replacing the scFv - encoding DNA fragments by restriction digests (*HindIII*, *NheI*, *NotI*) and subsequent T4 ligase - based ligation reactions. The final vectors #432, #433 and #434 were verified by analytic digestion with the endonucleases *AvrII*, *BstEII* or *NheI*.

The next step was the generation of pS/MARter vectors encoding human anti-NY-BR-1 CARs with mutated hFc (PELLGG → PPVAG; ISR → IAR) and hCD28 / Lck (PYAPA → AYAAA) domains. To address this issue, DNA sequences encoding the unmutated hFc_hCD28_h4-1BB domains were removed from vectors #273 (pS/MARter_hPGK_clone2scFv_hFc_hCD28_h4-1BB_CD3z_S/MAR) and #303 (pS/MARter_hPGK_clone3scFv_hFc_hCD28_h4-1BB_CD3z_S/MAR) by restriction digest with *NotI* and *XhoI* (see Figure 4.2.5). At the same time, the hFcΔ_hCD28Δ_h4-1BB_CD3z - encoding DNA sequence

was amplified from vector #68 (pENTR_attL1_TS7.3scFv_hFcΔ_hCD28Δ_h4-1BB_CD3z_attL2) by PCR (primers #531 and #532). Since the restriction site for the endonuclease *XhoI* was attached to one end of the PCR fragment during this process, the PCR amplicon was subsequently cut with the enzymes *NotI* and *XhoI* to generate cohesive ends. Afterwards, the cut PCR fragment was ligated to the sliced vectors #273 and #303 resulting in vectors #517 (pS/MARter_hPGK_clone2scFv_hFcΔ_hCD28Δ_h4-1BB_CD3z_S/MAR) and #519 (pS/MARter_hPGK_clone3scFv_hFcΔ_hCD28Δ_h4-1BB_CD3z_S/MAR). Vector #518, which should encode for the 10D11scFv_hFcΔ_hCD28Δ_h4-1BB_CD3z CAR fragment, was generated by exchanging the clone2scFv - encoding DNA sequence in vector #517 with the 10D11scFv - encoding DNA segment from vector #433 (pS/MARter_hPGK_10D11scFv_hFc_hCD28_CD3z_hOX40_S/MAR) by restriction digest (*NheI*, *NotI*) and subsequent T4 ligase – based ligation. All generated vectors were verified by analytical digest with different restriction enzymes such as *HindII, NcoI, SacI* and *SphI* leading to expected banding patterns of 2500 bp and 4200 bp (#517), 2800 bp and 4000 bp (#518) as well as 1800 bp, 2000 bp and 2900 bp (#519).

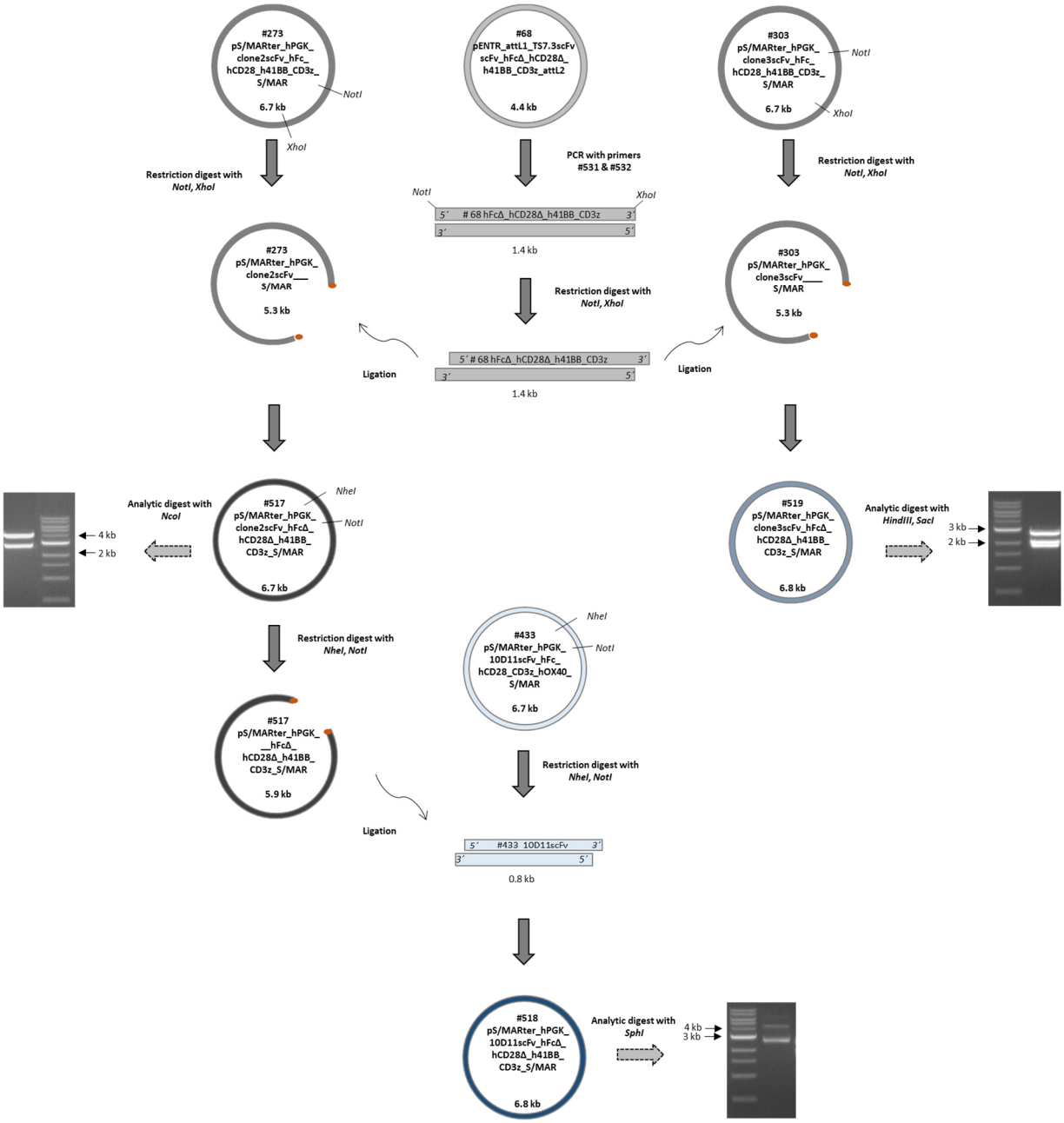

Figure 4.2.5: Cloning strategy of human pS/MARter vectors #517, #518 and #519
The pS/MARter vectors #517, #518 and #519, encoding three different anti-NY-BR-1 CARs with mutated hFc and hCD28 domains, were generated by replacing the hFc_hCD28_h4-1BB_CD3z fragments in vectors #273 and #303 with the hFcΔ_hCD28Δ_h4-1BB_CD3z fragment from vector #68 by PCR amplification and restriction digest (*NotI*, *XhoI*; *NheI*, *NotI*). Finally, the resulting vectors were verified by analytic digest with the endonucleases *HindII, NcoI, SacI* and *SphI*.

4.2.4 Cloning of human lentiviral vectors

Next to pS/MARter vectors, the corresponding lentiviral vectors encoding human anti-NY-BR-1 CARs with mutated hFc and hCD28 domains were generated in this section. Several intermediate cloning steps starting from vectors #200, #205 and #68 led to the pENTR vectors #511 (pENTR_attL1_clone2scFv_hFcΔ_hCD28Δ_h4-1BB_CD3z_attL2) #512

(pENTR_attL1_10D11cFv_hFcΔ_hCD28Δ_h4-1BB_CD3z_attL2) and #513 (pENTR_attL1_clone3cFv_hFcΔ_hCD28Δ_h4-1BB_CD3z_attL2) (cloning strategy not shown). Since gateway cloning did not work efficiently with these vectors (data not shown), the In-Fusion technology should be applied for the generation of the lentiviral transfer vectors #514 (pRRL_hPGK_clone2scFv_hFcΔ_hCD28Δ_h4-1BB_CD3z_WPRE), #515 (pRRL_hPGK_10D11scFv_hFcΔ_hCD28Δ_h4-1BB_CD3z_WPRE) and #516 (pRRL_hPGK_clone3scFv_hFcΔ_hCD28Δ_h4-1BB_CD3z_WPRE) (see Figure 4.2.6).

The attB1_clone2scFv_hFc_hCD28_h4-1BB_CD3z_attB2 - encoding fragment was removed from lentiviral transfer vector #85 by restriction digest with *BamHI* and *SalI*. Using PCR, the clone2scFv_hFcΔ_hCD28Δ_h4-1BB_CD3z - encoding DNA segment was amplified with specially designed In-Fusion primers (#534 and #535) from vector #511 and fused into the linearized vector #85 by using the In-Fusion technology, as described in chapter 3.1.9.3. Since the same In-Fusion reaction did not work for vectors #515 and #516, an alternative cloning strategy had to be used. Therefore, the 10D11scFv_hFcΔ_hCD28Δ_h4-1BB_CD3z and clone3scFv_hFcΔ_hCD28Δ_h4-1BB_CD3z - encoding fragments were amplified from vectors #512 and #513 by using PCR (primers #552 and #553). During this process, the restriction sites for the endonucleases *BamHI* and *SalI* were added to the ends of the PCR fragments. Following restriction digest of the PCR amplicons and vector #514 with the aforementioned enzymes, the sliced vector and amplicons were ligated by T4 ligase. The final ligation products were verified by analytical digests with the endonucleases *SmaI*, *SpeI* and *XbaI*. The resulting banding patterns with sizes of 600 bp, 1200 bp and 7100 bp (#514), 2100 bp and 6700 bp (#515) as well as 1000 bp and 7800 bp (#516) met the expectations.

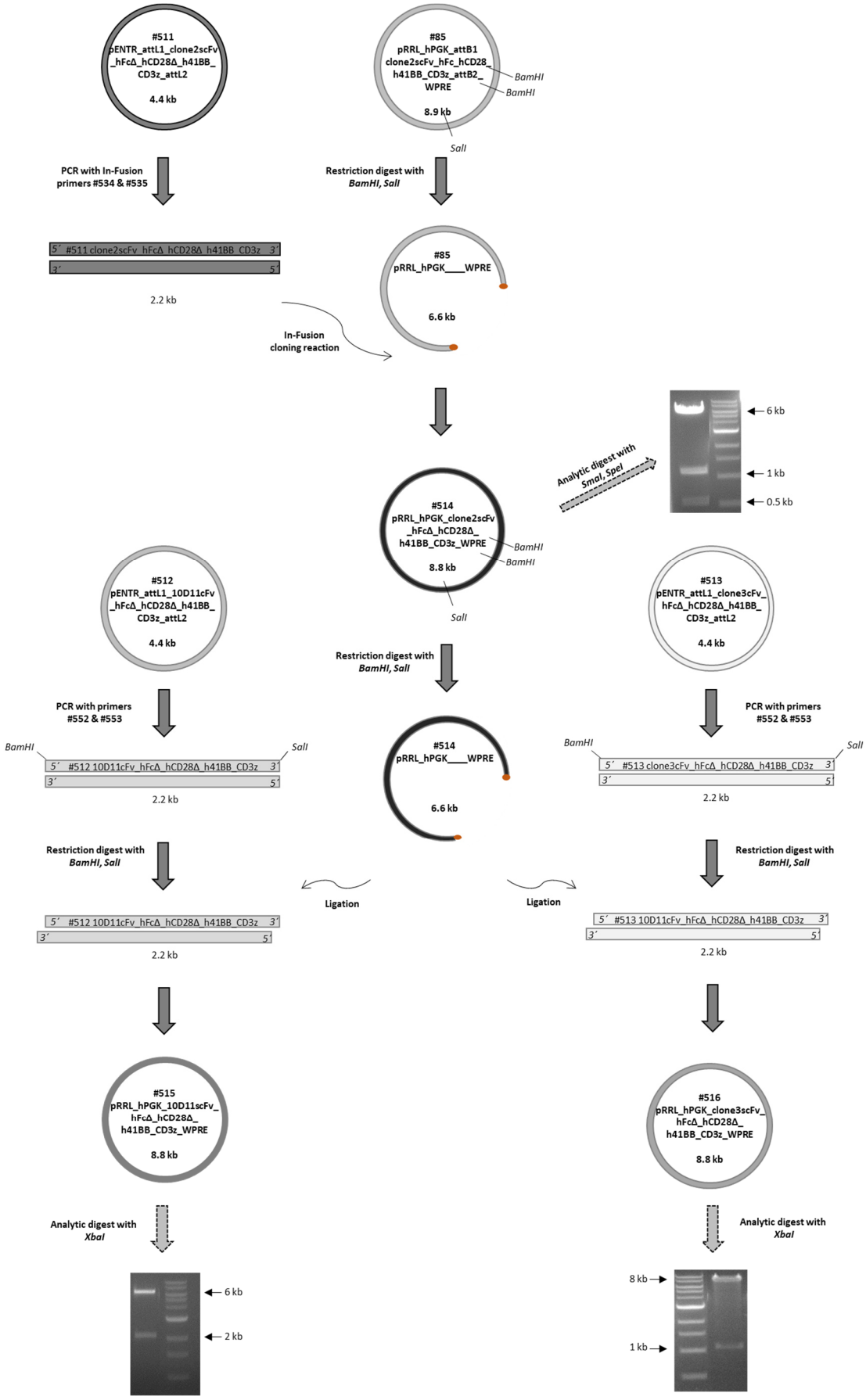

Figure 4.2.6: Cloning strategy of human lentiviral transfer vectors #514, #515 and #516
The lentiviral transfer vector #514 was generated from the lentiviral transfer vector #85 and pENTR vector #511 by exchanging the whole CAR - encoding sequences with the In-Fusion technology. The 10D11scFv_hFcΔ_hCD28Δ_h4-1BB_CD3z and

clone3scFv_hFcΔ_hCD28Δ_h4-1BB_CD3z - encoding DNA segments were amplified by PCR from the pENTR vectors #512 and #513 and ligated with the BamHI / SalI cut lentiviral transfer vector #514. Finally, the resulting vectors were verified by analytic digest with the endonucleases *SmaI*, *SpeI* and *XbaI*.

In the following section, lentiviral transfer vectors which encode for the three different human anti-NY-BR-1 CARs with hCD28_CD3z_hOX40 domains were generated (see Figure 4.2.7). For this purpose, the lentiviral transfer vector #514 was cut with the restriction enzymes *BamHI* and *SalI* in order to remove the clone2scFv_hFcΔ_hCD28Δ_h4-1BB_CD3z - encoding DNA fragment. The required DNA segments encoding the clone2/10D11/clone3scFv_hFc_hCD28_CD3z_hOX40 fragments were amplified from the pS/MARter vectors #432, #433 and #434 by PCR (In-Fusion primers #562, #563, #564). The linearized lentiviral transfer vector #514 was fused to the different PCR fragments using the In-Fusion technology, resulting in the lentiviral transfer vectors #537 (pRRL_hPGK_clone2scFv_hFc_hCD28_CD3z_hOX40_WPRE), #538 (pRRL_hPGK_10D11scFv_hFc_hCD28_CD3z_hOX40_WPRE) and #539 (pRRL_hPGK_clone3scFv_hFc_hCD28_CD3z_hOX40_WPRE). Finally, they were verified by analytical digest with the restriction enzymes *ScaI*, *XbaI* and *XhoI,* which led to the expected band sizes of 2300 bp, 2700 bp and 3700 bp for vector #537, 2700 bp and 6100 bp for vector #538 and 2100 bp and 6700 bp for vector #539.

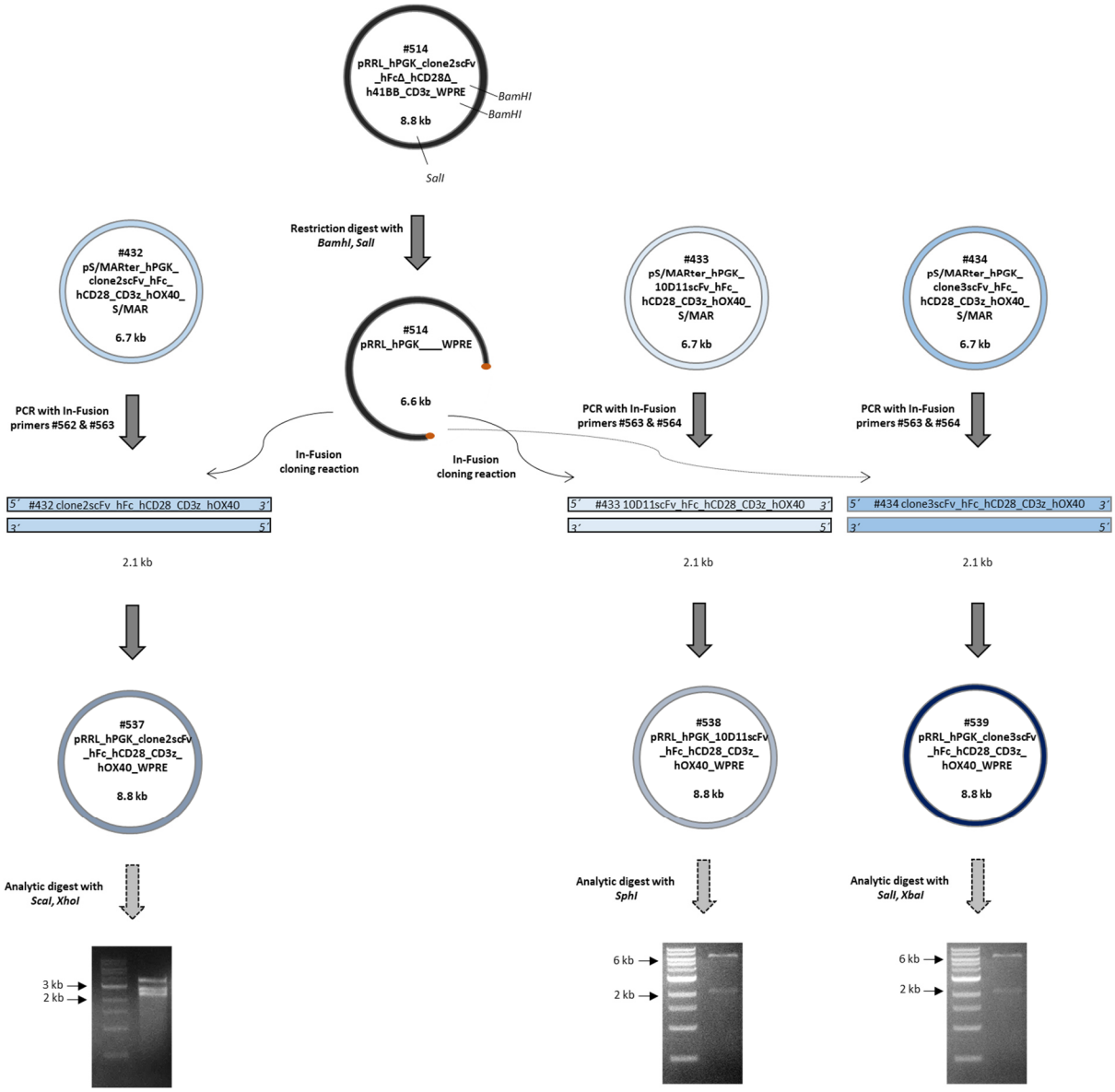

Figure 4.2.7: Cloning strategy of human lentiviral transfer vectors #537, #538 and #539
The lentiviral transfer vectors #537, #538 and #539 were generated by using the In-Fusion technology. Here, the clone2scFv_hFcΔ_hCD28Δ_h4-1BB_CD3z - encoding DNA fragment in vector #514 was removed by restriction digest and exchanged with the PCR amplicons clone2/10D11/clone3scFv_hFc_hCD28_CD3z_hOX40, derived from vectors #432, #433 and #434. Finally, the resulting vectors were verified by analytic digest with the endonucleases *SmaI*, *SpeI* and *XbaI*.

4.3 Functional characterization of human anti-NY-BR-1 chimeric antigen receptors *in vitro*

Experiments of this section were focusing on the expression of newly cloned anti-NY-BR-1 CAR constructs in lentivirally transduced or electroporated human T cells. In this context, the influence of different intracellular domains on CAR expression levels were examined in more detail. Furthermore, the specificity of the three different anti-NY-BR-1 CARs (clone2, 10D11, clone3) for the NY-BR-1 protein as well as possible cross reactivities with the NY-BR-1.1 protein were evaluated. Moreover, it was of great interest to find out whether anti-NY-BR-1 CAR^+ T cells detect and kill NY-BR-1 expressing target cells.

4.3.1 Expression analysis of human anti-NY-BR-1 CARs in lentivirally transduced HEK293T and human T cells

The lentiviral productions of expression vectors encoding the anti-NY-BR-1 CAR constructs clone2scFv_hFcΔ_hCD28Δ_h4-1BB_hCD3z (#514), 10D11scFv_hFcΔ_hCD28Δ_h4-1BB_hCD3z (#515), clone3scFv_hFcΔ_hCD28Δ_h4-1BB_hCD3z (#516) as well as clone2scFv_hFc_hCD28_hCD3z_hOX40 (#537), 10D11scFv_hFc_hCD28_hCD3z_hOX40 (#538) and clone3scFv_hFc_hCD28_hCD3z_hOX40 (#539) were performed by co-transfection of HEK 293T cells, as described in chapter 3.2.9.1. To test whether these CAR constructs can be expressed in human cells and to quantify the titer of the produced lentiviral particles, HEK 293T cells were transduced with 1 µL of freshly harvested, concentrated viral supernatant. Figure 4.3.1 A shows representative flow cytometry data of HEK 293T cells stained for anti-NY-BR-1 CARs with the PE or APC - conjugated anti-human IgG antibody 72 h post transduction. Indeed, all synthetically produced anti-NY-BR-1 CARs were successfully expressed in HEK 293T cells with different efficiencies, indicating differences in the lentiviral titers.

To examine the expression levels of different anti-NY-BR-1 CARs in human T cells, peripheral T cells were isolated from the same donor (LDA01), activated for 48 h, as described in chapter 3.2.9.4, and lentivirally transduced with all above mentioned CAR constructs at an MOI of 2. Two days post transduction, transduced T cells were tested for CAR expression by flow cytometric analysis with the APC - conjugated anti-human CD3 (UCHT1) and PE - conjugated anti-human IgG antibodies (see Figure 4.3.1 B). As already observed in HEK 293T cells, all CAR constructs were successfully expressed in human T cells. However, the expression levels of the various CAR constructs differed significantly. Anti-NY-BR-1 CARs incorporating the hOX40 domain (in a terminal position) achieved higher expression

levels with all three different scFvs (clone2*:* 23.8 %*,* 10D11*:* 22.8 %, clone3*:* 18.1 %) compared with CARs containing hFc_hCD28_h4-1BB domains (clone2: 15.8 %; 10D11: 9 %, clone3: 4.9 %). In addition, the frequency of CAR - expressing T cells differed slightly depending on the scFvs. In fact, lentiviral transductions with clone2 and 10D11 CAR constructs resulted in slightly increased CAR expression levels in T cells compared to clone3 CARs.

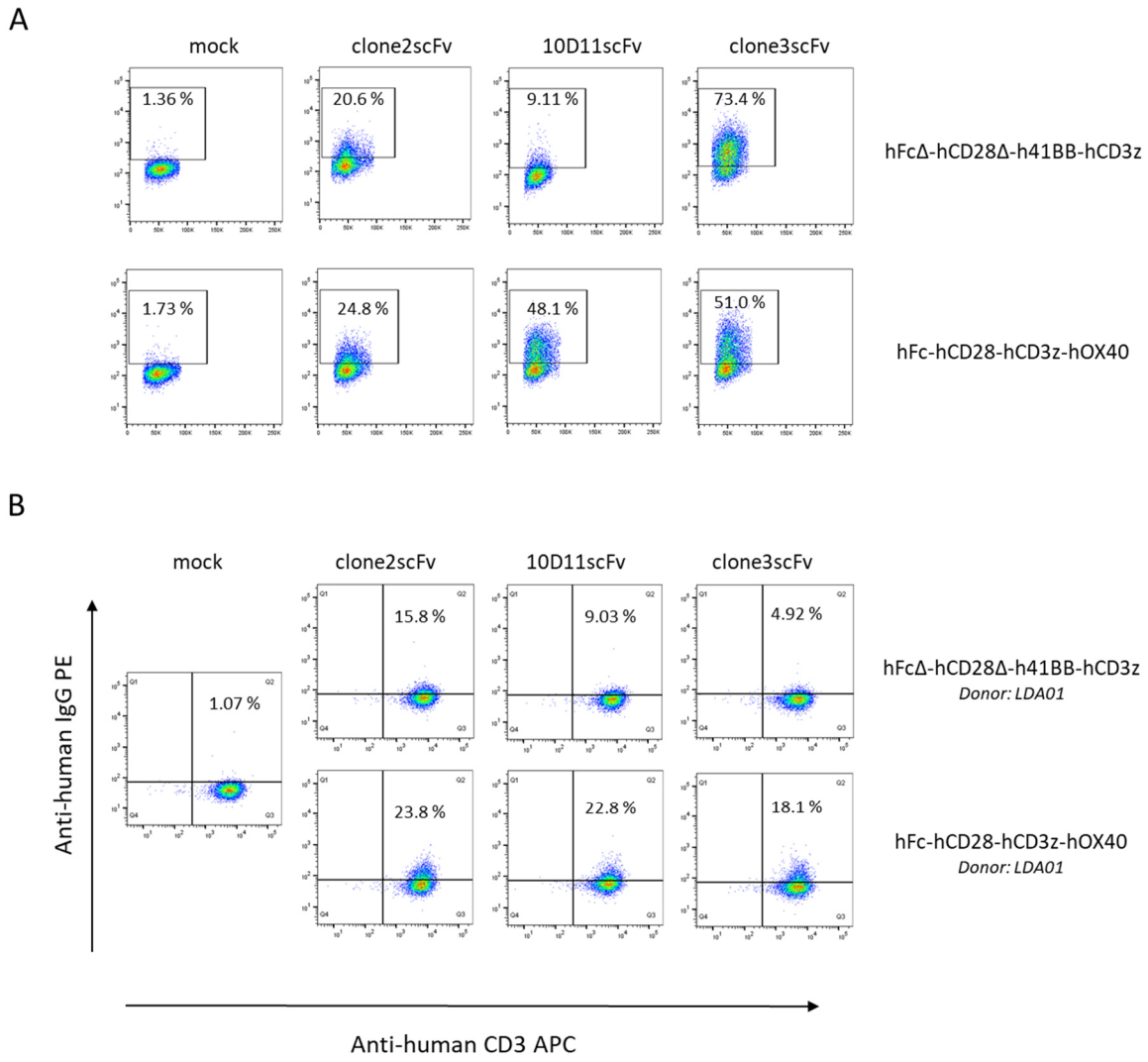

Figure 4.3.1: Expression analysis of human anti-NY-BR-1 CARs in lentivirally transduced HEK 293T and T cells
Flow cytometric - based quantification of CAR expression levels in [A] HEK 293T cells 72 h after lentiviral transduction with 1 µL of concentrated lentivirus (with unknown titer) in order to determine the lentiviral titers and to study the expression of human anti-NY-BR-1 CARs in an easily transducible cell line; and in [B] human T cells (isolated from the same donor LDA01) 48 h after lentiviral transduction at an MOI of 2. In [A] and [B] cells were lentivirally transduced with expression vectors encoding the anti-NY-BR-1 CAR constructs clone2scFv_hFcΔ_hCD28Δ_h4-1BB_hCD3z (#514), 10D11scFv_hFcΔ_hCD28Δ_h4-1BB_hCD3z (#515), clone3scFv_hFcΔ_hCD28Δ_h4-1BB_hCD3z (#516) as well as clone2scFv_hFc_hCD28_hCD3z_hOX40 (#537), 10D11scFv_hFc_hCD28_hCD3z_hOX40 (#538) and clone3scFv_hFc_hCD28_hCD3z_hOX40 (#539). For flow cytometric analysis, both transduced and untransduced cells were stained with the PE or APC-conjugated anti-human IgG antibody, which binds to the human Fc domain of the anti-NY-BR-1 CARs. Human T cells were additionally stained with the APC - conjugated anti-human CD3 antibody (UCHT1). Percentages indicate the proportion of CAR expression HEK 293T or T cells of the total number of lentivirally transduced HEK 293T or T cells.

4.3.2 Expression analysis of human anti-NY-BR-1 CARs in pS/MARter and NanoCMARter electroporated T cells

In addition to lentiviral transduction, a novel method - the electroporation of human T cells with pS/MARter and NanoCMARter vectors - was used for the generation of anti-NY-BR-1 CAR - expressing T cells. Both vector systems were kindly provided by Dr. Richard Harbottle and Dr. Matthias Bozza (DKFZ, DNA Vector Research Group) and have so-called scaffold/matrix attachment region (S/MAR) domains, which induce an interaction between chromatins (or DNA vectors) and the nuclear matrix by binding to matrix proteins [200,208,228]. Therefore, experiments of this section focused on the question whether electroporation with anti-NY-BR-1 CAR - encoding pS/MARter and NanoCMARter vectors can induce effective and stable CAR expression in human T cells.

Prior to electroporation with different pS/MARter vectors encoding the anti-NY-BR-1 CAR constructs clone2scFv_hFc_hCD28_h4-1BB_CD3z (#273), 10D11scFv_hFc_hCD28_h4-1BB_CD3z (#302), clone3scFv_hFc_hCD28_h4-1BB_CD3z (#303), clone2scFv_hFcΔ_hCD28Δ_h4-1BB_CD3z (#517), 10D11scFv_hFcΔ_hCD28Δ_h4-1BB_CD3z (#518), clone3scFv_hFcΔ_hCD28Δ_h4-1BB_CD3z (#519), clone2scFv_hFc_hCD28_CD3z_hOX40 (#432), 10D11scFv_hFc_hCD28_CD3z_hOX40 (#433), clone3scFv_hFc_hCD28_CD3z_hOX40 (#434), peripheral T cells were isolated from different donors and activated for 24h at least, as described in chapter 3.2.10.1. One day after electroporation (2200 V, 30 ms, 1 pulse) of human T cells via the Neon Transfection System (ThermoFisher), T cells were examined for CAR expression by surface staining with the PE - conjugated anti-human IgG and APC - conjugated anti-human CD3 (UCHT1) antibodies followed by flow cytometric analysis (see Figure 4.3.2). The average and maximal expression levels of the different anti-NY-BR-1 constructs varied significantly. While CARs containing the endodomain hOX40 demonstrated expression levels of up to 46 % (mean: clone2scFv: 21 %, 10D11scFv: 23 %; clone3scFv: 24%), hFc_hCD28_h4-1BB and hFcΔ_hCD28Δ_h4-1BB - containing CARs showed maximum expression levels of only 9 % and 7 %, respectively (see Figure 4.3.2).

Further optimizations of pS/MARter vectors such as a strongly minimized bacterial backbone and the resulting reduced molar mass led to so-called NanoCMARter vectors [172] (patent WO2019/060253Al). Electroporation of human T cells with those vectors encoding the anti-NY-BR-1 CAR constructs clone2scFv_hFc_hCD28_h4-1BB_CD3z (#418), 10D11scFv_hFc_hCD28_h4-1BB_CD3z (#419), clone3scFv_hFc_hCD28_h4-1BB_CD3z (#420), clone2scFv_hFc_hCD28_CD3z_hOX40 (531), 10D11scFv_hFc_hCD28_CD3z_hOX40 (#532) and clone3scFv_hFc_hCD28_CD3z_hOX40 (#533) resulted in high CAR expression levels, which, however, again varied depending on the intracellular domains (Figure 4.3.3 A). As already observed with pS/MARter vectors, CARs incorporating the hOX40 endodomain demonstrated higher expression levels with all three different anti-NY-BR-1 scFvs than

CARs containing hFc_hCD28_h4-1BB domains (see Figure 4.3.3). A direct comparison of pS/MARter and NanoCMARter vectors indicated no statistically significant differences in the expression patterns of hOX40 CARs. In contrast, hFc_hCD28_h4-1BB - containing CARs encoded by NanoCMARter vectors led to significantly higher expression levels than those encoded by pS/MARter vectors (see Figure 4.3.3).

Overall, these data illustrated that the hOX40 domain has a positive effect on the expression of anti-NY-BR-1 CARs in human T cells, regardless of the type of generation. In general, electroporation with pS/MARter and NanoCMARter vectors proved to be a well suited method to generate CAR - expressing T cells in a fast and cost-effective way, which, additionally, yielded CAR expression levels similar to those of lentiviral transduction.

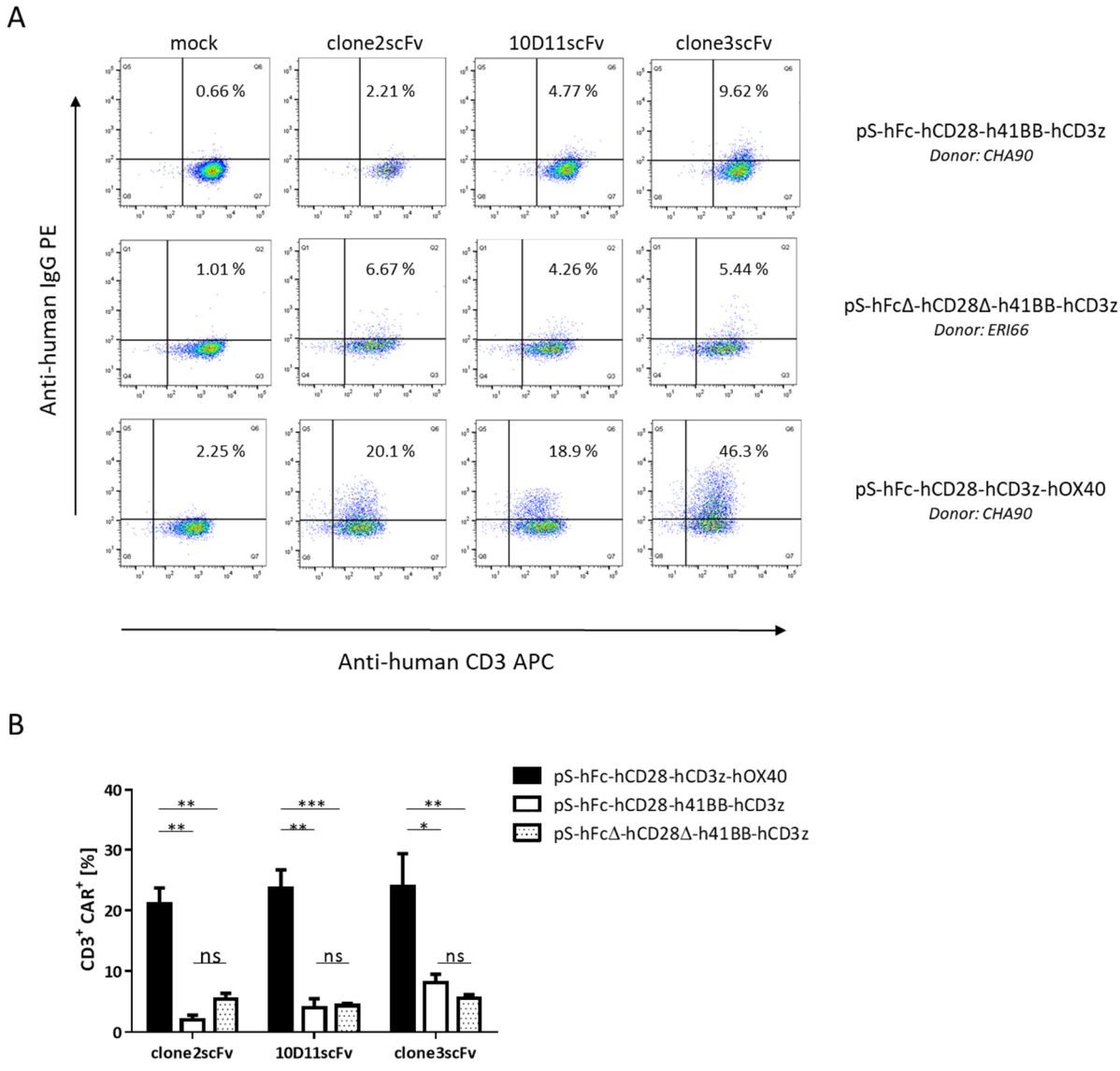

Figure 4.3.2: Expression analysis of human anti-NY-BR-1 CARs in pS/MARter electroporated T cells
Human T cells, isolated from different donors, were activated for at least 24 h and electroporated with pS/MARter vectors encoding the anti-NY-BR-1 constructs clone2scFv_hFc_hCD28_h4-1BB_CD3z(#273), 10D11scFv_hFc_hCD28_h4-1BB_CD3z (#302), clone3scFv_hFc_hCD28_h4-1BB_CD3z (#303), clone2scFv_hFcΔ_hCD28Δ_h4-1BB_CD3z (#517),

10D11scFv_hFcΔ_hCD28Δ_h4-1BB_CD3z (#518), clone3scFv_hFcΔ_hCD28Δ_h4-1BB_CD3z (#519), clone2scFv_hFc_hCD28_CD3z_hOX40 (#432), 10D11scFv_hFc_hCD28_CD3z_hOX40 (#433), clone3scFv_hFc_hCD28_CD3z_hOX40 (#434). One day post electroporation with the Neon Transfection System, electroporated and untransfected (mock) T cells were analyzed for surface expression of different CAR constructs by flow cytometric analysis. Here, T cells were stained with the PE-conjugated anti-human IgG antibody, which binds to the human Fc domain of anti-NY-BR-1 CARs, and the APC - conjugated anti-human CD3 antibody (UCHT1). [A] Representative flow cytometric analysis of CAR expression levels and [B] average achieved CAR expression levels in pS/MARter electroporated T cells in independently performed experiments (hOX40: n=9; BBz: n=3; ΔΔBBz: n=5). Percentages indicate the proportion of CAR - expressing T cells of the total number of electroporated T cells (mean values ± sem ;*, $p < 0.05$; **, $p < 0.01$; ***, $p < 0.001$; two-way ANOVA followed by Tukey's multiple comparison test).

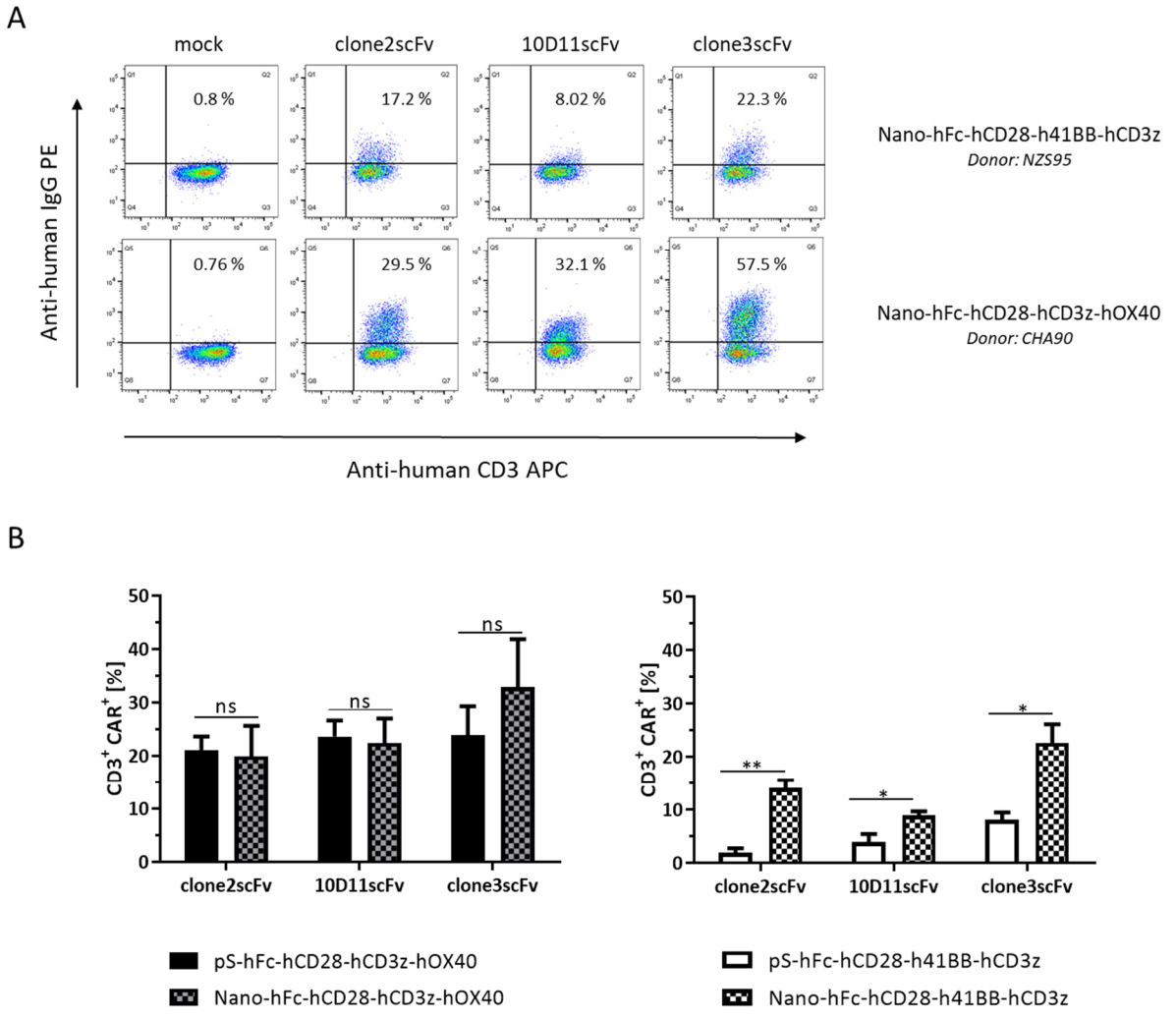

Figure 4.3.3: Expression analysis of human anti-NY-BR-1 CARs in NanoCMARter electroporated T cells
Human T cells, isolated from different donors, were activated for at least 24 h and electroporated with NanoCMARter vectors encoding the anti-NY-BR-1 constructs clone2scFv_hFc_hCD28_h4-1BB_CD3z (#418), 10D11scFv_hFc_hCD28_h4-1BB_CD3z (#419), clone3scFv_hFc_hCD28_h4-1BB_CD3z (#420), clone2scFv_hFc_hCD28_CD3z_hOX40 (531), 10D11scFv_hFc_hCD28_CD3z_hOX40 (#532), clone3scFv_hFc_hCD28_CD3z_hOX40 (#533). One day post electroporation with the Neon Transfection System, electroporated and untransfected (mock) T cells were analyzed for surface expression levels of different CAR constructs by flow cytometric analysis. Here, T cells were stained with the PE-conjugated anti-human IgG antibody, which binds to the human Fc domain of anti-NY-BR-1 CARs, and the APC - conjugated anti-human CD3 antibody (UCHT1). [A] Representative flow cytometric analysis of CAR expression levels and [B] average achieved CAR expression levels in NanoCMARter and pS/MARter electroporated T cells in independently performed experiments (pS-CD3z_hOX40: n=9; Nano-CD3z_hOX40: n=4; pS-CD28_4-1BB_CD3z: n=3; Nano-CD28_4-1BB_CD3z: n=3). Percentages indicate the proportion of CAR - expressing T cells of the total number of electroporated T cells (mean values ± sem; *, $p < 0.05$; **, $p < 0.005$; unpaired two-tailed Student's t-test).

4.3.3 Specific activation and cross-reactivity analysis of human anti-NY-BR-1 CAR T cells with NY-BR-1 and NY-BR-1.1 peptides

After successful generation of human anti-NY-BR-1 CAR - expressing T cells, the cytokine ELISA was used to evaluate the specificity of anti-NY-BR-1 CAR constructs by co-cultivation with the NY-BR-1 full length protein. In terms of specificity, it was also examined whether anti-NY-BR-1 CAR$^+$ T cells are activated by the related NY-BR-1.1 protein, which is expressed in the brain and has 54% amino acid homology to NY-BR-1 [85].

Peripheral T cells were isolated from one healthy donor and lentivirally transduced with the anti-NY-BR-1 CAR constructs clone2scFv_hFc_hCD28_hCD3z_hOX40 (#537), 10D11scFv_hFc_hCD28_hCD3z_hOX40 (#538) and clone3scFv_hFc_hCD28_hCD3z_hOX40 (#539). Following successful determination of CAR expression levels by flow cytometric analysis, CAR$^+$ T cells were cultivated in NY-BR-1 and NY-BR-1.1 coated plates (96 well plate, 3x10^4 CAR$^+$ T cells / well) for 24h. Untransduced (mock) T cells were used as controls. Subsequently, the level of T cell activation was evaluated by determining the concentration of secreted IFNγ in cell culture supernatants (see Figure 4.3.4). All three tested anti-NY-BR-1 CAR constructs led to the activation of T cells following incubation with the NY-BR-1 full length protein (3.75 µg / well). Interestingly, both 10D11 and clone3 CAR$^+$ T cells secreted lower levels of IFNγ upon antigen specific activation compared with clone2 CAR$^+$ T cells.

Moreover, strong T cell responses to the NY-BR-1.1 full length protein were also detected by clone2 (but not by 10D11) CAR - expressing T cells. Similarly, clone3 CAR$^+$ T cells showed a slight increase in IFNγ release (see Figure 4.3.4 C). Similar to the findings with NY-BR-1 protein co-cultivation, clone2 CAR$^+$ T cells exhibited the strongest activation levels with an average IFNγ concentration of 1300 pg / mL (in cell culture supernatant), whereas the activation levels of clone3 CAR$^+$ T cells were significantly lower with only 450 pg / mL.

A direct comparison of NY-BR-1 and NY-BR-1.1 co-cultured CAR$^+$ T cells illustrated that the activation levels of clone2 CAR$^+$ T cells were very similar (see Figure 4.3.4 D), whereas the measured IFNγ concentrations in the supernatants of 10D11 and clone3 CAR$^+$ T cells co-cultivated with NY-BR-1 protein doubled when compared to NY-BR-1.1 co-cultivation.

Overall, these data proved both the NY-BR-1 specificity of all three tested CAR constructs, whereby clone2 CAR led to the strongest activation of CAR$^+$ T cells, and the strong cross-reactivity of clone2 CAR$^+$ T cells with the NY-BR-1.1 protein.

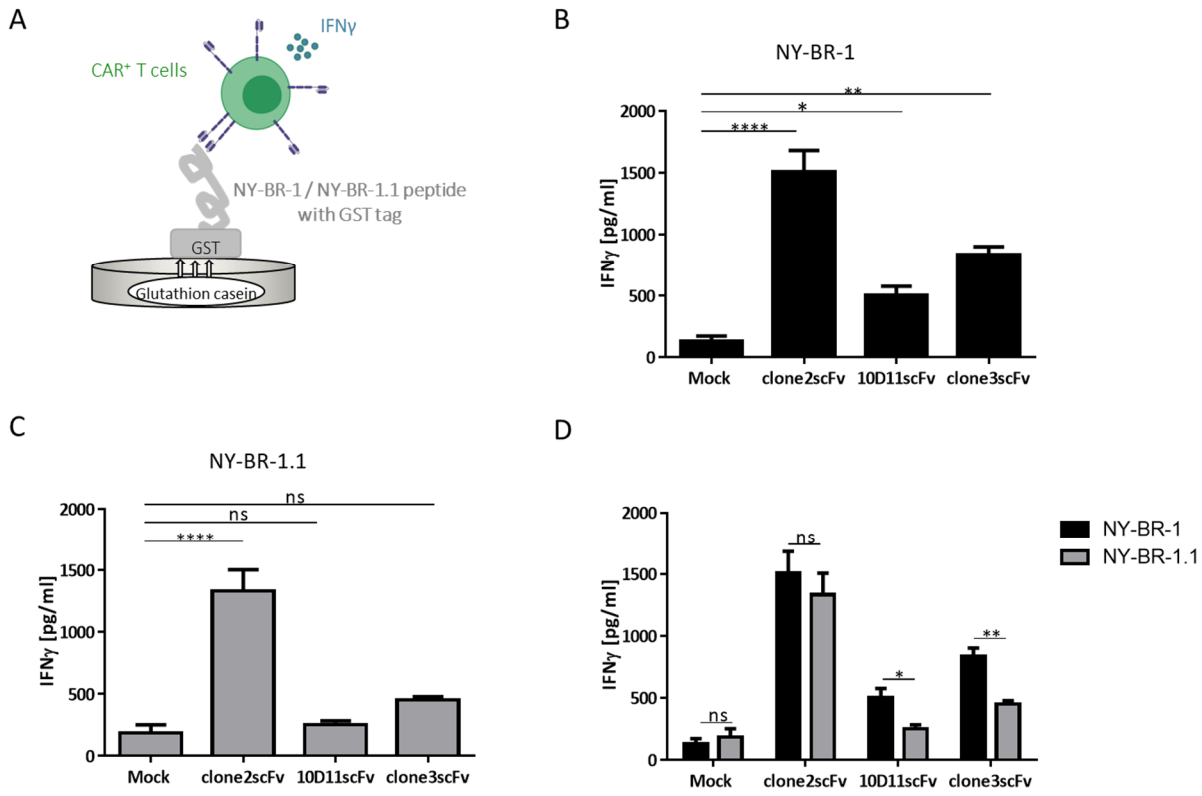

Figure 4.3.4: Activation of human anti-NY-BR-1 CAR - expressing T cells by NY-BR-1 and NY-BR-1.1 peptides
[A] Schematic representation of a NY-BR-1 / NY-BR-1.1 coated 96 well plate. GST-tagged NY-BR-1 / NY-BR-1.1 full length peptide - containing protein lysates, extracted from cell lysates of GST-tagged NY-BR-1 / NY-BR-1.1 transfected HEK 293T cells, were used to coat a 96 well plate. The final concentration of NY-BR-1 or NY-BR-1.1 peptides were 3.75 µg per well. [B], [C], [D] Human T cells were lentivirally transduced with the anti-NY-BR-1 CAR constructs clone2scFv_hFc_hCD28_hCD3z_hOX40 (#537), 10D11scFv_hFc_hCD28_hCD3z_hOX40 (#538) and clone3scFv_hFc_hCD28_hCD3z_hOX40 (#539) and were subsequently cultivated in NY-BR-1 [B] or NY-BR-1.1 [C] coated 96 well plates ($3x10^4$ CAR^+ T cells / well) for 24 h. Afterwards, the activation levels of CAR^+ T cells were evaluated by the measurement of IFNγ concentrations in cell culture supernatants by human IFNγ ELISA. All experiments were performed in triplicate. [B], [C] Mean values ± sem; *, $p < 0.05$; **, $p < 0.01$; ****, $p < 0.0001$; one-way ANOVA followed by Holm-Sidak's multiple comparison test. [D] Mean values ± sem; *, $p < 0.05$, **, $p < 0.01$; unpaired two-tailed Student's t-test.

4.3.4 Elimination of NY-BR-1 expressing Bosc23 cells by human anti-NY-BR-1 CAR - expressing T cells

To assess the cytolytic and NY-BR-1 specific activity of human anti-NY-BR-1 CAR - expressing T cells, the killing efficacy of pS/MARter electroporated T cells was determined by performing a xCELLigence - based killing assay with the NY-BR-1$^+$ Bosc23 cell line. This assay allows a real-time monitoring of cell proliferation and cell viability by permanent measurement of cellular impedance (see chapter 3.2.13).

Upon successful electroporation of peripheral T cells with the human anti-NY-BR-1 CAR constructs clone2scFv_hFc_hCD28_CD3z_hOX40 (#432), 10D11scFv_hFc_hCD28_CD3z_hOX40 (#433), clone3scFv_hFc_hCD28_CD3z_hOX40 (#434), Lactacystin-treated (NY-BR-1$^+$) Bosc cells were co-cultivated with untransfected (mock) and CAR$^+$ T cells in 96 well electronic microtiter plates (E-Plate 96, ACEA Biosciences) at a ratio of 1:1. Real-time monitoring of cell viabilities of (NY-BR-1$^+$) Bosc cells demonstrated significantly reduced viabilities rates of NY-BR-1$^+$ target cells when co-cultured with CAR$^+$ T cells. The highest cytotoxicity effects were observed with clone3 CAR$^+$ T cells leading to the lowest cell viability rates (app. 50 %) of NY-BR-1$^+$ Bosc23 cells, followed by the treatment with 10D11 (app. 59 %) and clone2 CAR$^+$ T cells (app. 71 %). In contrast, co-cultivation of wild-type Bosc23 cells with anti-NY-BR-1 CAR$^+$ T cells did not lead to significantly decreased cell viabilities compared to mock treated cells. With regard to activation levels of NY-BR-1$^+$ Bosc23 co-cultivated T cells, CAR$^+$ T cells, especially 10D11 CAR$^+$ T cells, released higher amounts of IFNγ than untransfected T cells. This suggests a specific NY-BR-1 or rather CAR-mediated activation of T cells, which is confirmed by the fact that CAR$^+$ T cells did not show significantly increased activation levels upon co-cultivation with wild-type Bosc23 cells.

Overall, these data reflected the specificity of all three CAR candidates for the NY-BR-1 protein and demonstrated that T cells expressing these CARs can be successfully activated by NY-BR-1 expressing target cells.

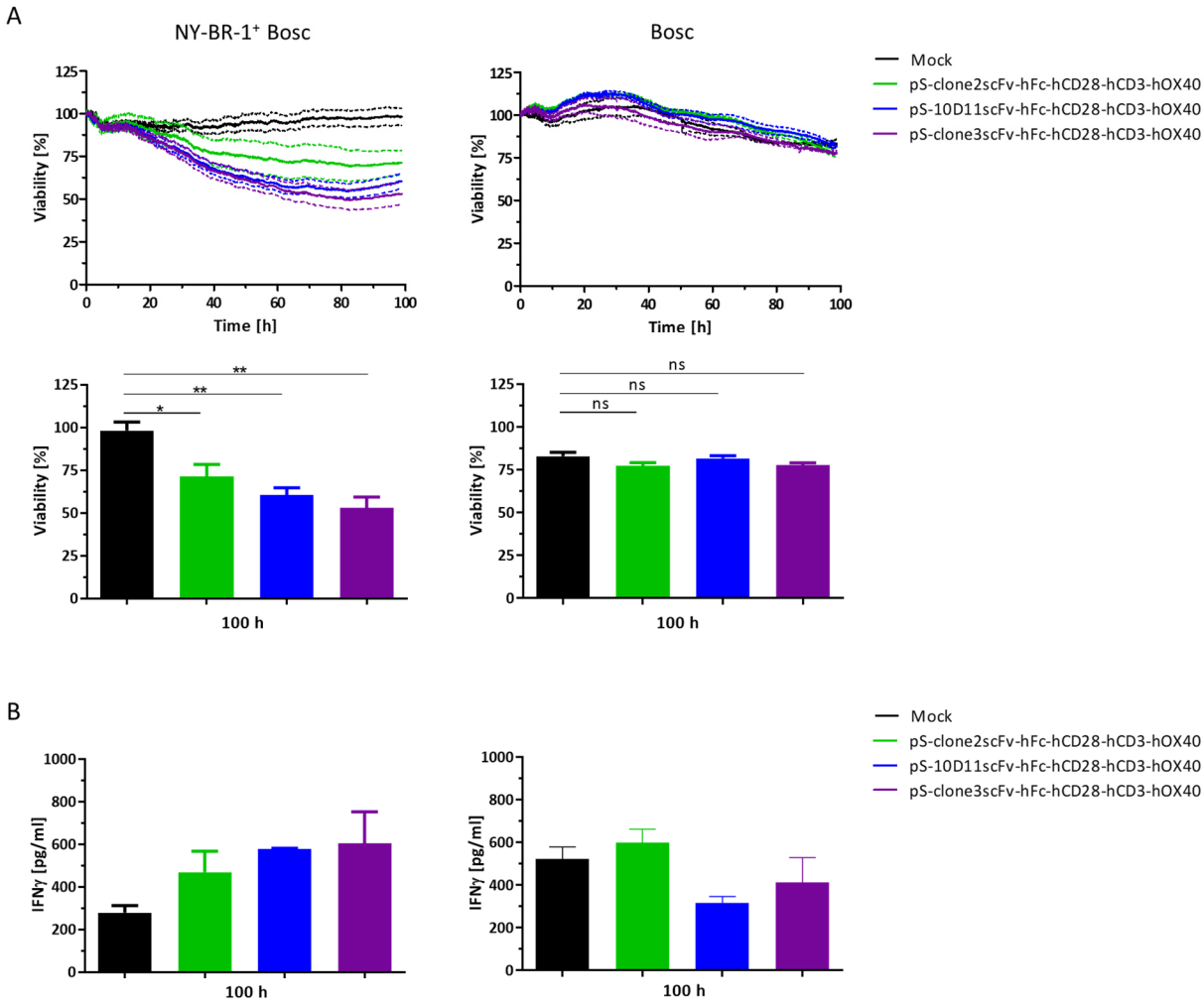

Figure 4.3.5: Activation of human anti-NY-BR-1 CAR - expressing T cells by NY-BR-1 expressing Bosc23 cells
xCELLigence based killing assay of NY-BR-1+ Bosc23 cells by human anti-NY-BR-1 CAR - expressing T cells. Isolated peripheral T cells were electroporated with pS/MARter vectors encoding the anti-NY-BR-1 CAR constructs clone2scFv_hFc_hCD28_CD3z_hOX40 (#432), 10D11scFv_hFc_hCD28_CD3z_hOX40 (#433), clone3scFv_hFc_hCD28_CD3z_hOX40 (#434) and subsequently co-cultivated with Lactacystin-treated (NY-BR-1+) Bosc cells at a ratio of 1:1 in 96 well electronic microtiter plates (E-Plate 96, ACEA Biosciences). Untransfected (mock) T cells were used as controls. [A] Cytolytic activity of mock and CAR+ T cells was monitored by using the xCELLigence RTCA instrument (ACEA Biosciences), enabling a real-time measurement of cell impedance or rather cell viability of adherent (NY-BR-1+) Bosc cells. Experiments were performed in triplicate. The given viabilities have been calculated in relation to untreated (NY-BR-1+) Bosc cells during (upper graphs; mean values ± sem) and at the end of the experiments (100 h) (lower graphs; mean values ± sem; *, $p < 0.05$; **, $p < 0.01$; one-way ANOVA followed by Holm-Sidak's multiple comparison test). [B] IFNγ concentrations in the cell culture supernatants of mock and CAR+ T cell treated NY-BR-1+ Bosc23 (left graph) and wild type Bosc23 cells (right graph) were recorded by IFNγ ELISA at the end of the experiments (100 h) (mean values ± sem; no statistically significant differences according to one-way ANOVA).

4.3.5 Elimination of primary pleural effusion cells by allogeneic anti-NY-BR-1 CAR - expressing T cells

Since human anti-NY-BR-1 CAR$^+$ T cells demonstrated convincing killing efficiencies of NY-BR-1$^+$ target cell lines, experiments of the next section were focusing on the elimination of NY-BR-1 expressing primary pleural effusion cells isolated from breast cancer patients. Here it should be clarified whether NY-BR-1$^+$ pleural effusion cells of different patients are recognized and eliminated by CAR$^+$ T cells in an allogeneic setting and if the method of CAR$^+$ T cell generation (electroporation with pS/MARter and NanoCMARter vectors and lentiviral transduction) affects the functional properties of those T cells.

To address this issue, pleural effusion cells were isolated from breast cancer patients and analyzed for the expression of NY-BR-1 by flow cytometric analysis using the murine anti-NY-BR-1 clone2 and secondary APC - conjugated anti-mouse IgG antibodies. In case of positive results, pleural effusion cells were co-cultivated with allogeneic pS/MARter or NanoCMARter electroporated or lentivirally transduced CAR$^+$ T cells in 96 well electronic microtiter plates (E-Plate 96, ACEA Biosciences) at a ratio of 1:1. The viability of primary target cells was monitored by real-time measurement of cell impedance using the xCELLigence RTCA platform. Moreover, the activation level of T cells was assessed by determination of IFNγ release via IFNγ ELISA.

T cells from two different donors (CHL93, CHA90) were electroporated with pS/MARter vectors encoding the anti-NY-BR-1 CAR constructs clone2scFv_hFc_hCD28_CD3z_hOX40 (#432), 10D11scFv_hFc_hCD28_CD3z_hOX40 (#433), clone3scFv_hFc_hCD28_CD3z_hOX40 (#434) and were subsequently co-cultivated with pleural effusion cells, isolated from two different patients (HD-A-185 with NY-BR-1 expression levels of 34.7 % , HD-A-213 with NY-BR-1 expression levels of 14 %; see Figure 4.3.7; Supplementary Figure 6.3). In both cases, CAR$^+$ T cells exhibited significantly increased killing efficiencies of primary target cells compared with untransfected (mock) T cells, whereas clone2 and 10D11 CAR$^+$ T cells lysed more efficiently than clone3 CAR$^+$ T cells (see Figure 4.3.6 A, B). The slightly improved lytic activities of clone2 and 10D11 CAR$^+$ T cells were also reflected in IFNγ ELISA assays. In both cases, all CAR candidates led to increased IFNγ secretions compared to respective mock T cells, but the IFNγ levels of 10D11 and clone2 CAR$^+$ T cells were slightly increased compared to clone3 CAR$^+$ T cells. To enable a direct comparison of NanoCMARter and pS/MARter electroporated CAR$^+$ T cells, T cells from donor CHA90 were also electroporated with the corresponding NanoCMARter vectors encoding the anti-NY-BR-1 CAR constructs clone2scFv_hFc_hCD28_CD3z_hOX40 (531), 10D11scFv_hFc_hCD28_CD3z_hOX40 (#532), clone3scFv_hFc_hCD28_CD3z_hOX40 (#533), and co-cultured with pleural effusion cells from patient HD-A-213 in the same approach. Surprisingly, NanoCMARter derived CAR$^+$ T cells killed the pleural effusion cells more efficiently than those derived

from pS/MARter vectors (see Figure 4.3.6 B). In fact, primary cells exhibited viability rates of less than 10 % following co-cultivation with NanoCMARter derived CAR$^+$ T cells. This observed phenomenon was also reflected in greatly enhanced IFNγ concentrations in the cell culture supernatants of all tested NanoCMARter CAR$^+$ T cells compared to pS/MARter CAR$^+$ T cells.

Next, the functional efficiencies of lentivirally transduced anti-NY-BR-1 CAR$^+$ T cells were investigated by co-cultivation of pleural effusion cells from patient HD-A-213 with CAR$^+$ T cells (donor: ERC97), generated by lentiviral transduction with the anti-NY-BR-1 CAR constructs clone2scFv_hFc_hCD28_hCD3z_hOX40 (#537), 10D11scFv_hFc_hCD28_hCD3z_hOX40 (#538) and clone3scFv_hFc_hCD28_hCD3z_hOX40 (#539). Indeed, the results in Figure 4.3.6 C reveal that lentivirally transduced clone2, 10D11 and clone3 CAR$^+$ T cells selectively killed primary target cells, resulting in 40 % reduced viability rates compared to mock treated target cells, wherein the killing efficiencies were very similar between the different CAR candidates. Using end point data, IFNγ release was significantly increased in all CAR$^+$ T cells compared to mock T cells.

Due to the observation that CAR$^+$ T cells selectively killed pleural effusion cells from breast cancer patients, it should be clarified if this selectivity is based on the NY-BR-1 expression in target cells. Therefore, the NY-BR-1 expression profile of remaining target cells was studied by flow cytometric analysis (see Figure 4.1.2, Supplementary Figure 6.3). As a representative example, NY-BR-1 expression levels of pleural effusion cells from patient HD-A-185 are illustrated prior and after co-cultivation with pS/MARter electroporated CAR$^+$ T cells (donor: CHL93) in Figure 4.3.7Figure 4.1.2. The frequencies of NY-BR-1 expressing pleural effusion cells decreased from 34.7 % to 17.6 % within a few days without any treatment. Surprisingly, mock treated pleural effusion cells indicated an increase in NY-BR-1$^+$ cells of up to 32.5 %. In agreement with their killing efficiencies, CAR$^+$ T cells significantly reduced the proportion of NY-BR-1 expressing target cells (clone2scFv: 7 %; 10D11scFv: 5.6 %; clone3scFv: 10.3 %) compared to mock and untreated target cells. Of particular note was the fact that mock-treated and CAR$^+$ T cell-treated pleural effusion cells had NY-BR-1 expression rates of 32% and lower than 10 %, respectively. This 20 % difference is reflected in the viability rates of the target cells, which had a 20 % lower viability when co-cultivated with CAR$^+$ T cells compared to mock treated as shown in Figure 4.3.6 A.

Taken together, these data showed that both electroporated and lentivirally transduced human anti-NY-BR-1 CAR - expressing T cells detect and eliminate breast cancer derived NY-BR-1$^+$ target cells in allogeneic settings.

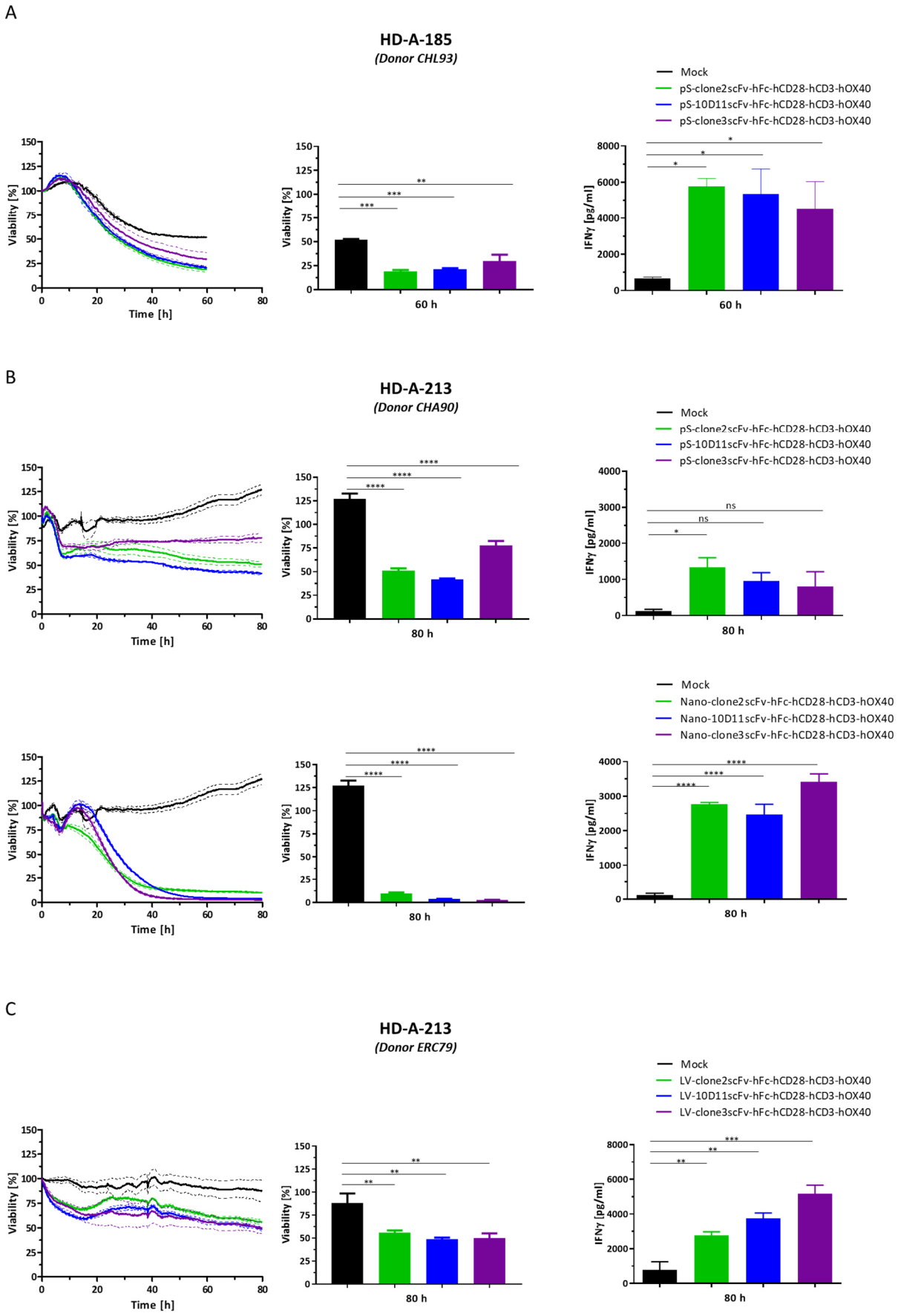

Figure 4.3.6: Killing of NY-BR-1^{+} pleural effusion cells by allogeneic anti-NY-BR-1 CAR^{+} T cells
xCELLigence based killing assay of human anti-NY-BR-1 CAR - expressing T cells with pleural effusion cells isolated from different breast cancer patients (HD-A-185, HD-A-213). Allogeneic, peripheral T cells from different donors (CHL93, CHA90,

ERC97) were [A], [B] electroporated with pS/MARter vectors encoding the anti-NY-BR-1 CAR constructs clone2scFv_hFc_hCD28_CD3z_hOX40 (#432), 10D11scFv_hFc_hCD28_CD3z_hOX40 (#433), clone3scFv_hFc_hCD28_CD3z_hOX40 (#434) and NanoCMARter vectors encoding the anti-NY-BR-1 CAR constructs clone2scFv_hFc_hCD28_CD3z_hOX40 (531), 10D11scFv_hFc_hCD28_CD3z_hOX40 (#532), clone3scFv_hFc_hCD28_CD3z_hOX40 (#533) or [C] lentivirally transduced with the anti-NY-BR-1 CAR constructs clone2scFv_hFc_hCD28_hCD3z_hOX40 (#537), 10D11scFv_hFc_hCD28_hCD3z_hOX40 (#538) and clone3scFv_hFc_hCD28_hCD3z_hOX40 (#539). Subsequently, CAR$^+$ T cells were co-cultivated with (NY-BR-1$^+$) pleural effusion cells in 96 well electronic microtiter plates (E-Plate 96, ACEA Biosciences) at a ratio of 1:1. Untransduced / untransfected (mock) T cells were used as controls. Cytolytic activity of mock and CAR$^+$ T cells was monitored using the xCELLigence RTCA instrument (ACEA Biosciences), enabling a real-time measurement of cell impedance or rather cell viability of adherent (NY-BR-1$^+$) target cells. Experiments were performed in triplicate. The given viabilities have been calculated in relation to untreated (NY-BR-1$^+$) target cells during (left graphs, mean values ± sem) and at the end of the experiments (60 h, 80 h) (mean values ± sem; *, $p < 0.05$; **, $p < 0.01$; ***, $p < 0.001$; ****, $p < 0.0001$; one-way ANOVA with Holm-Sidak's multiple comparison test). IFNγ concentrations in the cell culture supernatants were recorded by IFNγ ELISA at the end of the experiments (60 h, 80 h) (right graphs; mean values ± sem; *, $p < 0.05$, **, $p < 0.01$, ***, $p < 0.001$; ****, $p < 0.0001$; one-way ANOVA followed by Holm-Sidak's multiple comparison test).

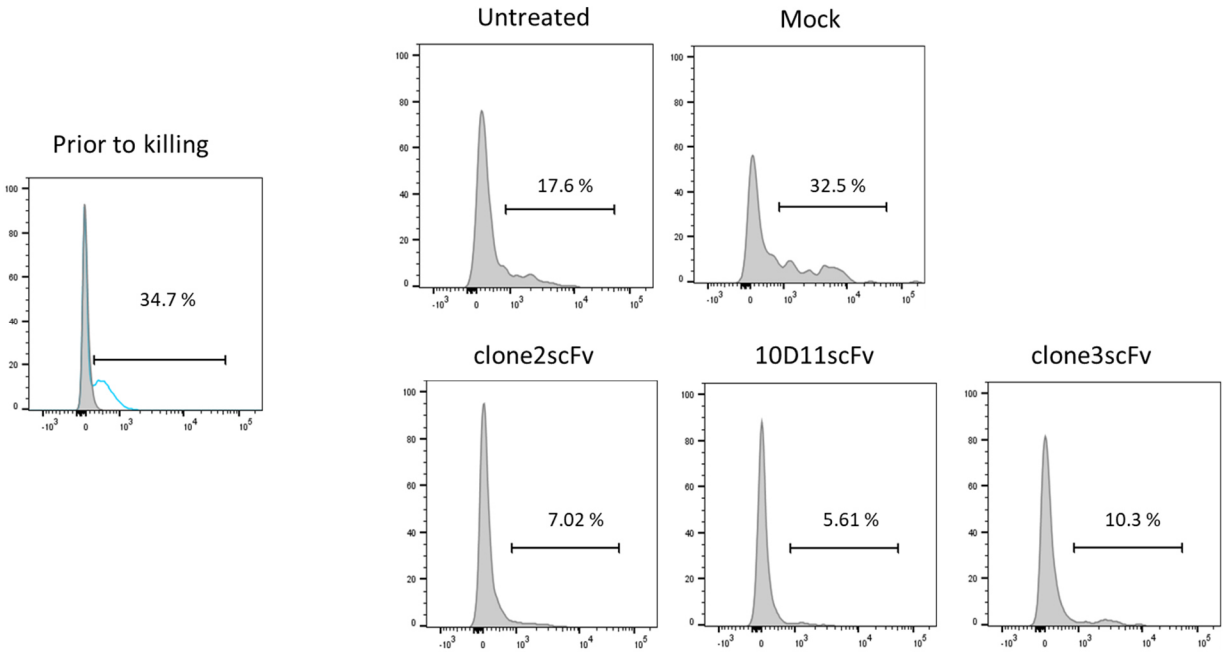

Figure 4.3.7: NY-BR-1 expression profile of pleural effusion cells (HD-A-185) prior and after co-cultivation with pS/MARter electroporated anti-NY-BR-1 CAR - expressing T cells (CHL93)
Pleural effusion cells, isolated from patient HD-A-185, were co-cultivated with allogeneic pS/MARter electroporated CAR (clone2scFv_hFc_hCD28_CD3z_hOX40 (#432), 10D11scFv_hFc_hCD28_CD3z_hOX40 (#433), clone3scFv_hFc_hCD28_CD3z_hOX40 (#434)) expressing T cells in 96 well electronic microtiter plates (E-Plate 96, ACEA Biosciences) at a ratio of 1:1 for 60 h. The frequency of NY-BR-1 positive target cells was determined by flow cytometric analysis prior and after the xCELLigence based killing assay. Cells were stained with the monoclonal anti-NY-BR-1 antibody clone2 and the secondary FITC or APC - conjugated anti-mouse IgG antibody. Percentages indicate the proportion of NY-BR-1 positive cells of the total number of survived pleural effusion cells.

4.4 Functional characterization of murine anti-NY-BR-1 chimeric antigen receptors *in vitro*

After successful demonstration that human anti-NY-BR-1 CAR$^+$ T cells generated by electroporation or lentiviral transduction specifically eliminate NY-BR-1 expressing target cells, experiments of the next chapter were focusing on the question to what extent murine CAR$^+$ T cells can be generated with similar protocols and whether they can also be specifically activated by murine NY-BR-1$^+$ target cells.

4.4.1 Expression analysis of murine anti-NY-BR-1 CARs in lentivirally transduced Jurkat, NIH/3T3, HEK 293T and murine T cells

The initial focus was on the production of lentiviral vectors encoding the murine CAR constructs #216 (CMV_attB1_clone2scFv_mFcΔ_mCD28Δ_m4-1BB_CD3z_attB2_hPGK_DsRed2_WPRE), #217 (CMV_attB1_10D11scFv_mFcΔ_mCD28Δ_m4-1BB_CD3z_attB2_hPGK_DsRed2_WPRE) and #218 (CMV_attB1_clone3scFv_mFcΔ_mCD28Δ_m4-1BB_CD3z_attB2_hPGK_DsRed2_WPRE) by co-transfection of HEK 293T cells (see chapter 3.2.9.1). The success of these productions and the determination of lentiviral titers were investigated by transduction of HEK 293T cells with 1 µL of purified and concentrated viral supernatant. The expression levels of these anti-NY-BR-1 CAR constructs in HEK 293T cells were examined by expression analysis of the red fluorescent protein DsRed2 using flow cytometric analysis (see Figure 4.4.1 A). Indeed, the lentiviral production of all three murine CAR constructs was successful and led to expression levels between 11 % and 44 % in HEK 293T cells, indicating differences in the lentiviral titers.

To further investigate the level of anti-NY-BR-1 CAR expression in different human and murine cell lines, Jurkat and NIH / 3T3 cells were lentivirally transduced with the aforementioned CAR constructs at an MOI of 10. Figure 4.4.1 B demonstrates that all three murine CAR constructs were successfully expressed in Jurkat cells upon lentiviral transduction, whereby clone2 and 10D11 CAR$^+$ Jurkat cells exhibited two fold higher DsRed2 expression levels than clone3 CAR$^+$ Jurkat cells. In comparison, transduced NIH / 3T3 cells even showed increased transduction efficiencies of about 95 % for clone2 and clone3 CARs, but decreased expression levels of the 10D11 CAR (30 %).

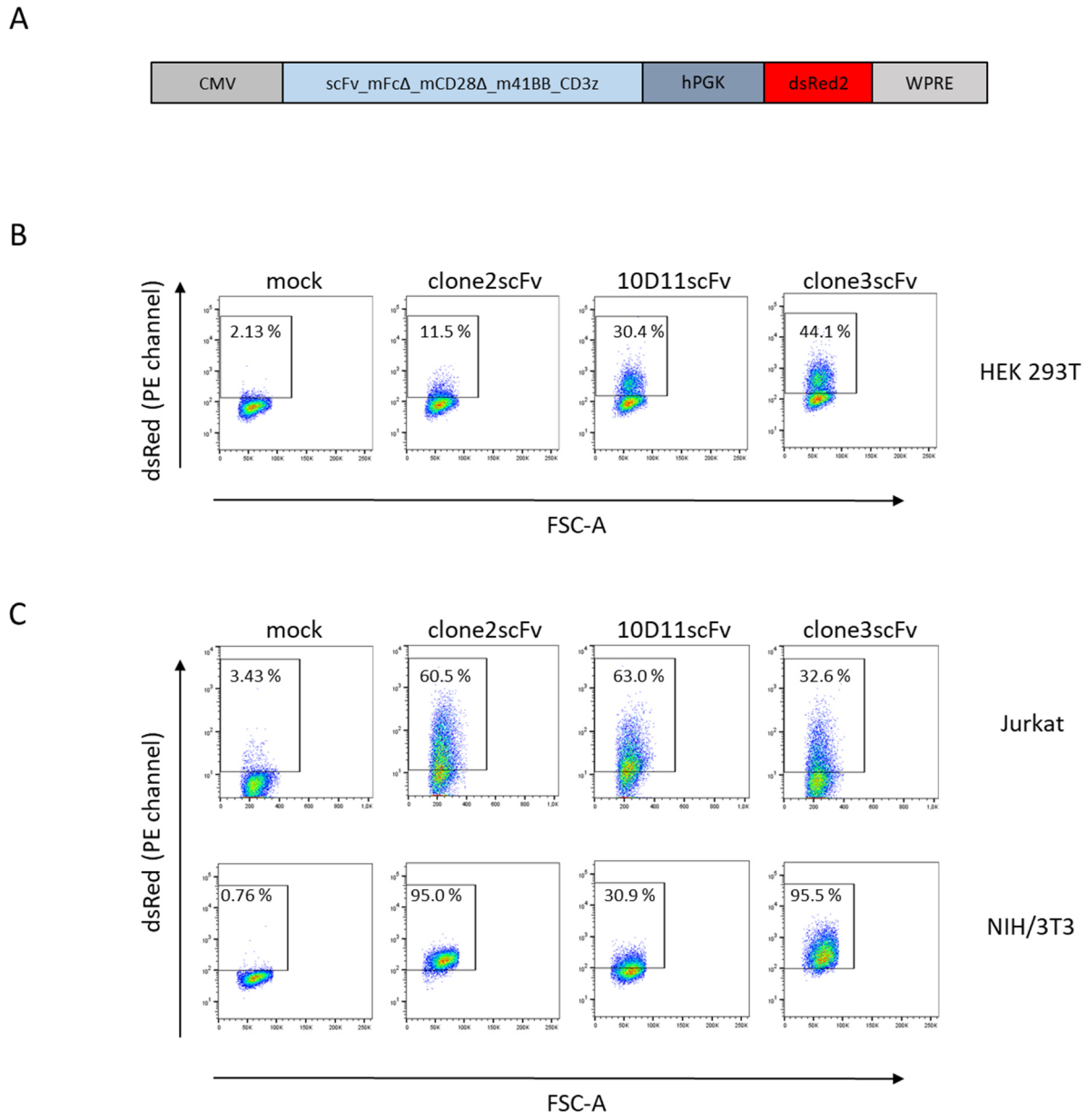

Figure 4.4.1: Expression analysis of murine anti-NY-BR-1 CARs in lentivirally transduced HEK 293T, Jurkat and NIH/3T3 cells
Flow cytometric based quantification of CAR expression levels in HEK 293T, Jurkat and NIH/3T3 cells 72 h following lentiviral transduction with the vectors #216 (CMV_attB1_clone2scFv_mFcΔ_mCD28Δ_m4-1BB_CD3z_attB2_hPGK_DsRed2_WPRE), #217 (CMV_attB1_10D11scFv_mFcΔ_mCD28Δ_m4-1BB_CD3z_attB2_hPGK_DsRed2_WPRE) and #218 (CMV_attB1_clone3scFv_mFcΔ_mCD28Δ_m4-1BB_CD3z_attB2_hPGK_DsRed2_WPRE). [A] HEK 293T cells were lentivirally transduced with 1 µL of concentrated viral supernatant in order to determine the lentiviral titers and to investigate the expression of murine anti-NY-BR-1 CARs in an easily transducible cell line. [B] Jurkat and NIH/3T3 cells were lentivirally transduced at an MOI of 10. In [A] and [B] CAR expression was detected by the DsRed2 signal in the PE channel. Untransduced cells served as controls. The percentages indicate the proportion of DsRed2 expressing cells of the total number of lentivirally transduced cells.

Upon successful lentiviral transduction of human and murine cell lines, the generation of murine CAR - expressing T cells moved into the focus. To address this issue, murine T cells were isolated from (C57BL/6) mouse spleen (see Supplementary Figure 6.2) and lentivirally transduced with the vectors #216, #217 and #218 at an MOI of 5 upon two days of activation. In detail, two distinct protocols, differing in the amount of lentiviral transductions (protocol I one time on day 3, protocol II two times

on day 3 and day 4), were compared regarding CAR expression levels and viability rates by flow cytometry. Since the DsRed2 signal was too weak in murine T cells for flow cytometric analysis, it was necessary to stain T cells with the APC - conjugated anti-mouse IgG antibody, which binds to the Fc domain of the murine CARs, 48 h after transduction.

Repetitions of protocol I and protocol II resulted in different CAR expression and viability rates in independently performed experiments (see Figure 4.4.2). Viability rates between 0.5 and 27 % (clone2 CAR), 0.5 and 40 % (10D11 CAR) or 1 and 48 % (clone3 CAR) were achieved with protocol I. The CAR expression levels varied only slightly between 0 % and 5 %. Using protocol II, lower viability rates (clone2 CAR: 0.2 – 21%; 10D11 CAR: 1.2 – 17 %; clone3 CAR: 0.3 – 16.8 %) but higher CAR expression levels were achieved. In fact, CAR expression levels fluctuated strongly between 2 % and 86 % for all CAR constructs, whereby it should be noted that the different CAR constructs demonstrated similar expression patterns during the same run (see Figure 4.4.2 A, B). Further optimizations such as extended or shortened activation periods or medium compositions did not lead to a significant improvement in expression and viability rates (data not shown).

Thus, lentiviral transduction of murine and human cell lines with murine anti-NY-BR-1 CARs (#216, #217 and #218) led to strong CAR expression levels. However, since murine T cells proved to be difficult to transduce and cultivate, an alternative to lentiviral transduction was required. Therefore, the establishment of a pS/MARter vector based electroporation protocol for murine T cells was considered as another possible approach (see chapter 4.4.2).

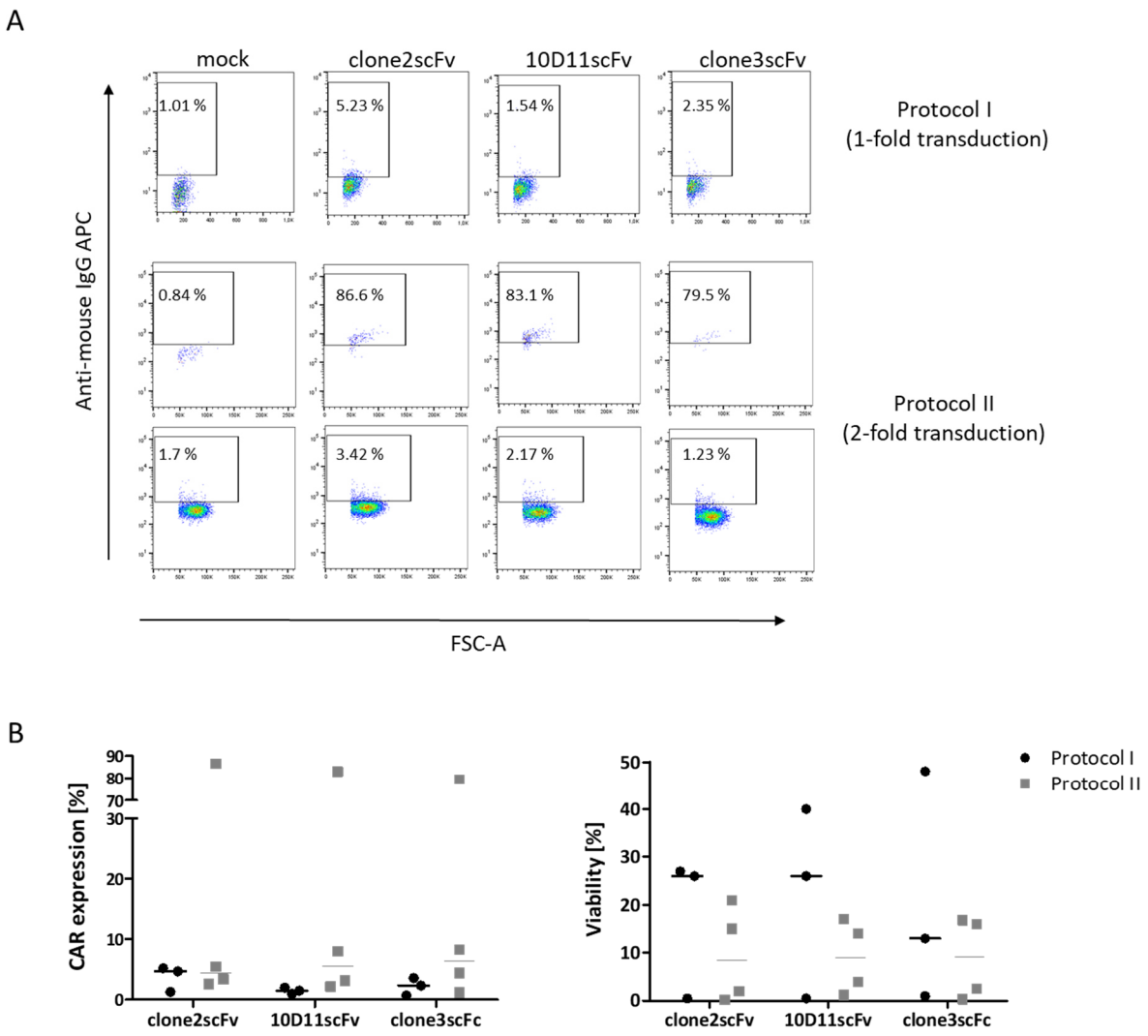

Figure 4.4.2: Expression analysis of murine anti-NY-BR-1 CARs in lentivirally transduced T cells
Murine T cells were isolated from mouse spleens and lentivirally transduced with the vectors #216 (CMV_attB1_clone2scFv_mFcΔ_mCD28Δ_m4-1BB_CD3z_attB2_hPGK_DsRed2_WPRE), #217 (CMV_attB1_10D11scFv_mFcΔ_mCD28Δ_m4-1BB_CD3z_attB2_hPGK_DsRed2_WPRE) and #218 (CMV_attB1_clone3scFv_mFcΔ_mCD28Δ_m4-1BB_CD3z_attB2_hPGK_DsRed2_WPRE) according to two different protocols. In both protocols, murine T cells were stimulated for 48 h prior to lentiviral transduction on day 3 (Protocol I) or two lentiviral transductions on day 3 and day 4 (Protocol II) with an MOI of 5 under the usage of retronectin-coated plates. [A] Representative flow cytometric data of lentivirally transduced T cells, stained with the APC - conjugated anti-mouse IgG antibody, 48 h after transduction. Percentages indicate the proportion of CAR - expressing T cells. Untransduced (mock) T cells served as controls. [B] Lentivirally transduced T cells were stained with both DAPI and the APC - conjugated anti-mouse IgG antibody in order to calculate the CAR expression levels and viability rates 48 h after transduction (lines indicate the medians; protocol I: n=3; protocol II: n=4).

4.4.2 Establishment of a pS/MARter based electroporation system for murine T cells

As the pS/MARter based electroporation system proved to be an effective alternative to lentiviral transduction for the generation of human CAR$^+$ T cells, it should now be applied to murine T cells, which have been particularly resistant to cultivation and lentivirally transduction in the past (see chapters 4.3.2, 4.4.1). However, the establishment of a suitable protocol included the optimization of the cultivation medium, time point for electroporation and electroporation in itself.

At the beginning, murine T cells were isolated from (C57BL/6) mouse spleens and cultivated in RPMI-1640 medium supplemented with 10 % FCS, IL-2 (100 IU / mL), L-glutamine (2 mM), non-essential amino acids (1x), anti-CD3 Ab (100 ng / mL) and anti-CD28 Ab (100 ng/ mL) for 24 h prior to electroporation with the pS/MARter construct #277 (clone2scFv_mFcΔ_mCD28Δ_m4-1BB_CD3z) using the Neon Transfection System (ThermoFisher) according to different protocols varying in voltage, number of pulses and pulse length. Following electroporation, T cells were cultivated in RPMI-1640 medium (w / o Phenol red) supplemented with 20 % FCS, IL-2 (100 IU / mL) and L-glutamine (2mM) for 24 h. Subsequently, the medium was exchanged with the standard cultivation medium, as described above, but without anti-CD3 and anti-CD28 antibodies. The efficiency of electroporation and the corresponding viability rates of CAR$^+$ T cells were determined by flow cytometric analysis one, two and six days after electroporation. Here, T cells were stained with DAPI and the APC - conjugated anti-mouse IgG antibody. Untransfected (mock) T cells served as controls.

As shown in Figure 4.4.3 A, all tested protocols led to surface expression of anti-NY-BR-1 clone2 CAR in murine T cells. However, different protocols provoked different CAR expression levels and viability rates. One day after electroporation, protocol IV showed the best results with CAR expression levels of about 22 %, followed by protocol III with 10 %, protocol I with 5 % and protocol II with 1 %. With the exception of protocol II, the CAR expression levels continued to rise to almost 30 % or more until the following day. On day 6, high frequencies of CAR - expressing T cells were still detectable when protocol III or IV were applied, suggesting a stable CAR transfection of murine T cells. In terms of viability rates of electroporated T cells, all protocols (except protocol II) resulted in a strong reduction in viability 24 and 48 h post electroporation compared to untransfected T cells (see Figure 4.4.3 B). On day 6, the viability levels of electroporated T cells were almost similar to those of untransfected cells. Surprisingly, CAR$^+$ T cells electroporated according to protocol IV exhibited even higher viability levels than untransfected cells on day 6. Overall, protocol III and IV seemed most suitable for the generation of murine CAR$^+$ T cells. In particular, protocol IV stood out with high CAR expression levels but simultaneously low viability rates one day post electroporation. However, electroporation with 2000 V combined with one or two pulses led to higher viability but lower

expression rates (data not shown). Based on these first electroporation experiments, the composition of the cultivation medium and the electroporation process were optimized in the further course of protocol establishment.

Since both electroporated and untransfected murine T cells showed very low viability rates after long cultivation periods (see Figure 4.4.3 A), it was investigated whether an exchange of IL-2 with IL-15 or increased concentrations of the anti-CD3 and anti-CD28 antibodies influences the survival of murine T cells. Therefore, untransfected T cells were cultivated in RPMI-1640 medium supplemented with anti-CD3 Ab (100 ng/ mL), anti-CD28 Ab (100 ng / mL), L-glutamine (2 mM) and non-essential amino acids (1x). In addition, different ingredients were added such as IL-2 (100 IU / mL), IL-15 (5 ng / mL) and ß-mercaptoethanol (50 µM) or/and increased concentrations of the anti-CD3 (2 µg / mL) and anti-CD28 (1 µg / mL) antibodies were used. After a cultivation period of 48 h, the viability rates of untransfected T cells were determined by flow cytometric analysis. As summarized in Figure 4.4.3 C, an exchange of IL-2 with IL-15 had a negative impact on cell viability rates, whereas, simultaneous application of IL-2 and ß-mercaptoethanol improved the viability of murine T cells compared to those cultivated with IL-2 only. After testing several combinations of cytokines and additives, the best results were achieved under increased anti-CD3 and anti-CD28 concentrations combined with the application of IL-2 and ß-mercaptoethanol.

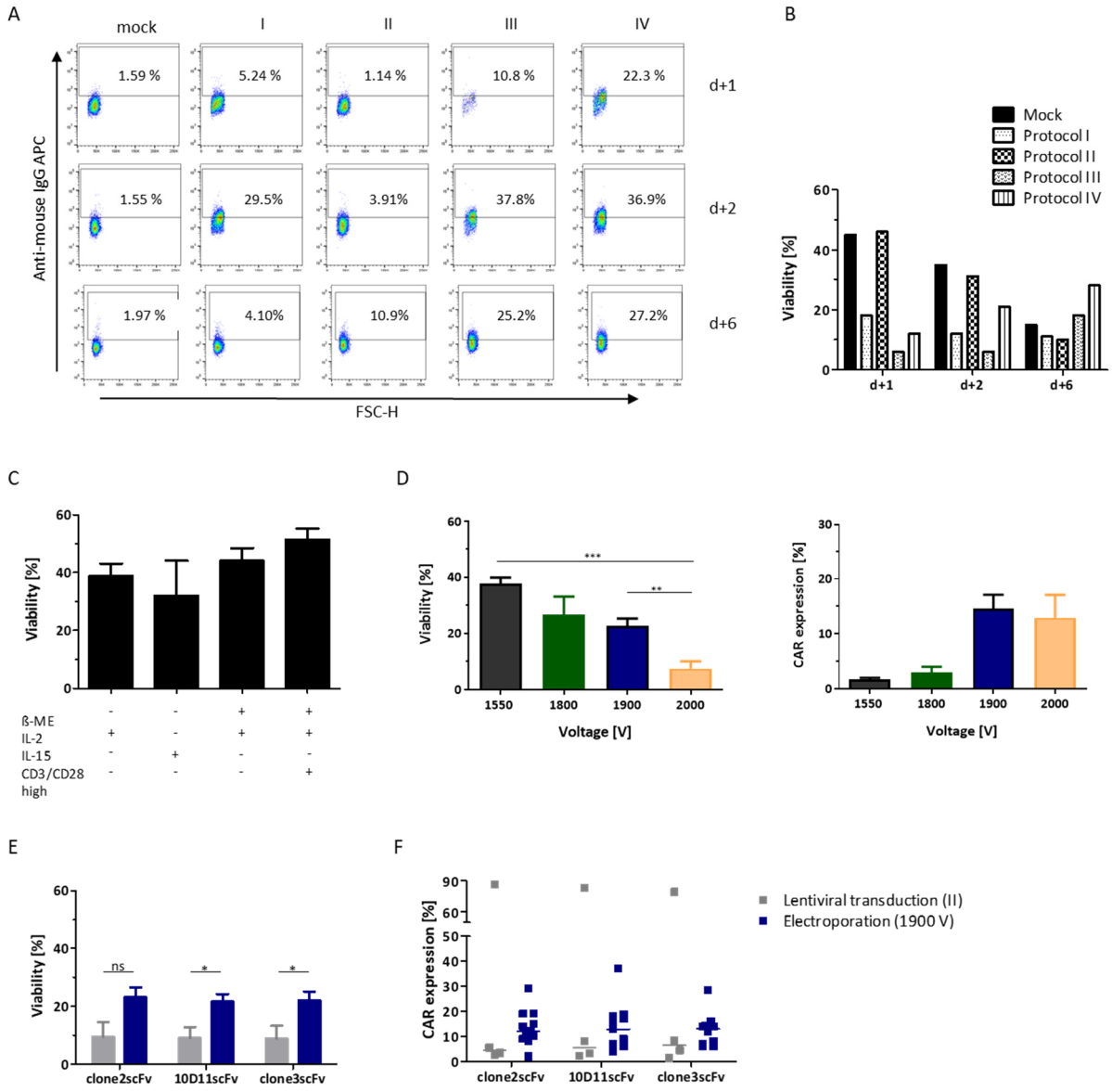

Figure 4.4.3: Generation of murine anti-NY-BR-1 CAR - expressing T cells by electroporation with pS/MARter vectors
Different electroporation protocols had to be evaluated and compared with lentiviral transductions. Following activation, murine T cells were electroporated with the pS/MARter vectors #277 (clone2scFv_mFcΔ_mCD28Δ_m4-1BB_CD3z), #295 (10D11scFv_mFcΔ_mCD28Δ_m4-1BB_CD3z) and #296 (clone3scFv_mFcΔ_mCD28Δ_m4-1BB_CD3z) by using the Neon Transfection system (ThermoFisher) or lentivirally transduced with the vectors #216 (CMV_attB1_clone2scFv_mFcΔ_mCD28Δ_m4-1BB_CD3z_attB2_hPGK_DsRed2_WPRE), #217 (CMV_attB1_10D11scFv_mFcΔ_mCD28Δ_m4-1BB_CD3z_attB2_hPGK_DsRed2_WPRE) and #218 (CMV_attB1_clone3scFv_mFcΔ_mCD28Δ_m4-1BB_CD3z_attB2_hPGK_DsRed2_WPRE). [A] Data represent the CAR expression levels in murine T cells one, two or six days upon electroporation with the pS/MARter vector #277. Four different electroporation protocols (Protocol I: 1550 V, 10ms, 3 pulses; II: 1080 V, 50 ms, 1 pulse; III: 1550 V, 30 ms, 1 pulse; IV: 2000 V, 10 ms, 3 pulses) were compared. Untransfected (mock) T cells served as controls. T cells were cultivated in RPMI-1640 medium supplemented with IL-2 (100 IU / mL), L-glutamine (2 mM), non-essential amino acids (1x), anti-CD3 Ab (100 ng / mL) and anti-CD28 Ab (100 ng / mL) prior to electroporation. Following electroporation, T cells were cultivated in RPMI-1640 medium (w / o Phenol red) supplemented with 20 % FCS, IL-2 (100 IU / mL) and L-glutamine (2mM) for 24 h. Subsequently, the medium was exchanged with the standard cultivation medium but without anti-CD3 and anti-CD28 antibodies [B] Corresponding viability rates are illustrated as bar graphs. [C] Viability rates of untransfected (mock) T cells after 48 h cultivation in RPMI-1640 medium (+ L-glutamine (2 mM), non-essential amino acids (1x)) supplemented with normal or high concentrations of anti-CD3 (100 ng / mL; 2 µg / mL) and anti-CD28 (100 ng / mL; 1 µg / mL) antibodies, ß-mercaptoethanol (50 µM) and IL-2 (100 IU / mL) or IL-15 (5ng / mL) (mean values ± sem; +IL-2: n = 2; +IL-15: n = 2; +ß-ME/IL-2: n = 7; +ß-ME/IL2/CD3/CD28high: n = 13). [D] T cells were cultivated in RPMI medium supplemented with ß-mercaptoethanol (50 µM), IL-2 (100 IU / mL), anti-CD3 (2 µg / mL) and anti-CD28 (1 µg / mL) antibodies, L-glutamine (2 mM) and non-essential amino acids (1x) for 24 h. Electroporation was performed according to different protocols (1550V, 1800V, 1900 V or 2000 V; always 10ms and 3 pulses per transfection) with the pS/MARter vector #277. Following electroporation, T cells were cultivated in

RPMI-1640 medium (w / o Phenol red) supplemented with 20 % FCS, IL-2 (100 IU / mL) and L-glutamine (2mM) for 24 h. Viability and CAR expression rates were determined 24 h after electroporation. The statistically significant differences are indicated by asterisks (mean values ± sem; 1500 V: n = 3; 1800 V: n = 2; 1900 V: n = 15; 2000 V: n = 6; **, $p < 0.01$; ***, $p \leq 0.0005$; one-way ANOVA followed by Tukey's multiple comparison test). Data display the viability [E] and CAR expression rates [F] of T cells two days after lentiviral transduction with the vectors #216, #217 and #218 according to protocol II (grey) and one day post electroporation (1900 V, 10ms, 3 pulses) with the vectors #277, #295 and #296 (blue) (electr. clone2, 10D11 CAR: n = 11; electr. clone3 CAR: n = 10; Lent. transd: n = 4), as described in [D]. [E] The statistically significant differences are indicated by asterisks (means ± sem; *, $p < 0.05$, unpaired two-tailed Student's t-test). Lines in [F] indicate the medians. [A] – [F] CAR expression levels were determined by staining with APC or PE - conjugated anti-mouse IgG antibodies. Viability rates were calculated by DAPI staining and flow cytometric analysis.

Next, the influence of different voltages on viability and CAR expression levels in murine T cells was explored in more detail. In these experiments, the variables of pulse length and pulse quantity were held constant at 10ms and 3, respectively. To address this issue, murine T cells were cultivated with the best optimized, above mentioned cultivation medium for 24 h, electroporated with the pS/MARter vector #277 by using different voltages (between 1550 V and 2000 V) and examined with respect to cell viability and CAR expression rates 24 h after electroporation by flow cytometry (see Figure 4.4.3 D, E). As already observed in preliminary experiments in Figure 4.4.3 A, increasing voltages led to lower survival but improved CAR expression levels. The optimal ratio of CAR expression and survival rates was achieved at 1900 V (see Figure 4.4.3 D, E; Supplementary Figure 6.5). To confirm these results, murine T cells were electroporated with 10D11 and clone3 CARs at 1900 V as well and, indeed, demonstrated similar CAR expression and survival rates as clone2 CAR^+ T cells (see Figure 4.4.3 E). However, the viability of CAR^+ T cells decreased within a few days after electroporation, so that murine T cells should be used as soon as possible for further assays (see Supplementary Figure 6.5).

Finally, the two different approaches – lentiviral transduction vs electroporation – were compared in terms of transfection efficiency and cell viability (see Figure 4.4.3 E, F). The comparison of both methods (with the respective best protocols) revealed that electroporation led to significantly improved viability as well as increased or rather more reliable CAR expression rates compared to lentiviral transduction. In addition, electroporated T cells exhibited CAR expression already one day post electroporation, in contrast to two days for lentivirally transduced T cells.

4.4.3 Elimination of NY-BR-1$^+$ EO771 cells by murine anti-NY-BR-1 CAR - expressing T cells

Following successful generation of murine CAR - expressing T cells by electroporation, the functional efficiencies of murine clone2, 10D11 and clone3 CARs against NY-BR-1 expressing target cells was investigated in this chapter.

First, NY-BR-1 transduced EO771 cells (see chapter 4.1.2) were pre-treated with Lactacystin for 24 to 48 h in order to increase NY-BR-1 surface expression (see chapter 4.1.2.1). Subsequently, (NY-BR-1$^+$) EO771 cells were labeled with CFSE, as described in chapter 3.2.14, and co-cultivated with murine untransfected (mock) or CAR$^+$ T cells, generated by electroporation with pS/MARter vectors encoding the anti-NY-BR-1 CAR constructs #277 (clone2scFv_mFcΔ_mCD28Δ_m4-1BB_CD3z), #295 (10D11scFv_mFcΔ_mCD28Δ_m4-1BB_CD3z) and #296 (clone3scFv_mFcΔ_mCD28Δ_m4-1BB_CD3z), at a ratio of 1:1 for 24 h. The killing efficiency was determined by DAPI staining and flow cytometric analysis (see Figure 4.4.4).

The exemplary flow cytometric data in Figure 4.4.4 A and summarized viability rates of CAR$^+$ T cell co-cultivated (NY-BR-1$^+$) EO771 cells in Figure 4.4.4 B illustrated significantly reduced viability rates of NY-BR-1$^+$ EO771 but not wild-type EO771 cells upon co-cultivation with CAR$^+$ T cells, whereby the killing efficiencies of all three CAR candidates were nearly equal. In fact, the viability rates of NY-BR-1$^+$ EO771 cells, co-cultured with CAR$^+$ T cells, were decreased by an average of 25 % compared to those co-cultivated with mock T cells, which corresponded to the average proportion of NY-BR-1 expressing EO771 cells (5 – 30 %) upon Lactacystin treatment (see chapter 4.1.2.1). In order to assess the activation level of murine CAR$^+$ T cells after co-cultivation with NY-BR-1$^+$ EO771 cells, various analyses including investigation of CD69 expression as well as the determination of IFNγ concentrations in the cell culture supernatant were performed (see Supplementary Figure 6.6). However, following electroporation, murine CAR$^+$ T cells showed such high levels of activation, independent of co-cultivation, that no statistically significant differences were detectable between monocultured and (NY-BR-1$^+$) EO771 co-cultured CAR$^+$ T cells.

Nevertheless, these data demonstrated that all three murine CAR candidates detected and eliminated NY-BR-1 expressing target cells.

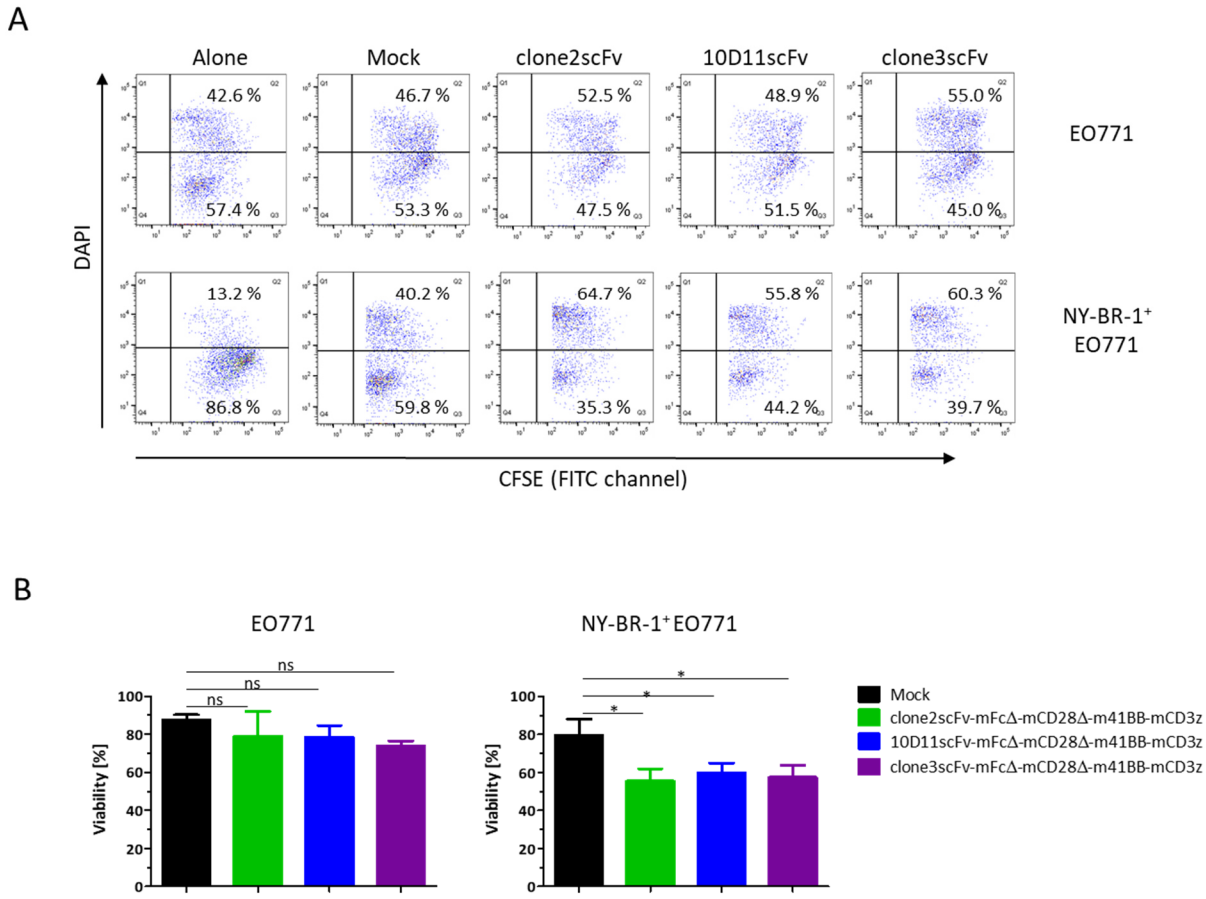

Figure 4.4.4: NY-BR-1⁺ EO771 cells were eliminated by murine anti-NY-BR-1 CAR - expressing T cells
CFSE based killing assay of murine anti-NY-BR-1 CAR - expressing T cells. Isolated murine T cells were electroporated with pS/MARter vectors encoding the anti-NY-BR-1 CAR constructs #277 (clone2scFv_mFcΔ_mCD28Δ_m4-1BB_CD3z), #295 (10D11scFv_mFcΔ_mCD28Δ_m4-1BB_CD3z) and #296 (clone3scFv_mFcΔ_mCD28Δ_m4-1BB_CD3z) and subsequently co-cultivated with CFSE labeled, Lactacystin pre-treated (NY-BR-1⁺) EO771 cells at a ratio of 1:1 in 96 well plates for 24 h. Untransfected (mock) T cells were used as controls. [A] Representative flow cytometric data of CFSE labeled (NY-BR-1⁺) EO771 cells after 24 h co-cultivation with murine CAR⁺ T cells. Percentages indicate the proportion of living (DAPI⁻) and dead (DAPI⁺) cells of the total number of CFSE labeled cells. [B] Viability rates of (NY-BR-1⁺) EO771 cells upon co-cultivation with murine CAR⁺ T cells in independently performed experiments. Viability rates were calculated in relation to untreated (NY-BR-1⁺) EO771 cells (mean values ± sem; EO771: n = 3; NY-BR-1⁺ EO771: n = 4; *, $p < 0.05$; one-way ANOVA followed by Holm-Sidak's multiple comparison test).

4.5 Preclinical safety and persistence of murine anti-NY-BR-1 CARs *in vivo*

The results of the last chapters demonstrated that human and murine anti-NY-BR-1 CAR constructs initiated immune responses against NY-BR-1 expressing target cells in diverse *in vitro* experiments. The following experiments were focusing on the questions whether these CAR constructs persist in C57BL/6 wild-type (wt) and NY-BR-1$^{tg/-}$ mice and to what extent they might contribute to toxic immune responses. In addition to the safety aspect, the remaining functionality of those CAR$^+$ T cells was further examined in *ex vivo* assays.

4.5.1 pS/MARter electroporated murine anti-NY-BR-1 CAR - expressing T cells persist in C57BL/6 and NY-BR-1$^{tg/-}$ mice without toxic side effects and remain functional

Murine T cells were isolated from C57BL/6 wt mice, electroporated with the pS/MARter vectors #277 (clone2scFv_mFcΔ_mCD28Δ_m4-1BB_CD3z), #295 (10D11scFv_mFcΔ_mCD28Δ_m4-1BB_CD3z) and #296 (clone3scFv_mFcΔ_mCD28Δ_m4-1BB_CD3z) and injected intravenously in C57BL/6 wt and NY-BR-1$^{tg/-}$ mice (5x10^5 CAR$^+$ T cells / mouse), which were subsequently monitored for any side effects such as behavioral abnormalities and weight loss over a period of 14 days, as illustrated in Figure 4.5.1 A. Subsequently, flow cytometric analysis of spleens and blood were performed in order to detect persisting CAR$^+$ T cells by co-staining with the APC - conjugated anti-mouse CD3 (17A2) and PE - conjugated anti-mouse IgG antibodies. Moreover, plasma cytokine concentrations were measured by using the Mouse 12-Plex Cytokine Kit (Ayoxxa) and different organs were examined for inflammatory processes or T cell infiltration by immunohistochemistry analysis.

Indeed, murine CAR$^+$ T cells were detected in spleens of CAR$^+$ T cell - treated C57BL/6 wt and NY-BR-1$^{tg/-}$ mice (see Figure 4.5.1 B, C), whereby the latter exhibited significantly higher frequencies of CAR$^+$ T cells. Additionally, clone2 and 10D11 CAR$^+$ T cell - treated C57BL/6 wt and NY-BR-1$^{tg/-}$ mice demonstrated higher proportions of CAR$^+$ T cells than those treated with clone3 CAR$^+$ T cells. Enhanced accumulation of CAR$^+$ T cells was also found in the blood of clone2 but not 10D11 or clone3 CAR$^+$ T cell treated NY-BR-1$^{tg/-}$ mice (see Figure 4.5.1 D). However, the peripheral blood of two mice each in 10D11 and clone3 C57BL/6 wt group evidenced low to moderate proportions of CAR$^+$ T cells.

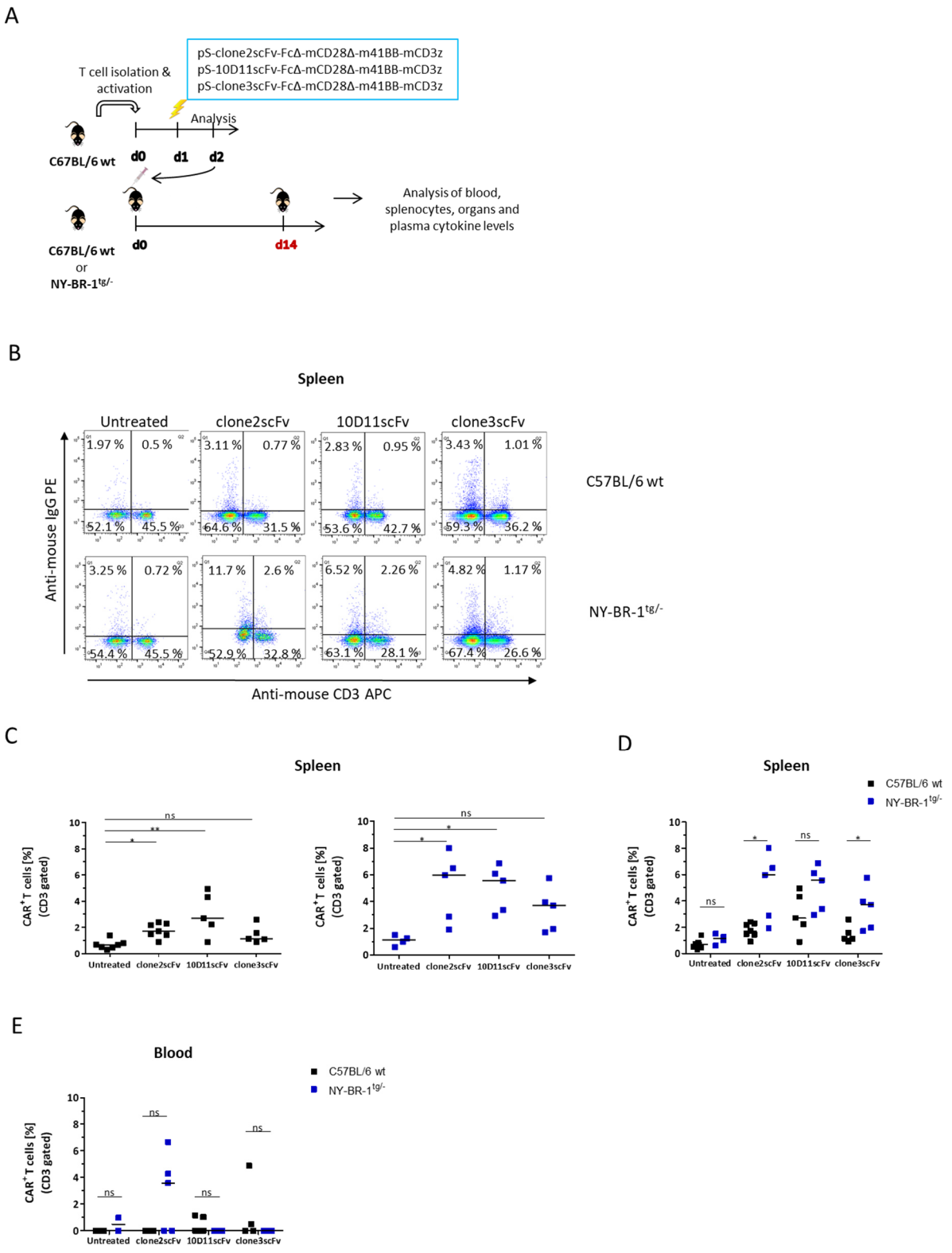

Figure 4.5.1: Murine anti-NY-BR-1 CAR⁺ T cells persist in C57BL/6 wt and NY-BR-1$^{tg/-}$ mice
[A] Murine T cells were isolated from C57BL/6 wt mice, electroporated with the pS/MARter vectors #277 (clone2scFv_mFcΔ_mCD28Δ_m4-1BB_CD3z), #295 (10D11scFv_mFcΔ_mCD28Δ_m4-1BB_CD3z) and #296 (clone3scFv_mFcΔ_mCD28Δ_m4-1BB_CD3z) and injected intravenously into C57BL/6 and NY-BR-1$^{tg/-}$ mice (5x10^5 CAR⁺ T cells / mouse) one day after electroporation. 14 days post CAR⁺ T cell engraftment [B], [C], [D] spleens and [E] blood were analyzed for persistence of CAR⁺ T cells by flow cytometric analysis. Cells were stained with the PE - conjugated anti-mouse IgG and APC - conjugated anti-mouse CD3 (17A2) antibodies. [C], [D] Percentages indicate the proportion of CAR⁺ T cells after gating on living CD3⁺ splenocytes (lines indicate the medians; C57BL/6: untreated, clone2 CAR n = 7; 10D11 CAR, clone3 CAR: n = 5; NY-BR-1$^{tg/-}$: untreated n = 4; clone2scFv, 10D11scFv, clone3scFv n= 5; * , p < 0.05; **, p < 0.005; Kruskal-Wallis test followed by Dunn's multiple comparison test in [C]; * , p < 0.05; two-tailed Mann-Whitney-U-test in [D]. [E] Percentages

indicate the proportion of CAR$^+$ T cells after gating on living CD3$^+$ blood cells (lines indicate the medians; C57BL/6: untreated, 10D11 CAR, clone3 CAR: n = 5, clone2 CAR n = 7; NY-BR-1$^{tg/-}$: untreated n = 2; clone2, 10D11 , clone3 CAR n= 5; no statistically significant differences according to two-tailed Mann-Whitney-U-test).

In addition, strongly enhanced levels of pro-inflammatory cytokines such as IL-1ß, IL-2, IFNγ, TNFα, IL-6 and IL-12 and of anti-inflammatory cytokines such as IL-4, IL-10 or IL-13 were detected in the plasma of clone2 CAR$^+$ T cell - treated NY-BR-1$^{tg/-}$ mice compared to both untreated NY-BR-1$^{tg/-}$ mice and clone2 CAR$^+$ T cell - treated C57BL/6 wt mice (see Figure 4.5.2 A). However, plasma cytokine levels remained always below toxic thresholds. In comparison, two 10D11 CAR$^+$ T cell - treated NY-BR-1$^{tg/-}$ mice showed occasionally slightly increased levels of IL-1ß, IFNγ, IL-2, IL-4, IL-6, IL-10 and IL-12, while similarly treated C57BL/6 wt mice showed almost no changes. With the exception of the cytokine IL-10, the clone3 CAR$^+$ T cell treatment did not result in significantly elevated cytokine levels in C57BL/6 wt and NY-BR-1$^{tg/-}$ mice compared to untreated mice.

In addition to the examination of plasma cytokine levels, the body weights and condition of all organs were examined during and post CAR$^+$ T cell therapy. The body weights of all CAR$^+$ T cell - treated mice remained almost constant during the observation period of 14 days and the organs (e.g. lung, heart, mammary gl., salivary gl., brain, stomach, small intestine, large intestine, skin, kidney, thymus, spleen) did not show any sights of inflammatory processes (data not shown). Nevertheless, due to the strongly enhanced plasma cytokine levels in clone2 CAR$^+$ T treated NY-BR-1$^{tg/-}$ mice, the organs of one mouse, which indicated highly increased cytokine levels, were examined for excessive T cell infiltration by immunohistochemical stainings. At DNA level, the NY-BR-1 transgene was detected in nearly all organs of transgenic mice (see Supplementary Figure 6.7). Since previous attempts have shown that high *NY-BR-1* RNA expression levels were especially detectable in the mammary glands, lung or salivary glands of NY-BR-1$^{tg/-}$ mice (unpublished data), these organs were of particular interest. A selection of the investigated organs is given in Figure 4.5.2 B. Surprisingly, clone2 CAR$^+$ T cell therapy did not provoke increased T cell infiltrations into the investigated organs (e.g. lung, heart, mammary gl., salivary gl., brain, stomach, small intestine, large intestine, skin, kidney, thymus, spleen) compared to untreated NY-BR-1$^{tg/-}$ mice (see Figure 4.5.2 B). Unfortunately, a protocol for the detection of NY-BR-1 protein in the organs of NY-BR-1$^{tg/-}$ mice using immunohistochemical stainings and the monoclonal antibodies clone2, 10D11 or clone3 was not successfully established (data not shown).

Overall, these experiments demonstrated that murine anti-NY-BR-1 CAR - expressing T cells, generated by electroporation with pS/MARter vectors, persisted in C57BL/6 wt and especially in NY-BR-1$^{tg/-}$ mice without inducing any toxic side effects.

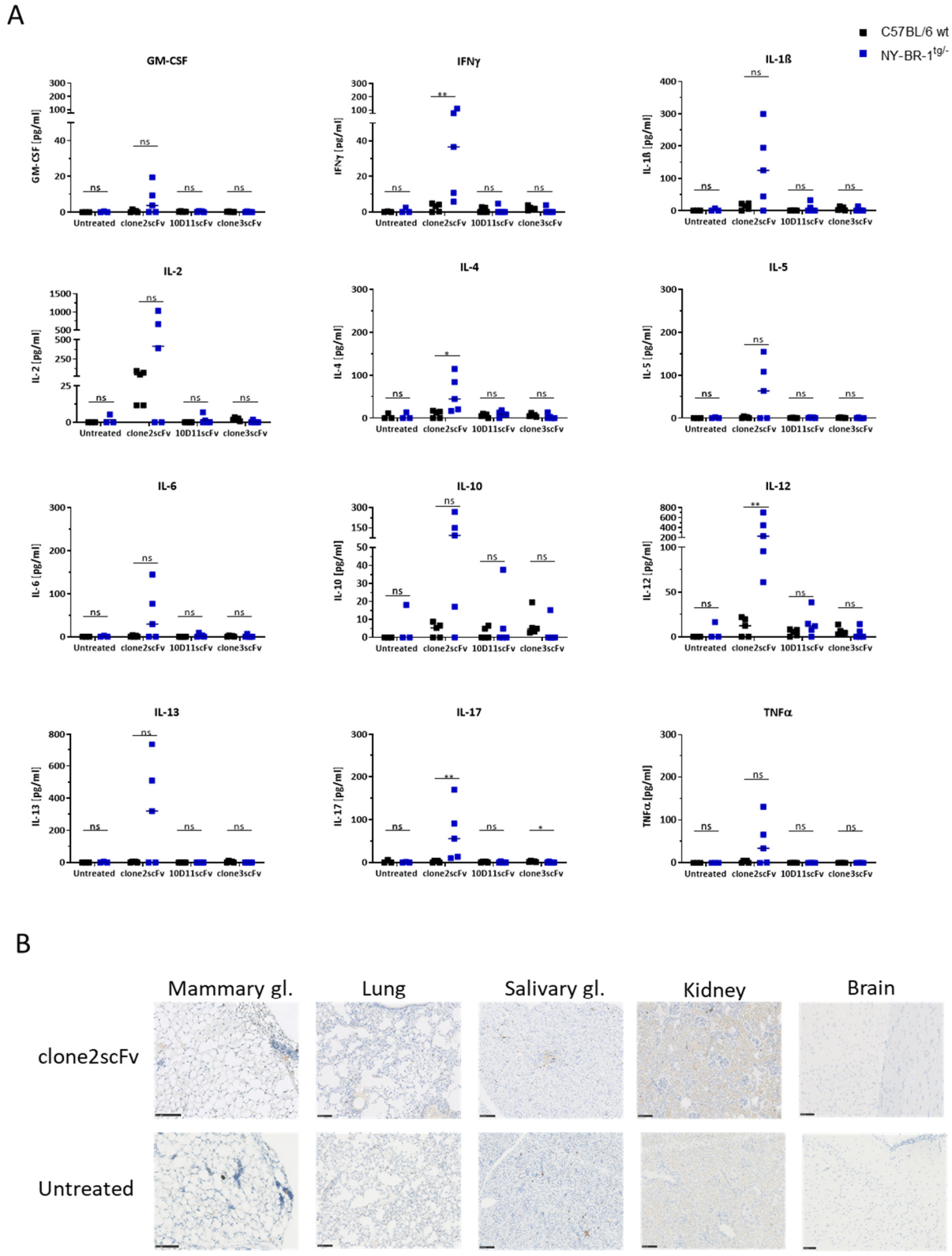

Figure 4.5.2: Plasma cytokine concentrations and T cell infiltration in different organs of C57BL/6 wt and NY-BR-1$^{tg/-}$ mice upon CAR$^+$ T cell engraftment

C57BL/6 wt and NY-BR-1$^{tg/-}$ mice were engrafted with anti-NY-BR-1 CAR$^+$ T cells (5x10^5 CAR$^+$ T cells / mouse) which were generated by electroporation with the pS/MARter vectors #277 (clone2scFv_mFcΔ_mCD28Δ_m4-1BB_CD3z), #295 (10D11scFv_mFcΔ_mCD28Δ_m4-1BB_CD3z) and #296 (clone3scFv_mFcΔ_mCD28Δ_m4-1BB_CD3z). [A] 14 days after CAR$^+$ T cell injection, cytokine concentrations in mouse plasma were determined by using the Mouse 12-Plex Cytokine Kit (Ayoxxa) (lines indicate the medians; untreated: n = 3; clone2, 10D11, clone3 CAR: n = 5; * , $p < 0.05$; ** , $p < 0.01$; two-tailed Mann Whitney-U-test). [B] Additionally, paraffin-embedded sections from different organs of untreated and clone2 CAR$^+$ T cell - treated NY-BR-1$^{tg/-}$ mice were prepared and, subsequently, analyzed for T cell infiltration by staining with the rabbit

anti-mouse CD3 (Abcam, 16669) and HRP - conjugated anti-rabbit IgG antibodies (staining was performed by Rosa Eurich). Scale bars present 100 µm.

To confirm the persistence and antigen specific activation of those CAR$^+$ T cells, an *ex vivo* killing assay was designed. In this assay, splenocytes of C57BL/6 wt and NY-BR-1$^{tg/-}$ mice, engrafted with pS/MARter (#277, #295, #296) electroporated murine CAR$^+$ T cells (5x10^5 CAR$^+$ T cells / mouse) or untransfected (mock) T cells, were isolated, analyzed for CAR$^+$ T cell persistence and co-cultivated with both EO771 and NY-BR-1$^+$ EO771 cells at a ratio of 1:1 for 24 h (see chapter 3.2.15; Figure 4.5.3 A). Subsequently, the killing efficiency was determined by DAPI staining and flow cytometric analysis. The cells were additionally stained with the APC - conjugated anti-mouse CD3 antibody (17A2) in order to distinguish murine T cells and EO771 cells. Moreover, the activation level of co-cultivated murine T cells was analyzed by intracellular staining for IFNγ, TNFα and GrB combined with extracellular staining for CD4 and CD8.

Indeed, splenocytes / CAR$^+$ T cells from both CAR$^+$ T cell - treated C57BL/6 wt and NY-BR-1$^{tg/-}$ mice induced efficient killing of NY-BR-1$^+$ EO771 cells (see Figure 4.5.3 B). As the killing efficiency of splenocytes isolated from CAR$^+$ T cell treated C57BL/6 wt did not differ from those isolated from CAR$^+$ T cell treated NY-BR-1$^{tg/-}$ mice, their killing efficiencies were summarized in the appropriate scatter plots in Figure 4.5.3 B. In particular, splenocytes / CAR$^+$ T cells from 10D11 CAR$^+$ T cell - treated mice led to significantly reduced viability rates of NY-BR-1$^+$ EO771 cells compared to mock treated cells. Similarly, splenocytes / CAR$^+$ T cells from three out of four clone2 CAR$^+$ T cell – treated mice provoked decreased viability rates of NY-BR-1$^+$ EO771 cells. These effects were not observed in co-cultivation with EO771 cells, reflecting again the specificity of anti-NY-BR-1 (clone2, 10D11) CAR$^+$ T cells for the NY-BR-1 protein. In contrast, splenocytes containing the persisted clone3 CAR$^+$ T cells provoked slightly decreased viability rates of both EO771 and NY-BR-1$^+$ EO771 cells, which, however, did not differ significantly from mock treated (NY-BR-1$^+$) EO771 cells (see Figure 4.5.3 B).

Despite highly increased mortality of NY-BR-1$^+$ EO771 cells following co-cultivation with clone2 and 10D11 CAR$^+$ T cell containing splenocytes, those T cells did not exhibit significantly increased intracellular expression levels of IFNγ, TNFα and GrB compared to co-cultivation with wild-type EO771 cells, according to the Wilcoxon matched-pairs signed ranked test (see Figure 4.5.3 C). Nevertheless, CD4$^+$ T cells derived from 10D11 CAR$^+$ T cell - treated mice showed slightly increased frequencies of TNFα, IFNγ and GrB producing cells after co-cultivation with NY-BR-1$^+$ EO771 cells compared to co-cultivation with EO771 cells. In addition, the proportion of CD8$^+$ GrB$^+$ cells was also slightly increased in those T cell populations. By comparison, T cells derived from clone2 CAR$^+$ T cell - treated mice showed lower frequencies of activated T cells, which is consistent with the different killing efficiencies shown in Figure 4.5.3 B. In contrast, T cells derived from clone3 CAR$^+$ T cell - treated mice did not

exhibit elevated activation potentials upon co-cultivation with wild-type EO771 and NY-BR-1^{+} EO771 cells compared to mock T cells.

Taken together, these experiments demonstrated that persistent murine pS/MARter electroporated anti-NY-BR-1 CAR^{+} T cells, especially 10D11 CAR^{+} T cells, remained functional and capable of specifically eliminating NY-BR-1 expressing target cells *ex vivo.*

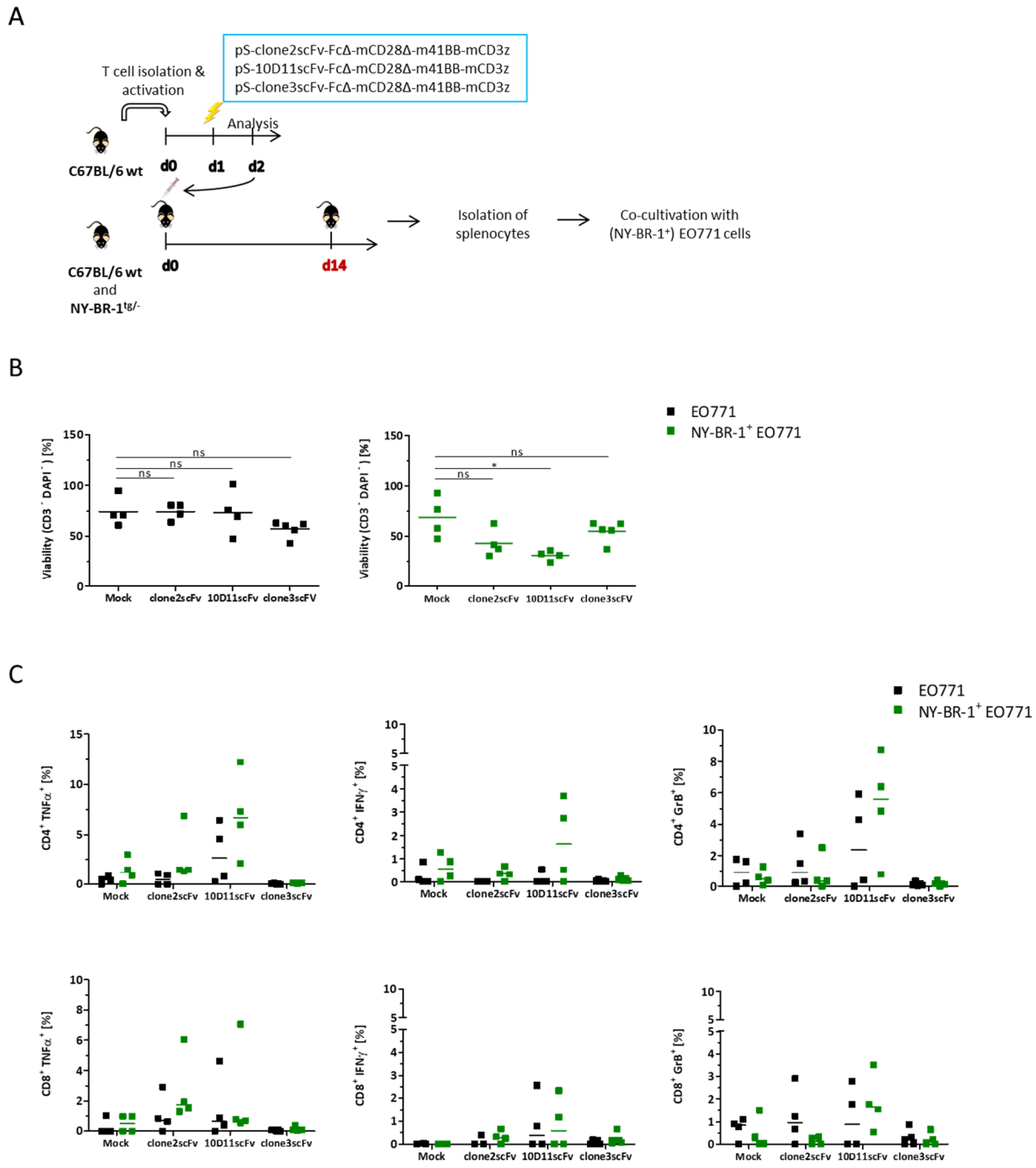

Figure 4.5.3: Functional analysis of anti-NY-BR-1 CAR^{+} T cells obtained from the spleens of treated C57BL/6 wt and NY-BR-1$^{tg/-}$ mice

[A] Splenocytes were isolated from C57BL/6 wt and NY-BR-1$^{tg/-}$ mice 14 days after engraftment with anti-NY-BR-1 CAR^{+} T cells (5x10^{5} CAR^{+} T cells / mouse) generated by electroporation with the pS/MARter vectors #277 (clone2scFv_mFcΔ_mCD28Δ_m4-1BB_CD3z), #295 (10D11scFv_mFcΔ_mCD28Δ_m4-1BB_CD3z) and #296 (clone3scFv_mFcΔ_mCD28Δ_m4-1BB_CD3z) and analyzed for CAR^{+} T cell persistence via flow cytometry. Afterwards, CAR^{+}

T cell containing splenocytes of each mouse were co-cultivated with both EO771 and NY-BR-1$^+$ EO771 cells at a ratio of 1:1 for 24 h. Splenocytes from mock treated mice were used as controls. [B] Viability rates of splenocyte / CAR$^+$ T cell co-cultivated (NY-BR-1$^+$) EO771 cells was analyzed by using flow cytometric analysis. The discrimination between (NY-BR-1$^+$) EO771 and splenocytes / T cells was done by staining with the APC - conjugated anti-mouse CD3 antibody (17A2). The viability was determined by DAPI staining. Percentages correspond to the proportion of living CD3 negative cells in relation to untreated (NY-BR-1$^+$) EO771 cells. Lines indicate the medians (mock, clone2, 10D11 CAR: n = 4; clone3 CAR: n = 5; *, $p < 0.05$; Kruskal Wallis test followed by Dunn's multiple comparison test). [C] Intracellular cytokine production of splenocytes / CAR$^+$ T cells co-cultivated with Lactacystin-treated (NY-BR-1$^+$) EO771, determined by using flow cytometric analysis. Cells were stained with the FITC - conjugated anti-mouse CD4, PerCp-Cy5.5 - conjugated anti-mouse CD8, APC - conjugated anti-mouse IFNγ, PE-Cγ7 - conjugated anti-mouse TNFα and the Pacificblue - conjugated anti-GranzymeB (GrB) antibodies. Percentages indicate the proportions of TNFα$^+$, IFNγ$^+$ and GrB$^+$ cells upon gating on CD4$^+$ or CD8$^+$ T cells (lines indicate the medians; mock, clone2, 10D11 CAR: n = 4; clone3 CAR: n = 5; no statistically significant differences according to Wilcoxon matched-pairs signed ranked test).

4.6 Establishment of NY-BR-1 subcutaneous mouse models

In order to confirm the anti-NY-BR-1 specificity of both human and murine CAR$^+$ T cells under physiological conditions, NY-BR-1$^+$ tumor bearing mouse models had to be established.

4.6.1 Rejection of NY-BR-1 expressing EO771 cells by both C57BL/6 and NY-BR-1$^{tg/-}$ mice

Since the results of previous chapters showed that pS/MARter electroporated murine CAR$^+$ T cells persist and remain functional in both C57BL/6 wt and NY-BR-1$^{tg/-}$ mice, the initial focus was on the establishment of subcutaneous C57BL/6 wt and NY-BR-1$^{tg/-}$ tumor mouse models using the murine NY-BR-1$^+$ EO771 cell line.

Surprisingly, subcutaneous injection of 2x10^6 NY-BR-1$^+$ EO771 cells led to tumor formation in only three out of seven C57BL/6 wt mice (Figure 4.6.1 A). However, two out of the three mice completely rejected NY-BR-1$^+$ EO771 derived tumors within 11 to 14 days upon tumor engraftment. Furthermore, the only remaining tumor showed a decrease in tumor volume from 20 mm³ to less than 10 mm³ after 14 days. These phenomenons were not observed in C57BL/6 wt mice engrafted with 2x10^6 EO771 cells (see Figure 4.6.1 A). In fact, seven out of seven C57BL/6 wt mice showed a constant outgrowing of EO771 derived tumors leading to tumor volumes of over 200 mm³ within 14 to 27 days and a median survival rate of 24 days (see Figure 4.6.1 C). The differences in the volumes of EO771 and NY-BR-1$^+$ EO771 derived tumors were also reflected by significantly different tumor weights illustrated in Figure 4.6.1 B. For clarification, two images of EO771 (left) and NY-BR-1$^+$ EO771 (right) derived tumors are additionally presented in Figure 4.6.1 B.

In order to enable an evaluation of the functionality of murine CAR$^+$ T cells in immunocompetent mice despite rejection of NY-BR-1$^+$ EO771 derived tumors in C57BL/6 wt mice, five NY-BR-1$^{tg/-}$ and two NY-BR-1$^{tg/tg}$ mice were also tested for the persistence of NY-BR-1$^+$ EO771 derived tumors by subcutaneous injection of 2x10^6 NY-BR-1$^+$ EO771 cells. Surprisingly, only four out of five NY-BR-1$^{tg/-}$ and one out of two NY-BR-1$^{tg/tg}$ mice showed an outgrowth of NY-BR-1$^+$ EO771 derived tumors, which, however, were ultimately rejected after a short time (see Figure 4.6.1 D).

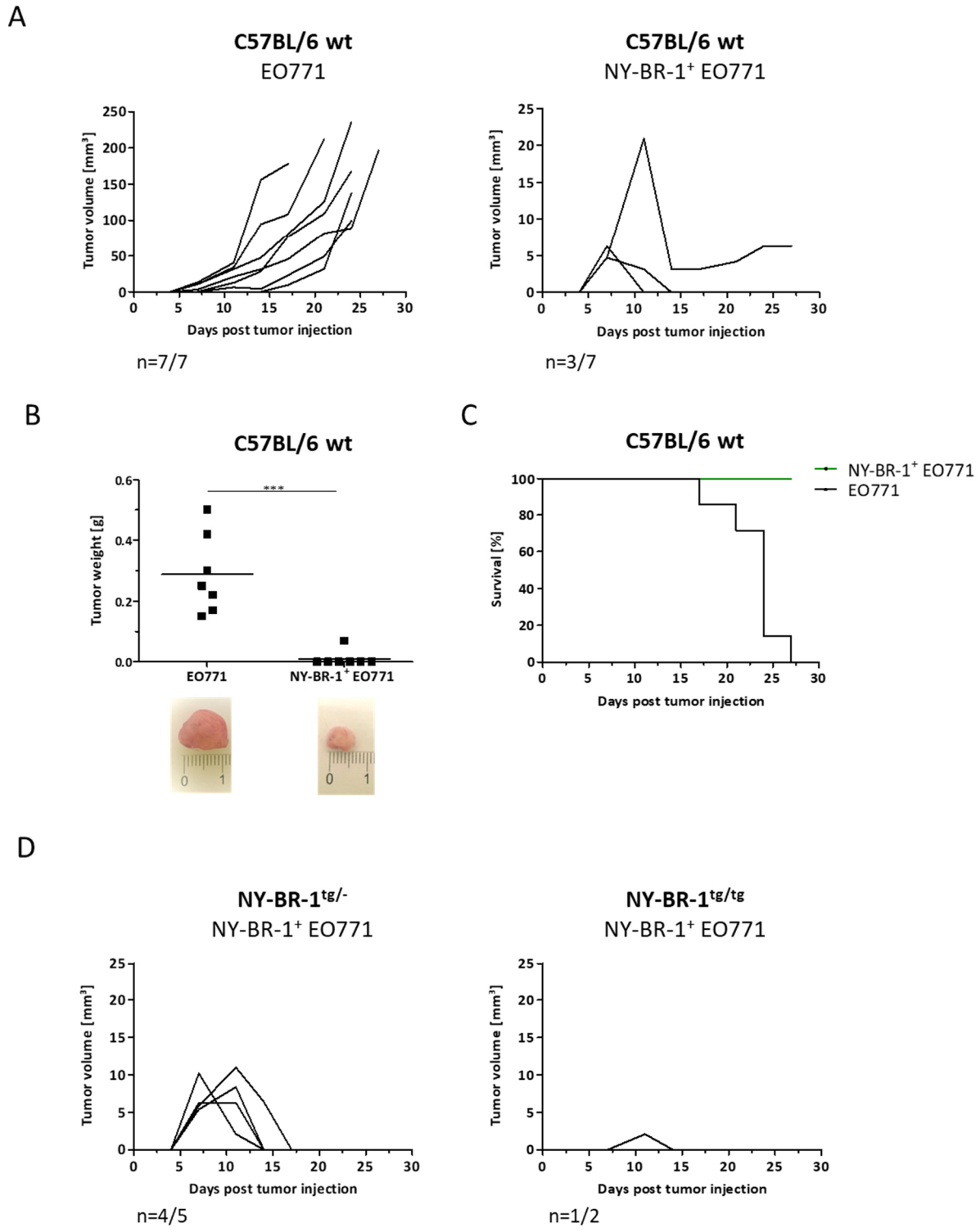

Figure 4.6.1: Growth analysis of (NY-BR-1⁺) EO771 derived tumors in C57BL/6 and NY-BR-1$^{tg/-}$ mice
[A] EO771 and NY-BR-1⁺ EO771 cells were injected subcutaneously in C57BL/6 wt mice (2x10^6 cells / mouse). Tumor sizes were measured every three to four days. Each line represents one mouse. Tumor engrafted mice were sacrificed at a tumor diameter of 15 mm or a tumor volume of 200 mm³, whatever occurred first. Tumor volumes were calculated with the ellipsoid formula (1/6 x π x length x width x depth). [B] The resulting tumor weights of EO771 and NY-BR-1⁺ EO771 derived tumors are displayed (lines indicate the means; n = 7; ***, p ≤ 0.0001; unpaired one-tailed Student's t-test). In addition, pictures of one EO771 (left) and the only remaining NY-BR-1⁺ EO771 (right) tumor are shown. [C] The corresponding survival rates are illustrated as Kaplan-Meier survival curves. [D] NY-BR-1⁺ EO771 cells were injected subcutaneously in both NY-BR-1$^{tg/-}$ and NY-BR-1$^{tg/tg}$ mice (2x10^6 cells / mouse). Tumor volumes were measured every three to four days according to the formula described in [A].

To examine the contribution of T cells and antibodies to the rejection of NY-BR-1^{+} EO771 derived tumors in immunocompetent C57BL/6 wt and NY-BR-1$^{tg/-}$ mice, those mice were analyzed for changes in plasma cytokine levels and the presence of anti-NY-BR-1 antibodies. Moreover, the only remaining NY-BR-1^{+} tumor was investigated for T cell infiltration by immunohistochemistry analysis.

Indeed, the only remaining NY-BR-1^{+} EO771 derived tumor, isolated from C57BL/6 wt mouse, showed a strong infiltration of murine T cells (see Figure 4.6.2 A) according to immunohistochemistry analysis. This suggested T cell - based immune response against NY-BR-1 expressing EO771 tumors was confirmed by further analysis of plasma cytokine levels. In fact, the cytokine levels, detected by the Mouse 12-Plex Cytokine Kit (Ayoxxa), were compared between untreated, EO771 and NY-BR-1^{+} EO771 tumor bearing C57BL/6 wt mice. An additional distinction was made between the one NY-BR-1^{+} EO771 tumor bearing C57BL/6 wt mouse with remained tumor and those showing complete tumor rejection (see Figure 4.6.2 B). Remarkable, the comparison of the mentioned tumor bearing mice revealed big differences in the plasma cytokine levels. In detail, the C57BL/6 wt mouse with remained NY-BR-1^{+} EO771 tumor showed highly elevated concentrations of T cell, B cell and macrophage associated pro- and anti-inflammatory cytokines. Particularly noteworthy were the strongly increased concentrations of IL-2 up to 650 pg/mL, IL-13 up to 400 pg/mL and IL-12 up to 250 pg/mL, whereas the cytokine levels of GM-CSF and IL-6 showed the smallest changes. Nevertheless, slightly increased levels of diverse pro- and anti-inflammatory cytokines were also found in C57BL/6 wt mice upon several days post complete rejection of NY-BR-1^{+} EO771 tumors. In contrast, except for TNFα, untreated and EO771 tumor bearing mice exhibited a similar cytokine profile.

To further investigate the question of B cell associated immune responses, the plasma of EO771 and NY-BR-1^{+} EO771 tumor bearing C57BL/6 wt as well as of untreated and NY-BR-1^{+} EO771 tumor bearing NY-BR-1$^{tg/-}$ mice were tested for the presence of anti-NY-BR-1 antibodies by using the special designed anti-NY-BR-1 antibody ELISA (see chapter 3.2.12.2). Since no standard was available in order to determine the exact concentration of anti-NY-BR-1 antibodies in murine plasma, only the differences in the absorption values, determined at a wavelength of 450 nm, could be compared (see Figure 4.6.2 C). Indeed, incubation of murine plasma, obtained from NY-BR-1^{+} EO771 tumor bearing C57BL/6 wt and NY-BR-1$^{tg/-}$ mice, in NY-BR-1 coated plates followed by the addition of the HRP - conjugated anti-mouse IgG antibody and incubation with the TMB substrate solution (BD OptEIA) provoked significantly enhanced absorbance values. Strikingly, all NY-BR-1^{+} tumor-bearing C57BL/6 wt mice exhibited nearly the same absorbance levels (0 to 0.3), whereas large variations (between 0.05 and 0.9) were observed within the NY-BR-1^{+} tumor bearing NY-BR-1$^{tg/-}$ mouse group.

Thus, these experiments demonstrated that both T cell and anti-NY-BR-1 antibodies are involved in the rejection of NY-BR-1^{+} EO771 tumors, so that immunodeficient mouse models, which do not exhibit mature T and B cells, had to be examined for their suitability.

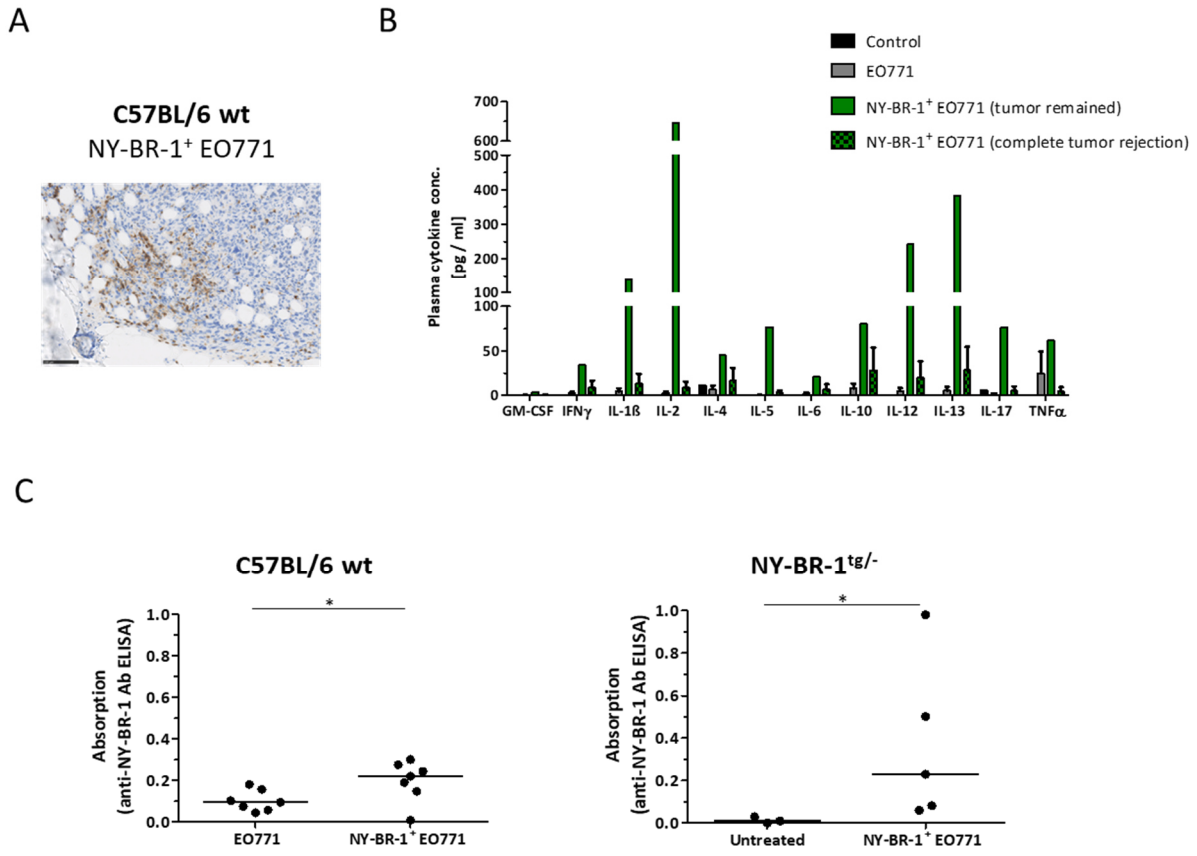

Figure 4.6.2: Analysis of tumor rejection in C57BL/6 and NY-BR-1$^{tg/-}$ mice
[A] The only remaining NY-BR-1^{+} EO771 tumor in C57BL/6 wt mice was investigated for T cell infiltration by immunohistochemistry analysis with the rabbit anti-mouse CD3 (Abcam, 16669) and HRP - conjugated anti-rabbit IgG antibodies (staining was performed by Rosa Eurich). [B] The plasma cytokine concentrations of untreated (control) as well as EO771 and NY-BR-1^{+} EO771 tumor engrafted C57BL/6 wt mice were analyzed by using the Mouse 12-Plex Cytokine Kit (Ayoxxa) (mean ± sem; control: n = 1; EO771: n = 6; NY-BR-1^{+} EO771 (remained): n = 1; NY-BR-1^{+} EO771 (tumor rejection): n = 6). [C] Plasma of untreated and tumor engrafted C57BL/6 wt and NY-BR-1$^{tg/-}$ mice were analyzed for the presence of anti-NY-BR-1 antibodies by applying the anti-NY-BR-1 antibody ELISA (lines indicate the medians; C57BL/6 wt: EO771, NY-BR-1^{+} EO771 n = 7; NY-BR-1$^{tg/-}$: untreated: n = 3; NY-BR-1^{+} EO771: n = 5;.* , $p < 0.05$; one-tailed Mann Whitney-U-test). The given absorptions were measured at 450 nm.

4.6.2 Analysis of tumor growth in NOD.CB17-Prkdc^{scid} and NSG mice

Due to the T cell and antibody based rejections of NY-BR-1^{+} EO771 tumors in C57BL/6 mice, the following section was focusing on the question whether these tumors grow and persist in immunodeficient NOD.CB17-Prkdc^{scid} mice. Besides the required murine tumor model, the evaluation of human anti-NY-BR-1 CAR^{+} T cells in a corresponding tumor mouse model was also of great interest. Therefore, both the established human NY-BR-1 expressing Bosc23 cell line and pleural effusion cells should be examined for their abilities to form subcutaneous tumors in NSG mice.

4.6.2.1 NY-BR-1 expressing EO771 cells form tumors in the NOD.CB17-Prkdc^{scid} ectopic mouse model

Following subcutaneous injection of 2x10^6 NY-BR-1$^+$ EO771 cells into the flank of nine NOD.CB17-Prkdc^{scid} mice, all mice actually indicated formation of subcutaneous tumors only four to eight days after injection and demonstrated very uniform growth kinetics (see Figure 4.6.3 A). In fact, tumors achieved volumes of over 400 to 500 mm³ after three weeks leading to median and overall survival rates of 21 days (Figure 4.6.3 B). Due to the very uniform growth kinetics of NY-BR-1$^+$ EO771 derived tumors in NOD.CB17-Prkdc^{scid}, this ectopic mouse model was utilized to evaluate the killing efficiency of murine anti-NY-BR-1 CAR$^+$ T cells in different *in vivo* assays (see chapter 4.8).

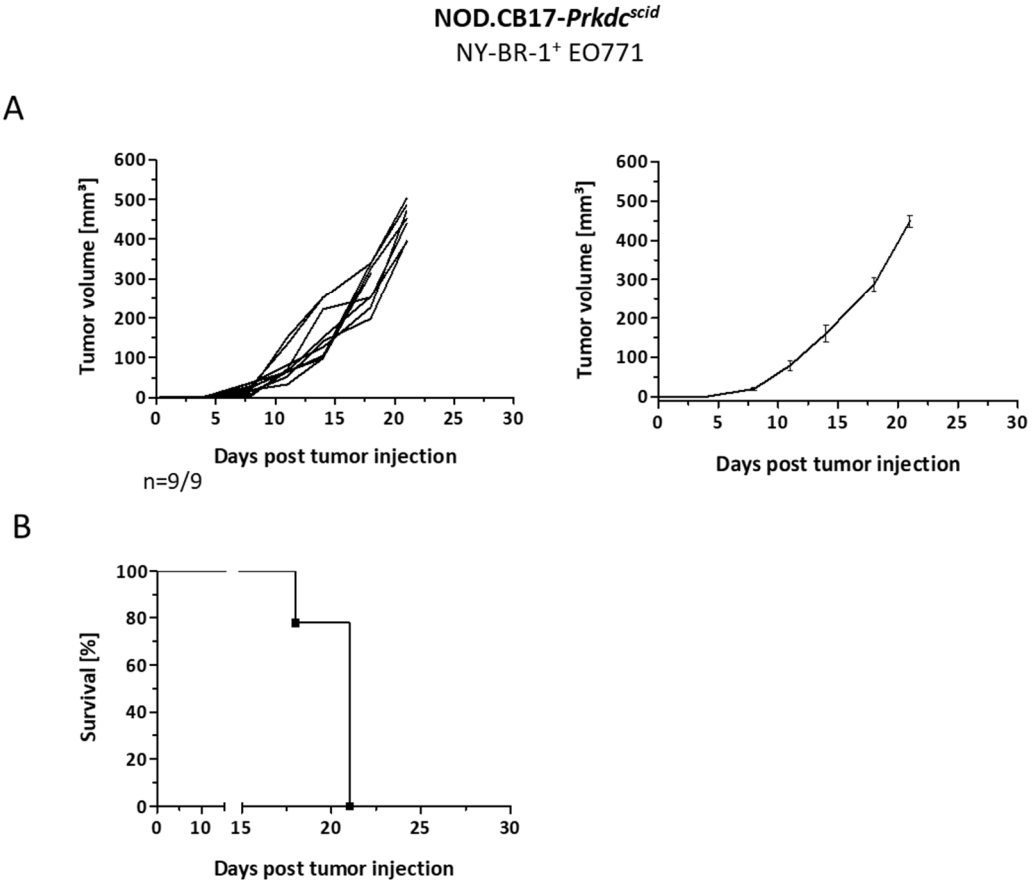

Figure 4.6.3: Growth analysis of NY-BR-1$^+$ EO771 derived tumors in NOD.CB17-Prkdc^{scid} mice
[A] 2x10^6 NY-BR-1$^+$ EO771 cells were injected subcutaneously in nine NOD.CB17-Prkdc^{scid} mice. Tumor sizes were measured every three to four days. Tumor engrafted mice were sacrified at a tumor diameter of 15 mm or a tumor volume of 450 mm³, whatever occurred first. Tumor volumes were calculated with the ellipsoid formula (1/6 x π x length x width x depth). Each line indicates one mouse (left graph). The average tumor growth rates are displayed in the right graph. [B] The corresponding survival rates are illustrated as a Kaplan-Meier survival curve.

4.6.2.2 NY-BR-1 expressing Bosc23 cells form tumors in the NSG xenograft model

The transfer of $2x10^6$ pleural effusion cells, isolated from breast cancer patients, into NSG mice did not lead to the formation of subcutaneous tumors in different approaches (data not shown).

However, the subcutaneous injection of $2x10^6$ NY-BR-1$^+$ Bosc23 cells into the flank of seven NSG mice resulted in the development of subcutaneous tumors with different growth kinetics (see Figure 4.6.4 A). Even though all mice showed palpable tumors eight days post injection, tumor volumes differed considerably with 54 to 300 mm³ after 21 days. The corresponding median and overall survival rates were 27 days, as illustrated in Figure 4.6.4 B. Due to the facts that the NY-BR-1$^+$ Bosc cell line was eliminated by human CAR$^+$ T cells in various *in vitro* assays and that these cells were now able to form tumors in NSG mice, this xenograft model was used for further functional analysis of human CAR$^+$ T cells (see chapter 4.7).

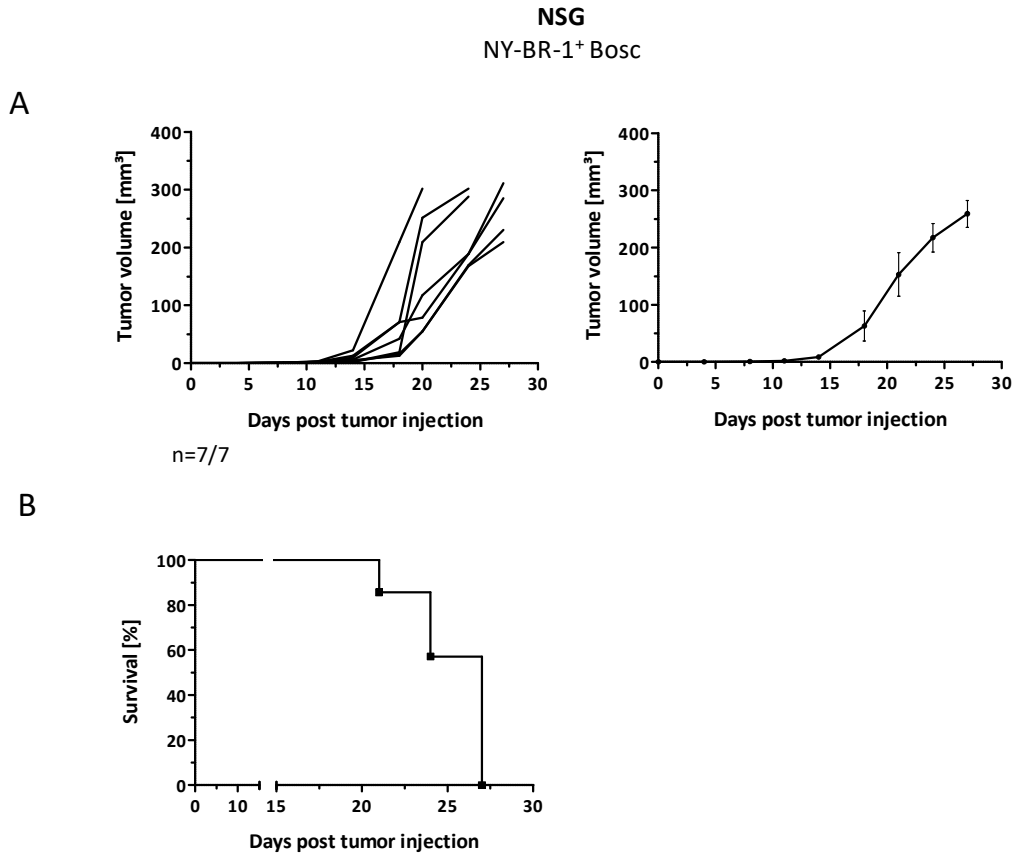

Figure 4.6.4: Growth analysis of NY-BR-1$^+$ Bosc23 derived tumors in NSG mice
[A] $2x10^6$ NY-BR-1$^+$ Bosc cells were injected subcutaneously in seven NSG mice. Tumor sizes were measured every three to four days. Tumor engrafted mice were sacrified at a tumor diameter of 15 mm or a tumor volume of 300 mm³, whatever occurred first. Tumor volumes were calculated with the ellipsoid formula (1/6 x π x length x width x depth). Each line indicates one mouse (left graph). The average tumor volumes are displayed in the right graph. [B] The corresponding survival rates are illustrated as a Kaplan-Meier survival curve.

4.7 Functional characterization of human anti-NY-BR-1 chimeric antigen receptors *in vivo*

After having shown that the successfully generated lentivirally transduced and pS/MARter / NanoCMARter electroporated human anti-NY-BR-1 CAR - expressing T cells achieved efficient anti-target reactivity in different *in vitro* assays, their potential of persistence and anti-tumoral efficacy should now be further investigated in the established NSG xenograft model.

4.7.1 Lentivirally transduced human anti-NY-BR-1 CAR$^+$ T cells mediate a delay in tumor progression in the NSG xenograft model

Anti-NY-BR-1 CAR - expressing T cells (donor: ERC97), generated by lentiviral transduction with the CAR constructs clone2scFv_hFc_hCD28_hCD3z_hOX40 (#537), 10D11scFv_hFc_hCD28_hCD3z_hOX40 (#538) and clone3scFv_hFc_hCD28_hCD3z_hOX40 (#539) upon two days of activation, or untransduced (mock) T cells were injected intravenously into NY-BR-1$^+$ Bosc tumor bearing NSG mice ($1x10^6$ CAR$^+$ T cells / mouse) eight days after tumor engraftment ($2x10^6$ NY-BR-1$^+$ Bosc cells / mouse) (see Figure 4.7.1 A). Each group consisted of seven mice. Tumor sizes were measured every three to four days over a period of 33 days.

The treatment of tumor-bearing NSG mice with CAR$^+$ T cells resulted in significantly delayed or even absent tumor growth compared to untreated and mock T cell treated mice (see Figure 4.7.1 B, C). In fact, four mice of clone2, two mice of 10D11 and three mice of clone3 CAR group had no tumors or rather tumors with volumes of less than 20 mm³ at the end of the experiment, which resulted in significantly prolonged overall and median survival rates (10D11scFv: 31 days; clone3scFv: 27 days) compared to mock and untreated mice (mock: 24 days; untreated: 21 days) (see Figure 4.7.1 D).

Since the persistence of CAR$^+$ T cells plays a key role for efficient and prolonged anti-tumor immune responses, blood, spleens and tumors (with volumes over 10 mm³) were analyzed for persisting T cells by staining with the APC - conjugated anti-human CD3 antibody (UCHT1) and flow cytometric analysis. Indeed, T cells were found in the spleens of two clone2, three 10D11 and two clone3 CAR$^+$ T cell but also of one mock treated mice. Additionally, blood and remaining tumors of CAR$^+$ T cell and mock treated mice showed small amounts of persisting T cells (see Figure 4.7.1 E, F). These results were confirmed by immunohistochemistry analysis showing that some remaining tumors from mock and CAR$^+$ T cell treated mice were infiltrated by T cells, whereby the infiltration rates did not differ significantly between mock and CAR$^+$ T cell - treated mice.

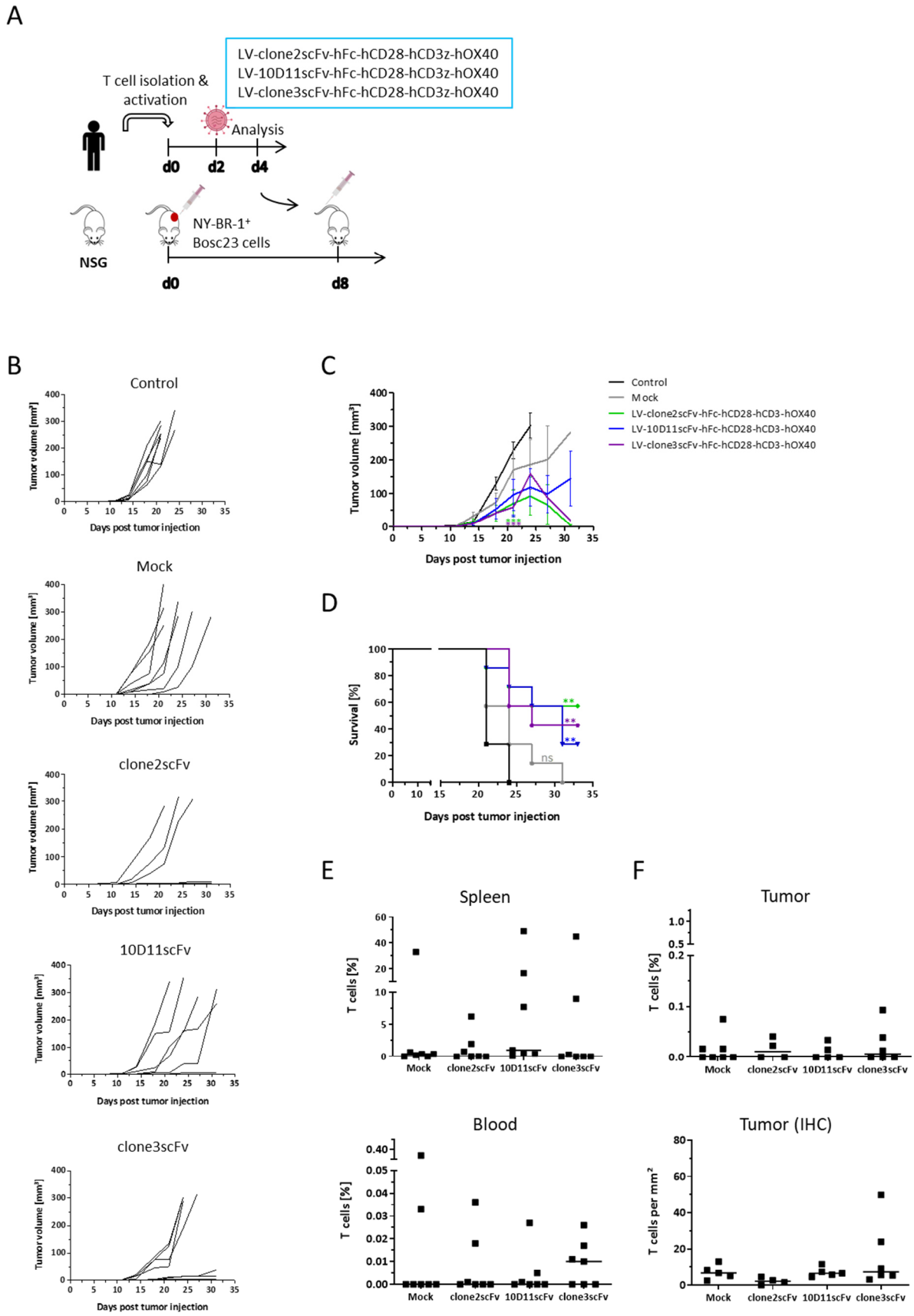

Figure 4.7.1: Effect of lentivirally transduced human anti-NY-BR-1 CAR+ T cells on outgrowth of NY-BR-1+ Bosc23 derived tumors in NSG mice

[A] Following two days of activation, human peripheral T cells (donor: ERC97) were lentivirally transduced with the anti-NY-BR-1 CAR constructs clone2scFv_hFc_hCD28_hCD3z_hOX40 (#537), 10D11scFv_hFc_hCD28_hCD3z_hOX40 (#538) and clone3scFv_hFc_hCD28_hCD3z_hOX40 (#539). Eight days post tumor engraftment of NSG mice (2x10^6 NY-BR-1+ Bosc23

cells / mouse), lentivirally transduced anti-NY-BR-1 CAR$^+$ T cells (1x10^6 CAR$^+$ T cells / mouse) or untransduced (mock) T cells were injected intravenously. Untreated mice served as controls. Each group consisted of seven mice. [B], [C] Tumor volumes were measured every three to four days. [B] Each line indicates one mouse. The average tumor volumes are illustrated in [C] (mean values ± sem; *, $p < 0.05$; ***, $p < 0.001$; Two-way ANOVA with Bonferroni post test for comparison with mock group). Tumor engrafted mice were sacrified at a tumor diameter of 15 mm or a tumor volume of 300 mm³, whatever occurred first. Tumor volumes were calculated with the ellipsoid formula (1/6 x π x length x width x depth). [D] The corresponding survival rates are illustrated as Kaplan-Meier survival curves. Survival rates were compared with control group by using Log-rank (Mantel-cox) test (**, $p < 0.005$). [E] Isolated spleens and blood were examined for T cell infiltration by flow cytometric analysis. Cells were stained with the APC - conjugated anti-human CD3 antibody (UCHT1). Percentages indicate the proportion of CD3$^+$ cells after gating on all living (DAPI$^-$) cells (lines indicate the medians; no statistically significant differences according to Kruskal-Wallis test followed by Dunn's multiple comparison test). [F] Tumors were investigated for T cell infiltration by flow cytometric analysis (upper graph; lines indicate the medians; mock: n = 7; clone2scFv: n = 4; 10D11scFv: n = 5; clone3scFv: n = 6; no statistically significant differences according to Kruskal-Wallis test followed by Dunn's multiple comparison test), as described in [E], and immunohistochemical stainings (lower graph) with the rabbit anti-human CD3 (Abcam, 16669) and HRP - conjugated anti-rabbit IgG antibodies (staining was performed by Rosa Eurich). The calculated T cell densities are given (lines indicate the medians; mock: n = 5; clone2scFv: n = 4; 10D11scFv: n = 5; clone3scFv: n = 6; no statistically significant differences according to Kruskal-Wallis test followed by Dunn's multiple comparison test).

To assess whether the remaining tumor cells express NY-BR-1 on their surface, tumors were examined with both flow cytometric and immunohistological analysis using the three monoclonal anti-NY-BR-1 antibodies clone2, 10D11 and clone3. Unfortunately, these analyses did not yield reliable results (data not shown).

Despite substantial prolonged survival rates and significant suppression of tumor growth, analysis of plasma cytokine concentrations, using the Human 11-Plex Cytokine Kit (Ayoxxa), did not reveal enhanced cytokine levels in CAR$^+$ T cell - treated mice (see Supplementary Figure 6.8). In contrast, analysis of the tumor milieu showed slight differences in the cytokine levels depending on CAR$^+$ T cell treatment (see Figure 4.7.2). Increased concentrations of pro-inflammatory cytokines such as IFNγ, IL-1ß, IL-2 and IL-12 were detected in some remaining tumors of clone2 and 10D11 CAR$^+$ T cell - treated mice, while the absolute concentrations of anti-inflammatory cytokines such as IL-10 and IL-4 remained very low. Strikingly, two mock treated mice also showed highly elevated cytokine levels, which is consistent with the increased persistence of T cells in these mice (see Figure 4.7.1). Furthermore, among all tested cytokines, IL-8 in particular stood out with strongly enhanced levels in both mock and CAR$^+$ T cell - treated mice. Unfortunately, the cytokine levels in tumors with volumes below 10 mm³ could not be reliably determined using this method (data not shown).

Based on these data, it can be assumed that lentivirally transduced anti-NY-BR-1$^+$ CAR T cells are similarly effective in anti-tumor responses *in vivo* as *in vitro*, whereby the different anti-NY-BR-1 CAR candidates did not vary significantly in their anti-tumoral reactivities. Nevertheless, spleens of 10D11 CAR$^+$ T cell - treated mice showed the highest accumulation of persisting T cells and, additionally, tumors of those mice displayed the highest average increase in T cell activation - associated cytokine levels.

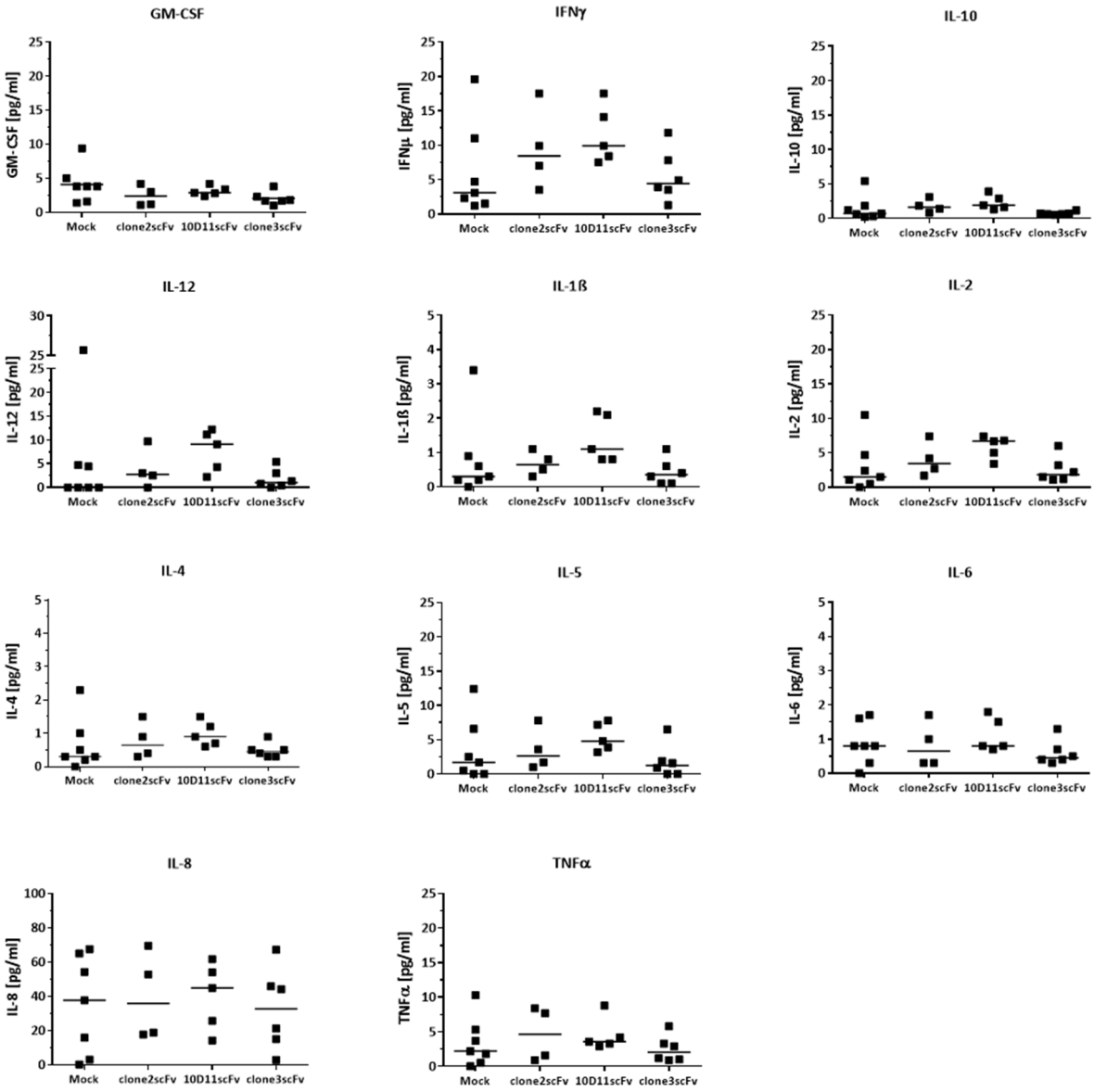

Figure 4.7.2: Cytokine levels in NY-BR-1$^+$ Bosc23 derived tumors isolated from NSG mice upon CAR$^+$ T cell therapy
NSG mice were engrafted with NY-BR-1$^+$ Bosc23 derived tumors (2x10^6 NY-BR-1$^+$ Bosc23 cells / mouse) and treated with lentivirally transduced anti-NY-BR-1 CAR (#537, #538, #539) expressing T cells (1x10^6 CAR$^+$ T cells / mouse) or untransduced (mock) T cells. Tumor engrafted mice were sacrified at a tumor diameter of 15 mm or a tumor volume of 300 mm³, whatever occurred first. Subsequently, isolated tumors were assessed for their cytokine profile by using the Human 11-Plex Cytokine Kit (Ayoxxa) (lines indicate the medians; mock: n = 7; clone2scFv: n = 4; 10D11scFv: n = 5, clone3scFv: n =6; no statistically significant differences according to Kruskal Wallis test followed by Dunn's multiple comparison test).

4.7.2 pS/MARter electroporated human anti-NY-BR-1 CAR$^+$ T cells mediate a delay in tumor progression in the NSG xenograft model

After several *in vitro* studies showed that the hOX40 domain has a positive impact on the expression of anti-NY-BR-1 CARs in electroporated T cells (see chapter 4.3.2), its effect on anti-tumor effectiveness should be further assessed in the established NSG xenograft model. Hence, human T cells (donor:

CHA90) were electroporated with the pS/MARter vectors clone2scFv_hFcΔ_hCD28Δ_h4-1BB_CD3z (#517), 10D11scFv_hFcΔ_hCD28Δ_h4-1BB_CD3z (#518) and clone3scFv_hFcΔ_hCD28Δ_h4-1BB_CD3z (#519) (see Figure 4.7.3) as well as clone2scFv_hFc_hCD28_CD3z_hOX40 (#432), 10D11scFv_hFc_hCD28_CD3z_hOX40 (#433) and clone3scFv_hFc_hCD28_CD3z_hOX40 (#434) (see Figure 4.7.4 A) after an one-day activation phase and were subsequently injected intravenously into tumor-bearing NSG mice (1x10^6 CAR$^+$ T cells / mouse) eight days post tumor engraftment (2x10^6 NY-BR-1$^+$ Bosc cells / mouse). Untreated mice or mice treated with untransfected (mock) T cells served as controls. Each group consisted of seven mice. Tumor sizes were measured every three to four days over a period of 27 or 42 days.

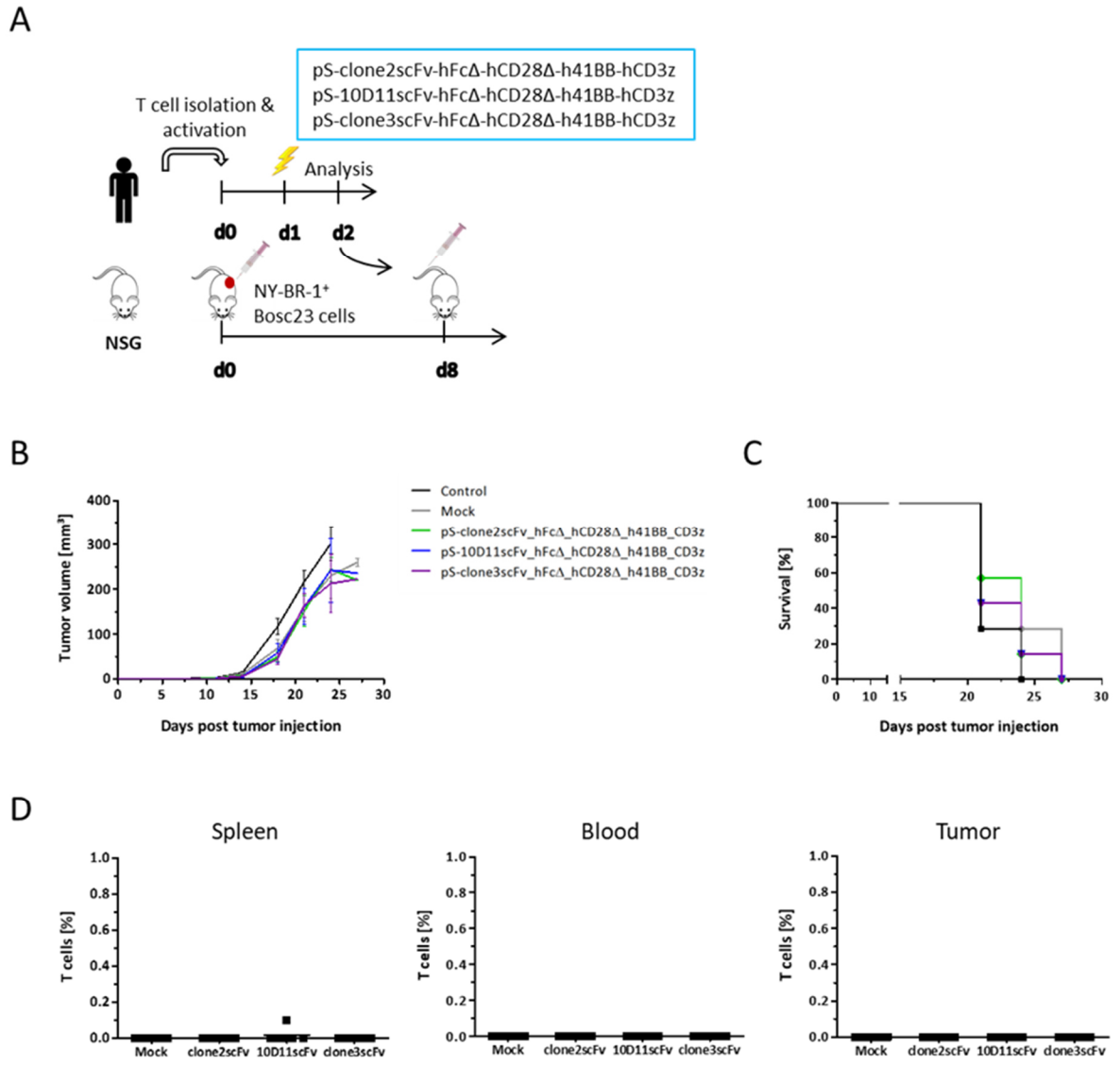

Figure 4.7.3: Effect of pS/MARter electroporated human T cells, engineered with hFcΔ_hCD28Δ_h4-1BB_hCD3z signaling anti-NY-BR-1 CARs, on outgrowth of NY-BR-1$^+$ Bosc23 derived tumors in NSG mice
[A] Following one day of activation, human peripheral T cells (donor: CHA90) were electroporated with the pS/MARter vectors clone2scFv_hFcΔ_hCD28Δ_h4-1BB_hCD3z (#517), 10D11scFv_hFcΔ_hCD28Δ_h4-1BB_hCD3z (#518) and clone3scFv_hFcΔ_hCD28Δ_h4-1BB_hCD3z (#519). Eight days post tumor engraftment of NSG mice (2x10^6 NY-BR-1$^+$ Bosc23 cells / mouse), anti-NY-BR-1 CAR$^+$ T cells (1x10^6 CAR$^+$ T cells / mouse) or untransfected (mock) T cells were injected

intravenously. Untreated mice served as controls. Each group consisted of seven mice. [B] Tumor volumes were measured every three to four days. The average tumor volumes are given (mean values ± sem; no statistically significant differences according to Two-way ANOVA with Bonferroni post test for comparison with control or mock group). Tumor engrafted mice were sacrified at a tumor diameter of 15 mm or at a tumor volume of 300 mm^3, whatever occurred first. Tumor volumes were calculated with the ellipsoid formula (1/6 x π x length x width x depth). [C] The corresponding survival rates are illustrated as Kaplan-Meier survival curves. No statistically significant differences according to Log-rank (Mantel-cox) test. [D] Isolated spleens, blood and tumors were examined for T cell infiltration by flow cytometric analysis. Cells were stained with the APC - conjugated anti-human CD3 antibody (UCHT1). Percentages indicate the proportion of $CD3^+$ cells after gating on all living ($DAPI^-$) cells (n = 7; no statistically significant differences according to Kruskal Wallis test followed by Dunn's multiple comparison test).

Indeed, the transfer of electroporated anti-NY-BR-1 CAR^+ T cells into tumor-bearing mice resulted in delayed progression of NY-BR-1^+ Bosc derived tumors, but the efficacy appeared much higher for hOX40 containing CARs (see Figure 4.7.3; Figure 4.7.4). While mice treated with #517, #518 or #519 CAR^+ T cells did neither show significantly reduced tumor volumes nor prolonged overall survival or persistence of T cells (in spleen, tumors or blood), #432, #433 and #434 CAR^+ T cells had very strong suppressive effects on tumor outgrowth, which provoked greatly prolonged overall survival rates (clone2scFv: 42 days; 10D11scFv: 42 days; clone3scFv: 38 days) compared to mock (31 days) and control (27 days). These results were confirmed by flow cytometric analysis of spleens, tumors and blood demonstrating high amounts of persisting and infiltrating T cells (see Figure 4.7.4). In fact, two each of the 10D11 and clone3 CAR^+ T cell - treated mice exhibited large amounts of tumor infiltrated T cells of over 150 to 300 T cells / mm^2 according to immunohistochemistry analysis (see Figure 4.7.5).

The strong antitumoral immune responses and T cell persistence in the peripheral blood were also reflected in elevated plasma cytokine levels, calculated by the Human 11-Plex Cytokine Kit (Ayoxxa). In particular, 10D11 CAR^+ T cell - treated mice displayed enhanced plasma levels of T cell activation-associated cytokines such as GM-CSF, IFNγ, IL-2, IL-4 and TNFα. By contrast, clone2 and clone3 CAR^+ T cell - treated mice had a very similar cytokine profile, with the exception of increased GM-CSF levels, compared to that of mock treated mice.

Overall, in agreement with the *in vitro* results, pS/MARter electroporated T cells expressing anti-NY-BR-1 CARs incorporating the hOX40 domain persist in NSG xenograft model and attack NY-BR-1 expressing tumor cells, whereby the best anti-tumoral immune responses were achieved with 10D11 followed by clone2 and clone3 CAR^+ T cells. In fact, pS/MARter electroporated CAR^+ T cells led to lower overall survival rates but displayed similar or even better T cell persistence profiles than lentivirally transduced CAR^+ T cells (see chapter 4.7.1). However, it should be noted that in both approaches T cells from different donors were used.

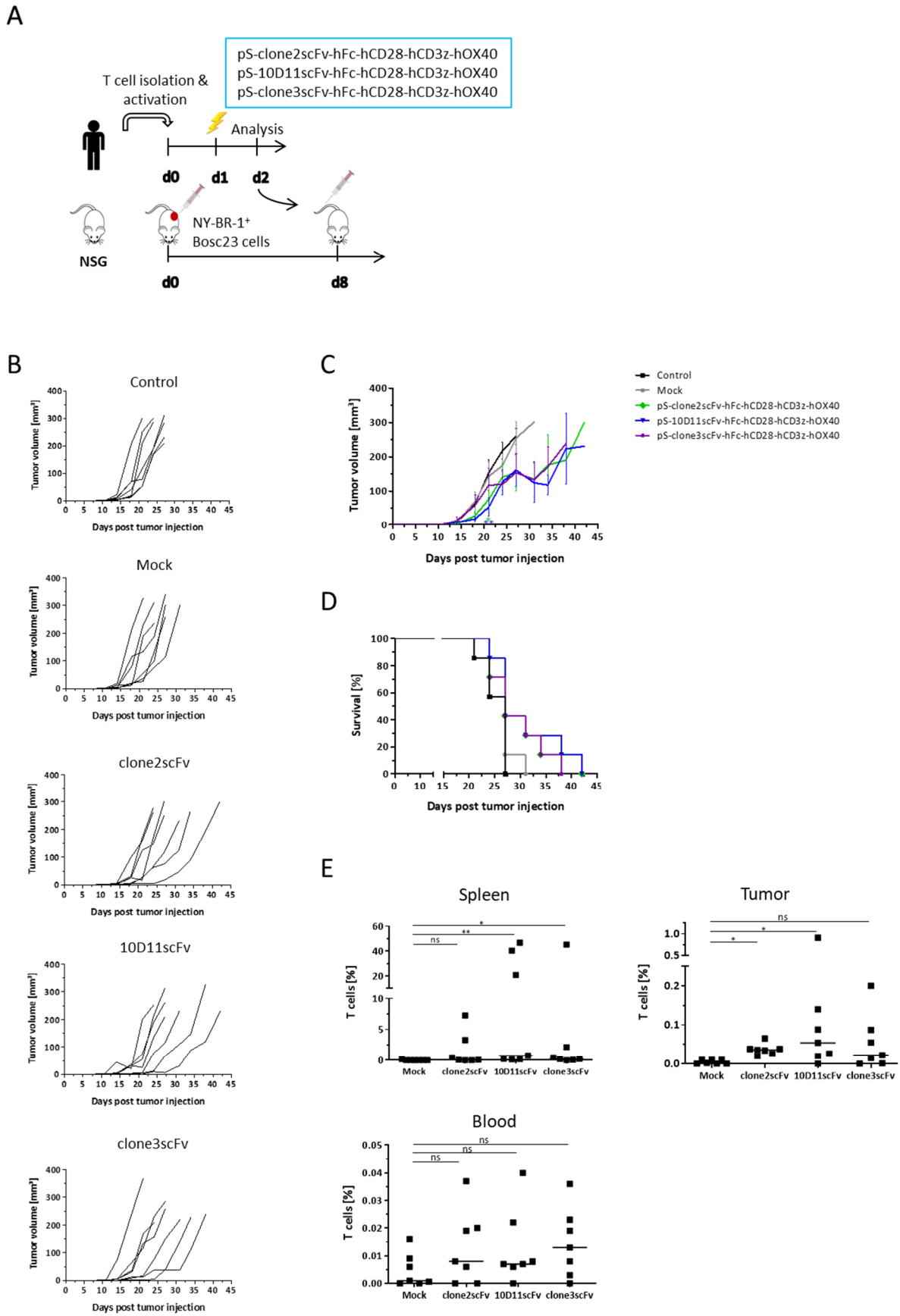

Figure 4.7.4: Effect of pS/MARter electroporated human T cells, engineered with hFc_hCD28_CD3z_hOX40 signaling anti-NY-BR-1 CARs, on outgrowth of NY-BR-1+ Bosc23 derived tumors in NSG mice

[A] Following one day of activation, human peripheral T cells (donor: CHA90) were electroporated with pS/MARter vectors clone2scFv_hFc_hCD28_CD3z_hOX40 (#432), 10D11scFv_hFc_hCD28_CD3z_hOX40 (#433) and

clone3scFv_hFc_hCD28_CD3z_hOX40 (#434). Eight days post tumor engraftment of NSG mice (2x10^6 NY-BR-1$^+$ Bosc23 cells / mouse), electroporated anti-NY-BR-1 CAR$^+$ T cells (1x10^6 CAR$^+$ T cells / mouse) or untransfected (mock) T cells were injected intravenously. Untreated mice served as controls. Each group consisted of seven mice. [B], [C] Tumor volumes were measured every three to four days. [B] Each line indicates one mouse. The average tumor volumes are illustrated in [C] (mean values ± sem; *, $p < 0.05$; **, $p < 0.01$; Two-way ANOVA with Bonferroni post test for comparison with mock group). Tumor engrafted mice were sacrified at a tumor diameter of 15 mm or a tumor volume of 300 mm³, whatever occurred first. Tumor volumes were calculated with the ellipsoid formula (1/6 x π x length x width x depth). [D] The corresponding survival rates are illustrated as Kaplan-Meier survival curves. No statistically significant differences according to Log-rank (Mantel-cox) test. [E] Isolated spleens, blood and tumors were examined for T cell infiltration by flow cytometric analysis. Cells were stained with the APC - conjugated anti-human CD3 antibody (UCHT1). Percentages indicate the proportion of CD3$^+$ cells after gating on all living (DAPI$^-$) cells (lines indicate the medians; n = 7; *, $p < 0.05$; **, $p < 0.01$; Kruskal Wallis test followed by Dunn's multiple comparison test).

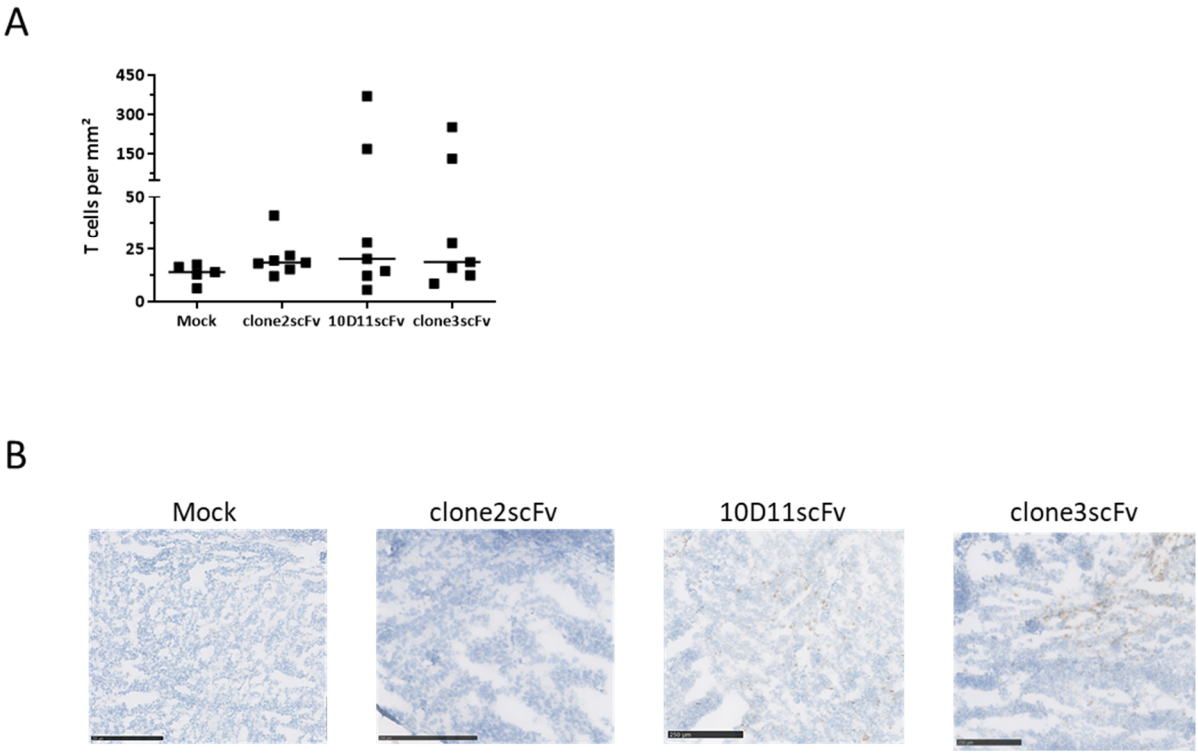

Figure 4.7.5: Immunohistochemistry analysis of NY-BR-1$^+$ Bosc23 tumor - infiltrating T cells
NY-BR-1$^+$ Bosc23 derived tumors, isolated from NSG xenograft mice upon CAR$^+$ T cell (#432, #433, #434) treatment, were analyzed for infiltrated T cells via immunohistochemistry analysis. Cryosections were stained with the rabbit anti-human CD3 (Abcam, 16669) and HRP - conjugated anti-rabbit IgG antibodies (staining was performed by Rosa Eurich). [A] The absolute numbers or rather densities of infiltrated T cells are illustrated as a scatter dot plot. Each dot represents one mock or CAR$^+$ T cell - treated mouse (lines indicate the medians; mock: n = 5; clone2scFv, 10D11scFv, clone3scFv: n = 7; no statistically significant differences according to Kruskal Wallis test followed by Dunn's multiple comparison test). [B] Representative examples of tumors stained for CD3$^+$ cells. Scale bars present 250 µm.

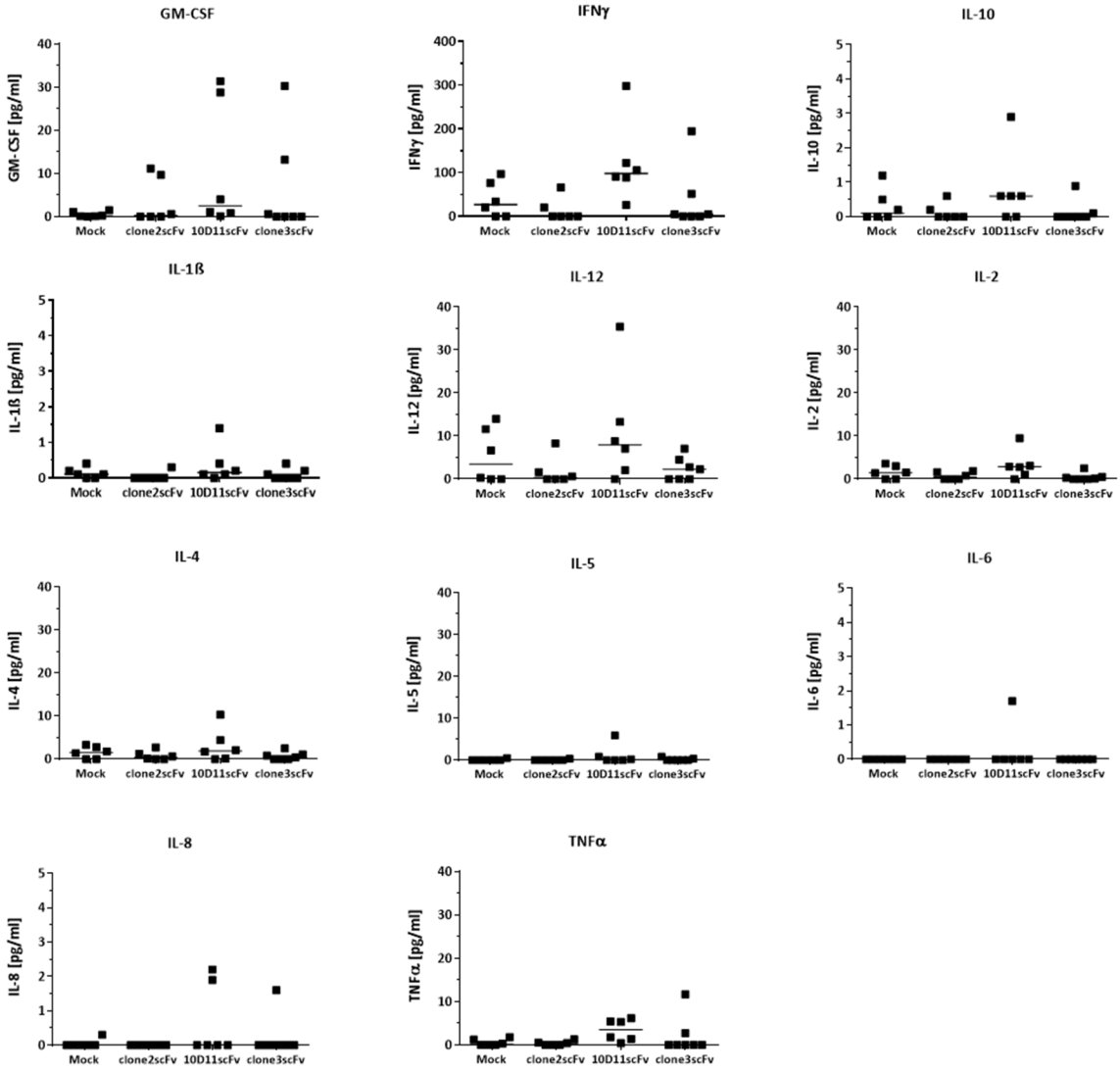

Figure 4.7.6: Plasma cytokine profile of tumor-bearing NSG mice upon treatment with pS/MARter electroporated CAR$^+$ T cells
NSG mice were engrafted with NY-BR-1$^+$ Bosc23 derived tumors (2x10^6 NY-BR-1$^+$ Bosc23 cells / mouse) and treated with anti-NY-BR-1 (#432, #433, #434) CAR$^+$ T cells (1x10^6 CAR$^+$ T cells / mouse) or untransfected (mock) T cells. Tumor engrafted mice were sacrified at a tumor diameter of 15 mm or a tumor volume of 300 mm^3, whatever occurred first. Tumor volumes were calculated with the ellipsoid formula (1/6 x π x length x width x depth). Subsequently, the cytokine concentrations in murine blood were assessed by using the Human 11-Plex Cytokine Kit (Ayoxxa) (lines indicate the medians; mock, clone2scFv, 10D11scFv: n = 6; clone3scFv: n = 7; no statistically significant differences according to Kruskal Wallis test followed by Dunn's multiple comparison test).

4.7.3 NanoCMARter electroporated human anti-NY-BR-1 CAR$^+$ T cells mediate a delay in tumor progression in the NSG xenograft model

An important property of NanoCMARter vectors is its minimized bacterial backbone compared to pS/MARter vectors, which might affect the functional properties of CAR$^+$ T cells *in vivo*. Therefore, the antitumoral efficacy of NanoCMARter vectors was assessed in the established NSG xenograft model by using T cells from the same donor (CHA90) as before and electroporated them with the NanoCMARter vectors clone2scFv_hFc_hCD28_CD3z_hOX40 (531), 10D11scFv_hFc_hCD28_CD3z_hOX40 (#532) and clone3scFv_hFc_hCD28_CD3z_hOX40 (#533). One day post electroporation, CAR$^+$ T cells were injected intravenously into tumor-bearing NSG mice (1x10^6 CAR$^+$ T cells / mouse) eight days after tumor engraftment (2x10^6 NY-BR-1$^+$ Bosc cells / mouse) (see Figure 4.7.7 A). Each group, except for mock (n = 6), consisted of seven mice. Tumor sizes were measured every three to four days over a period of 38 days.

Indeed, NanoCMARter anti-NY-BR-1 CAR$^+$ T cells exhibited suppressive effects on tumor outgrowth (see Figure 4.7.7). In fact, treatment with all three different anti-NY-BR-1 CARs led to decelerated tumor expansion compared to mock, whereby in particular one clone2, five 10D11 and five clone3 CAR$^+$ T cell - treated mice showed extremely delayed tumor progressions (see Figure 4.7.7 B), which in turn resulted in significantly prolonged median survival (clone2scFv: 31 days, 10D11scFv: 33 days, clone3scFv: 31 days, mock: 22.5 days, control: 21 days) and overall survival rates (clone2scFv: 38 days, 10D11scFv: 33 days, clone3scFv: 33 days, mock: 27 days, control: 24 days) (see Figure 4.7.7 D). Although spleens of CAR$^+$ T cell-treated mice, especially those treated with clone2 CAR$^+$ T cells, showed an accumulation of persisting T cells, additional flow cytometric analyses of tumors and blood revealed only low amounts of residual and infiltrating T cells (except for two tumors of clone2 CAR$^+$ T cell treated mice), which was accompanied by plasma cytokine concentrations below the detectable range (data not shown). This draws a sharp contrast to the convincing blood and tumor infiltration by pS/MARter 10D11 and clone3 CAR$^+$ T cells in the previous experiment. Immunohistochemistry analysis of isolated tumors confirmed the fact of low amounts of tumor - infiltrating T cells despite delayed tumor growth rates (see Figure 4.7.7 F).

Nevertheless, these data confirm the *in vitro* results showing that the three different NanoCMARter derived anti-NY-BR-1 CAR candidates (clone2, 10D11, clone3) induced strong anti-tumoral T cell responses in the NSG xenograft model. Despite low frequencies of tumor - infiltrating T cells, both median and overall survival rates were significantly extended by clone2, 10D11 and clone3 CAR$^+$ T cells.

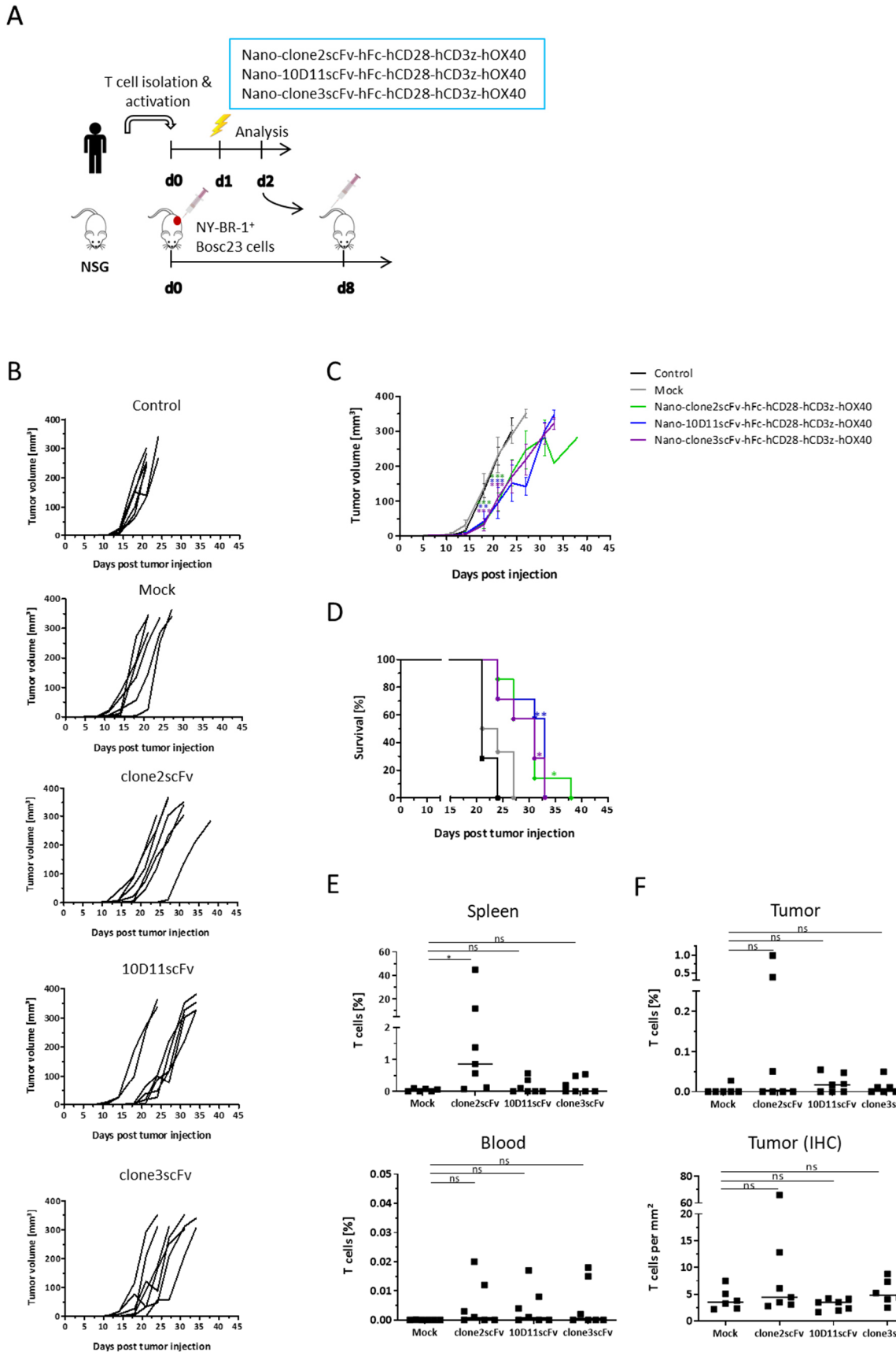

Figure 4.7.7: Effect of NanoCMARter electroporated human T cells, engineered with hFc_hCD28_CD3z_hOX40 signaling anti-NY-BR-1 CARs, on outgrowth of NY-BR-1+ Bosc23 derived tumors in NSG mice

[A] Following one day of activation, human peripheral T cells (donor: CHA90) were electroporated with NanoCMARter vectors encoding the anti-NY-BR-1 CAR constructs clone2scFv_hFc_hCD28_CD3z_hOX40 (#531), 10D11scFv_hFc_hCD28_CD3z_hOX40 (#532) and clone3scFv_hFc_hCD28_CD3z_hOX40 (#533). Eight days post tumor

engraftment of NSG mice ($2x10^6$ NY-BR-1^+ Bosc23 cells / mouse), electroporated anti-NY-BR-1 CAR^+ T cells ($1x10^6$ CAR^+ T cells / mouse) or untransfected (mock) T cells were injected intravenously. Untreated mice served as controls. Each group, except the mock (n = 6), consisted of seven mice. [B], [C] Tumor volumes were measured every three to four days. [B] Each line indicates one mouse. The average tumor volumes are illustrated in [C] (mean values ± sem; **, $p < 0.01$; ***, $p < 0.001$; Two-way ANOVA with Bonferroni post test for comparison with mock group). Tumor engrafted mice were sacrified at a tumor diameter of 15 mm or a tumor volume of 300 mm^3, whatever occurred first. Tumor volumes were calculated with the ellipsoid formula (1/6 x π x length x width x depth). [D] The corresponding survival rates are illustrated as Kaplan-Meier survival curves. Survival rates were compared with mock group by using Log-rank (Mantel-cox) test (*, $p < 0.05$; **, $p < 0.01$). [E] Isolated spleens and blood were examined for T cell infiltration by flow cytometric analysis. Cells were stained with the APC - conjugated anti-human CD3 antibody (UCHT1). Percentages indicate the proportion of $CD3^+$ cells after gating on all living ($DAPI^-$) cells (lines indicate the medians; mock: n = 6; clone2scFv, 10D11scFv, clone3scFv: n = 7; *, $p < 0.05$; Kruskal Wallis test followed by Dunn's multiple comparison test). [F] Tumors were investigated for T cell infiltration by flow cytometric analysis (upper graph; lines indicate the medians; mock: n = 6; clone2scFv, 10D11scFv, clone3scFv: n = 7; no statistically significant differences according to Kruskal Wallis Dunn's multiple comparison test), as described in [E], and immunohistochemical stainings (lower graph) with the rabbit anti-human CD3 (Abcam, 16669) and HRP - conjugated anti-rabbit IgG antibodies (staining was performed by Rosa Eurich). The calculated T cell densities are given (lines indicate the medians; mock: n = 6; clone2scFv, 10D11scFv, clone3scFv: n = 7; no statistically significant differences according to Kruskal Wallis test followed by Dunn's multiple comparisons test).

4.8 Functional characterization of murine anti-NY-BR-1 chimeric antigen receptors *in vivo*

After different *in vivo* studies demonstrated that human CAR$^+$ T cells induced effective anti-tumor immune responses against NY-BR-1 expressing target cells, the focus shifted toward the functional properties of murine CAR$^+$ T cells, which were examined in the established NOD.CB17-Prkdc^{scid} ectopic mouse model.

4.8.1 pS/MARter electroporated murine anti-NY-BR-1 expressing T cells mediate a delay in tumor progression in the NOD.CB17-Prkdc^{scid} ectopic mouse model

Murine anti-NY-BR-1 CAR - expressing T cells were successfully generated by electroporation with the pS/MARter vectors clone2scFv_mFcΔ_mCD28Δ_m4-1BB_mCD3z (#277), 10D11scFv_mFcΔ_mCD28Δ_m4-1BB_mCD3z (#295) and clone3scFv_mFcΔ_mCD28Δ_m4-1BB_mCD3z (#296) upon one day of activation. Eight days after subcutaneous engraftment of NOD.CB17-Prkdc^{scid} mice with 2x10^6 NY-BR-1$^+$ EO771 cells, mice were treated with murine CAR$^+$ T cells or untransfected (mock) T cells (5x10^5 CAR$^+$ T cells / mouse) (see Figure 4.8.1 A). Each group, except for control (n = 9), consisted of seven mice. Tumor sizes were measured every three to four days over a period of 28 days.

The treatment of tumor-bearing NOD.CB17-Prkdc^{scid} mice with murine CAR$^+$ T cells resulted in significantly slowed tumor progressions as well as significantly extended median and overall survival rates compared to untreated and mock treated mice (see Figure 4.8.1 B, C, D), whereby the best results were achieved with clone3 CAR$^+$ T cells, followed by 10D11 and clone2 CAR$^+$ T cells (control: 21 days; mock: 25 days; clone2scFv: 25 days; 10D11scFv: 27 days; clone3scFv 28 days).

Moreover, the persistence of murine CAR$^+$ T cells was investigated by flow cytometric analysis of spleens and blood under the usage of the APC - conjugated anti-mouse CD3 (17A2) and PE - conjugated anti-mouse IgG antibodies. Since all mice, including untreated mice, showed some cells weakly expressing the CD3 antigen, only the CD3 strongly positive cell populations were considered to be the injected ones (see Figure 4.8.1 E). Gating on these CD3$_{high}$ cell populations offered high frequencies of clone2 and 10D11 CAR$^+$ T cells but low frequencies of clone3 CAR$^+$ T cells persisting in spleens. Additional analyses of the blood revealed only low amounts of peripheral blood CAR$^+$ T cells.

However, immunohistochemistry analysis of the isolated tumors revealed significant differences in the amount of infiltrated T cells depending on CAR$^+$ T cell therapy. While clone2 and 10D11 CAR$^+$

T cell - treated mice showed only slightly increased amounts of tumor - infiltrating T cells compared to mock, all tumors of clone3 CAR$^+$ T cell - treated mice were strongly infiltrated by T cells (up to 900 T cells per mm²) (see Figure 4.8.2). Unfortunately, neither immunohistochemistry nor flow cytometric analyses using the monoclonal antibodies clone2, 10D11 and clone3 could reliably detect NY-BR-1 surface expression in the remaining EO771 derived tumors (data not shown).

Nevertheless, increased plasma cytokine levels, determined by the Mouse 12-Plex Cytokine Kit (Ayoxxa), confirmed the strong anti-tumoral immune reactivities in CAR$^+$ T cell - treated mice (see Figure 4.8.3). In particular, levels of many pro-inflammatory and T cell activation-associated cytokines such as GM-CSF, IL-1ß, IL-12, IL-2 and IL-6 were strongly increased upon CAR$^+$ T cell treatment. However, elevated concentrations of anti-inflammatory cytokines such as IL-4 and IL-10 were also found in those mice.

Overall, these data confirm the *in vitro* results showing that murine anti NY-BR-1 CAR$^+$ T cells, especially clone3 and 10D11 CAR$^+$ T cells, exerted strong suppressive effects on tumor outgrowth in the NOD.CB17-Prkdc^{scid} ectopic mouse model, which provoked prolonged median and overall survival rates.

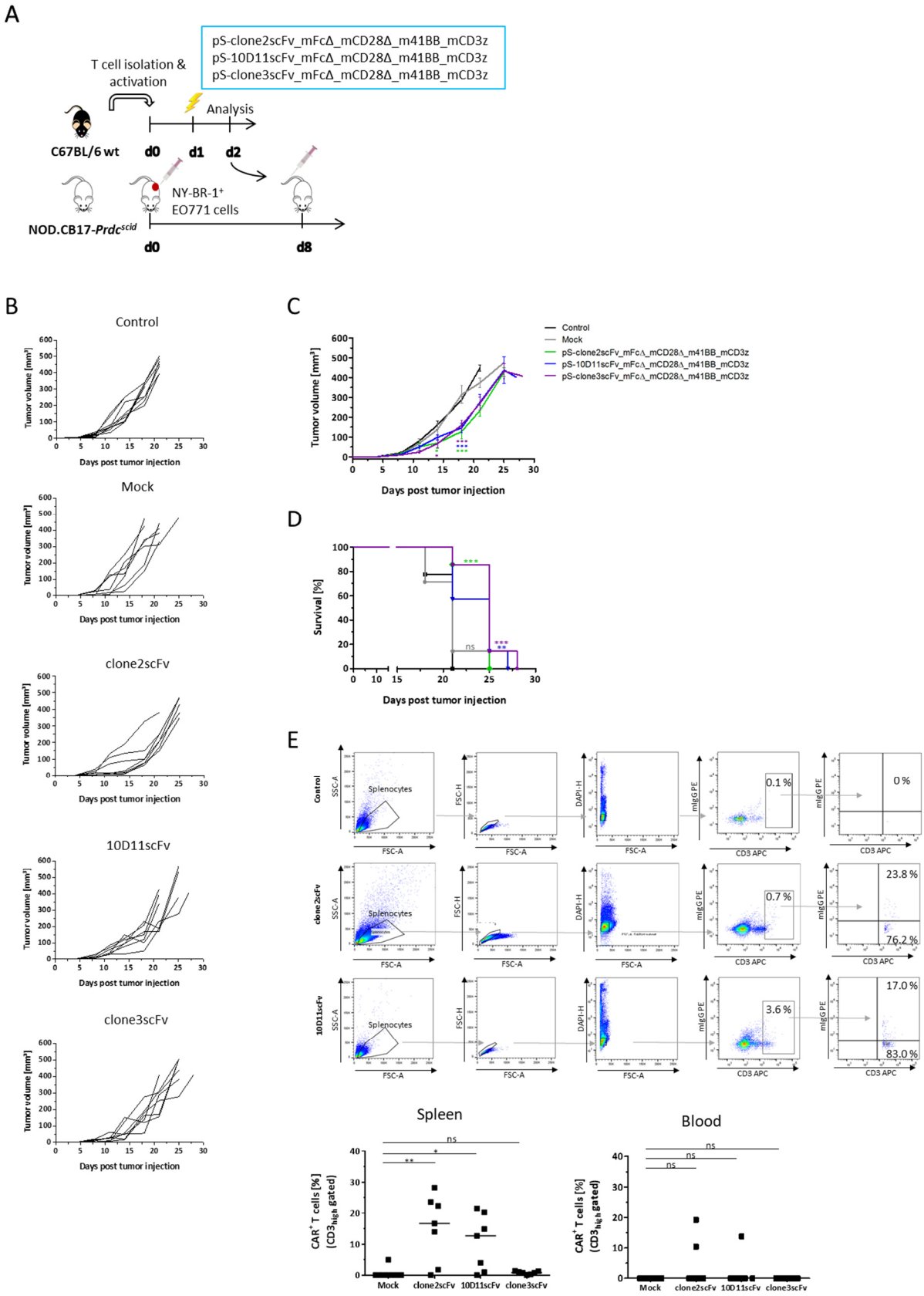

Figure 4.8.1: Effect of pS/MARter electroporated murine CAR+ T cells on outgrowth of NY-BR-1+ EO771 derived tumors in NOD.CB17-Prkdc*scid* mice

[A] Following one day of activation, murine T cells were electroporated with pS/MARter vectors encoding the anti-NY-BR-1 CAR constructs clone2scFv_mFcΔ_mCD28Δ_m4-1BB_mCD3z (#277), 10D11scFv_mFcΔ_mCD28Δ_m4-1BB_mCD3z (#295) and clone3scFv_mFcΔ_mCD28Δ_m4-1BB_mCD3z (#296). Eight days post tumor engraftment of NOD.CB17-Prkdc*scid* mice (2x10^6 NY-BR-1+ EO771 cells / mouse), electroporated anti-NY-BR-1 CAR+ T cells (5x10^5 CAR+ T cells / mouse) or untransfected (mock)

T cells were injected intravenously. Untreated mice served as controls. Each group, except for control (n = 9), consisted of seven mice. [B], [C] Tumor volumes were measured every three to four days. [B] Each line indicates one mouse. The average tumor volumes are illustrated in [C] (mean values ± sem; *, $p < 0.05$; ***, $p < 0.001$; Two-way ANOVA with Bonferroni post test for comparison with mock group). Tumor engrafted mice were sacrified at a tumor diameter of 15 mm or a tumor volume of 450 mm^3, whatever occurred first. Tumor volumes were calculated with the ellipsoid formula (1/6 x π x length x width x depth). [D] The corresponding survival rates are illustrated as Kaplan-Meier survival curves. Survival rates were compared with control group by using Log-rank (Mantel-cox) test (*, $p < 0.05$; **, $p < 0.01$; *** ≤ 0.001). [E] Isolated spleens and blood were examined for T cell infiltration by flow cytometric analysis. Cells were stained with the APC - conjugated anti-mouse CD3 (17A2) and PE - conjugated anti-mouse IgG antibodies. Exemplary gating strategy for the detection of $CD3^+$ CAR^+ cells in spleens of untreated or clone2 and 10D11 CAR^+ T cell – treated mice is displayed. Percentages indicate the proportion of $CD3^+$ CAR^+ cells after gating on all living ($DAPI^-$) $CD3_{high}^+$ cells (lines indicate the medians; n = 7; *,$p < 0.05$; ** , $p < 0.01$; Kruskal Wallis test followed by Dunn's multiple comparison test).

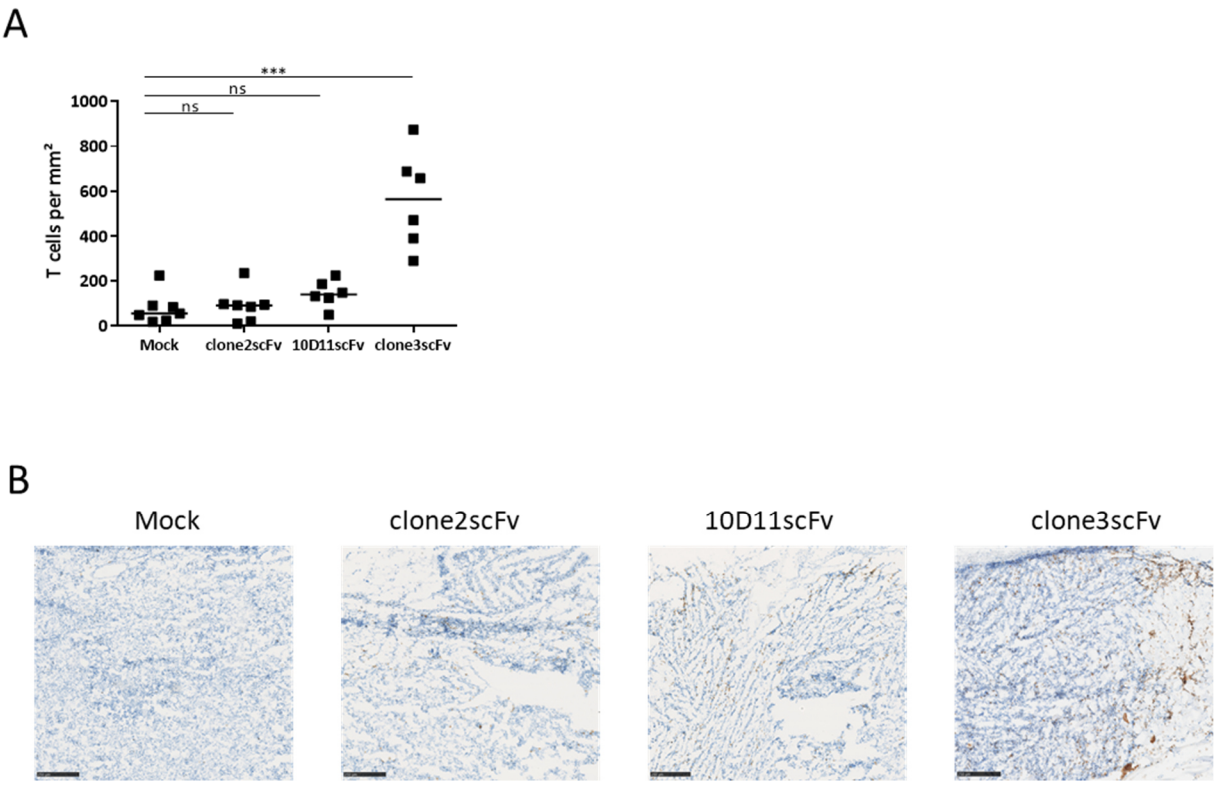

Figure 4.8.2: Immunohistochemistry analysis of NY-BR-1^+ EO771 tumor - infiltrating T cells
NY-BR-1^+ EO771 derived tumors, isolated from NOD.CB17-Prkdc^{scid} mice upon CAR^+ T cell (#277, #295, #296) treatment, were analyzed for infiltrated T cells via immunohistochemistry analysis. Cryosections were stained with the rabbit anti-mouse CD3 (Abcam, 16669) and HRP - conjugated anti-rabbit IgG antibodies (staining was performed by Rosa Eurich). [A] The absolute numbers or rather densities of infiltrated T cells are illustrated as a scatter dot plot. Each dot represents one mock or CAR^+ T cell - treated mouse (lines indicate the medians; mock, clone2scFv: n = 7; 10D11scFv, clone3scFv: n = 6; ***, $p < 0.005$; Kruskal-Wallis test and Dunn's multiple comparisons test). [B] Representative examples of tumors stained for $CD3^+$ cells. Scale bars present 250 µm.

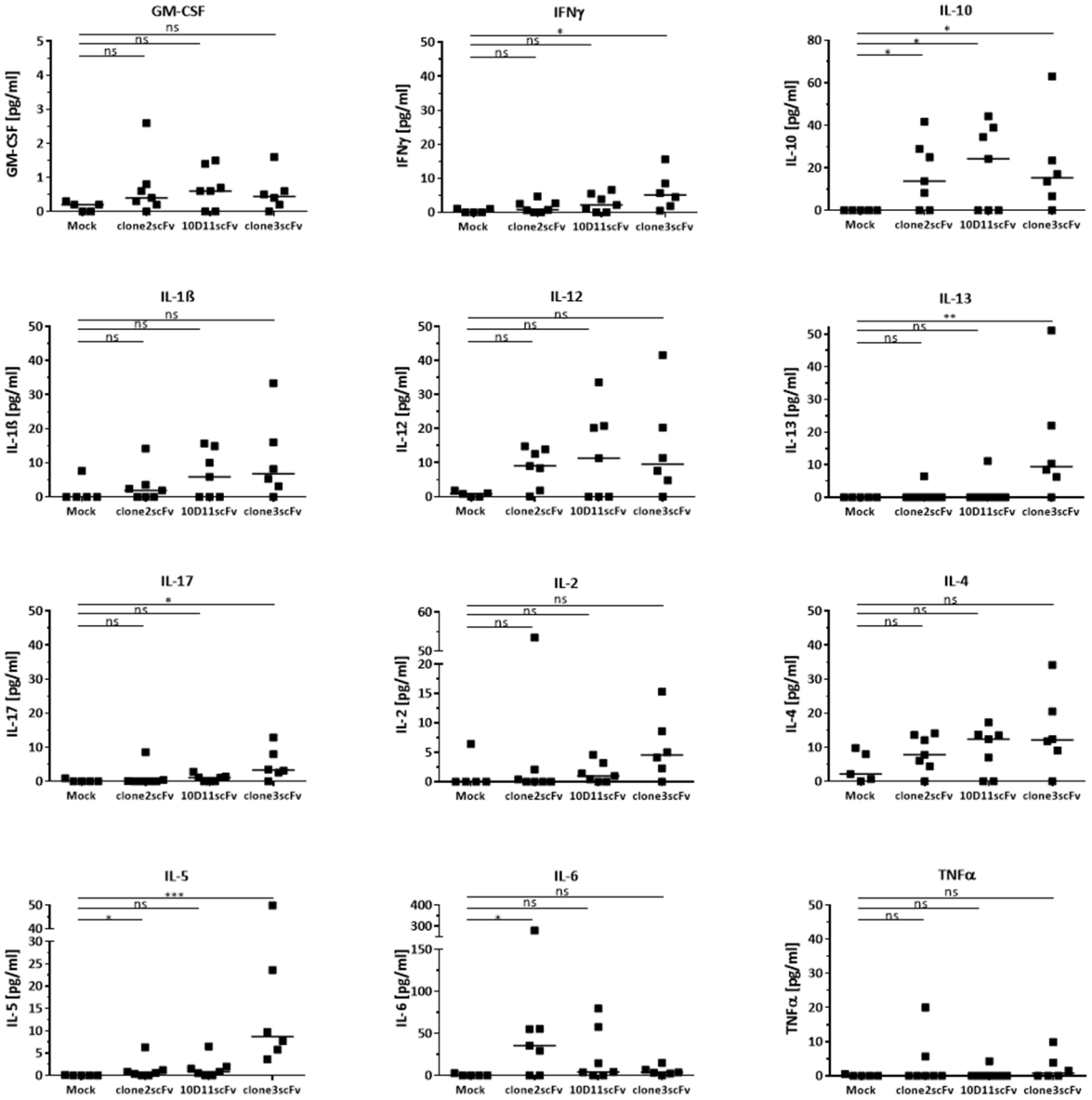

Figure 4.8.3: Plasma cytokine profile of tumor-bearing NOD.CB17-Prkdc^{scid} mice upon treatment with murine pS/MARter electroporated CAR$^+$ T cells

NOD.CB17-Prkdc^{scid} mice were engrafted with NY-BR-1$^+$ EO771 tumors (2x10^6 NY-BR-1$^+$ EO771 cells / mouse) and treated with anti-NY-BR-1 (#277, #295, #296) CAR$^+$ T cells (5x10^5 CAR$^+$ T cells / mouse) or untransfected (mock) T cells. Tumor engrafted mice were sacrified at a tumor diameter of 15 mm or a tumor volume of 450 mm³ at the latest, calculated with the ellipsoid formula (1/6 x π x length x width x depth). Subsequently, the cytokine concentrations in murine blood were assessed by using the Mouse 12-Plex Cytokine Kit (Ayoxxa) (lines indicate the medians; mock: n = 5; clone2scFv, 10D11scFv: n = 7; clone3scFv: n = 6; *, $p < 0.05$; **, $p < 0.01$; Kruskal-Wallis test followed by Dunn's multiple comparison test).

5 Discussion

The lack of tumor specific antigens represents a big obstacle for CAR$^+$ T cell - based therapies of solid tumors. Therefore, the aim of this work was to evaluate three CAR candidates directed against the breast cancer associated antigen NY-BR-1 for their efficacy and safety in preclinical studies.

5.1 Current state of CAR$^+$ T cell therapies for breast cancer

The use of CAR$^+$ T cells has been particularly successful in the treatment of hematological diseases. Indeed, CD19 CAR$^+$ T cell therapy has already been approved for certain hematological malignancies (such as Kymriah™ for recurrent ALL and Yescarta™ for relapsed or refractory DLBCL) in the USA and Europe [229]. However, the situation is different for solid tumors because of hampered CAR$^+$ T cell trafficking and infiltration into the tumor as well as immunosuppressive tumor microenvironments [160]. Moreover, the biggest problem represents the lack of targetable tumor specific antigens, so that CAR$^+$ T cell therapies are often associated with a high risk of on target / off tumor toxicity [162,230,231]. The breast cancer associated antigen NY-BR-1 might represent a targetable antigen, as it is expressed exclusively in healthy breast, testis and prostate tissue and shows strong over-expression in the majority of breast cancer tumors (> 70 %) and metastases [94,96,232], whereby the latter might play a key role for CAR - based immunotherapy, as most breast cancer patients die due to metastases [233].

Currently, there is no approved CAR$^+$ T cell therapy for the treatment of breast cancer worldwide. Several clinical trials targeting, for example, HER2 (NCT02547961), EpCAM (NCT02915445) ROR1 (NCT02706392), CD70 (NCT02830724), Mesothelin (NCT02792114), cMet (NCT03060356), Muc1 (NCT04025216) or Muc1* (NCT04020575) are ongoing. However, these therapies are usually limited in their applicability or carry certain risks of toxicity. For example, anti-HER2 CAR$^+$ T cell therapies are limited to HER2 positive breast cancer subtypes. As NY-BR-1 expression inversely correlates with *HER2* status [94], anti-NY-BR-1 CAR$^+$ T cell therapies might be useful to close this gap. In addition, toxic on target / off tumor reactivities have been observed in anti - HER2 CAR$^+$ T cell therapies [162]. Furthermore, the epithelial cell adhesion molecule (EpCAM) is over-expressed in many carcinomas [234-236] , including breast cancer [237], but is also found in normal epithelial tissues at low levels [238], which might lead to toxic side effects in CAR$^+$ T cell therapies. In addition, several studies demonstrated decreased EpCAM expression levels after chemotherapies [235,239], in contrast to NY-BR-1 [94]. Mesothelin, a glycosylphosphatidylinositol-linked cell surface antigen, is present in normal mesothelial cells and over-expressed in several malignancies, including breast cancer [240]. However, in contrast to NY-BR-1 [88,94], Mesothelin is mainly over-expressed in ER$^-$ or triple - negative breast cancer tumors [240].

Thus, breast cancer patients should be stratified for the expression of NY-BR-1, which might represent an additional, useful CAR target that addresses or fills many of the limitations or gaps of existing breast cancer targets. However, since the exact function of NY-BR-1 is unknown and pre-clinical studies using anti-NY-BR-1 CAR$^+$ T cells have not been conducted so far, it was unclear to what extent this protein would actually be suitable as a target. In the course of this work, this fundamental question should be answered and at the same time three different anti-NY-BR-1 CARs (clone2, 10D11 and clone3) should be examined for their applicability to clinical trials.

5.2 NY-BR-1 expression depends on the cell cycle phases in transduced cell lines

Due to the facts that breast cancer cell lines generally do not show surface expression of NY-BR-1 [93,96,224] and that NY-BR-1 transduction of different cell lines resulted in growth stop and loss of NY-BR-1 expression in preliminary experiments [224] (unpublished data) stable NY-BR-1 expressing target cell lines had to be generated at the beginning of this work. The human Bosc23 and HEK 293T as well as the murine EO771 cell lines were transduced with the HIV - derived lentiviral expression vector #44 (hPGK_NY-BR-1_IRES_Puromycin_WPRE) encoding for the full length NY-BR-1 protein and puromycin N-acetyltransferase.

Although lentiviral transductions were successful in both human cell lines, transduced Bosc23 cells showed generally higher NY-BR-1 surface expression levels than HEK 293T cells. In addition, NY-BR-1 expression levels decreased in both transduced cell lines after a short time and fluctuated daily despite puromycin selection pressure (see Figure 4.1.1; Figure 4.1.2), which will be discussed later in connection with EO771 cells. The differences in NY-BR-1 expression levels between Bosc23 and HEK 293T cells were surprising, as Bosc23 cells originally derived from HEK 293T cells by stable introduction of two retroviral (M-MuLV derived) packaging plasmids: pCRIPenv$^-$ (expressing gag, pol) and pCRIPgag-2 (expressing env) [220]. The reason for higher NY-BR-1 expression levels in transduced Bosc23 cells cannot be the permanent production of retroviral particles harboring the *NY-BR-1* transgene, since Bosc23 cells were originally transfected with vectors encoding for retroviral and not lentiviral packaging genes. Lentiviral (here HIV derived) and retroviral (here MLV derived) packaging genes, especially the packaging signals Ψ, and LTRs are different, which leads to the fact that (HIV derived) lentiviruses cannot be packaged by (M-MuLV derived) retroviruses [241,242]. Therefore, one possible reason might be the different activities of the non-receptor tyrosine kinase src, since this kinase is inactive in Bosc23 [243] but active in HEK 293T cells [244]. Possible interactions between the src kinase and NY-BR-1 have not been studied intensively so far, but the src kinase plays an important role in many signaling pathways via interactions with tyrosine kinases, steroid and G-protein-coupled receptors as

well as signal transducers and activators of transcription and molecules involved in cell adhesion and migration [245,246]. Indeed, the *src* proto-oncogene has also been attributed an important role in the development, growth and progression of many cancer types, including colon, breast, pancreas and brain [245,247,248]. In fact, strongly increased src activities have been documented in breast tumors, which appears to be more attributed to the deregulated protein src than to mutations in the gene [246]. In particular, results of various studies revealed interactions between src and hormone receptors such as ER or the protein HER2 [249] and, indeed, several src inhibitors have been successfully tested in clinical breast cancer trials [246]. Both the *NY-BR-1* gene [224]and promoter region [88] exhibit multiple binding sites for ER and, furthermore, positive correlations between NY-BR-1 and ER expression have already been reported [88,224]. However, despite these correlations between ER and src and ER and NY-BR-1 expression, it is unclear to what extent a negative correlation between src and NY-BR-1 may exist and need to be investigated in further experiments. For example, NY-BR-1 transduced HEK 293T cells and NY-BR-1 expressing primary cells could be treated with src inhibitors and examined for NY-BR-1 expression at both RNA and protein level. Since HEK 293T cells lack expression of estrogen receptors [250], these cells are ideal for further analysis in order to avoid additional effects of src and src inhibitors on ER expression, which in turn could influence NY-BR-1 expression.

In addition to the mentioned human cell lines, the murine EO771 cell line was also successfully engineered to express the NY-BR-1 full length protein (see Figure 4.1.3). All three monoclonal antibodies (clone2, 10D11, clone3) detected NY-BR-1 intracellular and on the cell surface, which is consistent with results of various studies on its intracellular and transmembrane localization [95,251]. However, significantly more cells showed cytoplasmic rather than surface NY-BR-1 expression (see Figure 4.1.3), which is consistent with other studies that observed a preferential cytoplasmic localization of NY-BR-1 [94,251]. Noteworthy here was that flow cytometric analyses using the clone3 antibody revealed significantly fewer cells with cytoplasmically expressed NY-BR-1 compared to intracellular stainings with the 10D11 and clone2 antibodies. Since this effect was not observed with cell surface stainings, it can be assumed that the epitope of the clone3 antibody was efficiently expressed. However, one possible reason for these different results might be that the cytoplasmic NY-BR-1 protein was in a folded state, which results in an inaccessibility to the binding site of the clone3 antibody.

Over time, lentivirally transduced EO771 cells showed strongly decreasing NY-BR-1 expression levels, both intracellular and on the cell surface, which was consistent with observations in transduced Bosc23 and HEK 293T cells (see above, Figure 4.1.3). Since the expression levels fluctuated daily and decreased to almost 0 % in NY-BR-1$^+$ EO771 or 9 % in NY-BR-1$^+$ Bosc23 cells, the influence of the cell cycle and possible degradation via proteasomes was examined in both transduced cell lines using various cell cycle inhibitors such as Nocodazole [252], Thymidine [253], Aphidicoline [252] and L-mimosine [254]

as well as the proteasome inhibitor Lactacystin [255]. Indeed, positive correlations between G1 phase and NY-BR-1 expression rates paired with simultaneous negative correlations between G2 phase and NY-BR-1 expression rates were found at both the RNA and protein levels (see Figure 4.1.2, Figure 4.1.4). In addition, Lactacystin treatment resulted in greatly increased NY-BR-1 surface expression levels in both transduced EO771 and Bosc23 cells, which indicates a possible degradation of the protein and may also explain the increased intracellular expression levels of NY-BR-1 compared to the surface in transduced EO771 cells (see Figure 4.1.2, Figure 4.1.3, Figure 4.1.4). The positive association between Lactacystin treatment and NY-BR-1 protein levels in transduced EO771 cells was also reported by Krishna Das (2017) [256]. However, Lactacystin acts not only on proteasome activity but also on the cell cycle by blocking the G0/G1 and G2/M phases [257]. Consequently, increased NY-BR-1 expression levels might be based on both impaired protein degradation and cell cycle inhibition. This is also supported by the 13-fold increase in *NY-BR-1* expression levels in Lactacystin treated transduced EO771 cells (see Figure 4.1.4). As the RNA expression levels were higher under Lactacystin than under Thymidine double block, the latter leads to G1 arrest, a positive feedback loop could alternatively be conceivable, in which increased levels of the NY-BR-1 protein have an additional positive effect on the expression itself. In order to explore the sole effect of proteasome inhibition on NY-BR-1 protein levels, experiments with further inhibitors that do not influence cell cycle progression should be performed.

If a closer look is taken again at the cell cycle, especially at the G1 phase, the fact that a combined treatment of Nocodazole, as a reversible G2 blocker, and Lactacystin, as an irreversible G1 and G2 blocker (and proteasome inhibitor), led to a greater proportion of G1 phase arresting cells in NY-BR-1$^+$ EO771 than in EO771 wild-type cells suggests that not only a G1 phase block leads to increased NY-BR-1 expression levels but also, reciprocally, increased NY-BR-1 expression levels result in enhanced frequencies of G1 arresting cells (see Figure 4.1.4). All these results are consistent with data from Bitzer (2015) [224], who demonstrated that NY-BR-1 over-expressing cell lines arrest in G1 phase and do not undergo apoptosis. Similar observations were made for the estrogen receptor (ER), whose expression is enhanced during G1 phase in Thymidine - synchronized MCF-7 cells [258]. That ER expression is generally positively correlated with NY-BR-1 in breast cancer tumors has already been demonstrated in several studies [88,224] and might be further supported by the data shown here.

However, a direct comparison of transduced EO771 and Bosc23 cells revealed lower NY-BR-1 expression rates in EO771 cells with and without Lactacystin treatment or G1 arrest (see Figure 4.1.2, Figure 4.1.4). To date, no murine equivalent of NY-BR-1 is known. Therefore, the reasons for different NY-BR-1 expression profiles might be manifold and could include both gene silencing and post-transcriptional modifications of the transgene, which has been attributed to loss of gene expression and mosaic-like expression patterns in numerous lentivirally transduced clones and transgenic organisms [259-262] . These phenomenons might be more prominent in murine EO771 cells than in human

Bosc23 cells. In this context, it is also conceivable that high NY-BR-1 protein levels are not tolerated in EO771 cells, which might lead to a protective down-regulation of NY-BR-1 expression. In addition, it is known that promoters affect the level of transgene expression [263-265] and that the strengths of promoters differ across various cell types [263,264]. However, since transduced EO771 cells initially exhibited high NY-BR-1 expression levels, a direct correlation between the strength of the hPGK promoter and loss of *NY-BR-1* expression is not assumed. Moreover, the activity of the src kinase in (NY-BR-1$^+$) EO771 cells should be investigated in more detail in order to identify a possible relationship between src and NY-BR-1, as suggested in transduced Bosc23 and HEK 293T cells.

G1 accumulation / arrest of NY-BR-1 expressing cells together with the mosaic-like expression pattern of NY-BR-1 protein in normal breast tissue [224] and the presence of NY-BR-1$^+$ cells in mammospheres [224] suggest that this protein might be a stem / progenitor marker. However, it is also known that NY-BR-1 expression is associated with “good prognosis” tumors which exhibit low malignant potentials (tumor grade 1) [251] and usually derive from mutations in differentiated progenitor cells [10]. All these results, as well as other studies such as the performance of a soft agar experiment in which NY-BR-1 transfected cells were able to form colonies [93], suggest that this protein might play an important role in tumorigenesis.

Next to NY-BR-1`s role in tumorigenesis and its effect on cell cycle, cell density also has a significant impact on NY-BR-1 expression, because prolonged cultivation periods without splitting led to higher cell densities and rising NY-BR-1 expression levels in transduced Bosc23 cells. This observation was confirmed by further experiments in which increasing seeded cell densities caused enhancing NY-BR-1 expression levels within a few days (see Figure 4.1.2). This phenomenon could be a result of G1 arrest, as cell proliferation, contact inhibition and cell cycle are related by different signaling pathways [266,267]. Another reason might be interactions between the ankyrin (ANK) repeat motifs within the NY-BR-1 protein [85] and other proteins associated with cell adhesion and cell-cell contacts. The exact function of NY-BR-1 is unknown so far, but ankyrin motifs generally mediate important protein-protein interactions which regulate or induce, among others, cell-cell signaling / interactions [268], cell development [269], cell adhesion [268,270], transcription of genes [271], cytoskeletal or membrane stability [270,272] or linkage between the spectrin-based cytoskeleton and integral membrane proteins [270,271], so that a role of NY-BR-1 in cell-cell interactions is also conceivable. These potential protein - protein and cell - cell interactions as well as NY-BR-1's possible role as a stem / progenitor marker [224] suggest that low NY-BR-1 expression levels, as found in healthy breast tissue [90,93], may even be protective for the cell and important for the maintenance of the entire breast tissue. Therefore, it might be important to avoid detection and killing of NY-BR-1 weakly expressing cells by high affinity anti-NY-BR-1 CARs (see chapter 5.6).

5.3 Expression analysis of human and murine anti-NY-BR-1 CARs in lentivirally transduced and electroporated T cells

On the basis of the three monoclonal antibodies clone2 [273], 10D11 (unpublished) and clone3 [273], which are directed against NY-BR-1 and differ in their corresponding epitopes (see chapter 1.2.1.2), human CARs were generated in previous work by our group (unpublished). To test these CARs in both human and murine systems, the human Fc (hIgG1), transmembrane and co-stimulatory domains were successfully exchanged for corresponding murine Fc (mIgG1), transmembrane and co-stimulatory domains by using classical cloning methods as well as the Gateway and In-Fusion technologies (see Figure 4.2.1, Figure 4.2.2, Figure 4.2.3). The cloned fragments exhibited mutations in the murine Fc / mIgG1 (TVPEV → NILGG) and CD28 (TRKPYQPYAPARDF → TRKAYQAYAAARDF) domains by exchanging mIgG1 amino acids indispensable for binding FcγR with mIgG3 amino acids and mutating the CD28 binding domain of the Lck enzyme to prevent, on the one hand, binding of Fcγ receptors to the Fc domain causing "off target" toxicity, undesirable activation of innate immune responses [274] and ,on the other hand, increased IL-2 secretion that usually promotes differentiation and maintenance of T_{reg} cells [275]. The murine CAR (scFv_ mFcΔ_mCD28Δ_m4-1BB_CD3z) – encoding DNA segments were successfully cloned into both lentiviral (pRRL) and S/MAR (pS/MARter) vector systems (the latter was kindly provided by Dr. Richard Harbottle and Dr. Matthias Bozza (DKFZ, DNA Vector Research Group)), to establish a new S/MAR based transfection technology for the generation of murine CAR - expressing T cells.

The anti-NY-BR-1 scFvs were additionally cloned into diverse human CAR backbones (hFcΔ_hCD28Δ_h4-1BB_CD3z; hFc_hCD28_CD3z_hOX40) with or without mutations in the Fc / hIgG1 (PELLGG → PPVAG; ISR → IAR) and CD28 (PYAPA → AYAAA) domains by exchanging hIgG1 amino acids indispensable for binding FcγR with hIgG2 amino acids and mutating the Lck binding motif in the CD28 domain for the above mentioned reasons. The different CAR backbones should allow study of the effect of different co-stimulatory domains on CAR expression and effectiveness. During this process, human anti-NY-BR-1 CAR – encoding DNA sequences were successfully cloned into different vector types (pRRL, pS/MARter, NanoCMARter (kindly provided by Dr. Richard Harbottle and Dr. Matthias Bozza (DKFZ, DNA Vector Research Group)) to compare different transfection systems regarding their effectiveness (see Figure 4.2.4, Figure 4.2.5, Figure 4.2.6, Figure 4.2.7).

5.3.1 Anti-NY-BR-1 CAR - expressing human T cells are reliably generated by the pS/MARter and NanoCMARter based electroporation systems

The productions of lentiviral expression vectors encoding for the human anti-NY-BR-1 CAR constructs with different scFvs (clone2, 10D11, clone3) and distinct intracellular signaling domains (hFcΔ_hCD28Δ_h4-1BB_CD3z; hFc_hCD28_CD3z_hOX40) were successful (see Figure 4.3.1). Upon lentiviral gene transfer into human T cells, all tested, synthetic immunoreceptors were detected on the cell surface via flow cytometric analyses using the fluorophore conjugated anti-human IgG antibodies that bind to the CARs' Fc domains. Indeed, the clone2 and 10D11 CARs were expressed with nearly same frequencies in human T cells, whereas the clone3 CAR showed slightly reduced expression levels (see Figure 4.3.1). The direct comparison of hCD28Δ_h4-1BB_CD3z and hCD28_CD3z_hOX40 CARs revealed higher CAR expression levels in lentivirally transduced human T cells when the hOX40 domain was used instead of the h4-1BB motif (see Figure 4.3.1). Similar observations were seen with electroporated T cells. Here, pS/MARter vectors expressing different anti-NY-BR-1 CAR constructs (scFv_hFcΔ_hCD28Δ_h4-1BB_CD3z; scFv_hFc_hCD28_h4-1BB_CD3z; scFv_hFc_hCD28_CD3z_hOX40) were applied for the electroporation of human T cells using the Neon Transfection System (ThermoFisher). This new S/MAR based system, which will be discussed in more detail later, actually resulted in the surface expression of all tested CAR constructs in human T cells, whereby no statistically significant differences between the scFvs were observed (see Figure 4.3.2). However, hFc_hCD28_CD3z_hOX40 CARs showed again significantly higher expression levels than hFcΔ_hCD28Δ_h4-1BB_CD3z and hFc_hCD28_h4-1BB_CD3z CARs. In this context, it was not surprising that mutated and non-mutated hCD28 and Fc domains provoked similar CAR expression levels, since this was consistent with other studies demonstrating that those mutations do not affect CAR expression levels [276-278]. However, the question arises why hFc_hCD28_CD3z_hOX40 CARs showed significantly increased expression levels upon both lentiviral transduction and pS/MARter electroporation of human T cells despite the same transmembrane (CD28) region, length of the spacer domain and (membrane-proximal) position of the CD28 domain, which usually all play crucial roles for surface CAR expression levels [274,277,279-281]. Consequently, in the case of the anti-NY-BR-1 CAR constructs tested here, the replacement of the membrane-proximal 4-1BB domain with the terminal OX40 motif might be of significant importance for different CAR expression levels.

CD28, 4-1BB and OX40 affect the metabolism of CAR - expressing T cells in different ways. While T cells expressing CD28_CD3z CARs of the second generation tend to exhibit an effector memory phenotype with increased glycolysis metabolism, 4-1BB_CD3z CAR^+ T cells show increased potential for persistence and exhibit a central memory phenotype with enhanced oxidative metabolism [142]. However, by direct comparison of the expression levels in human T cells, CD28 and 4-1BB containing

CARs of the second generation do not differ usually [142,282]. OX40 belongs together with 4-1BB to the "late" co-stimulatory domains, which are normally upregulated after T cell activation [283,284]. Several studies demonstrated that OX40 generally enhance effector cytokine secretion[283,285], augment CD28 activated T cell responses [283,285] and, in case of OX40 containing CARs, leads to reduced IL-10 secretion in CAR$^+$ T cells [286]. Nevertheless, different trials reported similar expression levels of CD28_CD3z CARs and CD28_CD3z_OX40 or CD28_OX40_CD3z CARs despite the diverse mentioned metabolic effects [279,286,287]. In comparison to the CARs used here, some CARs of the other studies [279,287] did not include OX40 at the terminal end, but instead between CD28 and CD3z, which might have different effects on the CAR expression levels. An additional and perhaps decisive difference to these trials is that they compared second generation (CD28_CD3z, 4-1BB_CD3z) and not third generation CD28_4-1BB_CD3z CARs with corresponding third generation OX40 containing CARs as it was done in this thesis, since third generation CARs with CD28_4-1BB_CD3z domains sometimes provoke lower expression levels than their second generation (CD28_CD3z; 4-1BB_CD3z) counterparts [288-290]. Therefore, further experiments with anti-NY-BR-1 CAR constructs containing only the individual CD28, 4-1BB and OX40 domains or combinations of these at different positions have to be carried out to allow a clear statement on whether this discovered phenomenon is actually based on OX40 per se or the deletion of 4-1BB. Moreover, these analyses have to be performed with different scFvs directed against other targets (like CD19, CEA) in order to rule out that this phenomenon is not limited to anti-NY-BR-1 CARs.

Apart from pS/MARter vectors, the further developed NanoCMARter vectors, which encoded for anti-NY-BR-1 CAR constructs with two different backbones (hFc_CD28_4-1BB_CD3z; hFc_CD28_CD3z_OX40), were also utilized for the generation of human CAR$^+$ T cells. Indeed, these vectors led to superior expression levels of hFc_CD28_4-1BB_CD3z CARs compared with the corresponding pS/MARter vectors, but hFc_CD28_CD3z_OX40 CAR expression levels did not differ significantly between both vector systems (see Figure 4.3.3). Hence, the pS/MARter and NanoCMARter based electroporation technologies yielded comparable and in some cases slightly higher expression levels of anti-NY-BR-1 CARs than lentiviral transduction. These results are consistent with data from further studies in which GFP, TCR or CAR - expressing T cells were successfully generated with pS/MARter vectors and displayed high expression levels of the transgenes over several weeks [172,291] (unpublished data). In fact, NanoCMARter vectors encoding for different CARs (e.g. anti-CD19 or CEA) provoked in some cases even better CAR expression rates than the corresponding pS/MARter vectors (unpublished), which is also in line with results presented here (see Figure 4.3.3). Both vector systems (pS/MARter and NanoCMARter) used here encode for the hPGK promoter, Element 40, which is known to act as an efficient anti-repressive insulator [292], as well as the ApoL MAR motif, which is composed of a repetitive mosaic of ATTA-ATTTA sequences [172]. Therefore, the biggest differences and reasons for diverse expression levels might lay in the vector sizes themselves and the strongly minimized bacterial

backbone (small bacterial ori, lack of antibiotic resistance genes) in NanoCMARter vectors, which are therefore expanded via a so-called RNA-OUT selection system. This system allows a sucrose selection in a specially engineered strain of *E.Coli* by a small interfering RNA (iRNA) motif encoded on NanoCMARter vectors [172] (see chapter 1.2.2.2). The fact that a minimized bacterial backbone leads to increased expression levels of the transgene has been shown for different cell types using so-called minicircles resembling NanoCMARter vectors [211,293-295]. This is based on the fact that bacterial sequences, especially bacterial oris and antibiotic resistance genes, are rich in unmethylated CpG dinucleotides, which trigger gene silencing by methylation in eukaryotic cells [211,293-295]. Furthermore, immune cells, including T cells, react very strongly to foreign (bacterial) DNA [296,297]. Toll-like receptors, such as TLR9, and the STING (Stimulator of Interferon Genes) protein play a major role in this process [297]. In fact, TLR9 recognizes unmethylated bacterial DNA [298,299], whereas STING is activated by binding to cyclic dinucleotides (CDNs) [300]. The latter are produced by bacteria themselves or by a host cyclic GMP-AMP synthase (cGAS) upon activation by cytoplasmic dsDNA [300-302]. Activation of TLR9 and STING leads to inflammatory responses including increased production of type I interferons, which contribute to anti-bacterial and -viral responses [297,300]. In the case of electroporated T cells, the pro-apoptotic effects of type I interferons [303,304] might also have a negative impact on survival and transfection efficiency of T cells. Indeed, a comparison of NanoCMARter and pS/MARter anti-CEA CAR^+ T cells revealed lower expression levels of type I interferons in NanoCMARter CAR^+ T cells (unpublished). In order to confirm these preliminary results and to investigate whether NanoCMARter vectors are actually superior to pS/MARter vectors, NanoCMARter and pS/MARter electroporated anti-NY-BR-1 CAR^+ T cells should also be examined for the production of these cytokines by, for example, intracellular flow cytometric analysis, and quantification of type I interferon concentrations in the cell culture supernatants as well as single-cell RNA analyses. Further analyses should be performed on the expression of pro-apoptotic proteins. In addition, the proportion of T_{reg}, exhausted and apoptotic T cells upon electroporation could also provide further information about the effects of these vectors on cytokine release as well as T cell metabolism and differentiation.

Additionally, the size of NanoCMARter vectors in respect to full length (pS/MARter) vectors might have a positive effect on transfection efficiency. Although equimass but not equimolar amounts of transfected pDNA of distinct lengths cause different number of DNA molecules per cell [305], transfection efficiency / transgene expression, mean fluorescence intensity and cell survival correlate inversely with plasmid size in both equimolar and equimass experiments [305-308]. Reasons for these effects might be manifold and the underlying mechanisms are not completely known but they may include, among others, prolonged permeabilization of the plasma membrane in the presence of large plasmids leading to a need for longer recovery time in order to reseal the membrane when compared to cells electroporated with smaller plasmids[306,309]. Indeed, Lesueur et al. (2016) [306] demonstrated that a

prolonged recovery time improves both cell survival and transfection efficiency for large plamids [306,310]. In this thesis, however, pS/MARter and NanoCMARter vectors were applied at equimass concentrations, resulting in higher copy number of the (anti-NY-BR-1) CAR transgene in NanoCMARter transfections. Hornstein et al. (2016) [305] also reported that the amount of DNA molecules per cell differs between minicircles and normal plasmids in equimass experiments. An additional reason for higher anti-NY-BR-1 CAR expression levels in NanoCMARter electroporated T cells might be the lower mobility of large plasmids, which in turn might lead to reduced DNA-membrane interactions and slower / weaker uptake of pS/MARter vectors compared to NanoCMARter vectors. However, Leseur et al. (2016) [306] showed that extended pulses do not positively affect the transfection efficiency of large plasmids, which contradicts the hypothesis of slower uptake. Thus, different anti-NY-BR-1 CAR expression profiles in pS/MARter and NanoCMARter electroporated T cells are probably caused by both the minimized bacterial backbone and the reduced vector length itself, which leads to partially unclear effects on transgene expression [305,306].

Overall, these results reveal that the refinement of the original famous S/MAR based pEPI vector to pS/MARter and NanoCMARter vectors [172] (patent WO2019/060253Al) created a useful tool for gene-engineering of human T cells. Hence, these novel S/MAR based technologies represent innovative, cheaper and simpler methods for the generation of human anti-NY-BR-1 CAR^+ T cells compared to the complex and expensive production of lentiviral particles.

5.3.2 The pS/MARter based electroporation system as a new tool for the generation of CAR - expressing murine T cells

Having successfully generated human anti-NY-BR-1 CAR - expressing T cells, the synthetically generated murine anti-NY-BR-1 immunoreceptors should also be investigated for their expression capacity. The lentiviral productions of expression vectors encoding for three different murine anti-NY-BR-1 CAR constructs (attB1_clone2/10D11/clone3scFv_mFcΔ_mCD28Δ_m4-1BB_CD3z_attB2_hPGK_DsRed2_WPRE) were successfully performed via co-transfection of HEK 293T cells and subsequently used for the transduction of human (Jurkat) and murine (NIH/3T3) cell lines (see Figure 4.4.1). Flow cytometric analysis of the dsRED signal revealed high expression levels of all tested CAR constructs in both Jurkat and NIH/3T3 cells. However, lentiviral transduction of primary murine T cells, isolated from C57BL/6 mouse spleens, resulted in strongly fluctuating transduction efficiencies and low viability rates (see Figure 4.4.2). It was noticeable that cultivation of murine T cells proved to be difficult even without transduction and, additionally, neither double transductions on two consecutive days nor prolonged

activation periods or different medium compositions led to significant improvements. These results are confirmed by various studies, which also showed that murine T cells are hardly transducible with HIV-based VSV-G pseutotyped vectors because of various barriers to the HIV replication cycle [311-315]. Depending on the study, these barriers are based on diminished efficiency of nuclear translocation [313,314], reverse transcription [314] and chromosomal integration [312] .

Since electroporation of human T cells with S/MAR based vectors proved to be a favorable alternative to lentiviral transduction, the applicability of this method to murine T cells was examined. As no studies on this novel approach have been published so far, a protocol for the generation of murine CAR^+ T cells using this S/MAR based electroporation system had to be established first. During this process an optimization of the culture medium was essential to improve the overall viability of murine T cells. Initial electroporation experiments using the Neon Transfection System (ThermoFisher) and pS/MARter vectors encoding for the murine CAR constructs (clone2/10D11/clone3scFv_mFcΔ_mCD28Δ_m4-1BB_CD3z) led to different transfection efficiencies depending on the applied voltages as well as the number and length of pulses (see Figure 4.4.3). High voltages of up to 2000 V led to low viability rates in the first days after transfection but high CAR expression levels detectable for at least six days, which indicated stable transfection (see Figure 4.4.3 A). In contrast, low voltages of only 1000 V led to opposite effects. The viability rates of such T cells transfected with a high voltage of 2000 V increased again over time, which might be attributed to proliferation of surviving T cells. However, several repetitions of electroporation assays with 1900 V did not confirm this observation (see Supplementary Figure 6.5). Based on these initial results and following optimization of the cultivation medium by adding high concentrations of IL-2 and anti-CD3 / anti-CD28 antibodies, various voltages between 1500 V and 2000 V were tested for their efficiencies. In this context, it was particularly important to find the optimal relationship between CAR expression level and viability rates. Using a high number of consecutive pulses at a voltage of 1900 V provided the best achievable results (see Figure 4.4.3 D). All these data are in accordance with previous research findings. For example, Chicaybam et al. (2013)[316] also demonstrated that murine T cells must exhibit a high activation potential in order to transfect them efficiently with low mortality rates. In addition, various studies have shown that the voltage level required to exceed the electrical potential of the cell membrane inversely correlates with cell size [317,318] which, in turn, differs for each cell type. Moreover, the activation of T cells is associated with an increase in cell size [319,320]. In general, higher voltages lead to enhanced transfection efficiencies [318,321] but simultaneously to greater cell damages due to the generation of reactive oxygen species (ROS) [317] as well as irreversible damaging of the cell membrane and intracellular organelles, leading to cell death [322]. This is also reflected in the data shown here. Furthermore, the pulse duration represents an additional key variable for the optimal protocol, because the longer a pulse lasts, the larger the size and smaller the amount of resulting pores [318,323-

[325]. It is further assumed that prolonged pulses induce more stable complexes between DNA and membrane [317,324,326], which in turn improves DNA transfer and transfection rates. However, temperature increases have been reported in association with rising pulse length in electroporated cells [322], which might contribute to cell death. Due to these facts, the pulse length should be reduced with increasing voltage and vice versa [322]. Nevertheless, in this thesis, murine T cells were electroporated at 1900 V with pulse lengths of 10 ms, whereas human T cells were electroporated with a pulse length of 30 ms at 2200 V. The decisive difference was that murine T cells had to be electroporated with three consecutive pulses of 10 ms length at 1900 V, since a single pulse was not sufficient to achieve high CAR expression levels one day post electroporation (data not shown). Further studies confirm that the use of several consecutive pulses has a beneficial effect on transfection efficiency [309,327,328], as the transport of larger macromolecules (such as pDNA) is an active process or rather based on electrophoretic forces. A single pulse enables the permeabilisation of the membrane, but is sometimes not sufficient to transport DNA to the membrane or rather into the cells [309,327]. Numerous studies showed that a combination of short high-voltage pulses and long low-voltage pulses are advantageous for both cell viability and transfection efficiency [328-332] . Since this procedure could not be evaluated for murine T cells on the device used here, further experiments on other devices would be useful to further improve viability and transfection efficiency of murine T cells. Furthermore, the use of OX40 containing CAR constructs and / or NanoCMARter vectors may have a positive impact on viability and CAR expression levels, as observed in human T cells (see Figure 4.3.2; Figure 4.3.3). Nevertheless, significantly higher viabilities and transfection efficiencies were already achieved with the most optimized pS/MARter based electroporation protocol than with lentiviral transduction (see Figure 4.4.3 E, F).

Overall, the pS/MARter electroporation of murine T cells proved to be a useful, cost-effective and reliable technique for the generation of murine CAR^+ T cells, because this novel technology efficiently solves many problems associated with lentiviral transduction of murine T cells.

5.4 The clone2 CAR shows a strong cross-reactivity with the NY-BR-1.1 protein

The specificity of the different anti-NY-BR-1 CARs was initially assessed by determining the activation level of lentivirally transduced human CAR (clone2/10D11/clone3scFv_hFc_hCD28_hCD3z_hOX40) expressing T cells after 24 h cultivation in 96 well plates coated with NY-BR-1 full length proteins. Indeed, all three CAR constructs induced strong immune responses in lentivirally transduced T cells evidenced by elevated IFNγ releases compared to untransduced T cells, which confirmed the specificity of all three CAR constructs for the NY-BR-1

protein (see Figure 4.3.4). Additionally, the activation levels of clone2 CAR - expressing T cells were markedly enhanced compared to 10D11 and clone3 CAR$^+$ T cells. Since the applied CAR constructs only differ in their antigen binding domains (scFvs), the differences might be based on varying affinities / avidities. Thus, low affinity CARs need higher antigen densities for being activated and to reach the highest possible activation potential than high affinity CARs [333-335]. However, in order to make a clear statement about the affinities of the different anti-NY-BR-1 CARs, the equilibrium dissociation constant (KD) would have to be determined. In this context, it is important to note that high affinity CARs do not necessarily contribute to better functionality but may even contribute to on-target / off tumor toxicities [333,336] or prevent serial killing of tumor cells due to excessive binding forces [336].

In terms of specificity, affinity and cross-reactivity it was unknown whether these anti-NY-BR-1 CARs also bind to NY-BR-1.1, as this protein has a nucleotide and amino acid homology of 62% and 54% to NY-BR-1 and is expressed in the breast, testis and brain [85]. In particular, its expression in the brain could pose a major risk in case of cross-reactivities, as various studies have already shown that T cells can overcome the blood-brain and blood-cerebrospinal fluid barriers under certain conditions, leading to inflammatory diseases of the brain [337] . Especially CD19 CAR$^+$ T cell therapies often provoke so-called neurotoxicities due to a high cytokine release, which causes disruption of the blood-brain barrier [338]. In addition, clinical studies on the treatment of brain tumors with intravenously injected CAR$^+$ T cells have already shown that CAR$^+$ T cells overcome the blood-brain barrier and migrate into the brain [339]. To answer this important question about possible cross-reactivities of the three NY-BR-1 CARs with NY-BR-1.1 protein, the aforementioned lentivirally transduced CAR$^+$ T cells were also cultivated in 96 well plates coated with the full-length NY-BR-1.1 protein for 24 h. The quantity of secreted IFNγ was again highest in clone2 CAR$^+$ T cells and corresponded roughly to the activation level of clone2 CAR$^+$ T cells cultured in NY-BR-1 coated wells (see Figure 4.3.4). In contrast, 10D11 CAR$^+$ T cells showed no evidence of cross-reactivity with NY-BR-1.1 and clone3 CAR$^+$ T cells were activated to a low degree, which was significantly below the level of NY-BR-1 co-cultured clone3 CAR$^+$ T cells. The strong cross-reactivity of clone2 CAR with NY-BR-1.1 can be justified with the strong homology between the proteins NY-BR-1 and NY-BR-1.1 within the clone2 CAR epitope, because both proteins differ only in one amino acid within this partial sequence (see chapter 1.2.1.2). By contrast, the slight activation of clone3 CAR$^+$ T cells was unexpected, as the amino acid sequences of both proteins differ significantly within the clone3 CAR epitope. Only 7 out of 17 amino acids are identical in this partial sequence. Even though only three of ten amino acids within the binding site of 10D11 CAR differ between the NY-BR-1 and NY-BR-1.1 proteins, this CAR was not activated by NY-BR-1.1 protein. In order to exclude interactions between clone3 CAR$^+$ T cells with NY-BR-1.1, cell lines expressing this protein should be generated and applied for further analyses.

On the one hand, these results reveal that all three anti-NY-BR-1 CARs recognize the NY-BR-1 protein and initiate an activation of human T cells upon binding to NY-BR-1. On the other hand, these data indicate the unsuitability of clone2 CAR for clinical trials due to strong cross-reactivities with NY-BR-1.1. However, according to the current status and further analyses performed within our group (unpublished), the 10D11 CAR does not exhibit any reactivities with NY-BR-1.1 and therefore displays a decisive advantage over the other CAR candidates.

5.5 All three anti-NY-BR-1 CAR candidates induce efficient anti-target immune responses *in vitro*

The functionality of human and murine pS/MARter electroporated CAR$^+$ T cells was examined in various *in vitro* experiments. First of all, stable NY-BR-1 transduced Bosc23 cells were co-cultivated with human CAR (clone2/10D11/clone3scFv_hFc_hCD28_CD3z_hOX40) expressing T cells at a ratio of 1:1 in order to perform a real-time monitoring of the target cell viability in an xCELLigence based system. All three anti-NY-BR-1 CAR constructs conferred T cells with the ability to specifically kill NY-BR-1$^+$ Bosc23 cells but not wild-type Bosc23 cells (see Figure 4.3.5). The target cell mediated activation of T cells was also reflected in increased IFNγ secretion. However, the survival rates of the target cells were still between approximately 50 and 70 % after four days of co-cultivation, whereby 10D11 and clone3 CAR$^+$ T cells led to higher mortality rates of the target cells than clone2 CAR$^+$ T cells. Furthermore, the IFNγ concentrations in the cell culture supernatants of NY-BR-1$^+$ Bosc23 co-cultured CAR$^+$ T cells were only about twice as high as those of mock T cells. These effects are probably based on fluctuating and mostly low NY-BR-1 surface expression levels in transduced Bosc23 cells (see Figure 4.1.2). Despite Lactacystin treatment, NY-BR-1 expression levels were usually between 30 and 50 % and also fluctuated greatly depending on cell density. Since increasing mortality rates are associated with decreasing cell densities, additional NY-BR-1 expression decreases in the remaining cells can be assumed. These facts may lead to a situation where only a part of the co-cultivated T cells are activated, which, in turn, results in the observed moderately increased IFNγ levels. Furthermore, IFNγ might be consumed or degraded during the killing process, which has a significant impact on end point data measurements and could be prevented by multiple measurements of IFNγ concentrations at different time points during the experiment.

Similar results were obtained when murine pS/MARter CAR (clone2/10D11/clone3scFv_mFcΔ_mCD28Δ_m4-1BB_CD3z) electroporated T cells were co-cultured with stably transduced NY-BR-1$^+$ EO771 cells. The viabilities rates after 24 h of co-cultivation (at an effector to target ratio of 1:1) were calculated by CFSE and DAPI staining under the usage of flow

cytometric analyses. Again, murine CARs caused an anti-target immune response in those T cells that were co-cultivated with NY-BR-1$^+$ EO771 but not with wild-type EO771 cells (see Figure 4.4.4). The average survival rates of NY-BR-1$^+$ target cells remained between 50 and 60 % after 24 h of co-cultivation, whereby no differences in anti-target functionality were observed between the different anti-NY-BR-1 CAR$^+$ T cells. This phenomenon can be explained again by low NY-BR-1 surface expression levels in transduced EO771 cells, which achieved a maximum of 15 - 30 % despite Lactacystin treatment (see Figure 4.1.4). These values correspond to the differences in the viability rates between mock and CAR$^+$ T cell co-cultured NY-BR-1$^+$ EO771 cells. However, surprisingly, analyses of the activation level of electroporated murine CAR$^+$ T cells by measurement of CD69 expression or secreted IFNγ indicated that even CAR$^+$ T cells cultivated alone showed a high level of activation, which was not significantly increased with killing of NY-BR-1$^+$ EO771 cells (see Supplementary Figure 6.6). As murine T cells had to be stimulated very strongly via CD28, CD3 and IL-2 in order to achieve high transfection efficiencies, the resulting increased IFNγ secretions and CD69 expression levels may persist for several days [340]. It was however difficult to perform killing assays at a later time point, as the viability rates decreased over time (see Supplementary Figure 6.5). In addition, the electroporation process itself or rather the introduction of foreign DNA might also contribute to cell-intrinsic activation of murine T cells because the use of pS/MARter vectors with many bacterial sequences does not rule out an immune reaction against such vectors [341-343]. Moreover, additional analyses performed within our group demonstrated enhanced expression levels of type I interferons in human anti-CEA CAR$^+$ T cells after electroporation with pS/MARter vectors (unpublished), as discussed in chapter 5.3.1. These interferons play a major role in pathogen defense in virally and bacterially infected cells [344,345]. The application of NanoCMARter vectors could possibly avoid this problem. Nevertheless, the high activation level of murine CAR$^+$ T cells did not cause an unspecific killing of wild-type EO771 cells (see Figure 4.4.4).

Established cell lines do not provide sufficient evidence for a possible clinical use of the immune receptors. Therefore, pleural effusion cells from breast cancer patients were analyzed for NY-BR-1 expression and co-cultured with both pS/MARter / NanoCMARter electroporated and lentivirally transduced CAR (clone2/10D11/clone3scFv_hFc_hCD28_CD3z_hOX40) expressing T cells in allogeneic settings. Regardless of the method of CAR$^+$ T cell production, the target cells were eliminated depending on their NY-BR-1 expression profiles, whereby 10D11 CAR$^+$ T cells mostly contributed to the highest mortality rates of target cells and the second highest IFNγ levels in cell culture supernatants compared to clone2 and clone3 CAR$^+$ T cells (see Figure 4.3.6). In contrast to mock T cell - treated cells, those target cells co-cultivated with CAR$^+$ T cells, especially with 10D11 CAR$^+$ T cells, exhibited no or only a small proportion of remaining NY-BR-1$^+$ cells at the end of the experiments (see Figure 4.3.7; Supplementary Figure 6.3).

In one exemplary case, however, high mortality rates of mock T cell - treated target cells were recorded (see Figure 4.3.6 A), which can be attributed, among others, to allogenic immune reactions. Since the breast cancer patients and healthy T cell donors were not HLA-matched, foreign HLA molecules or HLA-peptide complexes are recognized by TCRs leading to elimination of those target cells [346,347]. In addition, tumor cells usually have a high mutation load probably leading to the presentation of mutated / foreign peptides on HLA molecules. Since HLA matching does not automatically prevent allogeneic immune responses because of the presence of minor histocompatibility antigens (mHAgs) [346,347], which derive from polymorphic proteins, an autologous approach should be used to optimize the experimental setting.

The direct comparison of human pS/MARter and NanoCMARter electroporated CAR$^+$ T cells in the same experimental approach revealed that NanoCMARter CAR$^+$ T cells accounted for a nearly 100 % killing of the target cells, whereas pS/MARter CAR$^+$ T cells eliminated a maximum of 60 % (see Figure 4.3.6 B). In addition, the released IFNγ levels were more than twice as high with NanoCMARter as with pS/MARter CAR$^+$ T cells. Given that NY-BR-1 expression levels of these pleural effusion cells were very weak (about 14 %), the reasons for these results are manifold. The so-called bystander killing of CAR$^+$ T cells has been reported for various antigens. This phenomenon is based on CAR$^+$ T cells that kill surrounding antigen negative cells via a cell-cell contact dependent Fas/FasL interaction after prior antigen-dependent activation [149,348,349]. FasL is upregulated on activated CAR$^+$ T cells and leads to trimerization of the Fas receptor on target cells, which in turn, causes downstream activation of caspase 8 and a perforin independent apoptotic death of the target cells [149,348]. However, Fas expression levels were not studied for the pleural effusion cells used here. Furthermore, the proportion of CAR expressing T cells was significantly higher upon electroporation with NanoCMARter vectors compared to pS/MARter vectors this time (see Supplementary Figure 6.4), although no statistically significant differences in the OX40 CAR expression patterns of both electroporation systems were observed in multiple experiments (see Figure 4.3.3). In addition, the density of CAR expression, represented by mean fluorescence intensity (MFI), was elevated in NanoCMARter compared to pS/MARter CAR$^+$ T cells this time (see Supplementary Figure 6.4). As enhanced CAR surface expression levels are associated with improved functionality [350], the different CAR expression profiles in pS/MARter and NanoCMARter electroporated T cells might have affected experimental outcomes. Furthermore, pS/MARter electroporated CAR$^+$ T cells exhibit increased expression levels of type I interferons in contrast to NanoCMARter CAR$^+$ T cells (unpublished). These type I interferons may have proapoptotic effects and trigger the generation of IL-10 producing T_{reg} cells [344,351] leading to impaired long-term efficiency of pS/MARter CAR$^+$ T cells in direct comparison to NanoCMARter CAR$^+$ T cells. However, the generation of IL-10 - producing T_{reg} cells upon electroporation with pS/MARter OX40 CARs needs to be further investigated, as OX40 CARs have been shown to suppress IL-10

secretion in lentivirally transduced CAR$^+$ T_{reg} cells [286]. In addition, the dynamics of NY-BR-1 expression levels pose the problem that NY-BR-1 expression levels cannot be exactly determined in real-time. For transduced cell lines, it was shown that NY-BR-1 expression is dependent on cell cycle and cell density (see Figure 4.1.2). To what extent this dynamic also applies to pleural effusion cells is not known currently, but according to results shown in Figure 4.3.7 and group internal analyses, NY-BR-1 expression fluctuates in pleural cells over time as well. Nevertheless, end point analyses of NY-BR-1 expression levels demonstrated that both pS/MARter and NanoCMARter CAR$^+$ T cells eliminated all NY-BR-1$^+$ target cells (see Supplementary Figure 6.3).

The lentivirally transduced CAR$^+$ T cells were similarly efficient as pS/MARter electroporated CAR$^+$ T cells in killing of NY-BR-1$^+$ pleural effusion cells, but lentivirally transduced clone3 and 10D11 CAR$^+$ T cells exhibited minimally higher lytic activities and increased IFNγ secretion than clone2 CAR$^+$ T cells (see Figure 4.3.6 C).

The different *in vitro* killing assays, however, not only confirmed that stable CAR - expressing T cells can be generated by pS/MARter and NanoCMARter vectors, but also that they are as efficient as CAR$^+$ T cells generated by classical lentiviral transduction. In addition, it became clear in both murine and human settings that all three CAR candidates act specifically on NY-BR-1. Using human transduced or primary target cells, the 10D11 CAR$^+$ T cells often led to higher mortality rates than clone2 CAR$^+$ T cells, even though clone2 CAR$^+$ T cells showed higher activation levels in NY-BR-1 protein co-cultures than 10D11 and clone3 CAR$^+$ T cells (see Figure 4.3.4). The reasons for these results are unknown up to now, so that various hypotheses exist.

All these findings may suggest that the clone2 CAR has a higher affinity than 10D11 and clone3 CARs, but has worse functional properties due to, for example, excessive binding and resulting impaired serial killing of target cells [336]. Another hypothesis might be a more specific binding of clone2 CAR to the NY-BR-1 protein compared with 10D11 and clone3 CARs, which leads to a more specific elimination of target cells and sparing of target negative cells. However, this is more likely the case for low affinity CARs [335,336,352]. In addition, the 10D11 CAR binding site might be more accessible than the clone2 CAR binding site in the transmembrane NY-BR-1 protein. However, surface stainings of NY-BR-1$^+$ EO771 cells with all three antibody formats did not reveal significant differences (see Figure 4.1.3). In order to prove all these hypotheses, further *in vitro* experiments using primary cells or lentivirally transduced cells with different levels of NY-BR-1 expression are necessary to investigate the relationship between target expression level and killing efficiency of CAR$^+$ T cells as well as the discrimination of tumor cells from normal breast tissues expressing NY-BR-1 protein at lower levels by the different anti-NY-BR-1 CAR types. In addition, various *in vivo* safety and efficiency analyses were carried out in this thesis in order to scrutinize the question of CAR specificities (see chapters 5.6, 5.8).

5.6 Safety and functional analyses of the anti-NY-BR-1 CARs in C57BL/6 wt and NY-BR-1$^{tg/-}$ mice

One of the major hazards in CAR$^+$ T cell treatment of solid tumors is the on target / off tumor toxicity due to potentially low levels of target expression in normal tissues [353]. Furthermore, certain cross-reactivities with proteins similar to the target antigen cannot be excluded [353]. Due to the fact that NY-BR-1 is slightly expressed in healthy breast tissue [85,273], these risks may also exist for anti-NY-BR-1 CARs. In order to assess and preclude these threats, both CD57BL/6 wt and NY-BR-1$^{tg/-}$ mice were treated with pS/MARter electroporated CAR (clone2/10D11/clone3scFv_mFcΔ_mCD28Δ_m4-1BB_CD3z) expressing T cells by intravenous injection over a period of 14 days. The significant aspect of this NY-BR-1$^{tg/-}$ model is that NY-BR-1 expression is not restricted to the mammary glands (unpublished, see chapter 1.2.3.1). At DNA level, the inserted transgene was detected in almost all organs (see Supplementary Figure 6.7). Further group internal analyses revealed *NY-BR-1* expression in different tissues including mammary glands, lung and salivary glands at RNA level as well, even though *NY-BR-1* expression is controlled by the MMTV promoter (unpublished, see chapter 1.2.3.1). These results are consistent with other studies which proved the functionality of the MMTV long terminal repeat in several organs [354,355]. However, immunohistochemical stainings of NY-BR-1$^{tg/-}$ mouse tissues using the clone2, 10D11 and clone3 antibodies were not successfully established (data not shown). The reasons might include too low NY-BR-1 surface expression levels or masked epitopes by formaldehyde - based fixatives. Furthermore, only heterozygous transgenic mice were used leading to the fact that each mouse has to be tested for the presence of the transgene.

Furthermore, the comparison of various heterozygous and homozygous transgenic animal models demonstrated that heterozygous animals usually show significantly lower levels of transgene expression / activity than homozygous animals [356-362]. This effect might be attributed to homozygous cells expressing both alleles. However, in case of mosaic transgenic animals, elevated protein levels were also associated with a higher number of homozygous cells expressing the transgene [357]. Therefore, the generation of a homozygous NY-BR-1 transgenic mouse model might be useful to increase NY-BR-1 expression levels. In addition, both the integration site and copy number of *NY-BR-1* should be studied in the NY-BR-1$^{tg/-}$ mouse model as the former affects silencing and formation of mosaic-like expression patterns of the transgene [363,364] and high transgene copy numbers may lead to epigenetic modifications and transgene silencing [365].

Nevertheless, anti-NY-BR-1 CAR$^+$ T cells persisted in the spleens of NY-BR-1$^{tg/-}$ mice to a higher rate than in C57BL/6 wt mice, indicating that NY-BR-1 expression in NY-BR-1$^{tg/-}$ mice contributed to the persistence of pS/MARter electroporated CAR$^+$ T cells (see Figure 4.5.1). It is already known that in

addition to many other factors including CAR design (e.g. co-stimulatory domains) [366] and phenotype of the starter T cell population [367], antigen density / load plays a crucial role in the persistence of CAR$^+$ T cells because of antigen driven expansion and memory formation [368]. To further investigate these aspects in the case of the anti-NY-BR-1 CAR$^+$ T cells used here, phenotypic analyses on the expression of memory and naive stem cell markers such as CD45RA, CD45RO, CD62L and CCR7 might be helpful [369]. Furthermore, the increased persistence of clone2 CAR$^+$ T cells in blood and spleens of NY-BR-1$^{tg/-}$ mice was associated with strongly elevated cytokine concentrations in the plasma, whereas, the treatment with 10D11 and clone3 CAR$^+$ T cells did not result in significantly elevated cytokine levels in C57BL/6 wt and NY-BR-1$^{tg/-}$ mice (see Figure 4.5.2). In fact, clone2 CAR$^+$ T cell - treated NY-BR-1$^{tg/-}$ mice exhibited elevated levels of pro-inflammatory, T cell activation - associated cytokines such as IL-2 [370], TNFα [371] and IFNγ [372]. Raised concentrations of the pro-inflammatory cytokines IL-1ß and IL-12, which are mainly produced by activated macrophages and dendritic cells [373,374], were also detected in those mice. In fact, IL-12 exhibits positive effects on IFNγ production in T cells and TH1 type cellular immune responses [373,375]. A high release of the cytokine IL-13, which is associated with TH2 immune derived pro- and anti-inflammatory immune responses [376-378], was also particularly noticeable. In addition to pro-inflammatory cytokines, three out of five clone2 CAR$^+$ T cell - treated NY-BR-1$^{tg/-}$ mice demonstrated increased levels of IL-10, which is secreted by macrophages, mast cells, B cells as well as regulatory and helper T cells and is known to act immune suppressively by directly affecting expansion and differentiation of T_{reg} cells [379] and cytotoxicity of CD8$^+$ T cells [379,380]. The cytokine release syndrome (CRS) is characterized by increased levels of several cytokines such as IFNγ, IL-1ß, IL-2, IL-6, IL-8 and IL-12, whereby the cytokine IL-6 plays a key role [381,382]. The latter is mainly secreted by macrophages, monocytes and endothelial cells and, at high concentrations, it causes trans-activation of different cell types via soluble IL-6 receptors [381,383], which, in turn, results in the activation of a pro-inflammatory signaling cascade [381,383]. Various CRS models were established in mice and were also associated with elevated levels of various cytokines such as IFNγ, IL-2 and IL-6 as well as weight loss [384,385]. However, the measured cytokine levels in clone2 CAR$^+$ T cell - treated NY-BR-1$^{tg/-}$ mice were below the toxic thresholds reported in the study by Giavridis *et al.* (2018)[384] and none of the anti-NY-BR-1 CAR$^+$ T cell - treated mice displayed any weight changes.

To exclude additional inflammatory processes or strong T cell infiltrations in mouse tissues, all organs of CAR$^+$ T cell - treated mice were examined for visible abnormal changes. Neither inflammatory nor necrotic processes were seen in any organ of CAR$^+$ T cell - treated mice, which represents an important safety aspect for the application of anti-NY-BR-1 CARs in breast cancer patients. Furthermore, immunohistochemical analyses of clone2 CAR$^+$ T cell - treated NY-BR-1$^{tg/-}$ mouse organs did not reveal increased amounts of infiltrated T cells (see Figure 4.5.2). The results correlate with a

report showing that anti-HER2 CAR$^+$ T cells infiltrate HER2 expressing tumors but not HER2$^+$ organs in HER2 transgenic mice [386].

Thus, these data indicate that all three CAR candidates, apart from the cross-reactivity of clone2 CAR with the NY-BR-1.1 protein (see Figure 4.3.4), can be considered safe, at least in the pre-clinical setting. The elevated cytokine levels as a result of clone2 CAR$^+$ T cell treatment rather seem to indicate mediate immune responses against the NY-BR-1 protein, which represents an important functional aspect. In addition, these findings support the hypothesis that clone2 CAR$^+$ T cells require lower levels of NY-BR-1 protein for full activation than 10D11 and clone3 CAR$^+$ T cells. Considering the low expression levels of NY-BR-1 in healthy breast tissue and its over-expression in primary breast cancer tumors and metastases in breast cancer patients, the administration of 10D11 and clone3 CAR$^+$ T cells in the patient setting might be beneficial over treatment with clone2 CAR$^+$ T cells. In addition, the anti-tumor efficacy of these CAR$^+$ T cells has been further investigated *in vivo* in the course of this work (see chapter 5.8).

In order to confirm persistence, remaining functionality and antigen specificity of those CAR$^+$ T cells, splenocytes of NY-BR-1$^{tg/-}$ and C57BL/6 wt mice, treated with pS/MARter electroporated CAR$^+$ (clone2/10D11/clone3scFv_mFcΔ_mCD28Δ_m4-1BB_CD3z) T cells over a period of 14 days, were co-cultivated with Lactacystin-treated (NY-BR-1$^+$) EO771 cells for 24 h. The strongly reduced viability of NY-BR-1$^+$ EO771 cells after co-cultivation with clone2 and 10D11 CAR$^+$ T cell containing splenocytes confirmed the persistence of those CAR$^+$ T cells and their remaining functionality (see Figure 4.5.3). Strikingly, splenocytes from clone3 CAR$^+$ T cell - treated mice led to slightly decreased viability rates in wild-type EO771 and NY-BR-1$^+$ EO771 cells to the same extent, whereas clone2 and 10D11 CAR$^+$ T cell containing splenocytes did not attack wild-type EO771 cells confirming their specificity. As no functional differences between C57BL/6 wt and NY-BR-1$^{tg/-}$ mice persistent untransfected (mock) or CAR$^+$ T cells were observed, even though the T cells were originally isolated from C57BL/6 wt mice, electroporated and injected in both C57BL/6 wt and NY-BR-1$^{tg/-}$ mice, they were summarized in the same graphs (see Figure 4.5.3). This shows that regardless of whether the CAR$^+$ T cells have previously bound their antigen or not, they remain functional to the same extent *ex vivo*.

Nevertheless, since the mortality rates between mock T cell and clone3 CAR$^+$ T cell - treated EO771 and NY-BR-1$^+$ EO771 cells did not differ significantly, it can be assumed that the abovementioned slightly reduced viability rates are not attributable to clone3 CAR$^+$ T cells but rather to killing by untransfected (mock) T cells and other immune cells. This hypothesis is supported by the fact that after co-cultivation with EO771 wild-type and NY-BR-1$^+$ EO771 cells, clone3 CAR$^+$ T cell containing splenocytes exhibited lower proportions proportions of CD4$^+$TNFα$^+$, CD8$^+$TNFα$^+$, CD4$^+$IFNγ$^+$, CD4$^+$GrB$^+$ and CD8$^+$GrB$^+$ T cells than splenocytes derived from mock T cell - treated mice (see Figure 4.5.3). The

detection of TNFα as a very early activation marker of T cells [371] and IFNγ as an activation marker and important cytokine, which promotes the cytotoxicity of T cells [372], triggers upregulation of IL-12 receptors on T cells [372] and MHCI molecules on target cells [372], is an effective tool to investigate the different actual activation levels of the variously cultivated T cells. Moreover, the detection of GrB expressing cells reveals the actual proportion of T cells involved in the elimination of target cells via the GrB / perforin dependent pathway [387,388]. The highest mortality rate of NY-BR-1$^+$ EO771 cells achieved by 10D11 CAR$^+$ T cells was reflected in moderately increased proportions of IFNγ, TNFα and GrB expressing T cells. In contrast, clone2 CAR$^+$ T cells / splenocytes displayed lower amounts of activated T cells, consistent with the weaker killing efficiencies of those cells compared to 10D11 CAR$^+$ T cells / splenocytes. CD4$^+$GrB$^+$ cells were also detected, which was not surprising, as various studies have confirmed that human CD4 CAR$^+$ T cells have cytotoxic properties and even lead to long-lasting anti-tumor responses *in vivo* [149,389]. In the murine system, GrB expression has been reported for CD4$^+$ helper and regulatory T cells as well [390-392]. However, Stalder et al. (1994) [393] reported that murine T cells primarily resort to the Fas/FasL pathway to eliminate target cells. Furthermore, recent studies have found negative effects of perforin and GrB on the effectiveness of murine CD4$^+$ T cells by interfering with the calcium signaling pathway in T cells [394] or by perforin secretion of T_{reg} cells, which inhibits B cell proliferation [391] and NK / CD8$^+$ T cell induced anti-tumor responses [392]. In contrast, perforin dependent murine CD4$^+$ T cell cytotoxicity has also been reported in association with infections [395].

Overall, it was demonstrated that pS/MARter electroporated CAR$^+$ T cells persist and remain functional *in vivo*, whereby 10D11 and clone2 CAR$^+$ T cells were clearly superior to clone3 CAR$^+$ T cells. For a further improvement of this experimental setup, expression analyses of exhaustion markers such as TIM-3, PD-1 or LAG-3 would be helpful, as T cell exhaustion, first identified during chronic infections and characterized by loss of IL-2 production, proliferative capacity and killing [396,397], can attribute to the failure of long-lasting anti-tumor responses in CAR$^+$ T cell therapies [397,398] and may also have had negative effects on killing efficiencies and activation levels of anti-NY-BR-1 CAR$^+$ T cells in the performed *ex vivo* experiments. Furthermore, the isolation of anti-NY-BR-1 CAR$^+$ T cells from splenocytes and subsequent co-cultivation with target cells would allow the investigation of the actual effectiveness of CAR$^+$ T cells without the impact of macrophages, B cells or dendritic cells. Additionally, the resulting increased number of CAR$^+$ T cells could possibly lead to more significant differences in the activation levels of T cells depending on the presence of NY-BR-1 positive or negative target cells.

5.7 Establishment of NY-BR-1 subcutaneous tumor models

Having shown that CAR$^+$ T cells persist and remain functional in C57BL/6 wt and NY-BR-1$^{tg/-}$ mice, the anti-tumor effectiveness of these CAR$^+$ T cells should also be investigated in murine tumor models. Based on the fact that NY-BR-1$^+$ EO771 cells turned out to be useful target cells for *in vitro* and *ex vivo* efficiency analyses, these cells were originally intended for establishing a tumor mouse model but, surprisingly, these cells were rejected after subcutaneous injection in both C57BL/6 wt and NY-BR-1$^{tg/-}$ mice, whereas wild-type EO771 cells formed subcutaneous tumors (see Figure 4.6.1). The rejection of NY-BR-1$^+$ EO771 derived tumors was mainly based on tumor - infiltrating T cells and macrophages, which was reflected in increased levels of different cytokines including IL-1ß, IL-2, IL-12, IL-13 and TNFα, whereby significant differences were observed between mice with complete tumor rejection and the one mouse with a small remained tumor (see Figure 4.6.2). This effect can be explained by the fact that at the time point of plasma cytokine quantifications, NY-BR-1$^+$ EO771 tumors had already been completely rejected by most mice 10 to 14 days before, whereas one mouse still exhibited a small tumor. This means that cytokine levels or rather the entire anti-tumor immune response had decreased significantly 10 to 14 days after complete rejection compared to one mouse in which the rejection process was still ongoing. Nevertheless, as it has already been repeatedly reported that subcutaneously injected EO771 cells can form tumors in immunocompetent mice [399,400] and since that has also been observed here with EO771 wild-type cells, rejection of NY-BR-1$^+$ EO771 cells is probably directly based on NY-BR-1 expression.

Studies by Jäger et al. (2005) [96], Krishna Das (2017) [256] and Gardyan (2015) [98] confirm these results and the existence of MHCI and MHCII restricted NY-BR-1 epitopes. In fact, Krishna Das (2017) [256] showed that NY-BR-1$^+$ EO771 tumors grow slower than EO771 wild-type tumors in HLA-DRB1*0401 tg mice due to increased amounts of tumor - infiltrating T cells, especially CD8$^+$ cells, and macrophages. In this study, NY-BR-1 specific T cells were identified in splenocytes from NY-BR-1$^+$ EO771 tumor bearing mice by co-cultivation of those splenocytes with synthetic peptides representing HLA-DR-4 and H2-D^b - restricted NY-BR-1 epitopes. The reason for complete rejection of the NY-BR-1$^+$ EO771 cells used here in contrast to the cells tested in the work of Krishna Das (2017) [256] might be due to different NY-BR-1 expression levels, because Krishna Das (2017) [256] demonstrated that the growth rate of NY-BR-1$^+$ EO771 cells negatively correlates with *NY-BR-1* expression level. In addition, NY-BR-1$^+$ EO771 cells provoked a B cell induced immune response in both C57BL/6 wt and NY-BR-1$^{tg/-}$ mice, as demonstrated by the detection of anti-NY-BR-1 antibodies in mouse plasma (see Figure 4.6.2), indicating high surface expression levels of NY-BR-1 protein. Therefore, both strong antibody and T cell responses led to the complete rejection of NY-BR-1$^+$ EO771 tumors in immunocompetent mice.

The observable intolerance in NY-BR-1$^{tg/-}$ mice towards NY-BR-1 is nonetheless surprising. In general, maturing T cells undergo a so-called positive and negative selection in the thymus. Positive selection of CD4 CD8 double positive T cells takes place in the cortex of the thymus by MHC peptide presentation on cortical thymic epithelial cells [401] . If the affinity of the TCR to the MHC:peptide complex is insufficient, the TCRα locus is rearranged several times (receptor editing) [402]. If this does not lead to sufficient specificity towards the MHC:peptide complexes, T cells do not receive "rescue signals" and undergo apoptosis. T cells that have successfully overcome positive selection, differentiate into CD4 or CD8 single positive T cells, depending on their affinity to MHC I or MHC II, express the chemokine receptor CCR7 and migrate into the medulla where the CCR7 ligands CCL19 and CCL21 are expressed on the surface of medullary thymic epithelial cells (mTECs) [401]. Due to the interaction of T cells with mTECs and dendritic cells, autoreactive T cells, which are characterized by a too high affinity to self-peptide MHC complexes, are eliminated or differentiate into T_{reg} cells [401,403], which play an important role in peripheral immune tolerance. Similar to T cells, B cells are also selected depending on their binding affinity of the B cell receptor (BCR) to self-antigens during their development in the bone marrow. It is assumed that positive and negative selection processes occur in early B cell stages (pro-/ and pre-B cell) and in pre- and immature B cell stages, respectively [404-406]. Indeed, several studies have reported that over 70 % of human late pre BCRs are autoreactive leading to the elimination of the majority of these cells [406]. However, another possibility represents the down-regulation of the BCR / surface antibody and rearrangement of the light chain [404,405]. If the autoreactivity of the BCR continues, apoptosis is initiated. If not, unselected immature B cells are exposed to a renewed negative selection process after their arrival in the spleen [404-406]. In several transgenic mouse models (RhHEL [407], CEAGe18FJP [408], HER2 [409], Muc1 [410]), immune tolerances to appropriate transgenes were observed, so that even transgene - expressing tumors were tolerated without inducing B cell or T cell responses [408-410]. Moreover, expressions of the transgenes were proven in the thymi of these mice at RNA or protein level [407,408]. *NY-BR-1* expression was also detected at low levels in the thymi of NY-BR-1$^{tg/-}$ mice (unpublished), but, however, the antigen expression levels might be not sufficient to develop a complete immunotolerance against this transgene. It has already been confirmed that the expression levels of different antigens vary in the thymus [407,411,412], so that low thymic expression levels allow T cells with low avidity to overcome negative selection in thymus. Since rejection of NY-BR-1^{+} EO771 tumors was also observed in two homozygous NY-BR-1 transgenic mice, the problem of insufficient immunotolerance seems to be present here as well (see Figure 4.6.1; Figure 4.6.2). However, due to a limited number of homozygous offsprings, the rejection responses in those mice could not be studied in detail. Overall, due to the fact that no inflammation or increased T cell infiltration in both untreated and CAR^{+} T cell - treated NY-BR-1$^{tg/-}$ mouse organs was detected (see

chapter 5.6), it can be assumed that a high transgene expression density, as it was the case with NY-BR-1$^+$ EO771 tumors, was responsible for the induction of an anti-NY-BR-1 immune response.

As a result of T cell and antibody based rejection of NY-BR-1$^+$ EO771 tumors, immunocompromised mice were used for growth analyses of these tumors. The applied NOD.CB17-*Prdkc^{scid}* mouse model has a nonobese diabetic (NOD) background, which means that these mice are genetically predisposed for the spontaneous development of type 1 diabetes because of the specific destruction of insulin producing ß-cells by lymphocytes [413,414], but, however, NOD.CB17-Prkdc^{scid} mice do not develop this autoimmune disease due to additional mutations in the *Prkdc* gene encoding the DNA-dependent protein kinase catalytic subunit (DNA-PKcs) [415]. The latter plays an important role in the nonhomologous end-joining (NHEJ) based repair mechanism of DNA double strand breaks. As the VDJ recombination processes of TCRs and BCRs / immunoglobulins are based on the NHEJ pathway, the non-sense mutation in the *Prkdc* gene in NOD.CB17-*Prdkc^{scid}* mice prevents the generation of mature T and B cells [416-418]. Nevertheless, those mice still have an innate immunity including NK, myeloid and monocytic cells [415]. Hence, as expected, the subcutaneous engraftment of NOD.CB17-*Prdkc^{scid}* with NY-BR-1$^+$ EO771 cells led to an uniform tumor progression in all mice confirming the important roles of T cells and antibodies in the rejection process of NY-BR-1$^+$ EO771 cells (see Figure 4.6.3).

To circumvent rejection of NY-BR-1$^+$ EO771 tumors in C57BL/6 mice in the future, strong immunogens within the NY-BR-1 protein should be identified by, for example, bioinformatic analysis [419] and peptide vaccination of C57BL/6 mice. Based on these results, deletion variants of NY-BR-1, which hopefully still contain the specific epitopes targeted by the anti-NY-BR-1 CARs, could be used to generate a variety of NY-BR-1$^+$ EO771 cell lines for subsequent injection as subcutaneous tumors.

To examine the functionality of human anti-NY-BR-1 CAR$^+$ T cells in tumor mouse models, NY-BR-1$^+$ Bosc23 cells were injected subcutaneously into NOD.Prkdc^{scid}.IL2rγ^{null} (NSG) mice. In comparison to NOD.CB17-Prkdc^{scid} mice, these mice additionally carry a mutation in the gamma chain of the IL-2 receptor [420,421], which prevents cytokine signaling in various receptors (IL-2, IL-4, IL-7, IL-9, IL-15, and IL-21) [422-424] and thus, in turn, leads to the absence of functional NK cells [425] and allows a better growth and persistence of human lymphocytes and tumor cells [420,421]. In spite of the fact that Bosc23 cells are primarily used for the production of retroviral particles, they formed subcutaneous tumors in all NSG mice (see Figure 4.6.4). These results were not surprising, as Bosc23 cells were originally derived from HEK 293T cells [220] which obtained characteristics of cancer cells due to their generation by transformation of normal human embryonic kidney cells with sheared DNA from the human adenovirus type 5 [426,427]. It has been confirmed that HEK 293T cells can form tumors in different mouse models [428] and even exhibit cancer stem cell characteristics [429].

5.8 Functional properties of human and murine anti-NY-BR-1 CAR - expressing T cells in different *in vivo* settings

The concept of anti-NY-BR-1 CAR therapy for NY-BR-1 positive breast cancer tumors has only been investigated *in vitro* so far. Since treatment of solid tumors is generally challenging as CAR$^+$ T cells must migrate to and infiltrate the tumor, subcutaneous NY-BR-1$^+$ Bosc23 and NY-BR-1$^+$ EO771 tumor models were used to evaluate the functionality of both human and murine CAR$^+$ T cells *in vivo*.

Human lentivirally transduced CAR$^+$ (clone2/10D11/clone3scFv_hFc_hCD28_hCD3z_hOX40) T cells led to strongly delayed tumor growth rates in NY-BR-1$^+$ Bosc23 tumor-bearing NSG mice and some mice even remained tumor-free or exhibited tumors with volumes of less than 20 mm³ (clone2scFv: 4 out of 7; 10D11scFv: 2 out of 7; clone3scFv: 3 out of 7 mice), so that clone2 CAR$^+$ T cells achieved the best overall survival rates followed by clone3 and 10D11 CAR$^+$ T cells (see Figure 4.7.1). Such tumors, which grew out over a longer period of time, were infiltrated by T cells, mainly in clone3 and 10D11 CAR$^+$ T cell - treated mice. However, some tumors showed increased T cell infiltration rates and still grew faster than tumors with lower T cell infiltration rates and vice versa. In addition, no clear relation between the amount of spleen and tumor persisting T cells was found. In fact, some mice showed increased levels of tumor - infiltrating and spleen persisting T cells, while other mice showed only one of both or T cells did not persist at all, whereby the latter led to a shortened overall survival. In addition, NY-BR-1$^+$ Bosc23 tumor cells were also attacked by untransfected T cells up to a certain point in mock T cell - treated mice (most likely via TCR-MHC induced responses). All these findings and other studies suggest that in addition to the total amount of tumor - infiltrating T cells, other factors such as the CAR type, CAR affinity [231], T cell phenotype [231,430] and tumor microenvironment [231,430] play important roles for the functionality of the individual tumor - infiltrating T cells. In addition, the proportion of bystander (CAR negative) T cells can also play an important role. In this context, it is important to note that immunohistochemical analyses (of Bosc23 tumors) allowed detection of CD3$^+$ but not CAR$^+$ CD3$^+$ cells as the anti-human IgG antibody required for CAR detection also binds to Fcγ receptors on tumor cells. In addition, due to insufficient image resolution, flow cytometric analyses are not well suited to reliably detect CAR$^+$ T cells in mouse tissues such as spleens and tumors. Due to these technical limitations and significantly different outcomes in mock and CAR$^+$ T cell treated mice, it is assumed that the majority of persisted / infiltrated T cells in CAR$^+$ T cell treated mice were CAR expressing T cells. For a better understanding, mainly CAR$^+$ T cells will be discussed in the context of tumor infiltrating T cells in CAR$^+$ T cell treated mice. In order to improve the detection of CAR expressing T cells in the future, CAR$^+$ T cells might be labeled by using reporters such as GFP (green fluorescent protein), but these reporters are immunogenic [431-433] and cause cellular damage [431]. Therefore, detection of infiltrated CAR$^+$ T cells could be achieved by the detection of anti-NY-BR-1 CAR - encoding DNA and RNA via RT-

qPCRs. However, in order to improve visualization and quantification of persisting bystander (CAR negative) T cells and CAR$^+$ T cells, the fluorescence in-situ hybridization (FISH) technique could be applied. In particular, the novel single molecule FISH - based technology – HuluFish[434]- allows the identification and quantification of multiple gene expressions in single cells by hybridizing multiple fluorophore-coupled nucleotides onto the complementary sequences. In fact, single RNA molecules are visualized as bright spots by fluorescence microscopy[434], which might enable the simultaneous visualization of CAR positive and CAR negative T cells in mouse tissues.

In general, the level of tumor - infiltrating T cells is determined by various aspects such as the trafficking to the tumor, cytokine milieu in the tumor and quantity of antigen positive tumor cells [430,435]. To direct T cells to the tumor site, expression of chemokine receptors on T cells and release of T cell - attracting chemokines, including CCL2, CCL3, CCL4, CCL5, CXCL 9 and CXCL10 by the tumor (especially myeloid and stromal cells) or tumor infiltrated lymphocytes is necessary [430]. In particular, high levels of CXCR3 expression by tumor - infiltrating lymphocytes in melanoma [436] and breast cancers [437] are associated with improved antitumor responses [438]. Also, high levels of CXCR3 ligands (such as CXCL9, CXCL10 or CXCL11) released by the tumor, which can be induced by IFNγ [430,439], positively influence T cell recruitment to the tumor site [437,438], so that a lack of these chemokines impairs the outcome of T cell - based immunotherapies [438]. As this could also be one reason for the weak tumor infiltration by lentivirally transduced anti-NY-BR-1 CAR$^+$ T cells in some mice, the secretion of many important T cell - attracting chemokines by NY-BR-1 expressing Bosc23 derived tumors will be investigated in the near future. Nevertheless, the concentration of one chemoattractant cytokine, IL-8, naturally secreted by various cell types including macrophages and cancer cells [440], was determined in all tumors and was actually elevated regardless of the kind of treatment (see Figure 4.7.2). It is known that this cytokine contributes to invasion and angiogenesis in breast cancer and correlates negatively with ERα expression [441]. To what extent IL-8 is also secreted by wild-type Bosc23 cells is unknown and would need to be investigated in further studies. Nevertheless, it might have contributed to the chemotaxis of anti-NY-BR-1 CAR$^+$ T cells. In addition, IL-8 has pro- and anti-inhibitory properties on T cells [440] (such as the suppression of IL-4 secretion in CD4$^+$ T cells [442]) as well as on neutrophils and granulocytes [440].

Surprisingly, the determination of T cell - associated cytokine levels in the blood of CAR$^+$ T cell - treated tumor bearing NSG mice did not reveal significant increases in pro-inflammatory cytokines, even not in those that remained tumor - free (see Supplementary Figure 6.8). The reason for this might be the low number of T cells in the blood of those mice and the strong dilution of the cytokines originally derived from the tumor or rather tumor-infiltrated T cells (see Figure 4.7.1). However, outgrown tumors showed slightly elevated levels of pro-inflammatory cytokines such as IFNγ, IL-1ß, IL-2 and IL-12, indicating T cell, especially TH1 [370,443,444] and CD8$^+$ T cell [370,372], mediated immune responses (see Figure 4.7.2). Although 10D11 CAR$^+$ T cell - treated mice showed sometimes

lower quantities of tumor - infiltrating T cells than those treated with clone3 CAR$^+$ T cells, the highest increases in pro-inflammatory cytokine levels were observed in 10D11 CAR$^+$ T cell - treated tumors, suggesting that tumor - infiltrating human 10D11 CAR$^+$ T cells may induce stronger anti-tumor responses than clone3 CAR$^+$ T cells at equal infiltration rates. By contrast, the concentration of IL-10, a cytokine that is mainly secreted by T_{reg} cells and negatively affects the potency of tumor - infiltrating CTLs by advancing the exhaustion of tumor - infiltrating CD8$^+$ T cells [445], was very low to undetectable in all tumors. This may also be related to the CAR OX40 domain, which is known to prevent induction of T_{reg} cells [446]. However, there are also several controversial studies showing that IL-10 has anti-tumor properties in breast cancer [447,448] and stimulatory effects on different lymphocytes including CD8$^+$ and CD4$^+$ T cells [448,449]. Nevertheless, to what extent tumor cells secreted further inhibitory chemokines and molecules [450,451] such as TGF-ß, prostaglandin E2 (PGE2), soluble Fas, adenosine, ROS and vascular endothelial growth factor (VEGF) or express inhibitory receptors including PD-L1 or down-regulate death-receptors (such as Fas) has to be investigated in more detail, because an immunosuppressive tumor milieu is one of the main reasons for the failure of CAR - based immunotherapies in solid tumors [231].

Apart from the tumor microenvironment itself, antigen expression has a decisive role in the infiltration and effectiveness of CAR$^+$ T cells. *In vitro*, it has already been observed that NY-BR-1 expression decreases significantly on the surface of transduced Bosc23 cells as a function of cell cycle, cell density and protein degradation (see chapter 5.2). Therefore, it is possible that loss of expression occurs in adult tumors over time as well. These results are consistent with the study by Krishna Das (2017) [256], reporting about undetectable NY-BR-1 surface expression in transduced, outgrown tumors. The declining NY-BR-1 expression levels may have impaired the effectiveness of anti-NY-BR-1 CAR$^+$ T cells, as several studies have shown that antigen expression levels directly correlate with tumor growth rates and overall survival in CAR$^+$ T cell - treated mice [350]. Moreover, antigen loss can be caused by mutations in the tumor or the selection pressure exerted by the immune system or rather CAR$^+$ T cells [452-454]. Once NY-BR-1$^+$ tumor cells have been eliminated by CAR$^+$ T cells, antigen negative cells can grow out or even overgrow antigen positive cells. In addition, CAR$^+$ T cell mediated trogocytosis has been reported for hematological malignancies [455]. In this active process, the antigen is transferred to CAR$^+$ T cells, resulting in a lower antigen density on tumor cells [455]. To what extent this process plays a role in anti-NY-BR-1 CAR therapies is unclear.

These results indicate that lentivirally transduced anti-NY-BR-1 CAR$^+$ T cells infiltrated and attacked NY-BR-1 expressing Bosc23 tumors. No significant differences were observed between the different CARs, as all three candidates led to significantly prolonged median and overall survival rates. However, most mice remained tumor - free when treated with human lentivirally transduced clone2 CAR$^+$ T cells, which may indicate that Bosc23 tumors with very low NY-BR-1 expression levels might be better

infiltrated and eliminated by clone2 CAR$^+$ T cells than by 10D11 and clone3 CAR$^+$ T cells. The facts that the NY-BR-1 expression levels in transduced Boc23 cells were very variable and heterogeneous *in vitro* (see chapter 5.2), and that NY-BR-1 expression in normal breast tissue is very mosaic-like [224], suggest that NY-BR-1 expression levels were not identical in all outgrowing NY-BR-1$^+$ Bosc23 derived tumors and mice. In addition, murine clone2 CAR$^+$ T cells responded significantly more strongly to very low NY-BR-1 expression levels in NY-BR-1$^{tg/-}$ mice than 10D11 and clone3 CAR$^+$ T cells (see chapter 5.6). In contrast, the infiltration capacities of human lentivirally transduced clone2, 10D11 and clone3 CAR$^+$ T cells probably do not differ in the case of NY-BR-1 high expressing Bosc23 tumors. In fact, human 10D11 CAR$^+$ T cells showed sometimes stronger anti-tumor immune responses than clone2 CAR$^+$ T cells (at the same infiltration rates), which was reflected in slightly higher cytokine levels inside the tumors and more delayed tumor growth when considering the individual tumor growth curves in the respective mice. These hypotheses are consistent with a study by Liu et al. (2015) [335] on anti-EGFR and anti-HER2 CARs with different affinities. In this study, effectiveness and infiltration capacity of low affinity CARs correlated with the antigen expression profile of the tumors, while at the same time antigen overexpressing tumors were more strongly attacked by low affinity CARs than by high affinity CARs [335].

In addition to the basic anti-tumor functionality of human anti-NY-BR-1 CAR$^+$ T cells, the impact of both the process of CAR$^+$ T cell generation and the choice of co-stimulatory domains on their anti-tumor efficiency was also of great interest, and, indeed, similarities but also small differences between electroporated and lentivirally transduced CAR$^+$ T cells were found.

In fact, it was shown that the selection of co-stimulatory domains does not only influence the CAR expression levels (see Figure 4.3.2) but also functionality and persistence of anti-NY-BR-1 CAR$^+$ T cells *in vivo*. Human pS/MARter electroporated T cells expressing the clone2/10D11/clone3scFv_hFcΔ_hCD28Δ_h4-1BB_hCD3z CD28_4-1BB CARs were not able to persist in tumor bearing NSG mice (see Figure 4.7.3), whereas both pS/MARter and NanoCMARter electroporated T cells expressing anti-NY-BR-1 CARs containing the OX40 domain (clone2/10D11/clone3scFv_hFc_hCD28_CD3z_hOX40) instead of the 4-1BB domain persisted in tumor-bearing NSG mouse spleens and infiltrated into NY-BR-1$^+$ Bosc23 tumors (see Figure 4.7.4, Figure 4.7.7). The effect of co-stimulatory domains on the efficiency of CAR$^+$ T cells is discussed very controversially and seems to be associated with the general architecture of the CAR. Several studies have shown that CD28, which is generally known as an early co-stimulatory signal during T cell activation [456], leads to high IL-2 secretions when incorporated as a co-stimulatory domain in CARs, which in turn promotes the generation of T_{reg} cells, negatively affecting anti-tumoral immune responses [275,457]. In addition, these CAR$^+$ T cells have been shown to persist poorly in different mouse

models because they exhibit a high activation potential independent of antigen activation, high proliferation rates and an effector memory / effector T cell phenotype, leading to rapid cell apoptosis [142,458,459]. A mutation in the Lck binding site of the CD28 domain, which is also present in pS/MARter anti-NY-BR-1 CARs (clone2/10D11/clone3scFv_hFcΔ_hCD28Δ_h4-1BB_hCD3z), has been shown to result in lower permanent IL-2 releases and higher antigen-specific proliferation [458]. Especially in the context of solid tumors infiltrated by T_{reg} cells, CARs with mutated CD28 domains are known to be significantly more efficient [275]. However, it was also demonstrated that second generation CARs with a mutated CD28 domain cannot persist or induce a sufficient anti-tumoral immune response due to the lack of Lck activation, which can be compensated with an additional co-stimulatory domain such as 4-1BB [460].

4-1BB is known to be a late co-stimulatory signal in T cell activation [461] and induces a central memory phenotype [142] in second generation CARs with sustained persistence and expansion of $CD8^+$ T cells and simultaneously reduced exhaustion [143,459]. A combination of both mutated [460] and unmutated CD28 [460,462,463] with 4-1BB domains was therefore found to be very effective. Nevertheless, a combination of these two co-stimulatory domains did neither lead to persistence of anti-NY-BR-1 CAR^+ T cells nor to reactivity against NY-BR-1 expressing Bosc23 tumors, in contrast to CD28_CD3z_OX40 CARs. The reason for this phenomenon is possibly based on the fact that antigen expression in Bosc23 tumors is very weak, so that the non-mutated CD28 domain in clone2/10D11/clone3scFv_hFc_hCD28_CD3z_hOX40 CARs might contribute to a better persistence, stronger activation and initial expansion of those T cells by a higher IL-2 release and / or partially antigen-independent activation [458]. To further investigate the role of non-mutated CD28 domains, anti-NY-BR-1 CARs with unmutated CD28 domains combined with 4-1BB or mutated CD28 domains in combination with OX40 should be evaluated. However, OX40 generally exhibits a positive effect on anti-NY-BR-1 CAR expression, as CD28_CD3z_OX40 CARs achieved higher CAR expression levels than CARs incorporating the CD28Δ_4-1BB and CD28_4-1BB domains (see Figure 4.3.2, see chapter 5.3.1). In addition, the OX40 domain is known to provide a late co-stimulatory signal in T cell activation [464] and to reduce the release of IL-10 in CD28_OX40 CAR^+ T cells, negatively affecting T_{reg} cells [286] and possibly facilitating the persistence and activation of anti-NY-BR-1 CAR^+ T cells *in vivo*. Although OX40 and 4-1BB belong to the TNFR family, they differ in their binding to various subsets of TRAFs [465,466]. Furthermore, there is evidence that 4-1BB is more strongly expressed on activated $CD8^+$ T cells than OX40, whereas the opposite may be true for $CD4^+$ T cells [467,468]. However, both domains act via TNFR2 and contribute to T cell survival by upregulating anti-apoptotic Bcl-2 family members following CD28 signaling [465,466]. A study by Hombach et al. (2011) [282] showed that anti-CEA CARs incorporating CD28_CD3z_OX40 domains were superior to anti-CEA CARs with CD28_CD3z domains both *in vitro* and *in vivo* and promoted the persistence of CD62L negative memory T cells. However, a direct comparison to

CD28_4-1BB_CD3z anti-CEA CAR$^+$ T cells was missing in this study [282]. In contrast to results obtained with anti-NY-BR-1 CAR$^+$ T cells, third generation anti-GD2 CARs with CD28_OX40_CD3z domains were significantly inferior to CD28_4-1BB_CD3z anti-GD2 CAR T cells *in vivo* according to a study by Quintarelli et al. (2018) [462]. They also showed a higher antigen-independent proliferation of OX40 anti-GD2 CAR$^+$ T cells *in vitro* compared to 4-1BB anti-GD2 CAR$^+$ T cells, which is probably due to a larger cluster formation of OX40 anti-GD2 CAR$^+$ T cells on the T cell's surface. However, the difference to anti-NY-BR-1 CARs is the distinct arrangement of co-stimulatory domains. While anti-NY-BR-1 CARs had a terminally positioned OX40 domain, the OX40 domain of GD2 CARs was located between CD28 and CD3z [462]. Therefore, further CAR$^+$ T cell studies with different targets and positioning of the OX40 domain would be necessary to provide a clear statement about the role of this domain in the anti-tumor reactivity of CAR$^+$ T cells. Moreover, these results indicate that NY-BR-1 expression levels in breast tumors could be used as a stratification strategy to select the most appropriate CAR with respect to its co-stimulatory domains for each patient.

A direct comparison of the functionality of pS/MARter, NanoCMARter and lentivirally transfected human CAR$^+$ (clone2/10D11/clone3scFv_hFc_hCD28_CD3z_hOX40) T cells reveals that there was no complete tumor regression in tumor engrafted NSG mice treated with electroporated pS/MARter and NanoCMARter CAR$^+$ T cells in contrast to the treatment with lentivirally transduced CAR$^+$ T cells (see Figure 4.7.1, Figure 4.7.4, Figure 4.7.7). However, electroporated CAR$^+$ T cells, especially pS/MARter CAR$^+$ T cells, persisted in some remaining tumors and mouse blood. The reason for higher numbers of tumor - free mice when lentivirally transduced CAR$^+$ T cells were applied, is probably caused by the fact that a different T cell donor was used for the lentiviral experiment than for the pS/MARter and NanoCMARter approaches. In fact, mock T cells in the lentiviral experiment even showed a stronger persistence and anti-tumor effectiveness than mock T cells in the other two experiments, which may affect the overall effectiveness of (CAR$^+$) T cells and thereby make these experiments only conditionally comparable.

Nevertheless, in contrast to lentivirally transduced and NanoCMARter electroporated CAR$^+$ T cells, the persistence of pS/MARter CAR$^+$ T cells in mouse tumors and blood led to increased cytokine levels in the blood (see Figure 4.7.6). In particular, the concentrations of pro-inflammatory cytokines such as GM-CSF, IFNγ, IL-2 and IL-12 were more elevated in 10D11 CAR$^+$ T cell - treated mice than in mock, clone2 and clone3 CAR$^+$ T cell - treated mice. Compared to IFNγ, however, IL-2 levels remained very low. To what extent this could be related to the OX40 domain is questionable, since different studies showed either negative effects or nearly no effects of the OX40 domain on IL-2 release [286,462]. The concentrations of immunosuppressive cytokines such as IL-10 remained low, which might be related to the OX40 domain and is associated with improved efficiency of CAR$^+$ T cells [286]. Similarly, tumors of mice treated with lentivirally transduced 10D11 CAR$^+$ T cells also exhibited a higher increase in pro-

inflammatory cytokines compared to clone2 and clone3 CAR$^+$ T cell treatment. For an even better comparison, cytokine levels in the tumors (and not only in the blood) of pS/MARter and NanoCMARter CAR$^+$ T cell - treated mice should also be investigated.

The general impression gained from Bosc23 tumor bearing mouse experiment using lentivirally transduced CAR$^+$ T cells and different other *in vivo* and *in vitro* studies that clone2 CAR$^+$ T cells might be able to infiltrate NY-BR-1 low-expressing tumor cells better than 10D11 CAR$^+$ T cells (see also chapters 5.4, 5.6), was not confirmed in pS/MARter CAR$^+$ T cell - treated mice. In fact, 10D11 and clone3 CAR$^+$ T cells even showed higher tumor infiltration rates in some mice than clone2 CAR$^+$ T cells but, nevertheless, the median survival rates were identical in clone2, 10D11 and clone3 CAR$^+$ T cell - treated mice and, additionally, 10D11 and clone2 CAR$^+$ T cells led to better overall survival rates than clone3 CAR$^+$ T cells (see Figure 4.7.4). In contrast to pS/MARter CAR$^+$ T cell treated mice, NanoCMARter CAR$^+$ T cell - treated mice exhibited higher tumor infiltration rates when clone2 CAR$^+$ T cells were applied compared to 10D11 CAR$^+$ T cell treatment (see Figure 4.7.7). However, NanoCMARter 10D11 CAR$^+$ T cells provoked delayed tumor growth in more mice than clone2 CAR$^+$ T cells, which in turn confirms the observations of the lentiviral experiment, in which lentivirally transduced 10D11 CAR$^+$ T cells seemed to be more effective than clone2 CAR$^+$ T cells at same / similar infiltration rates.

Although significantly more T cells infiltrated into NY-BR-1$^+$ Bosc23 tumors when using pS/MARter compared to NanoCMARter CAR$^+$ T cells, treatment with the latter provoked significantly longer median survival rates than pS/MARter CAR$^+$ T cells with regard to the respective mock control groups. This could be an indication that NanoCMARter CAR$^+$ T cells do not necessarily infiltrate better in tumors, but may act more effectively inside of NY-BR-1$^+$ tumors. This hypothesis is strengthened by the fact that NanoCMARter CAR$^+$ T cells eliminated significantly more pleural effusion cells *in vitro* than pS/MARter CAR$^+$ T cells (see Figure 4.3.6 B). These effects could be due to the reduced bacterial backbone and decreased expression of type I interferons in NanoCMARter compared to pS/MARter electroporated CAR$^+$ T cells (unpublished).

The reasons why the tumors were not completely eliminated despite of infiltrated pS/MARter and NanoCMARter human CAR$^+$ T cells were already discussed in the context of lentivirally transduced CAR$^+$ T cells and might be based on weak or lack NY-BR-1 expression, the already completed elimination of NY-BR-1$^+$ tumor cells and an immunosuppressive tumor microenvironment, whereby the latter has to be investigated in more detail.

In order to get an even better understanding of the functionality of anti-NY-BR-1 CARs, the optimal approach would be the evaluation of murine CAR$^+$ T cells in wild-type mice providing a functional immune system. However, due to rejection of NY-BR-1$^+$ EO771 cells in both C57BL/6 wt and NY-BR-1$^{tg/-}$ mice, the subcutaneous NY-BR-1$^+$ EO771 tumor bearing NOD.CB17-Prkdc^{scid} mouse model had to be

used (see chapter 5.7). In contrast to human T cells, pS/MARter electroporated murine T cells expressing anti-NY-BR-1 CARs with mFcΔ_mCD28Δ_m4-1BB_mCD3z domains persisted in mouse spleens and tumors (see Figure 4.8.1, Figure 4.8.2). The reason for this might lie in the strong activation of murine T cells upon electroporation with pS/MARter vectors (encoding the clone2/10D11/clone3scFv_mFcΔ_mCD28Δ_m4-1BB_mCD3z CARs), which was not observed to this extent in human T cells (see Supplementary Figure 6.6). This activation may have had a positive effect on the initial expansion and persistence of murine CAR$^+$ T cells. On the basis of the results obtained with different human anti-NY-BR-1 CAR constructs, even better results could be achieved with murine OX40 CAR$^+$ T cells, which needs to be examined in further experiments.

Nevertheless, murine clone2 and 10D11 CAR$^+$ T cells highly persisted in the spleens, whereas clone3 CAR$^+$ T cells surprisingly infiltrated the tumors in much larger amounts than clone2 and 10D11 CAR$^+$ T cells. In spite of very different quantities of tumor - infiltrating T cells, no statistically significant differences in the tumor growth curves between the CAR$^+$ T cell treatment groups were noted. Only the overall survival was slightly extended upon treatment with clone3 CAR$^+$ T cells, closely followed by 10D11 CAR$^+$ T cells compared to mock and clone2 CAR$^+$ T cell - treated mice. The reason for this phenomenon might be, as already described for Bosc23 tumor-bearing NSG mice, low NY-BR-1 expression rates in outgrowing EO771 tumor, whereby the tumors probably exhibit high NY-BR-1 expression levels at initial growth leading to rejection in immunocompetent mice and allowing an initially high infiltration with (CAR$^+$) T cells (see chapter 5.7). In addition, CAR$^+$ T cells might have eliminated all NY-BR-1$^+$ EO771 cells, resulting in the overgrowth of antigen negative tumor cells. These hypotheses are supported by the facts that, as described for NY-BR-1$^+$ Bosc23 tumors, immunohistological stainings against NY-BR-1 protein could not be established for adult tumors and that Krishna Das (2017) [256] also reported about the failure of NY-BR-1 detection on the surface of outgrown NY-BR-1$^+$ EO771 tumors. On top of that, untreated NY-BR-1$^+$ EO771 cells mostly showed lower NY-BR-1 expression levels than NY-BR-1$^+$ Bosc23 cells *in vitro* (see Figure 4.1.2, Figure 4.1.4), which may lead to an even weaker anti-tumor immune response and less suppression of tumor growth in NY-BR-1$^+$ EO771 NOD.CB17-Prkdc^{scid} mice compared to NY-BR-1$^+$ Bosc23 NSG mice.

Further reasons for the weak anti-tumoral immune response despite T cell infiltration might also be related to the mouse model used. While the functionality of human T cells was evaluated in NSG mice, which do not exhibit mature T cells, B cells, macrophages and NK cells [425], NOD.CB17-Prkdc^{scid} mice show impaired but not absent function of NK and myeloid cells [415,469]. In addition, flow cytometric analyses of untreated and CAR$^+$ T cell - treated NOD.CB17-Prkdc^{scid} mouse spleens and blood revealed CD3 weakly positive cells, which might indicate T cell leakiness [470,471]. Macrophages, in particular, play a critical role in the immune response to solid tumors. They polarize to the M1 phenotype in the presence of TH1 cytokines such as IL-12 and IL-18 or by activation via TLRs [472]. These macrophages are

generally known to act immunostimulatory by secreting pro-inflammatory cytokines including IL-1ß, IL-6 and TNFα and play a key role in the killing of tumor cells by secretion of ROS [472]. TH2 cytokines such as IL-4, IL-10 and IL-13 trigger the polarization of macrophages into the M2 type, which secrete anti-inflammatory cytokines such as IL-10, IL-13 and TGF-ß and thereby promoting tumor growth [472]. Despite phagocytosis by macrophages, a high intratumoral accumulation of macrophages is often associated with a poor prognosis in many solid tumors [473-475]. In particular, high concentrations of IL-4 and IL-6, secreted by tumor-associated macrophages and TH2 cells, contribute to resistance to chemotherapies and radiotherapies [472,476]. Breast cancer tumors are generally highly infiltrated by macrophages [477] and Krishna Das (2017) [256] also found high levels of tumor infiltrated macrophages in EO771 and especially in NY-BR-1$^+$ EO771 derived tumors. Considering the cytokine concentrations in the blood of NY-BR-1$^+$ CAR T cell - treated NY-BR-1$^+$ EO771 NOD.CB17-Prkdc^{scid} mice, it is striking that high concentrations of the immunosuppressive cytokine IL-10 [380,445] were measured in all CAR$^+$ T cell groups (see Figure 4.8.3). In addition, high concentrations of TH2 cytokines such as IL-4, IL-5 and IL-13 [478] were found in clone3 CAR$^+$ T cell - treated mice. TH2 immune responses, especially the release of IL-4, have an antagonistic effect on TH1 polarization [479] and promote both tumor growth and immunosuppressive effects of T_{reg} cells [480,481]. Breast cancer tumors in the MMTV-PyMT mouse model were also infiltrated by IL-4 producing TH2 cells, which in turn promoted M2 macrophage differentiation and formation of metastases [482]. Moreover, highly elevated levels of IL-6 were detected in clone2 CAR$^+$ T cell - treated mice, which generally indicates a strong immune response [483] and the presence of macrophages [472]. With regard to other pro-inflammatory cytokines, high concentrations of IL-12 were detected in all CAR$^+$ T cell groups, but the absolute concentrations of CTL-associated cytokines such as IFNγ or IL-2 were only minimally increased, whereby the low IL-2 release is mainly due to the mutation in the CD28 domain [484].

Consequently, the recorded cytokine concentrations in mouse blood suggest that high concentrations of immunosuppressive cytokines, which were presumably released by TH2 cells, T_{reg} cells and M2 macrophages, reduced the immune responses of murine anti-NY-BR-1 CAR$^+$ T cells. In particular, the high IL-10 release could possibly be reduced by using the murine OX40 endodomain. In addition, the cytokine and chemokine concentrations as well as the amount of infiltrated macrophages in the tumor need to be investigated in order to better examine the types and concentrations of the cytokines released by the tumor itself or the immune cells located in the tumor.

Overall, these analyses confirmed that all three anti-NY-BR-1 CARs exhibit high reactivities against NY-BR-1 expressing tumors. In particular, human 10D11 CAR$^+$ T cells showed high anti-tumor reactivities, whereby several indications appeared that human clone2 CAR$^+$ T cells possibly infiltrate better into NY-BR-1 weakly expressing tumors. However, to prove this hypothesis, further mouse experiments with high and low NY-NR-1 expressing tumors are necessary. Using murine CAR$^+$ T cells,

clone3 CAR$^+$ T cells proved to be more beneficial, as they infiltrated to a higher degree than clone2 and 10D11 CAR$^+$ T cells. Nonetheless, they did not lead to a significantly better tumor response than murine 10D11 CAR$^+$ T cells. Furthermore, it was shown that the pS/MARter and NanoCMARter based electroporation technologies can be used for stable CAR transfections of human and murine CAR$^+$ T cells without limiting their functionality. Further experiments with other target antigens as well as the investigation of gene expression patterns in human and murine CAR$^+$ T cells will have to show the extent to which NanoCMARter vectors are more suitable compared to pS/MARter vectors.

In order to generally improve the functionality of anti-NY-BR-1 CARs, combination therapies with radiotherapy [485], chemotherapy [486], checkpoint inhibitors [160,485] or PD-1 disruption in CAR$^+$ T cells by genome editing [487,488] might be useful. To improve tumor infiltration and trafficking to the solid tumor, anti-NY-BR-1 CAR$^+$ T cells could be equipped with chemokine receptors [489,490]. A further possibility is a more detailed examination of T cell phenotypes and expression of exhaustion markers. In fact, injection of CAR - expressing T_{SCM} instead of a total T cell population has been shown to be beneficial in several studies [491,492].

5.9 The 10D11 CAR - a suitable candidate for clinical breast cancer studies

Basically, all three evaluated anti-NY-BR-1 CARs proved to be functional against NY-BR-1 expressing lentivirally transduced cell lines and primary cells. However, the use of clone2 CAR for clinical trials poses a risk in view of strong cross-reactivities to the homologous protein NY-BR-1.1. Similarly, clone3 CAR exhibited weak reactions to the NY-BR-1.1 protein as well. In addition, clone2 CAR showed a strong immune response to NY-BR-1 weakly expressing tissues in NY-BR-1$^{tg/-}$ mice, which could be beneficial for low expressing tumor cells but also might cause strong side effects to normal breast tissue. Furthermore, the 10D11 CAR proved to be superior to clone3 CAR in several experiments, which was especially evident in the absence or weak expression of the NY-BR-1 protein. In fact, murine 10D11 CAR$^+$ T cells persisted better than clone3 CAR$^+$ T cells in C57BL/6 wt and NY-BR-1$^{tg/-}$ mice. Furthermore, murine 10D11 CAR$^+$ T cells retained their functionality against NY-BR-1 expressing target cells even after two weeks of persistence, which was not observed to the same extent with clone3 CAR$^+$ T cells. In tumor-bearing mice, human 10D11 and clone3 CAR$^+$ T cells mostly persisted to a similar extent, whereby the 10D11 CAR often led to higher anti-tumor immune responses, which was reflected in higher cytokine levels in blood and tumors. When expressed in murine T cells, clone3 CAR facilitated a more strongly tumor infiltration than 10D11 CAR, but both led to similarly good outcomes. Consequently, both 10D11 and clone3 CAR$^+$ T cells display very similar characteristics and both might contribute to the control of NY-BR-1$^+$ tumors in patients. However, since the 10D11 CAR did not show

any cross reactivities so far, led to better persistence of T cells than clone3 CAR in the absence of the NY-BR-1 target, and performed equally well or better than clone3 CAR despite weaker or equally good tumor infiltration, the 10D11 CAR represents the most suitable CAR for clinical trials according to current research. Due to significantly higher expression levels of OX40 CARs in human T cells as well as better persistence and efficiencies of OX40 CAR^+ T cells in direct comparison to T cells expressing CD28_4-1BB CARs, the application of 10D11scFv_hFc_CD28_CD3z_OX40 CAR – expressing T cells is recommended.

6 Supplement

DNA sequence encoding the NY-BR-1 full length protein

atggaggagatctctgccgccgctgtcaaggtcgtgccgggcccggagcgcccgagccctttcagccagctagtctataccagcaacgactc
ctacatcgtccactctggggatcttagaaagatccataaagctgcctcccggggacaagtccggaagctggagaagatgacaaagaggaagaa
gaccatcaaccttaatatacaagacgcccagaagaggactgctctacactgggcctgtgtcaatggccatgaggaagtagtaacatttctggtag
acagaaagtgccagcttgacgtccttgatggcgaacacaggacacctctgatgaaggctctacaatgccatcaggaggcttgtgcaaatattctg
atagattctggtgccgatataaatctcgtagatgtgtatggcaacacggctctccattatgctgtttatagtgagattttgtcagtggtggcaaaact
gctgtcccatggtgcagtcatcgaagtgcacaacaaggctagcctcacaccacttttactatccataacgaaaagaagtgagcaaattgtggaat
ttttgctgataaaaaatgcaaatgcgaatgcagttaataagtataaatgcacagccctcatgcttgctgtatgtcatggatcatcagagatagttg
gcatgcttcttcagcaaaatgttgacgtctttgctgcagatatatgtggagtaactgcagaacattatgctgttacttgtggatttcatcacattcatg
aacaaattatggaatatatacgaaaattatctaaaaatcatcaaaataccaatccagaaggaacatctgcaggaacacctgatgaggctgcacc
cttggcggaaagaacacctgacacagctgaaagcttggtggaaaaaacacctgatgaggctgcacccttggtggaaagaacacctgacacggc
tgaaagcttggtggaaaaaacacctgatgaggctgcatccttggtggagggaacatctgacaaaattcaatgtttggagaaagcgacatctgga
aagttcgaacagtcagcagaagaaacacctagggaaattacgagtcctgcaaaagaaacatctgagaaatttacgtggccagcaaaaggaag
acctaggaagatcgcatgggagaaaaaagaagacacacctagggaaattatgagtcccgcaaaagaaacatctgagaaatttacgtgggcag
caaaaggaagacctaggaagatcgcatgggagaaaaaagaaacacctgtaaagactggatgcgtggcaagagtaacatctaataaaactaaa
gttttggaaaaaggaagatctaagatgattgcatgtcctacaaaagaatcatctacaaaagcaagtgccaatgatcagaggttcccatcagaatc
caaacaagaggaagatgaagaatattcttgtgattctcggagtctctttgagagttctgcaaagattcaagtgtgtatacctgagtctatatatcaa
aaagtaatggagataaatagagaagtagaagagcctcctaagaagccatctgccttcaagcctgccattgaaatgcaaaactctgttccaaata
aagcctttgaattgaagaatgaacaaacattgagagcagatccgatgttcccaccagaatccaaacaaaaggactatgaagaaaattcttgggga
ttctgagagtctctgtgagactgtttcacagaaggatgtgtgtttacccaaggctacacatcaaaaagaaatagataaaataaatggaaaattag
aagagtctcctaataaagatggtcttctgaaggctacctgcggaatgaaagtttctattccaactaaagccttagaattgaaggacatgcaaactt
tcaaagcagagcctccggggaagccatctgccttcgagcctgccactgaaatgcaaaagtctgtcccaaataaagccttggaattgaaaaatga
acaaacattgagagcagatgagatactcccatcagaatccaaagaaaaggactatgaagaaaattcttgggatactgagagtctctgtgagact
gtttcacagaaggatgtgtgtttacccaaggctgcgcatcaaaaagaaatagataaaataaatggaaaattagaagggtctcctgttaaagatg
gtcttctgaaggctaactgcggaatgaaagtttctattccaactaaagccttagaattgatggacatgcaaactttcaaagcagagcctcccgaga
agccatctgccttcgagcctgccattgaaatgcaaaagtctgttccaaataaagccttggaattgaagaatgaacaaacattgagagcagatga
gatactcccatcagaatccaaacaaaaggactatgaagaaagttcttgggattctgagagtctctgtgagactgtttcacagaaggatgtgtgttt
acccaaggctacacatcaaaaagaaatagataaaataaatggaaaattagaagagtctcctgataatgatggttttctgaaggctccctgcaga
atgaaagtttctattccaactaaagccttagaattgatggacatgcaaactttcaaagcagagcctcccgagaagccatctgccttcgagcctgcc
attgaaatgcaaaagtctgttccaaataaagccttggaattgaagaatgaacaaacattgagagcagatcagatgttcccttcagaatcaaaac
aaaagaaggttgaagaaaattcttgggattctgagagtctccgtgagactgtttcacagaaggatgtgtgtgtacccaaggctacacatcaaaaa
gaaatggataaaataagtggaaaattagaagattcaactagcctatcaaaaatcttggatacagttcattcttgtgaaagagcaagggaacttca
aaaagatcactgtgaacaacgtacaggaaaaatggaacaaatgaaaaagaagttttgtgtactgaaaaagaaactgtcagaagcaaaagaaa
taaaatcacagttagagaaccaaaaagttaaatgggaacaagagctctgcagtgtgagattgactttaaaccaagaagaagagaagagaaga
aatgccgatatattaaatgaaaaaattagggaagaattaggaagaatcgaagagcagcataggaaagagttagaagtgaaacaacaacttga
acaggctctcagaatacaagatatagaattgaagagtgtagaaagtaatttgaatcaggtttctcacactcatgaaaatgaaaattatctcttaca
tgaaaattgcatgttgaaaaaggaaattgccatgctaaaactggaaatagccacactgaaacaccaataccaggaaaaggaaaataaatactt
tgaggacattaagattttaaaagaaaagaatgctgaacttcagatgaccctaaaactgaaagaggaatcattaactaaaagggcatctcaatat
agtgggcagcttaaagttctgatagctgagaacacaatgctcacttctaaattgaaggaaaaacaagacaaagaaatactagaggcagaaatt
gaatcacaccatcctagactggcttctgctgtacaagaccatgatcaaattgtgacatcaagaaaaagtcaagaacctgctttccacattgcagg
agatgcttgtttgcaaagaaaaatgaatgttgatgtgagtagtacgatatataacaatgaggtgctccatcaaccactttctgaagctcaaagga
aatccaaaagcctaaaaattaatctcaattatgccggagatgctctaagagaaaatacattggtttcagaacatgcacaaagagaccaacgtga
aacacagtgtcaaatgaaggaagctgaacacatgtatcaaaacgaacaagataatgtgaacaaacacactgaacagcaggagtctctagatca
gaaattatttcaactacaaagcaaaaatatgtggcttcaacagcaattagttcatgcacataagaaagctgacaacaaaagcaagataacaatt
gatattcattttcttgagaggaaaatgcaacatcatctcctaaaagagaaaaatgaggagatatttaattacaataaccatttaaaaaaccgtat
atatcaatatgaaaaagagaaagcagaaacagaaaactcatga

Supplementary Figure 6.1: DNA sequence of vector #44 (hPGK_NY-BR-1_IRES_Puromycin_WPRE) encoding the NY-BR-1 full length protein

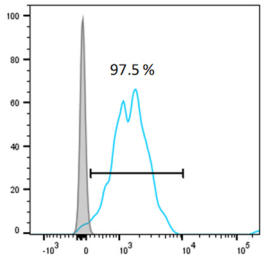

Supplementary Figure 6.2: Staining of CD3 positive murine T cells 48 h upon isolation
Murine T cells were stained with the APC - conjugated anti-mouse CD3 antibody 48 h after isolation using the *Pan T cell Isolation Kit II* (Miltenyi). Unstained cells were used as controls (grey). The percentage indicate the proportion of CD3 positive cells of the total number of isolated cells.

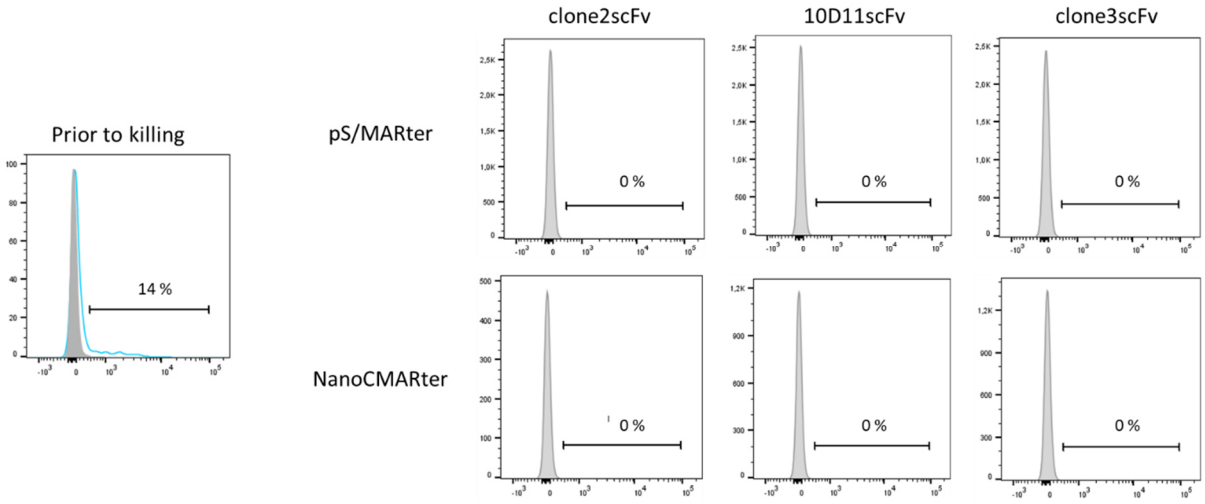

Supplementary Figure 6.3: NY-BR-1 expression profile of pleural effusion cells (HD-A-213) prior and after co-cultivation with pS/MARter and NanoCMARter electroporated anti-NY-BR-1 CAR - expressing T cells (CHA90)
Pleural effusion cells, isolated from patient HD-A-213, were co-cultivated with allogeneic pS/MARter (clone2scFv_hFc_hCD28_CD3z_hOX40 (#432), 10D11scFv_hFc_hCD28_CD3z_hOX40 (#433), clone3scFv_hFc_hCD28_CD3z_hOX40 (#434)) and NanoCMARter (clone2scFv_hFc_hCD28_CD3z_hOX40 (531), 10D11scFv_hFc_hCD28_CD3z_hOX40 (#532), clone3scFv_hFc_hCD28_CD3z_hOX40 (#533)) electroporated CAR^+ T cells in 96 well electronic microtiter plates (E-Plate 96, ACEA Biosciences) at a ratio of 1:1 for 80 h. The frequency of NY-BR-1 positive target cells was determined by flow cytometric analysis prior and after the xCELLigence based killing assay. Cells were stained with the monoclonal anti-NY-BR-1 antibody clone2 and the secondary APC - conjugated anti-mouse IgG antibody. The percentages indicate the proportion of NY-BR-1 positive cells of the total number of survived pleural effusion cells.

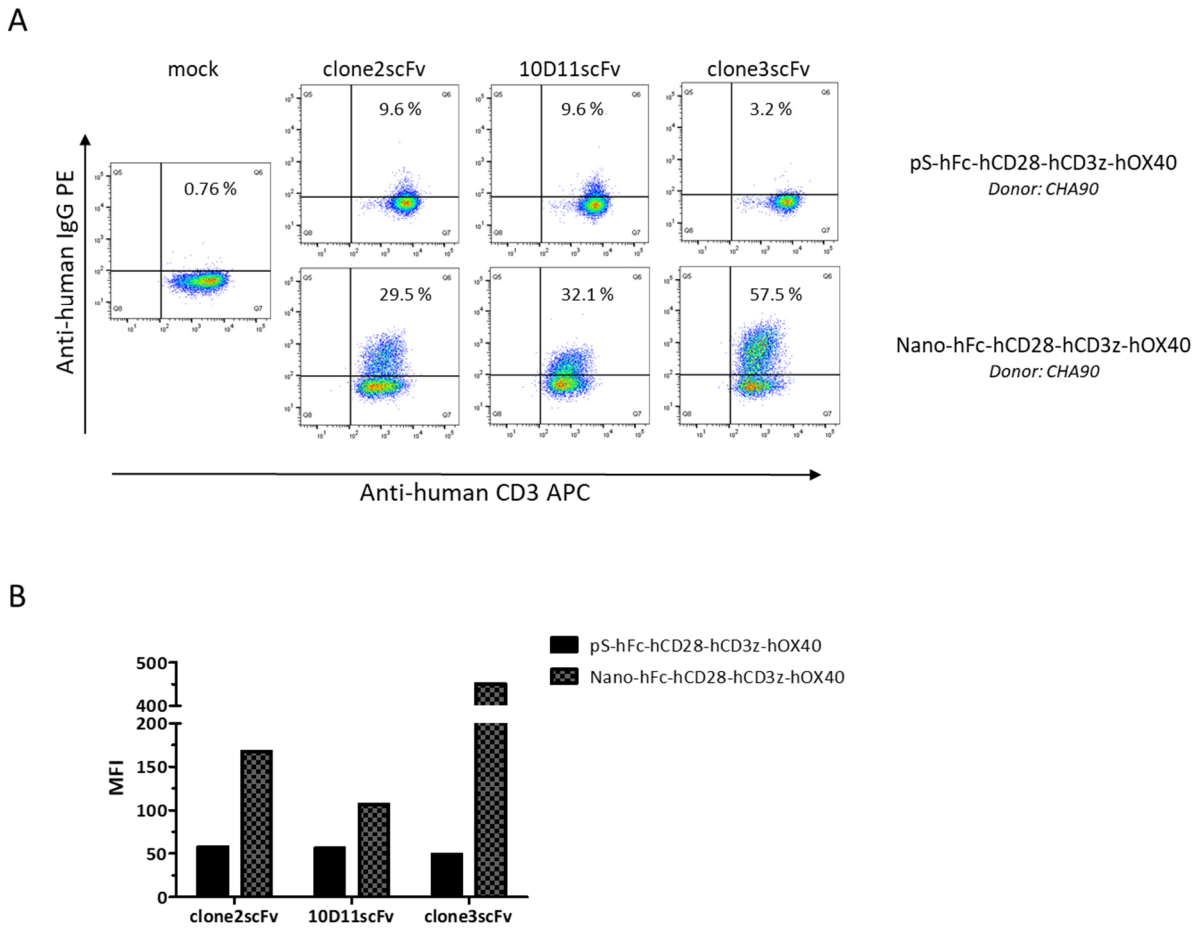

Supplementary Figure 6.4: Expression analysis of human anti-NY-BR-1 CARs in pS/MARter and NanoCMARter electroporated T cells (CHA90) prior to xCELLigence based killing assay of pleural effusion cells (HD-A-213)
pS/MARter (clone2scFv_hFc_hCD28_CD3z_hOX40 (#432), 10D11scFv_hFc_hCD28_CD3z_hOX40 (#433), clone3scFv_hFc_hCD28_CD3z_hOX40 (#434)) and NanoCMARter (clone2scFv_hFc_hCD28_CD3z_hOX40 (531), 10D11scFv_hFc_hCD28_CD3z_hOX40 (#532), clone3scFv_hFc_hCD28_CD3z_hOX40 (#533)) electroporated T cells (donor CHA90) were analyzed for the surface expression levels of the different CAR constructs prior to co-cultivation with the pleural effusion cells (HD-A-213). T cells were stained with the PE-conjugated anti-human IgG and the APC - conjugated anti-human CD3 antibodies. [A] The percentages indicate the proportion of CAR - expressing T cells of the total number of electroporated T cells. Untransfected (mock) T cells were used as controls. [B] Surface CAR density reflected by mean fluorescence intensity (MFI).

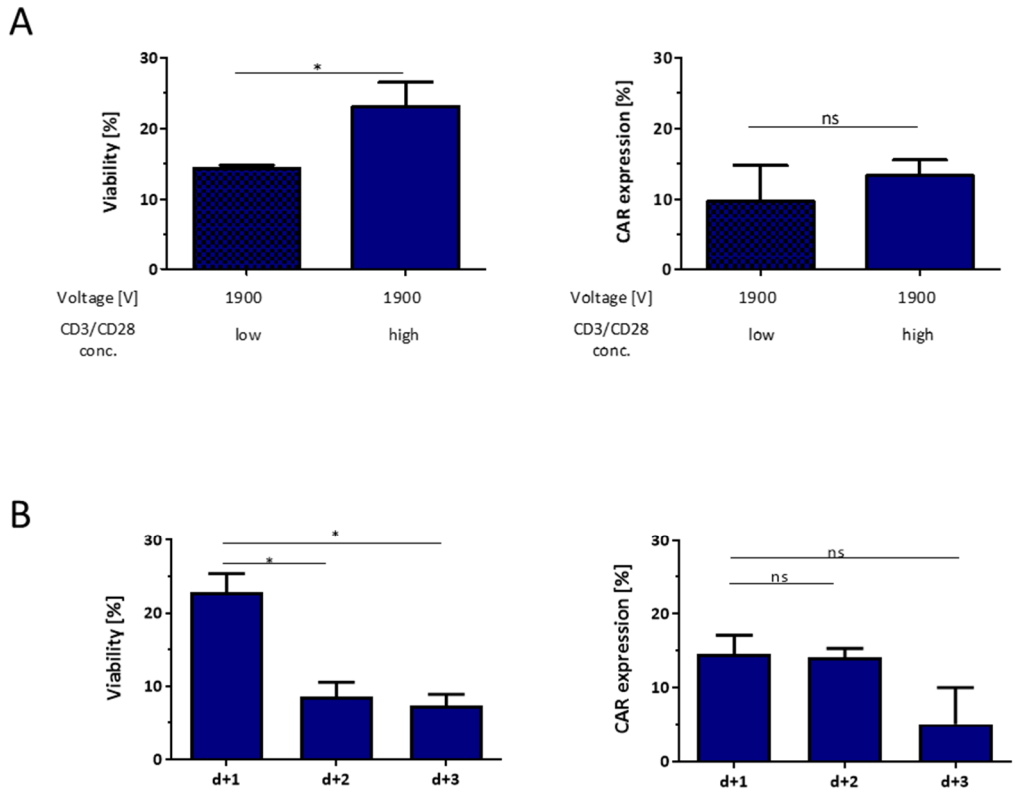

Supplementary Figure 6.5: Viability and CAR expression rates in murine pS/MARter electroporated T cells
Murine T cells were electroporated with the pS/MARter vectors (clone2scFv_mFcΔ_mCD28Δ_m4-1BB_CD3z), #295 (10D11scFv_mFcΔ_mCD28Δ_m4-1BB_CD3z) and #296 (clone3scFv_mFcΔ_mCD28Δ_m4-1BB_CD3z) at 1900 V (10ms, 3 pulses). [A] T cells were cultivated in RPMI medium supplemented with ß-mercaptoethanol (50 µM), IL-2 (100 IU / mL) anti-CD3 Ab (100ng / mL), anti-CD28 Ab (100 ng / mL), L-glutamine (2 mM) and non-essential amino acids (1x) for 24 h before electroporation. CD3 / CD28 high means that increased concentrations of the anti-CD3 (2 µg / mL) and anti-CD28 (1 µg / mL) antibodies were applied. Following electroporation, T cells were cultivated in RPMI-1640 medium (w / o Phenol red) supplemented with 20 % FCS, IL-2 (100 IU / mL) and L-glutamine (2mM). Data represent the viability and CAR expression levels 24 h after electroporation (mean values ± sem; 1900 V, low: n = 5; 1900 V, high: n = 11; *, $p < 0.05$; Welch corrected unpaired one-tailed Student's t-test). [B] T cells were cultivated as described in [A] under the usage of increased concentrations of the anti-CD3 and anti-CD28 antibodies. Data represent the viability and CAR expression levels in murine T cells one, two and three days after electroporation (mean values ± sem; d+1: n = 15; d+2: n = 5; d+3: n = 2; *, $p < 0.05$; **, $p < 0.01$; one-way ANOVA followed by Holm-Sidak's multiple comparison test). CAR expression levels were determined by staining with the APC or PE - conjugated anti-mouse IgG antibodies. Viability rates were calculated using DAPI staining and flow cytometric analysis.

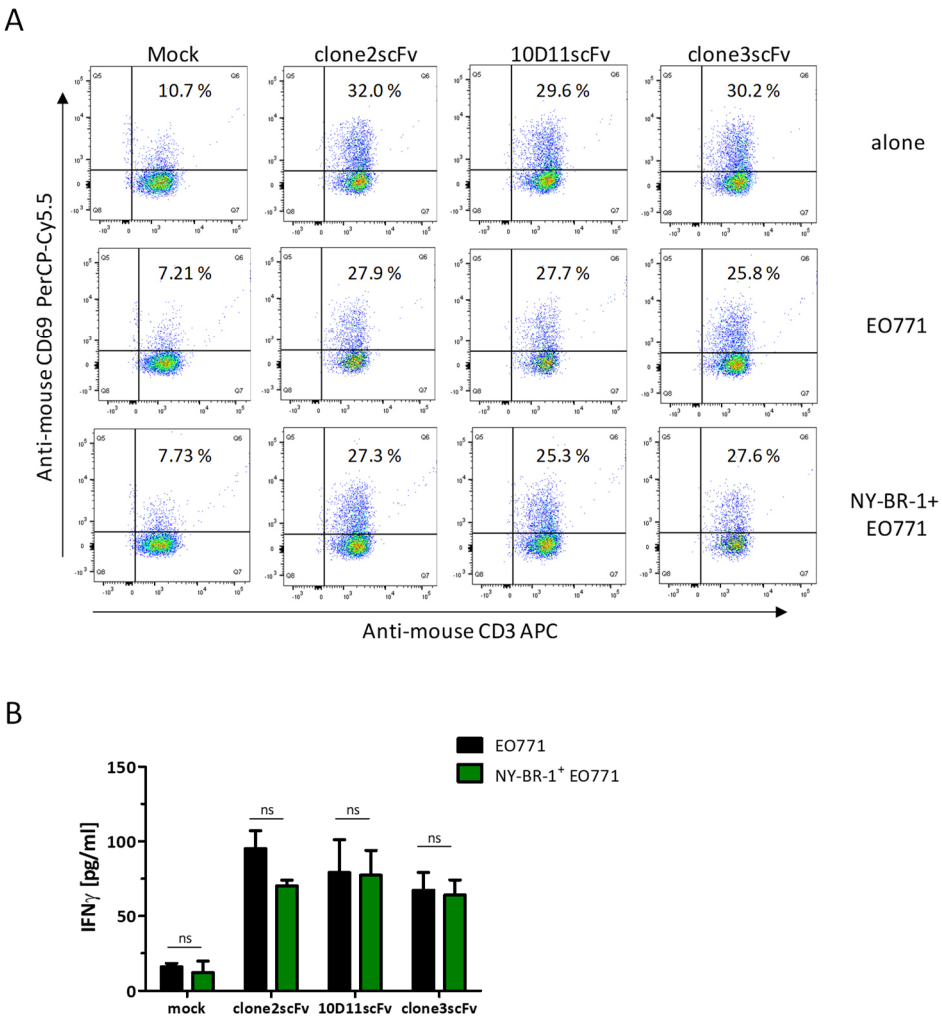

Supplementary Figure 6.6: Activation level of murine pS/MARter electroporated CAR$^+$ T cells upon co-cultivation with (NY-BR-1$^+$) EO771 cells

Murine T cells were electroporated with pS/MARter vectors encoding the anti-NY-BR-1 CAR constructs #277 (clone2scFv_mFcΔ_mCD28Δ_m4-1BB_CD3z), #295 (10D11scFv_mFcΔ_mCD28Δ_m4-1BB_CD3z) and #296 (clone3scFv_mFcΔ_mCD28Δ_m4-1BB_CD3z) and subsequently co-cultivated with Lactacystin-treated (NY-BR-1$^+$) EO771 cells at a ratio of 1:1 in 96 well plates for 24 h. Untransfected (mock) T cells were used as controls. [A] Cells were stained with the APC - conjugated anti-mouse CD3 and PerCP-Cy5.5- conjugated anti-mouse CD69 antibodies. The percentages indicate the proportion of living (DAPI$^-$) CD3$^+$ CD69$^+$ cells of the total number of alone or (NY-BR-1$^+$) EO771 co-cultivated T cells. [B] The IFNγ concentrations in the cell culture supernatants were recorded by IFNγ ELISA at the end of the experiment. Experiments were performed in triplicate (mean values ± sem; no statistically significant differences according to paired two-tailed Student's t-test).

A

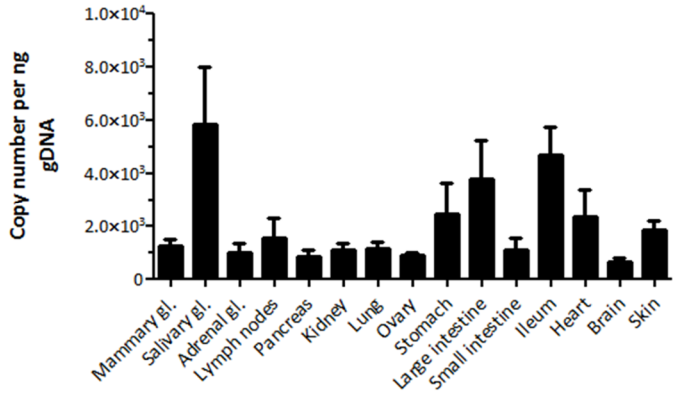

B

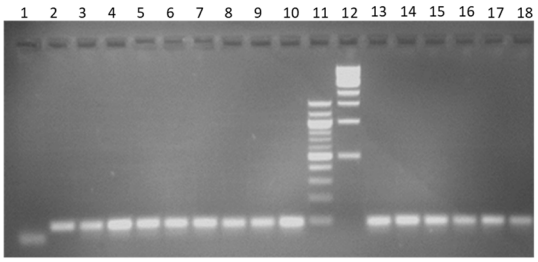

1) H_2O neg. control
2) Mammary gl.
3) Adrenal gl.
4) Salivary gl.
5) Lymph nodes
6) Pancreas
7) Kidney
8) Lung
9) Ovary
10) Stomach
11) 100 bp DNA ladder
12) 1 kb DNA ladder
13) Large intestine
14) Ileum
15) Heart
16) Small intestine
17) Skin
18) Brain

Supplementary Figure 6.7: Real-time qPCR based determination of transgene (NY-BR-1) copy number in NY-BR-1$^{tg/-}$ mice
Following gDNA isolation from different organs of NY-BR-1$^{tg/-}$ mice, absolute transgene copy numbers were determined using real-time qPCR and primers #370 and #371, which generate an amplicon of 99 bps within the SV40 poly A – encoding DNA sequence. Reactions were done in triplicate. The standard curve was generated by amplifying a dilution series of plasmid #44 (hPGK_NY-BR-1_IRES_Puromycin_WPRE). [A] The absolute transgene copy number per ng gDNA is given for every organ. [B] Gel electrophoresis of the qPCR products.

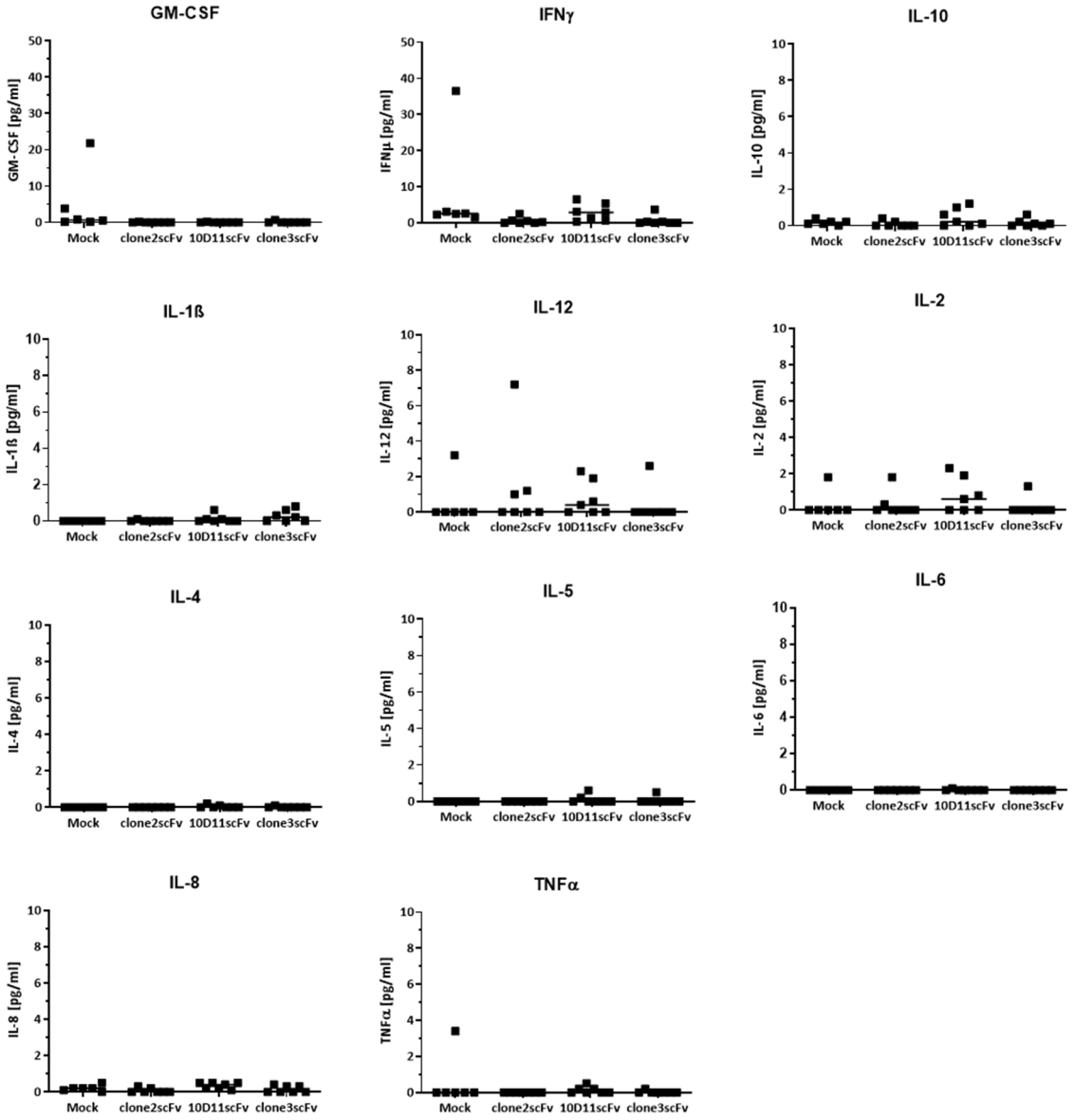

Supplementary Figure 6.8: Plasma cytokine profile of tumor-bearing NSG mice upon treatment with lentivirally transduced CAR$^+$ T cells

NSG mice were engrafted with NY-BR-1$^+$ Bosc23 derived tumors (2x10^6 NY-BR-1$^+$ Bosc23 cells / mouse) and treated with anti-NY-BR-1 (#537, #538, #539) CAR$^+$ T cells (1x10^6 CAR$^+$ T cells / mouse) or untransduced (mock) T cells. Tumor engrafted mice were sacrified at a tumor diameter of 15 mm or a tumor volume of 300 mm, whatever occurred first. The tumor volumes were calculated with the ellipsoid formula (1/6 x π x length x width x depth). Subsequently, the cytokine concentrations in the murine blood were assessed by using the Human 11-Plex Cytokine Kit (Ayoxxa) (lines indicate the medians; mock: n = 6; clone2scFv, 10D11scFv, clone3scFv: n = 7; clone3scFv: n = 7; no statistically significant differences according to Kruskal Wallis Dunn's multiple comparison tests).

7 Abbreviations

°C	degree Celsius
µg	microgram
µL	microliter
µM	micromolar
ACT	Adoptive cell transfer
ADCC	Antibody-dependent cell-mediated cytotoxicity
ALL	Acute lymphocytic leukemia
AML	Acute myeloid leukemia
ANK	Ankyrin
ANOVA	Analysis of variance
app	approximately
BCR	B cell receptor
bp	base pair
CAR	Chimeric antigen receptor
CD	Cluster of differentiation
CK	Cytokeratin
CLL	Chronic lymphocytic leukemia
cMet	Tyrosine-protein kinase Met
CML	Chronic myeloid leukemia
CMV	*Cytomegalovirus*
DC	Dendritic cell
dH_2O	Distilled water
DLBCL	Diffuse large B-cell lymphoma
DMEM	Dulbecco's Modified Eagle Medium
DMSO	Dimethyl Sulfoxide
DNA	Deoxyribonucleic acid
E.*coli*	Escherichia coli
EBNA1	EBV nuclear antigen-1
EBV	Epstein-Barr virus
EC	European Commission
EDTA	Ethylenediaminetetraacetic acid
EGFR	Epidermal growth factor receptor
ELISA	Enzyme-linked Immunosorbent Assay
ER	Estrogen receptor

ERBB2	Erb-b2 receptor tyrosine kinase 2
ERE	Estrogen receptor response elements
ESA	Epithelial surface antigen
FasL	Fas ligand
FCS	Fetal calf serum
FDA	U. S. Food and Drug Administration
FISH	Fluorescence in situ hybridization
FITC	Fluorescein isothiocyanate
g	gram
GEM	Genetically engineered mouse
GM-CSF	Granulocyte–macrophage colony-stimulating factor
HER2	Human epidermal growth factor receptor 2
HIV	Human immunodeficiency virus
HLA	Human leukocyte antigen
hPGK	Human phosphoglycerate kinase 1 promoter
h	hour
HSC	Hematopoietic stem cell
(q)PCR	(quantitative) Polymerase chain reaction
ICOS	Inducible costimulator
IFN	Interferon
Ig	Immunoglobulin
IL	Interleukin
IRES	Internal ribosomal entry site
ITAM(s)	Immunoreceptor tyrosine-based activation motifs
IU	International Unit
kb	Kilobase
kDa	Kilodaltons
LB-medium	Lysogeny broth medium
LTR	Long terminal repeat
M	Molar
mAb	Monoclonal antibody
MACS	Magnetic activated cell sorting
mHAg	Minor Histocompatibility antigen
min(s)	minute(s)
mL	Milliliter

MLV	Murine leukemia virus
mM	Millimolar
MMTV-LTR	Mouse mammary tumor virus long terminal repeat
mPGK	Murine phosphoglycerate kinase
mRNA	*messenger* RNA
ms	milliseconds
mTEC	Medullary thymic epithelial cells
Muc1	Mucin 1
Nano	NanoCMARter
ng	Nanogram
NK cell	Natural killer cell
NY-BR-1	New York Breast 1
ORC	Origin replication complex
ORF	Open reading frame
ori	Origin of replication
P / S	Penicillin / Streptomycin
PBMCs	Peripheral blood mononuclear cell
PBS	Phosphate buffered saline
PCR	Polymerase chain reaction
PD-1	Programmed death 1
PDK	Phosphoinositide-dependent protein kinase
PD-L1	Programmed death ligand 1
PE	Phycoerythrin
PEG	Polyethylene glycol
PFA	Paraformaldehyde
PI	Propidium iodide
PR	Progesterone receptor
pS	pS/MARter
Puro	Puromycin
RNA	Ribonucleic acid
rpm	Rounds per minute
RPMI medium	Roswell Park Memorial Institute Medium
RTK	Receptor tyrosine kinase
S/MAR	Scaffold/matrix attachment region
SAF	Scaffold attachment factor

scFv	Single chain variable fragment
SD	Stable disease
sec(s)	Second(s)
SERMs	Selective estrogen receptor modulators
shRNA	Small hairpin RNA
SV40	Simian virus 40
Ta	Annealing temperature
TAA	Tumor associated antigen
TCR	T cell receptor
TGF-ß	Transforming-growth factor ß
Th	T helper cell
TIL	Tumor - infiltrating lymphocytes
Tm	Melting temperature
TM	transmembrane
TNBC	Triple negative breast cancer
T_{reg} cells	Regulatory T cells
TRUCK	T cells redirected for universal cytokine killing
T_{SCM}	Stem cell like memory T cell
U	Unit
UV	Ultraviolet
V	Volt(s)
v/v	Volume per volume
VSV-G	Vesicular stomatitis virus glycoprotein G
WPRE	Woodchuck Hepatitis Virus (WHP) Posttranscriptional Regulatory Element

8 References

1 Bray, F. *et al.* Global cancer statistics 2018: GLOBOCAN estimates of incidence and mortality worldwide for 36 cancers in 185 countries. *CA Cancer J Clin* **68**, 394-424, doi:10.3322/caac.21492 (2018).

2 Lin, L. *et al.* Incidence and death in 29 cancer groups in 2017 and trend analysis from 1990 to 2017 from the Global Burden of Disease Study. *J Hematol Oncol* **12**, 96, doi:10.1186/s13045-019-0783-9 (2019).

3 You, W. & Henneberg, M. Cancer incidence increasing globally: The role of relaxed natural selection. *Evol Appl* **11**, 140-152, doi:10.1111/eva.12523 (2018).

4 Ghoncheh, M., Pournamdar, Z. & Salehiniya, H. Incidence and Mortality and Epidemiology of Breast Cancer in the World. *Asian Pac J Cancer Prev* **17**, 43-46, doi:10.7314/apjcp.2016.17.s3.43 (2016).

5 Baselga, J. & Norton, L. Focus on breast cancer. *Cancer Cell* **1**, 319-322, doi:10.1016/s1535-6108(02)00066-1 (2002).

6 Ma, H., Bernstein, L., Ross, R. K. & Ursin, G. Hormone-related risk factors for breast cancer in women under age 50 years by estrogen and progesterone receptor status: results from a case-control and a case-case comparison. *Breast Cancer Res* **8**, R39, doi:10.1186/bcr1514 (2006).

7 Feigelson, H. S. & Henderson, B. E. Future possibilities in the prevention of breast cancer: role of genetic variation in breast cancer prevention. *Breast Cancer Res* **2**, 277-282, doi:10.1186/bcr69 (2000).

8 Sun, Y. S. *et al.* Risk Factors and Preventions of Breast Cancer. *Int J Biol Sci* **13**, 1387-1397, doi:10.7150/ijbs.21635 (2017).

9 Rauh, C. *et al.* Association of molecular subtypes with breast cancer risk factors: a case-only analysis. *Eur J Cancer Prev* **24**, 484-490, doi:10.1097/CEJ.0000000000000111 (2015).

10 Weigelt, B., Peterse, J. L. & van 't Veer, L. J. Breast cancer metastasis: markers and models. *Nat Rev Cancer* **5**, 591-602, doi:10.1038/nrc1670 (2005).

11 Ward, E. M. *et al.* Cancer statistics: Breast cancer in situ. *CA Cancer J Clin* **65**, 481-495, doi:10.3322/caac.21321 (2015).

12 Lee, R. J. *et al.* Ductal carcinoma in situ of the breast. *Int J Surg Oncol* **2012**, 123549, doi:10.1155/2012/123549 (2012).

13 Korkola, J. E. *et al.* Differentiation of lobular versus ductal breast carcinomas by expression microarray analysis. *Cancer Res* **63**, 7167-7175 (2003).

14 Chiu, A. M., Mitra, M., Boymoushakian, L. & Coller, H. A. Integrative analysis of the inter-tumoral heterogeneity of triple-negative breast cancer. *Sci Rep* **8**, 11807, doi:10.1038/s41598-018-29992-5 (2018).

15 Gao, J. J. & Swain, S. M. Luminal A Breast Cancer and Molecular Assays: A Review. *Oncologist* **23**, 556-565, doi:10.1634/theoncologist.2017-0535 (2018).

16 Goldhirsch, A. *et al.* Personalizing the treatment of women with early breast cancer: highlights of the St Gallen International Expert Consensus on the Primary Therapy of Early Breast Cancer 2013. *Ann Oncol* **24**, 2206-2223, doi:10.1093/annonc/mdt303 (2013).

17 Fallahpour, S., Navaneelan, T., De, P. & Borgo, A. Breast cancer survival by molecular subtype: a population-based analysis of cancer registry data. *CMAJ Open* **5**, E734-E739, doi:10.9778/cmajo.20170030 (2017).

18 Ding, N. H. *et al.* Prognostic Factors for Luminal B-like Breast Cancer. *Curr Med Sci* **39**, 396-402, doi:10.1007/s11596-019-2049-8 (2019).

19 Cheang, M. C. *et al.* Ki67 index, HER2 status, and prognosis of patients with luminal B breast cancer. *J Natl Cancer Inst* **101**, 736-750, doi:10.1093/jnci/djp082 (2009).

20 Wesolowski, R. & Ramaswamy, B. Gene expression profiling: changing face of breast cancer classification and management. *Gene Expr* **15**, 105-115, doi:10.3727/105221611x13176664479241 (2011).

21 Buonomo, O. C. *et al.* New insights into the metastatic behavior after breast cancer surgery, according to well-established clinicopathological variables and molecular subtypes. *PLoS One* **12**, e0184680, doi:10.1371/journal.pone.0184680 (2017).

22 Daemen, A. & Manning, G. Her2 is not a cancer subtype but rather a driver found in all intrinsic subtypes and highly enriched in molecular apocrine tumors. *Cancer Research* **77**, doi:10.1158/1538-7445.Sabcs16-P4-21-21 (2017).

23 Lachapelle, J. & Foulkes, W. D. Triple-negative and basal-like breast cancer: implications for oncologists. *Curr Oncol* **18**, 161-164, doi:10.3747/co.v18i4.824 (2011).

24 Garrido-Castro, A. C., Lin, N. U. & Polyak, K. Insights into Molecular Classifications of Triple-Negative Breast Cancer: Improving Patient Selection for Treatment. *Cancer Discov* **9**, 176-198, doi:10.1158/2159-8290.Cd-18-1177 (2019).

25 Badve, S. *et al.* Basal-like and triple-negative breast cancers: a critical review with an emphasis on the implications for pathologists and oncologists. *Mod Pathol* **24**, 157-167, doi:10.1038/modpathol.2010.200 (2011).

26 Toft, D. J. & Cryns, V. L. Minireview: Basal-like breast cancer: from molecular profiles to targeted therapies. *Mol Endocrinol* **25**, 199-211, doi:10.1210/me.2010-0164 (2011).

27 Rakha, E. A. *et al.* Are triple-negative tumours and basal-like breast cancer synonymous? *Breast Cancer Research* **9**, doi:ARTN 40410.1186/bcr1827 (2007).

28 Rakha, E. A. *et al.* Are triple-negative tumours and basal-like breast cancer synonymous? *Breast Cancer Res* **9**, 404; author reply 405, doi:10.1186/bcr1827 (2007).

29 Polyak, K. Breast cancer: origins and evolution. *J Clin Invest* **117**, 3155-3163, doi:10.1172/JCI33295 (2007).

30 Frank, N. Y., Schatton, T. & Frank, M. H. The therapeutic promise of the cancer stem cell concept. *J Clin Invest* **120**, 41-50, doi:10.1172/JCI41004 (2010).

31 Al-Hajj, M., Wicha, M. S., Benito-Hernandez, A., Morrison, S. J. & Clarke, M. F. Prospective identification of tumorigenic breast cancer cells. *P Natl Acad Sci USA* **100**, 3983-3988, doi:10.1073/pnas.0530291100 (2003).

32 Ponti, D. *et al.* Isolation and in vitro propagation of tumorigenic breast cancer cells with stem/progenitor cell properties. *Cancer Research* **65**, 5506-5511, doi:Doi 10.1158/0008-5472.Can-05-0626 (2005).

33 Crabtree, J. S. & Miele, L. Breast Cancer Stem Cells. *Biomedicines* **6**, doi:10.3390/biomedicines6030077 (2018).

34 Tharmapalan, P., Mahendralingam, M., Berman, H. K. & Khokha, R. Mammary stem cells and progenitors: targeting the roots of breast cancer for prevention. *EMBO J* **38**, e100852, doi:10.15252/embj.2018100852 (2019).

35 Kumar, B. *et al.* Normal Breast-Derived Epithelial Cells with Luminal and Intrinsic Subtype-Enriched Gene Expression Document Interindividual Differences in Their Differentiation Cascade. *Cancer Res* **78**, 5107-5123, doi:10.1158/0008-5472.CAN-18-0509 (2018).

36 Chiche, A. *et al.* p53 controls the plasticity of mammary luminal progenitor cells downstream of Met signaling. *Breast Cancer Res* **21**, 13, doi:10.1186/s13058-019-1101-8 (2019).

37 Skibinski, A. & Kuperwasser, C. The origin of breast tumor heterogeneity. *Oncogene* **34**, 5309-5316, doi:10.1038/onc.2014.475 (2015).

38 Al-Hajj, M. & Clarke, M. F. Self-renewal and solid tumor stem cells. *Oncogene* **23**, 7274-7282, doi:10.1038/sj.onc.1207947 (2004).

39 Mook, S. *et al.* The 70-gene prognosis signature predicts early metastasis in breast cancer patients between 55 and 70 years of age. *Annals of Oncology* **21**, 717-722, doi:10.1093/annonc/mdp388 (2010).

40 Slodkowska, E. A. & Ross, J. S. MammaPrint (TM) 70-gene signature: another milestone in personalized medical care for breast cancer patients. *Expert Rev Mol Diagn* **9**, 417-422, doi:10.1586/Erm.09.32 (2009).

41 Pleijhuis, R. G. *et al.* Obtaining adequate surgical margins in breast-conserving therapy for patients with early-stage breast cancer: current modalities and future directions. *Ann Surg Oncol* **16**, 2717-2730, doi:10.1245/s10434-009-0609-z (2009).

42 Waks, A. G. & Winer, E. P. Breast Cancer Treatment A Review. *Jama-J Am Med Assoc* **321**, 288-300, doi:10.1001/jama.2018.19323 (2019).

43 Chakraborty, S. & Biswas, P. K. Structural insights into selective agonist actions of tamoxifen on human estrogen receptor alpha. *J Mol Model* **20**, doi:ARTN 233810.1007/s00894-014-2338-x (2014).

44 Pan, H. C. *et al.* 20-Year Risks of Breast-Cancer Recurrence after Stopping Endocrine Therapy at 5 Years. *New Engl J Med* **377**, 1836-1846, doi:10.1056/NEJMoa1701830 (2017).

45 Martinkovich, S., Shah, D., Planey, S. L. & Arnott, J. A. Selective estrogen receptor modulators: tissue specificity and clinical utility. *Clin Interv Aging* **9**, 1437-1452, doi:10.2147/CIA.S66690 (2014).

46 Lumachi, F., Santeufemia, D. A. & Basso, S. M. Current medical treatment of estrogen receptor-positive breast cancer. *World J Biol Chem* **6**, 231-239, doi:10.4331/wjbc.v6.i3.231 (2015).

47 Lewis, J. S. & Jordan, V. C. Selective estrogen receptor modulators (SERMs): mechanisms of anticarcinogenesis and drug resistance. *Mutat Res* **591**, 247-263, doi:10.1016/j.mrfmmm.2005.02.028 (2005).

48 Chang, M. Tamoxifen Resistance in Breast Cancer. *Biomol Ther* **20**, 256-267, doi:10.4062/biomolther.2012.20.3.256 (2012).

49 Schneider, R., Barakat, A., Pippen, J. & Osborne, C. Aromatase inhibitors in the treatment of breast cancer in post-menopausal female patients: an update. *Breast Cancer (Dove Med Press)* **3**, 113-125, doi:10.2147/BCTT.S22905 (2011).

50 El Sayed, R. *et al.* Endocrine and Targeted Therapy for Hormone-Receptor-Positive, HER2-Negative Advanced Breast Cancer: Insights to Sequencing Treatment and Overcoming Resistance Based on Clinical Trials. *Front Oncol* **9**, 510, doi:10.3389/fonc.2019.00510 (2019).

51 Agrawal, A. *et al.* Biological effects of fulvestrant on estrogen receptor positive human breast cancer: short, medium and long-term effects based on sequential biopsies. *Int J Cancer* **138**, 146-159, doi:10.1002/ijc.29682 (2016).

52 Wakeling, A. E. Similarities and distinctions in the mode of action of different classes of antioestrogens. *Endocr-Relat Cancer* **7**, 17-28, doi:DOI 10.1677/erc.0.0070017 (2000).

53 Sobhani, N. *et al.* Updates on the CDK4/6 Inhibitory Strategy and Combinations in Breast Cancer. *Cells* **8**, doi:10.3390/cells8040321 (2019).

54 Chen, S. S., Liang, Y., Feng, Z. Y. & Wang, M. X. Efficacy and safety of HER2 inhibitors in combination with or without pertuzumab for HER2-positive breast cancer: a systematic review and meta-analysis. *Bmc Cancer* **19**, doi:ARTN 97310.1186/s12885-019-6132-0 (2019).

55 Burstein, H. J. The distinctive nature of HER2-positive breast cancers. *N Engl J Med* **353**, 1652-1654, doi:10.1056/NEJMp058197 (2005).

56 Maadi, H., Nami, B., Tong, J., Li, G. & Wang, Z. The effects of trastuzumab on HER2-mediated cell signaling in CHO cells expressing human HER2. *BMC Cancer* **18**, 238, doi:10.1186/s12885-018-4143-x (2018).

57 Schettini, F., Giuliano, M., De Placido, S. & Arpino, G. Nab-paclitaxel for the treatment of triple-negative breast cancer: Rationale, clinical data and future perspectives. *Cancer Treat Rev* **50**, 129-141, doi:10.1016/j.ctrv.2016.09.004 (2016).

58 Schneeweiss, A. *et al.* Diagnosis and Therapy of Triple-Negative Breast Cancer (TNBC) - Recommendations for Daily Routine Practice. *Geburtsh Frauenheilk* **79**, 605-617, doi:DOI 10.1055/a-0887-0285 (2019).

59 Swoboda, A. & Nanda, R. Immune Checkpoint Blockade for Breast Cancer. *Cancer Treat Res* **173**, 155-165, doi:10.1007/978-3-319-70197-4_10 (2018).

60 Makhoul, I., Atiq, M., Alwbari, A. & Kieber-Emmons, T. Breast Cancer Immunotherapy: An Update. *Breast Cancer (Auckl)* **12**, 1178223418774802, doi:10.1177/1178223418774802 (2018).

61 Qin, S. *et al.* Novel immune checkpoint targets: moving beyond PD-1 and CTLA-4. *Mol Cancer* **18**, 155, doi:10.1186/s12943-019-1091-2 (2019).

62 Donini, C., D'Ambrosio, L., Grignani, G., Aglietta, M. & Sangiolo, D. Next generation immune-checkpoints for cancer therapy. *J Thorac Dis* **10**, S1581-S1601, doi:10.21037/jtd.2018.02.79 (2018).

63 Wei, S. C., Duffy, C. R. & Allison, J. P. Fundamental Mechanisms of Immune Checkpoint Blockade Therapy. *Cancer Discov* **8**, 1069-1086, doi:10.1158/2159-8290.CD-18-0367 (2018).

64 Vonderheide, R. H. *et al.* Tremelimumab in combination with exemestane in patients with advanced breast cancer and treatment-associated modulation of inducible costimulator expression on patient T cells. *Clin Cancer Res* **16**, 3485-3494, doi:10.1158/1078-0432.CCR-10-0505 (2010).

65 Hu, Z. I. & McArthur, H. L. Immunotherapy in Breast Cancer: the New Frontier. *Curr Breast Cancer Rep* **10**, 35-40, doi:10.1007/s12609-018-0274-y (2018).

66 Sobral-Leite, M. *et al.* Assessment of PD-L1 expression across breast cancer molecular subtypes, in relation to mutation rate, BRCA1-like status, tumor-infiltrating immune cells and survival. *Oncoimmunology* **7**, e1509820, doi:10.1080/2162402X.2018.1509820 (2018).

67 Keir, M. E. *et al.* Tissue expression of PD-L1 mediates peripheral T cell tolerance. *J Exp Med* **203**, 883-895, doi:10.1084/jem.20051776 (2006).

68 Uchiumi, K. *et al.* Cancer stem-like properties of hormonal therapy-resistant breast cancer cells. *Breast Cancer-Tokyo* **26**, 459-470, doi:10.1007/s12282-018-00944-1 (2019).

69 Li, X. X. *et al.* Intrinsic resistance of tumorigenic breast cancer cells to chemotherapy. *J Natl Cancer I* **100**, 672-679, doi:10.1093/jnci/djn123 (2008).

70 Rodriguez, D. *et al.* The Central Contributions of Breast Cancer Stem Cells in Developing Resistance to Endocrine Therapy in Estrogen Receptor (ER)-Positive Breast Cancer. *Cancers* **11**, doi:ARTN 102810.3390/cancers11071028 (2019).

71 Rani, A., Stebbing, J., Giamas, G. & Murphy, J. Endocrine Resistance in Hormone Receptor Positive Breast Cancer-From Mechanism to Therapy. *Front Endocrinol* **10**, doi:ARTN 24510.3389/fendo.2019.00245 (2019).

72 Li, S. Y. *et al.* Combination therapy with epigenetic-targeted and chemotherapeutic drugs delivered by nanoparticles to enhance the chemotherapy response and overcome resistance by breast cancer stem cells. *J Control Release* **205**, 7-14, doi:10.1016/j.jconrel.2014.11.011 (2015).

73 Scioli, M. G. *et al.* The Role of Breast Cancer Stem Cells as a Prognostic Marker and a Target to Improve the Efficacy of Breast Cancer Therapy. *Cancers* **11**, doi:ARTN 102110.3390/cancers11071021 (2019).

74 Saeg, F. & Anbalagan, M. Breast cancer stem cells and the challenges of eradication: a review of novel therapies. *Stem Cell Investig* **5**, 39, doi:10.21037/sci.2018.10.05 (2018).

75 Nardecchia, S., Sanchez-Moreno, P., de Vicente, J., Marchal, J. A. & Boulaiz, H. Clinical Trials of Thermosensitive Nanomaterials: An Overview. *Nanomaterials-Basel* **9**, doi:ARTN 19110.3390/nano9020191 (2019).

76 Menke-van der Houven van Oordt, C. W. *et al.* First-in-human phase I clinical trial of RG7356, an anti-CD44 humanized antibody, in patients with advanced, CD44-expressing solid tumors. *Oncotarget* **7**, 80046-80058, doi:10.18632/oncotarget.11098 (2016).

77 Benedetti, R., Dell'Aversana, C., Giorgio, C., Astorri, R. & Altucci, L. Breast Cancer Vaccines: New Insights. *Front Endocrinol* **8**, doi:ARTN 27010.3389/fendo.2017.00270 (2017).

78 Allahverdiyev, A., Tari, G., Bagirova, M. & Abamor, E. S. Current Approaches in Development of Immunotherapeutic Vaccines for Breast Cancer. *J Breast Cancer* **21**, 343-353, doi:10.4048/jbc.2018.21.e47 (2018).

79 Schmidt, M. *et al.* Highly innovative personalized RNA-immunotherapy for patients with triple negative breast cancer. *Cancer Research* **79**, doi:10.1158/1538-7445.Sabcs18-Ot2-06-01 (2019).

80 Garber, K. Pursuit of tumor-infiltrating lymphocyte immunotherapy speeds up. *Nat Biotechnol* **37**, 969-971, doi:10.1038/d41587-019-00023-6 (2019).

81 Wang, J. H. & Zhou, P. H. New Approaches in CAR-T Cell Immunotherapy for Breast Cancer. *Adv Exp Med Biol* **1026**, 371-381, doi:10.1007/978-981-10-6020-5_17 (2017).

82 Bright, R. K., Bright, J. D. & Byrne, J. A. Overexpressed oncogenic tumor-self antigens. *Hum Vaccin Immunother* **10**, 3297-3305, doi:10.4161/hv.29475 (2014).

83 Vigneron, N. Human Tumor Antigens and Cancer Immunotherapy. *Biomed Res Int* **2015**, 948501, doi:10.1155/2015/948501 (2015).

84 Ilyas, S. & Yang, J. C. Landscape of Tumor Antigens in T Cell Immunotherapy. *J Immunol* **195**, 5117-5122, doi:10.4049/jimmunol.1501657 (2015).

85 Jäger, D. *et al.* Identification of a tissue-specific putative transcription factor in breast tissue by serological screening of a breast cancer library. *Cancer Res* **61**, 2055-2061 (2001).

86 Sahin, U. *et al.* Human Neoplasms Elicit Multiple Specific Immune-Responses in the Autologous Host. *P Natl Acad Sci USA* **92**, 11810-11813, doi:DOI 10.1073/pnas.92.25.11810 (1995).

87 Chen, Y. T., Gure, A. O. & Scanlan, M. J. Serological analysis of expression cDNA libraries (SEREX): an immunoscreening technique for identifying immunogenic tumor antigens. *Methods Mol Med* **103**, 207-216 (2005).

88 Theurillat, J. P. *et al.* Distinct expression patterns of the immunogenic differentiation antigen NY-BR-1 in normal breast, testis and their malignant counterparts. *International Journal of Cancer* **122**, 1585-1591, doi:10.1002/ijc.23241 (2008).

89 Seil, I. *et al.* The differentiation antigen NY-BR-1 is a potential target for antibody-based therapies in breast cancer. *Int J Cancer* **120**, 2635-2642, doi:10.1002/ijc.22620 (2007).

90 Jäger, D. *et al.* NY-BR-1 is a differentiation antigen of the mammary gland. *Appl Immunohistochem Mol Morphol* **15**, 77-83 (2007).

91 Varga, Z. *et al.* Preferential nuclear and cytoplasmic NY-BR-1 protein expression in primary breast cancer and lymph node metastases. *Clin Cancer Res* **12**, 2745-2751, doi:10.1158/1078-0432.CCR-05-2192 (2006).

92 Radvanyi, L. *et al.* The gene associated with trichorhinophalangeal syndrome in humans is overexpressed in breast cancer. *P Natl Acad Sci USA* **102**, 11005-11010, doi:10.1073/pnas.0500904102 (2005).

93 Seil, I. *Molecular biological characterization and expression analysis of the breast tumor antigen NY-BR-1* PhD thesis, Goethe University Frankfurt, (2005).

94 Theurillat, J. P. *et al.* NY-BR-1 protein expression in breast carcinoma: a mammary gland differentiation antigen as target for cancer immunotherapy. *Cancer Immunol Immun* **56**, 1723-1731, doi:10.1007/s00262-007-0316-1 (2007).

95 Seil, I. *et al.* The differentiation antigen NY-BR-1 is a potential target for antibody-based therapies in breast cancer. *International Journal of Cancer* **120**, 2635-2642, doi:10.1002/ijc.22620 (2007).

96 Jäger, D. *et al.* Humoral and cellular immune responses against the breast cancer antigen NY-BR-1: definition of two HLA-A2 restricted peptide epitopes. *Cancer Immun* **5**, 11 (2005).

97 Wang, W., Epler, J., Salazar, L. G. & Riddell, S. R. Recognition of breast cancer cells by CD8+ cytotoxic T-cell clones specific for NY-BR-1. *Cancer Res* **66**, 6826-6833, doi:10.1158/0008-5472.CAN-05-3529 (2006).

98 Gardyan, A. *et al.* Identification of NY-BR-1-specific CD4(+) T cell epitopes using HLA-transgenic mice. *Int J Cancer* **136**, 2588-2597, doi:10.1002/ijc.29322 (2015).

99 Dunn, G. P., Bruce, A. T., Ikeda, H., Old, L. J. & Schreiber, R. D. Cancer immunoediting: from immunosurveillance to tumor escape. *Nat Immunol* **3**, 991-998, doi:10.1038/ni1102-991 (2002).

100 Swann, J. B. & Smyth, M. J. Immune surveillance of tumors. *J Clin Invest* **117**, 1137-1146, doi:10.1172/JCI31405 (2007).

101 Steven, A. & Seliger, B. The Role of Immune Escape and Immune Cell Infiltration in Breast Cancer. *Breast Care (Basel)* **13**, 16-21, doi:10.1159/000486585 (2018).

102 Riley, R. S., June, C. H., Langer, R. & Mitchell, M. J. Delivery technologies for cancer immunotherapy. *Nat Rev Drug Discov* **18**, 175-196, doi:10.1038/s41573-018-0006-z (2019).

103 Lee, H. J. *et al.* Expansion of tumor-infiltrating lymphocytes and their potential for application as adoptive cell transfer therapy in human breast cancer. *Oncotarget* **8**, 113345-113359, doi:10.18632/oncotarget.23007 (2017).

104 Rohaan, M. W., Wilgenhof, S. & Haanen, J. B. A. G. Adoptive cellular therapies: the current landscape. *Virchows Arch* **474**, 449-461, doi:10.1007/s00428-018-2484-0 (2019).

105 Restifo, N. P., Dudley, M. E. & Rosenberg, S. A. Adoptive immunotherapy for cancer: harnessing the T cell response. *Nat Rev Immunol* **12**, 269-281, doi:10.1038/nri3191 (2012).

106 Rosenberg, S. A. *et al.* Durable Complete Responses in Heavily Pretreated Patients with Metastatic Melanoma Using T-Cell Transfer Immunotherapy. *Clinical Cancer Research* **17**, 4550-4557, doi:10.1158/1078-0432.Ccr-11-0116 (2011).

107 Besser, M. J. *et al.* Clinical Responses in a Phase II Study Using Adoptive Transfer of Short-term Cultured Tumor Infiltration Lymphocytes in Metastatic Melanoma Patients. *Clinical Cancer Research* **16**, 2646-2655, doi:10.1158/1078-0432.Ccr-10-0041 (2010).

108 Radvanyi, L. G. *et al.* Specific Lymphocyte Subsets Predict Response to Adoptive Cell Therapy Using Expanded Autologous Tumor-Infiltrating Lymphocytes in Metastatic Melanoma Patients. *Clinical Cancer Research* **18**, 6758-6770, doi:10.1158/1078-0432.Ccr-12-1177 (2012).

109 Goff, S. L. *et al.* Randomized, Prospective Evaluation Comparing Intensity of Lymphodepletion Before Adoptive Transfer of Tumor-Infiltrating Lymphocytes for Patients With Metastatic Melanoma. *J Clin Oncol* **34**, 2389-U2145, doi:10.1200/Jco.2016.66.7220 (2016).

110 Dudley, M. E., Wunderlich, J. R., Shelton, T. E., Even, J. & Rosenberg, S. A. Generation of tumor-infiltrating lymphocyte cultures for use in adoptive transfer therapy for melanoma patients. *J Immunother* **26**, 332-342, doi:Doi 10.1097/00002371-200307000-00005 (2003).

111 Restifo, N. P., Dudley, M. E. & Rosenberg, S. A. Adoptive immunotherapy for cancer: harnessing the T cell response. *Nat Rev Immunol* **12**, 269-281, doi:10.1038/nri3191 (2012).

112 Gros, A. *et al.* PD-1 identifies the patient-specific CD8(+) tumor-reactive repertoire infiltrating human tumors. *Journal of Clinical Investigation* **124**, 2246-2259, doi:10.1172/Jc173639 (2014).

113 Shitaoka, K. *et al.* Identification of Tumoricidal TCRs from Tumor-Infiltrating Lymphocytes by Single-Cell Analysis. *Cancer Immunol Res* **6**, 378-388, doi:10.1158/2326-6066.Cir-17-0489 (2018).

114 Tan, Q. *et al.* Isolation of T cell receptor specifically reactive with autologous tumour cells from tumour-infiltrating lymphocytes and construction of T cell receptor engineered T cells for esophageal squamous cell carcinoma. *J Immunother Cancer* **7**, doi:ARTN 23210.1186/s40425-019-0709-7 (2019).

115 Zhao, Y. B. *et al.* Primary human lymphocytes transduced with NY-ESO-1 antigen-specific TCR genes recognize and kill diverse human tunior cell lines. *Journal of Immunology* **174**, 4415-4423, doi:DOI 10.4049/jimmunol.174.7.4415 (2005).

116 Zhang, J. X. & Wang, L. Y. The Emerging World of TCR-T Cell Trials Against Cancer: A Systematic Review. *Technol Cancer Res T* **18**, doi:Unsp 153303381983106810.1177/1533033819831068 (2019).

117 Haworth, K. B. *et al.* Going Back to Class I: MHC and Immunotherapies for Childhood Cancer. *Pediatr Blood Cancer* **62**, 571-576, doi:10.1002/pbc.25359 (2015).

118 Garrido, F., Aptsiauri, N., Doorduijn, E. M., Lora, A. M. G. & van Hall, T. The urgent need to recover MHC class I in cancers for effective immunotherapy. *Curr Opin Immunol* **39**, 44-51, doi:10.1016/j.coi.2015.12.007 (2016).

119 Seliger, B., Maeurer, M. J. & Ferrone, S. TAP off - Tumors on. *Immunol Today* **18**, 292-299, doi:Doi 10.1016/S0167-5699(97)01052-9 (1997).

120 Jin, P. & Wang, E. Polymorphism in clinical immunology - From HLA typing to immunogenetic profiling. *J Transl Med* **1**, 8, doi:10.1186/1479-5876-1-8 (2003).
121 Zabaneh, D. *et al.* Fine mapping genetic associations between the HLA region and extremely high intelligence. *Sci Rep-Uk* **7**, doi:ARTN 4118210.1038/srep41182 (2017).
122 Burrows, S. R. & Miles, J. J. Immune parameters to consider when choosing T-cell receptors for therapy. *Frontiers in Immunology* **4**, doi:UNSP 22910.3389/fimmu.2013.00229 (2013).
123 Aggen, D. H. *et al.* Single-chain V alpha V beta T-cell receptors function without mispairing with endogenous TCR chains. *Gene Therapy* **19**, 365-374, doi:10.1038/gt.2011.104 (2012).
124 Legut, M., Dolton, G., Mian, A. A., Ottmann, O. G. & Sewell, A. K. CRISPR-mediated TCR replacement generates superior anticancer transgenic T cells. *Blood* **131**, 311-322, doi:10.1182/blood-2017-05-787598 (2018).
125 Bethune, M. T. *et al.* Domain-swapped T cell receptors improve the safety of TCR gene therapy. *Elife* **5**, doi:ARTN e1909510.7554/eLife.19095 (2016).
126 Cohen, C. J., Zhao, Y. B., Zheng, Z. L., Rosenberg, S. A. & Morgan, R. A. Enhanced antitumor activity of murine-human hybrid T-cell receptor (TCR) in human lymphocytes is associated with improved pairing and TCR/CD3 stability. *Cancer Research* **66**, 8878-8886, doi:10.1158/0008-5472.Can-06-1450 (2006).
127 Sebestyen, Z. *et al.* Human TCR that incorporate CD3 zeta induce highly preferred pairing between TCR alpha and beta chains following gene transfer. *Journal of Immunology* **180**, 7736-7746, doi:DOI 10.4049/jimmunol.180.11.7736 (2008).
128 Cohen, C. J. *et al.* Enhanced antitumor activity of T cells engineered to express T-cell receptors with a second disulfide bond. *Cancer Research* **67**, 3898-3903, doi:10.1158/0008-5472.Can-06-3986 (2007).
129 Feins, S., Kong, W., Williams, E. F., Milone, M. C. & Fraietta, J. A. An introduction to chimeric antigen receptor (CAR) T-cell immunotherapy for human cancer. *Am J Hematol* **94**, S3-S9, doi:10.1002/ajh.25418 (2019).
130 Guedan, S., Calderon, H., Posey, A. D., Jr. & Maus, M. V. Engineering and Design of Chimeric Antigen Receptors. *Mol Ther Methods Clin Dev* **12**, 145-156, doi:10.1016/j.omtm.2018.12.009 (2019).
131 Chandran, S. S. & Klebanoff, C. A. T cell receptor-based cancer immunotherapy: Emerging efficacy and pathways of resistance. *Immunol Rev* **290**, 127-147, doi:10.1111/imr.12772 (2019).
132 Murad, J. M., Graber, D. J. & Sentman, C. L. Advances in the use of natural receptor- or ligand-based chimeric antigen receptors (CARs) in haematologic malignancies. *Best Pract Res Cl Ha* **31**, 176-183, doi:10.1016/j.beha.2018.03.003 (2018).
133 De Munter, S. *et al.* Nanobody Based Dual Specific CARs. *Int J Mol Sci* **19**, doi:10.3390/ijms19020403 (2018).
134 Zhang, T., Wu, M. R. & Sentman, C. L. An NKp30-based chimeric antigen receptor promotes T cell effector functions and antitumor efficacy in vivo. *J Immunol* **189**, 2290-2299, doi:10.4049/jimmunol.1103495 (2012).
135 Kochenderfer, J. N. *et al.* Construction and preclinical evaluation of an anti-CD19 chimeric antigen receptor. *J Immunother* **32**, 689-702, doi:10.1097/CJI.0b013e3181ac6138 (2009).
136 Gross, G., Waks, T. & Eshhar, Z. Expression of Immunoglobulin-T-Cell Receptor Chimeric Molecules as Functional Receptors with Antibody-Type Specificity. *P Natl Acad Sci USA* **86**, 10024-10028, doi:DOI 10.1073/pnas.86.24.10024 (1989).
137 Eshhar, Z., Waks, T., Gross, G. & Schindler, D. G. Specific Activation and Targeting of Cytotoxic Lymphocytes through Chimeric Single Chains Consisting of Antibody-Binding Domains and the Gamma-Subunit or Zeta-Subunit of the Immunoglobulin and T-Cell Receptors. *P Natl Acad Sci USA* **90**, 720-724, doi:DOI 10.1073/pnas.90.2.720 (1993).
138 Zhang, C., Liu, J., Zhong, J. F. & Zhang, X. Engineering CAR-T cells. *Biomark Res* **5**, doi:ARTN 2210.1186/s40364-017-0102-y (2017).

139 Chmielewski, M., Hombach, A. A. & Abken, H. Of CARs and TRUCKs: chimeric antigen receptor (CAR) T cells engineered with an inducible cytokine to modulate the tumor stroma. *Immunol Rev* **257**, 83-90, doi:10.1111/imr.12125 (2014).

140 Kawalekar, O. U. *et al.* Distinct Signaling of Coreceptors Regulates Specific Metabolism Pathways and Impacts Memory Development in CAR T Cells. *Immunity* **44**, 380-390, doi:10.1016/j.immuni.2016.01.021 (2016).

141 Labanieh, L., Majzner, R. G. & Mackall, C. L. Programming CAR-T cells to kill cancer. *Nat Biomed Eng* **2**, 377-391, doi:10.1038/s41551-018-0235-9 (2018).

142 Kawalekar, O. U. *et al.* Distinct Signaling of Coreceptors Regulates Specific Metabolism Pathways and Impacts Memory Development in CAR T Cells (vol 44, pg 380, 2016). *Immunity* **44**, 712-712, doi:10.1016/j.immuni.2016.02.023 (2016).

143 Weinkove, R., George, P., Dasyam, N. & McLellan, A. D. Selecting costimulatory domains for chimeric antigen receptors: functional and clinical considerations. *Clin Transl Immunol* **8**, doi:ARTN e104910.1002/cti2.1049 (2019).

144 Love, P. E. & Hayes, S. M. ITAM-mediated Signaling by the T-Cell Antigen Receptor. *Csh Perspect Biol* **2**, doi:ARTN a00248510.1101/cshperspect.a002485 (2010).

145 Karlsson, H. *et al.* Evaluation of Intracellular Signaling Downstream Chimeric Antigen Receptors. *Plos One* **10**, doi:ARTN e014478710.1371/journal.pone.0144787 (2015).

146 Palacios, E. H. & Weiss, A. Function of the Src-family kinases, Lck and Fyn, in T-cell development and activation. *Oncogene* **23**, 7990-8000, doi:10.1038/sj.onc.1208074 (2004).

147 van der Stegen, S. J. C., Hamieh, M. & Sadelain, M. The pharmacology of second-generation chimeric antigen receptors. *Nat Rev Drug Discov* **14**, 499-509, doi:10.1038/nrd4597 (2015).

148 Osinska, I., Popko, K. & Demkow, U. Perforin: an important player in immune response. *Cent Eur J Immunol* **39**, 109-115, doi:10.5114/ceji.2014.42135 (2014).

149 Benmebarek, M. R. *et al.* Killing Mechanisms of Chimeric Antigen Receptor (CAR) T Cells. *Int J Mol Sci* **20**, doi:ARTN 128310.3390/ijms20061283 (2019).

150 Jackson, H. J., Rafiq, S. & Brentjens, R. J. Driving CAR T-cells forward. *Nat Rev Clin Oncol* **13**, 370-383, doi:10.1038/nrclinonc.2016.36 (2016).

151 Chavez, J. C., Bachmeier, C. & Kharfan-Dabaja, M. A. CAR T-cell therapy for B-cell lymphomas: clinical trial results of available products. *Ther Adv Hematol* **10**, doi:Unsp 204062071984158110.1177/2040620719841581 (2019).

152 Maude, S. L., Teachey, D. T., Porter, D. L. & Grupp, S. A. CD19-targeted chimeric antigen receptor T-cell therapy for acute lymphoblastic leukemia. *Blood* **125**, 4017-4023, doi:10.1182/blood-2014-12-580068 (2015).

153 Brentjens, R. J. *et al.* CD19-Targeted T Cells Rapidly Induce Molecular Remissions in Adults with Chemotherapy-Refractory Acute Lymphoblastic Leukemia. *Sci Transl Med* **5**, doi:ARTN 177ra3810.1126/scitranslmed.3005930 (2013).

154 Park, J. H., Geyer, M. B. & Brentjens, R. J. CD19-targeted CAR T-cell therapeutics for hematologic malignancies: interpreting clinical outcomes to date. *Blood* **127**, 3312-3320, doi:10.1182/blood-2016-02-629063 (2016).

155 Xu, X. J. *et al.* Mechanisms of Relapse After CD19 CAR T-Cell Therapy for Acute Lymphoblastic Leukemia and Its Prevention and Treatment Strategies. *Frontiers in Immunology* **10**, doi:ARTN 266410.3389/fimmu.2019.02664 (2019).

156 Chou, C. K. & Turtle, C. J. Insight into mechanisms associated with cytokine release syndrome and neurotoxicity after CD19 CAR-T cell immunotherapy. *Bone Marrow Transpl* **54**, 780-784, doi:10.1038/s41409-019-0602-5 (2019).

157 Lee, Y. G. *et al.* Regulation of CAR T cell-mediated cytokine release syndrome-like toxicity using low molecular weight adapters. *Nat Commun* **10**, doi:ARTN 268110.1038/s41467-019-10565-7 (2019).

158 Giavridis, T. *et al.* CAR T cell-induced cytokine release syndrome is mediated by macrophages and abated by IL-1 blockade. *Nat Med* **24**, 731-+, doi:10.1038/s41591-018-0041-7 (2018).

159 Murthy, H., Iqbal, M., Chavez, J. C. & Kharfan-Dabaja, M. A. Cytokine Release Syndrome: Current Perspectives. *Immunotargets Ther* **8**, 43-52, doi:10.2147/ITT.S202015 (2019).
160 Ma, S. *et al.* Current Progress in CAR-T Cell Therapy for Solid Tumors. *International Journal of Biological Sciences* **15**, 2548-2560, doi:10.7150/ijbs.34213 (2019).
161 Tomuleasa, C. *et al.* Chimeric Antigen Receptor T-Cells for the Treatment of B-Cell Acute Lymphoblastic Leukemia. *Front Immunol* **9**, 239, doi:10.3389/fimmu.2018.00239 (2018).
162 Morgan, R. A. *et al.* Case Report of a Serious Adverse Event Following the Administration of T Cells Transduced With a Chimeric Antigen Receptor Recognizing ERBB2. *Molecular Therapy* **18**, 843-851, doi:10.1038/mt.2010.24 (2010).
163 Liu, K. Y. *et al.* Retargeted human avidin-CAR T cells for adoptive immunotherapy of EGFRvIII expressing gliomas and their evaluation via optical imaging. *Oncotarget* **6**, 23735-23747, doi:10.18632/oncotarget.4362 (2015).
164 Heimberger, A. B. *et al.* Prognostic effect of epidermal growth factor receptor and EGFRvIII in glioblastoma multiforme patients. *Clin Cancer Res* **11**, 1462-1466, doi:10.1158/1078-0432.CCR-04-1737 (2005).
165 Del Vecchio, C. A. *et al.* Epidermal growth factor receptor variant III contributes to cancer stem cell phenotypes in invasive breast carcinoma. *Cancer Res* **72**, 2657-2671, doi:10.1158/0008-5472.CAN-11-2656 (2012).
166 Luo, X., Gong, X. & Tang, C. K. Suppression of EGFRvIII-mediated proliferation and tumorigenesis of breast cancer cells by ribozyme. *Int J Cancer* **104**, 716-721, doi:10.1002/ijc.11007 (2003).
167 Jager, D. *et al.* NY-BR-1 is a differentiation antigen of the mammary gland. *Appl Immunohisto M M* **15**, 77-83 (2007).
168 Milone, M. C. & O'Doherty, U. Clinical use of lentiviral vectors. *Leukemia* **32**, 1529-1541, doi:10.1038/s41375-018-0106-0 (2018).
169 Liu, J., Zhou, G. Y., Zhang, L. & Zhao, Q. Building Potent Chimeric Antigen Receptor T Cells With CRISPR Genome Editing. *Frontiers in Immunology* **10**, doi:ARTN 45610.3389/fimmu.2019.00456 (2019).
170 Stadtmauer, E. A. *et al.* CRISPR-engineered T cells in patients with refractory cancer. *Science* **367**, doi:10.1126/science.aba7365 (2020).
171 Monjezi, R. *et al.* Enhanced CAR T-cell engineering using non-viral Sleeping Beauty transposition from minicircle vectors. *Leukemia* **31**, 186-194, doi:10.1038/leu.2016.180 (2017).
172 Bozza, M. *The development of a novel S/MAR DNA vector platform for the stable, persistent and safe Genetic Engineering of Dividing Cells*, Heidelberg University, (2017).
173 Escors, D. & Breckpot, K. Lentiviral Vectors in Gene Therapy: Their Current Status and Future Potential. *Arch Immunol Ther Ex* **58**, 107-119, doi:10.1007/s00005-010-0063-4 (2010).
174 Gurtler, L. *et al.* Human Immunodeficiency Virus (HIV). *Transfus Med Hemoth* **43**, 203-222, doi:10.1159/000445852 (2016).
175 Milone, M. C. & O'Doherty, U. Clinical use of lentiviral vectors. *Leukemia* **32**, 1529-1541, doi:10.1038/s41375-018-0106-0 (2018).
176 Zufferey, R. *et al.* Self-inactivating lentivirus vector for safe and efficient in vivo gene delivery. *Journal of Virology* **72**, 9873-9880, doi:Doi 10.1128/Jvi.72.12.9873-9880.1998 (1998).
177 Miyoshi, H., Blomer, U., Takahashi, M., Gage, F. H. & Verma, I. M. Development of a self-inactivating lentivirus vector. *Journal of Virology* **72**, 8150-8157, doi:Doi 10.1128/Jvi.72.10.8150-8157.1998 (1998).
178 Iwakuma, T., Cui, Y. & Chang, L. J. Self-inactivating lentiviral vectors with U3 and U5 modifications. *Virology* **261**, 120-132, doi:DOI 10.1006/viro.1999.9850 (1999).
179 Swiggard, W. J. *et al.* Human immunodeficiency virus type 1 can establish latent infection in resting CD4(+) T cells in the absence of activating stimuli. *Journal of Virology* **79**, 14179-14188, doi:10.1128/Jvi.79.22.14179-14188.2005 (2005).

180 Frimpong, K. & Spector, S. A. Cotransduction of nondividing cells using lentiviral vectors. *Gene Therapy* **7**, 1562-1569, doi:DOI 10.1038/sj.gt.3301283 (2000).

181 Bai, Y. *et al.* Effective transduction and stable transgene expression in human blood cells by a third-generation lentiviral vector. *Gene Therapy* **10**, 1446-1457, doi:10.1038/sj.gt.3302026 (2003).

182 Froelich, S., Tai, A. & Wang, P. Lentiviral vectors for immune cells targeting. *Immunopharm Immunot* **32**, 208-218, doi:10.3109/08923970903420582 (2010).

183 Schroder, A. R. W. *et al.* HIV-1 integration in the human genome favors active genes and local hotspots. *Cell* **110**, 521-529, doi:Doi 10.1016/S0092-8674(02)00864-4 (2002).

184 Morgan, R. A. & Boyerinas, B. Genetic Modification of T Cells. *Biomedicines* **4**, doi:10.3390/biomedicines4020009 (2016).

185 Themis, M. *et al.* Oncogenesis following delivery of a nonprimate lentiviral gene therapy vector to fetal and neonatal mice. *Mol Ther* **12**, 763-771, doi:10.1016/j.ymthe.2005.07.358 (2005).

186 Van Craenenbroeck, K., Vanhoenacker, P. & Haegeman, G. Episomal vectors for gene expression in mammalian cells. *Eur J Biochem* **267**, 5665-5678, doi:10.1046/j.1432-1327.2000.01645.x (2000).

187 Wong, S. P., Argyros, O. & Harbottle, R. P. Sustained expression from DNA vectors. *Adv Genet* **89**, 113-152, doi:10.1016/bs.adgen.2014.11.002 (2015).

188 Heinzel, S. S., Krysan, P. J., Calos, M. P. & Dubridge, R. B. Use of Simian Virus-40 Replication to Amplify Epstein-Barr Virus Shuttle Vectors in Human-Cells. *Journal of Virology* **62**, 3738-3746, doi:Doi 10.1128/Jvi.62.10.3738-3746.1988 (1988).

189 Gai, D., Wang, D., Li, S. X. & Chen, X. S. The structure of SV40 large T hexameric helicase in complex with AT-rich origin DNA. *Elife* **5**, doi:10.7554/eLife.18129 (2016).

190 Yates, J. L., Warren, N. & Sugden, B. Stable Replication of Plasmids Derived from Epstein-Barr Virus in Various Mammalian-Cells. *Nature* **313**, 812-815, doi:DOI 10.1038/313812a0 (1985).

191 Yates, J., Warren, N., Reisman, D. & Sugden, B. A Cis-Acting Element from the Epstein-Barr Viral Genome That Permits Stable Replication of Recombinant Plasmids in Latently Infected-Cells. *P Natl Acad Sci-Biol* **81**, 3806-3810, doi:DOI 10.1073/pnas.81.12.3806 (1984).

192 Lupton, S. & Levine, A. J. Mapping Genetic Elements of Epstein-Barr Virus That Facilitate Extrachromosomal Persistence of Epstein-Barr Virus-Derived Plasmids in Human-Cells. *Mol Cell Biol* **5**, 2533-2542, doi:Doi 10.1128/Mcb.5.10.2533 (1985).

193 Wu, H., Ceccarelli, D. F. & Frappier, L. The DNA segregation mechanism of Epstein-Barr virus nuclear antigen 1. *EMBO Rep* **1**, 140-144, doi:10.1093/embo-reports/kvd026 (2000).

194 Lufino, M. M., Edser, P. A. & Wade-Martins, R. Advances in high-capacity extrachromosomal vector technology: episomal maintenance, vector delivery, and transgene expression. *Mol Ther* **16**, 1525-1538, doi:10.1038/mt.2008.156 (2008).

195 Mirkovitch, J., Mirault, M. E. & Laemmli, U. K. Organization of the higher-order chromatin loop: specific DNA attachment sites on nuclear scaffold. *Cell* **39**, 223-232, doi:10.1016/0092-8674(84)90208-3 (1984).

196 Jackson, D. A. & Cook, P. R. The structural basis of nuclear function. *International Review of Cytology, Vol 162a* **162a**, 125-149 (1995).

197 Kalos, M. & Fournier, R. E. K. Position-Independent Transgene Expression Mediated by Boundary Elements from the Apolipoprotein-B Chromatin Domain. *Mol Cell Biol* **15**, 198-207, doi:Doi 10.1128/Mcb.15.1.198 (1995).

198 Lichtenstein, M., Keini, G., Cedar, H. & Bergman, Y. B-Cell-Specific Demethylation - a Novel Role for the Intronic Kappa-Chain Enhancer Sequence. *Cell* **76**, 913-923, doi:Doi 10.1016/0092-8674(94)90365-4 (1994).

199 Forrester, W. C., Fernandez, L. A. & Grosschedl, R. Nuclear matrix attachment regions antagonize methylation-dependent repression of long-range enhancer-promoter interactions. *Genes Dev* **13**, 3003-3014, doi:10.1101/gad.13.22.3003 (1999).

200 Jenke, B. H. *et al.* An episomally replicating vector binds to the nuclear matrix protein SAF-A in vivo. *EMBO Rep* **3**, 349-354, doi:10.1093/embo-reports/kvf070 (2002).
201 Kaplan, M. H., Zong, R. T., Herrscher, R. F., Scheuermann, R. H. & Tucker, P. W. Transcriptional activation by a matrix associating region-binding protein. contextual requirements for the function of bright. *J Biol Chem* **276**, 21325-21330, doi:10.1074/jbc.M100836200 (2001).
202 Martens, J. H., Verlaan, M., Kalkhoven, E., Dorsman, J. C. & Zantema, A. Scaffold/matrix attachment region elements interact with a p300-scaffold attachment factor A complex and are bound by acetylated nucleosomes. *Mol Cell Biol* **22**, 2598-2606, doi:10.1128/mcb.22.8.2598-2606.2002 (2002).
203 Piechaczek, C., Fetzer, C., Baiker, A., Bode, J. & Lipps, H. J. A. *Nucleic Acids Res* **27**, 426-428, doi:DOI 10.1093/nar/27.2.426 (1999).
204 Piechaczek, C., Fetzer, C., Baiker, A., Bode, J. & Lipps, H. J. A vector based on the SV40 origin of replication and chromosomal S/MARs replicates episomally in CHO cells. *Nucleic Acids Res* **27**, 426-428, doi:10.1093/nar/27.2.426 (1999).
205 Schaarschmidt, D., Baltin, J., Stehle, I. M., Lipps, H. J. & Knippers, R. An episomal mammalian replicon: sequence-independent binding of the origin recognition complex. *EMBO J* **23**, 191-201, doi:10.1038/sj.emboj.7600029 (2004).
206 Sotirova, V. N., Calciano, M. A., Krueger, W. & Lalande, M. Inclusion of a matrix-attached region in a 7SK pol III vector increases the efficiency of shRNA-mediated gene silencing in embryonic carcinoma cells. *Plasmid* **55**, 216-226, doi:10.1016/j.plasmid.2005.11.008 (2006).
207 Papapetrou, E. P., Ziros, P. G., Micheva, I. D., Zoumbos, N. C. & Athanassiadou, A. Gene transfer into human hematopoietic progenitor cells with an episomal vector carrying an S/MAR element. *Gene Therapy* **13**, 40-51, doi:10.1038/sj.gt.3302593 (2006).
208 Argyros, O. *et al.* Persistent episomal transgene expression in liver following delivery of a scaffold/matrix attachment region containing non-viral vector. *Gene Ther* **15**, 1593-1605, doi:10.1038/gt.2008.113 (2008).
209 Hagedorn, C., Antoniou, M. N. & Lipps, H. J. Genomic cis-acting Sequences Improve Expression and Establishment of a Nonviral Vector. *Mol Ther Nucleic Acids* **2**, e118, doi:10.1038/mtna.2013.47 (2013).
210 Chen, Z. Y., He, C. Y., Ehrhardt, A. & Kay, M. A. Minicircle DNA vectors devoid of bacterial DNA result in persistent and high-level transgene expression in vivo. *Mol Ther* **8**, 495-500, doi:10.1016/s1525-0016(03)00168-0 (2003).
211 Argyros, O. *et al.* Development of S/MAR minicircles for enhanced and persistent transgene expression in the mouse liver. *J Mol Med* **89**, 515-529, doi:10.1007/s00109-010-0713-3 (2011).
212 Nehlsen, K., Broll, S. & Bode, J. Replicating minicircles: Generation of nonviral episomes for the efficient modification of dividing cells - Research article. *Gene Ther Mol Biol* **10b**, 233-243 (2006).
213 Lampreht Tratar, U., Horvat, S. & Cemazar, M. Transgenic Mouse Models in Cancer Research. *Front Oncol* **8**, 268, doi:10.3389/fonc.2018.00268 (2018).
214 Gengenbacher, N., Singhal, M. & Augustin, H. G. Preclinical mouse solid tumour models: status quo, challenges and perspectives. *Nat Rev Cancer* **17**, 751-765, doi:10.1038/nrc.2017.92 (2017).
215 Gurumurthy, C. B. & Lloyd, K. C. K. Generating mouse models for biomedical research: technological advances. *Dis Model Mech* **12**, doi:10.1242/dmm.029462 (2019).
216 Lin, E. Y. *et al.* Progression to malignancy in the polyoma middle T oncoprotein mouse breast cancer model provides a reliable model for human diseases. *American Journal of Pathology* **163**, 2113-2126, doi:Doi 10.1016/S0002-9440(10)63568-7 (2003).
217 Guy, C. T., Cardiff, R. D. & Muller, W. J. Induction of Mammary-Tumors by Expression of Polyomavirus Middle T-Oncogene - a Transgenic Mouse Model for Metastatic Disease. *Mol Cell Biol* **12**, 954-961, doi:Doi 10.1128/Mcb.12.3.954 (1992).

218 Pear, W. S., Nolan, G. P., Scott, M. L. & Baltimore, D. Production of high-titer helper-free retroviruses by transient transfection. *Proc Natl Acad Sci U S A* **90**, 8392-8396, doi:10.1073/pnas.90.18.8392 (1993).

219 Dubridge, R. B. *et al.* Analysis of Mutation in Human-Cells by Using an Epstein-Barr-Virus Shuttle System. *Mol Cell Biol* **7**, 379-387, doi:Doi 10.1128/Mcb.7.1.379 (1987).

220 Pear, W. S., Nolan, G. P., Scott, M. L. & Baltimore, D. Production of High-Titer Helper-Free Retroviruses by Transient Transfection. *P Natl Acad Sci USA* **90**, 8392-8396, doi:DOI 10.1073/pnas.90.18.8392 (1993).

221 Schneider, U., Schwenk, H. U. & Bornkamm, G. Characterization of Ebv-Genome Negative Null and T-Cell Lines Derived from Children with Acute Lymphoblastic Leukemia and Leukemic Transformed Non-Hodgkin Lymphoma. *International Journal of Cancer* **19**, 621-626, doi:DOI 10.1002/ijc.2910190505 (1977).

222 Sugiura, K. & Stock, C. C. Studies in a Tumor Spectrum .1. Comparison of the Action of Methylbis(2-Chloroethyl)Amine and 3-Bis(2-Chloroethyl)Aminomethyl-4-Methoxymethyl-5-Hydroxy-6-Methylpyridine on the Growth of a Variety of Mouse and Rat Tumors. *Cancer* **5**, 382-402, doi:Doi 10.1002/1097-0142(195203)5:2<382::Aid-Cncr2820050229>3.0.Co;2-3 (1952).

223 Todaro, G. J. & Green, H. Quantitative studies of the growth of mouse embryo cells in culture and their development into established lines. *J Cell Biol* **17**, 299-313, doi:10.1083/jcb.17.2.299 (1963).

224 Bitzer, J. *Molecular characterization of the breast cancer associated antigen NY-BR-1* PhD thesis, Ruperto-Carola University of Heidelberg, (2015).

225 Sirotnak, F. M., DeGraw, J. I., Moccio, D. M., Samuels, L. L. & Goutas, L. J. New folate analogs of the 10-deaza-aminopterin series. Basis for structural design and biochemical and pharmacologic properties. *Cancer Chemother Pharmacol* **12**, 18-25, doi:10.1007/bf00255903 (1984).

226 John, L. B. *et al.* Anti-PD-1 antibody therapy potently enhances the eradication of established tumors by gene-modified T cells. *Clin Cancer Res* **19**, 5636-5646, doi:10.1158/1078-0432.CCR-13-0458 (2013).

227 Ewens, A. *et al.* Doxorubicin plus interleukin-2 chemoimmunotherapy against breast cancer in mice. *Cancer Res* **66**, 5419-5426, doi:10.1158/0008-5472.CAN-05-3963 (2006).

228 Argyros, O. *et al.* Development of S/MAR minicircles for enhanced and persistent transgene expression in the mouse liver. *J Mol Med (Berl)* **89**, 515-529, doi:10.1007/s00109-010-0713-3 (2011).

229 Holstein, S. A. & Lunning, M. A. CAR T-Cell Therapy in Hematologic Malignancies: A Voyage in Progress. *Clin Pharmacol Ther* **107**, 112-122, doi:10.1002/cpt.1674 (2020).

230 Junghans, R. P. The challenges of solid tumors for designer CAR-T therapies: a 25-year perspective. *Cancer Gene Ther* **24**, 89-99, doi:10.1038/cgt.2016.82 (2017).

231 Martinez, M. & Moon, E. K. CAR T Cells for Solid Tumors: New Strategies for Finding, Infiltrating, and Surviving in the Tumor Microenvironment. *Front Immunol* **10**, 128, doi:10.3389/fimmu.2019.00128 (2019).

232 Jäger, D. *et al.* The breast differentiation antigen NY-BR-1: A novel target antigen for active immunotherapy in breast cancer. *J Clin Oncol* **22**, 181s-181s (2004).

233 Chen, M. T. *et al.* Comparison of patterns and prognosis among distant metastatic breast cancer patients by age groups: a SEER population-based analysis. *Sci Rep-Uk* **7**, doi:ARTN 925410.1038/s41598-017-10166-8 (2017).

234 Went, P. *et al.* Expression of epithelial cell adhesion molecule (EpCam) in renal epithelial tumors. *Am J Surg Pathol* **29**, 83-88, doi:DOI 10.1097/01.pas.0000.146028.70868.7a (2005).

235 Massoner, P. *et al.* EpCAM is overexpressed in local and metastatic prostate cancer, suppressed by chemotherapy and modulated by MET-associated miRNA-200c/205. *Brit J Cancer* **111**, 955-964, doi:10.1038/bjc.2014.366 (2014).

236 Went, P. *et al.* Frequent high-level expression of the immunotherapeutic target Ep-CAM in colon, stomach, prostate and lung cancers. *Br J Cancer* **94**, 128-135, doi:10.1038/sj.bjc.6602924 (2006).

237 Osta, W. A. *et al.* EpCAM is overexpressed in breast cancer and is a potential target for breast cancer gene therapy. *Cancer Research* **64**, 5818-5824, doi:Doi 10.1158/0008-5472.Can-04-0754 (2004).

238 Trzpis, M., McLaughlin, P. M., de Leij, L. M. & Harmsen, M. C. Epithelial cell adhesion molecule: more than a carcinoma marker and adhesion molecule. *Am J Pathol* **171**, 386-395, doi:10.2353/ajpath.2007.070152 (2007).

239 Thurm, H. *et al.* Rare expression of epithelial cell adhesion molecule on residual micrometastatic breast cancer cells after adjuvant chemotherapy. *Clinical Cancer Research* **9**, 2598-2604 (2003).

240 Tozbikian, G. *et al.* Mesothelin Expression in Triple Negative Breast Carcinomas Correlates Significantly with Basal-Like Phenotype, Distant Metastases and Decreased Survival. *Plos One* **9**, doi:ARTN e11490010.1371/journal.pone.0114900 (2014).

241 Mougel, M. & Barklis, E. A role for two hairpin structures as a core RNA encapsidation signal in murine leukemia virus virions. *Journal of Virology* **71**, 8061-8065, doi:Doi 10.1128/Jvi.71.10.8061-8065.1997 (1997).

242 Ali, L. M., Rizvi, T. A. & Mustafa, F. Cross- and Co-Packaging of Retroviral RNAs and Their Consequences. *Viruses-Basel* **8**, doi:ARTN 27610.3390/v8100276 (2016).

243 He, Y. *et al.* C-Src-mediated phosphorylation of delta-catenin increases its protein stability and the ability of inducing nuclear distribution of beta-catenin. *Biochim Biophys Acta* **1843**, 758-768, doi:10.1016/j.bbamcr.2013.12.021 (2014).

244 Abrahamsen, H., Vang, T. & Tasken, K. Protein kinase A intersects SRC signaling in membrane microdomains. *J Biol Chem* **278**, 17170-17177, doi:10.1074/jbc.M211426200 (2003).

245 Wheeler, D. L., Iida, M. & Dunn, E. F. The role of Src in solid tumors. *Oncologist* **14**, 667-678, doi:10.1634/theoncologist.2009-0009 (2009).

246 Hiscox, S. & Nicholson, R. I. Src inhibitors in breast cancer therapy. *Expert Opin Ther Tar* **12**, 757-767, doi:10.1517/14728222.12.6.757 (2008).

247 Irby, R. B. & Yeatman, T. J. Role of Src expression and activation in human cancer. *Oncogene* **19**, 5636-5642, doi:10.1038/sj.onc.1203912 (2000).

248 Broecker, F. *et al.* Transcriptional signature induced by a metastasis-promoting c-Src mutant in a human breast cell line. *FEBS J* **283**, 1669-1688, doi:10.1111/febs.13694 (2016).

249 Mayer, E. L. & Krop, I. E. Advances in targeting SRC in the treatment of breast cancer and other solid malignancies. *Clin Cancer Res* **16**, 3526-3532, doi:10.1158/1078-0432.CCR-09-1834 (2010).

250 Kahlert, S. *et al.* Estrogen receptor alpha rapidly activates the IGF-1 receptor pathway. *J Biol Chem* **275**, 18447-18453, doi:10.1074/jbc.M910345199 (2000).

251 Varga, Z. *et al.* Preferential nuclear and cytoplasmic NY-BR-1 protein expression in primary breast cancer and lymph node metastases. *Clinical Cancer Research* **12**, 2745-2751, doi:10.1158/1078-0432.Ccr-05-2192 (2006).

252 Poxleitner, M. K., Dawson, S. C. & Cande, W. Z. Cell cycle synchrony in Giardia intestinalis cultures achieved by using nocodazole and aphidicolin. *Eukaryot Cell* **7**, 569-574, doi:10.1128/Ec.00415-07 (2008).

253 Thomas, D. B. & Lingwood, C. A. A model of cell cycle control: effects of thymidine on synchronous cell cultures. *Cell* **5**, 37-42, doi:10.1016/0092-8674(75)90089-6 (1975).

254 Watson, P. A., Hanauskeabel, H. H., Flint, A. & Lalande, M. Mimosine Reversibly Arrests Cell-Cycle Progression at the G1-S Phase Border. *Cytometry* **12**, 242-246, doi:DOI 10.1002/cyto.990120306 (1991).

255 Fenteany, G. *et al.* Inhibition of proteasome activities and subunit-specific amino-terminal threonine modification by lactacystin. *Science* **268**, 726-731, doi:10.1126/science.7732382 (1995).

256 Das, K. *Generation of a transplantable murine tumor model expressing the human breast cancer associated tumor antigen NY-BR-1 in HLA-DRB1*0401-transgenic mice*, Heidelberg University, (2017).

257 Katagiri, M., Hayashi, M., Matsuzaki, K., Tanaka, H. & Omura, S. The Neuritogenesis Inducer Lactacystin Arrests Cell-Cycle at Both G0/G1 and G2 Phases in Neuro 2a Cells. *J Antibiot* **48**, 344-346, doi:DOI 10.7164/antibiotics.48.344 (1995).
258 Jakesz, R. *et al.* Influence of cell proliferation and cell cycle phase on expression of estrogen receptor in MCF-7 breast cancer cells. *Cancer Res* **44**, 619-625 (1984).
259 Whitelaw, E. *et al.* Epigenetic effects on transgene expression. *Methods Mol Biol* **158**, 351-368, doi:10.1385/1-59259-220-1:351 (2001).
260 Kaufman, W. L. *et al.* Homogeneity and persistence of transgene expression by omitting antibiotic selection in cell line isolation. *Nucleic Acids Res* **36**, e111, doi:10.1093/nar/gkn508 (2008).
261 Bestor, T. H. Gene silencing as a threat to the success of gene therapy. *Journal of Clinical Investigation* **105**, 409-411, doi:Doi 10.1172/Jci9459 (2000).
262 Chicas, A. & Macino, G. Characteristics of post-transcriptional gene silencing. *Embo Reports* **2**, 992-996, doi:DOI 10.1093/embo-reports/kve231 (2001).
263 Qin, J. Y. *et al.* Systematic Comparison of Constitutive Promoters and the Doxycycline-Inducible Promoter. *Plos One* **5**, doi:ARTN e1061110.1371/journal.pone.0010611 (2010).
264 Chung, S. M. *et al.* Analysis of different promoter systems for efficient transgene expression in mouse embryonic stem cell lines. *Stem Cells* **20**, 139-145, doi:DOI 10.1634/stemcells.20-2-139 (2002).
265 Jones, S. *et al.* Lentiviral Vector Design for Optimal T Cell Receptor Gene Expression in the Transduction of Peripheral Blood Lymphocytes and Tumor-Infiltrating Lymphocytes. *Hum Gene Ther* **20**, 630-640, doi:10.1089/hum.2008.048 (2009).
266 Leontieva, O. V., Demidenko, Z. N. & Blagosklonny, M. V. Contact inhibition and high cell density deactivate the mammalian target of rapamycin pathway, thus suppressing the senescence program. *P Natl Acad Sci USA* **111**, 8832-8837, doi:10.1073/pnas.1405723111 (2014).
267 Wierstra, I. The Transcription Factor FOXM1 (Forkhead box M1): Proliferation-Specific Expression, Transcription Factor Function, Target Genes, Mouse Models, and Normal Biological Roles. *Adv Cancer Res* **118**, 97-+, doi:10.1016/B978-0-12-407173-5.00004-2 (2013).
268 Bennett, V. & Healy, J. Membrane domains based on ankyrin and spectrin associated with cell-cell interactions. *Cold Spring Harb Perspect Biol* **1**, a003012, doi:10.1101/cshperspect.a003012 (2009).
269 Li, J., Mahajan, A. & Tsai, M. D. Ankyrin repeat: a unique motif mediating protein-protein interactions. *Biochemistry* **45**, 15168-15178, doi:10.1021/bi062188q (2006).
270 Cunha, S. R. & Mohler, P. J. Ankyrin protein networks in membrane formation and stabilization. *J Cell Mol Med* **13**, 4364-4376, doi:10.1111/j.1582-4934.2009.00943.x (2009).
271 Batrukova, M. A., Betin, V. L., Rubtsov, A. M. & Lopina, O. D. Ankyrin: structure, properties, and functions. *Biochemistry (Mosc)* **65**, 395-408 (2000).
272 Wolf, D. *et al.* Ankyrin repeat-containing N-Ank proteins shape cellular membranes. *Nat Cell Biol* **21**, 1191-1205, doi:10.1038/s41556-019-0381-7 (2019).
273 Jäger, D. *et al.* NY-BR-1 is a differentiation antigen of the mammary gland. *Appl Immunohisto M M* **15**, 77-83 (2007).
274 Hombach, A., Hombach, A. A. & Abken, H. Adoptive immunotherapy with genetically engineered T cells: modification of the IgG1 Fc 'spacer' domain in the extracellular moiety of chimeric antigen receptors avoids 'off-target' activation and unintended initiation of an innate immune response. *Gene Therapy* **17**, 1206-1213, doi:10.1038/gt.2010.91 (2010).
275 Kofler, D. M. *et al.* CD28 costimulation Impairs the efficacy of a redirected t-cell antitumor attack in the presence of regulatory t cells which can be overcome by preventing Lck activation. *Mol Ther* **19**, 760-767, doi:10.1038/mt.2011.9 (2011).
276 Hombach, A., Hombach, A. A. & Abken, H. Adoptive immunotherapy with genetically engineered T cells: modification of the IgG1 Fc 'spacer' domain in the extracellular moiety of chimeric antigen receptors avoids 'off-target' activation and unintended

initiation of an innate immune response. *Gene Ther* **17**, 1206-1213, doi:10.1038/gt.2010.91 (2010).

277 Golumba-Nagy, V., Kuehle, J., Hombach, A. A. & Abken, H. CD28-zeta CAR T Cells Resist TGF-beta Repression through IL-2 Signaling, Which Can Be Mimicked by an Engineered IL-7 Autocrine Loop. *Mol Ther* **26**, 2218-2230, doi:10.1016/j.ymthe.2018.07.005 (2018).

278 Watanabe, N. *et al.* Fine-tuning the CAR spacer improves T-cell potency. *Oncoimmunology* **5**, doi:ARTN e125365610.1080/2162402X.2016.1253656 (2016).

279 Pule, M. A. *et al.* A chimeric T cell antigen receptor that augments cytokine release and supports clonal expansion of primary human T cells. *Molecular Therapy* **12**, 933-941, doi:10.1016/j.ymthe.2005.04.016 (2005).

280 Bridgeman, J. S., Hawkins, R. E., Hombach, A. A., Abken, H. & Gilham, D. E. Building Better Chimeric Antigen Receptors for Adoptive T Cell Therapy. *Curr Gene Ther* **10**, 77-90 (2010).

281 Krenciute, G. *et al.* Characterization and Functional Analysis of scFv-based Chimeric Antigen Receptors to Redirect T Cells to IL13R alpha 2-positive Glioma. *Molecular Therapy* **24**, 354-363, doi:10.1038/mt.2015.199 (2016).

282 Hombach, A. A. & Abken, H. Costimulation by chimeric antigen receptors revisited: the T cell antitumor response benefits from combined CD28-OX40 signalling. *International Journal of Cancer* **129**, 2935-2944, doi:10.1002/ijc.25960 (2011).

283 Gramaglia, I., Weinberg, A. D., Lemon, M. & Croft, M. Ox-40 ligand: A potent costimulatory molecule for sustaining primary CD4 T cell responses. *Journal of Immunology* **161**, 6510-6517 (1998).

284 Dawicki, W., Bertram, E. M., Sharpe, A. H. & Watts, T. H. 4-1BB and OX40 act independently to facilitate robust CD8 and CD4 recall responses. *J Immunol* **173**, 5944-5951, doi:10.4049/jimmunol.173.10.5944 (2004).

285 Chen, A. I. *et al.* Ox40-ligand has a critical costimulatory role in dendritic cell: T cell interactions. *Immunity* **11**, 689-698, doi:Doi 10.1016/S1074-7613(00)80143-0 (1999).

286 Hombach, A. A., Heiders, J., Foppe, M., Chmielewski, M. & Abken, H. OX40 costimulation by a chimeric antigen receptor abrogates CD28 and IL-2 induced IL-10 secretion by redirected CD4(+) T cells. *Oncoimmunology* **1**, 458-466, doi:10.4161/onci.19855 (2012).

287 Wilkie, S. *et al.* Retargeting of human T cells to tumor-associated MUC1: the evolution of a chimeric antigen receptor. *J Immunol* **180**, 4901-4909, doi:10.4049/jimmunol.180.7.4901 (2008).

288 Tammana, S. *et al.* 4-1BB and CD28 signaling plays a synergistic role in redirecting umbilical cord blood T cells against B-cell malignancies. *Hum Gene Ther* **21**, 75-86, doi:10.1089/hum.2009.122 (2010).

289 Zhao, Y. *et al.* A herceptin-based chimeric antigen receptor with modified signaling domains leads to enhanced survival of transduced T lymphocytes and antitumor activity. *J Immunol* **183**, 5563-5574, doi:10.4049/jimmunol.0900447 (2009).

290 Haso, W. *et al.* Anti-CD22-chimeric antigen receptors targeting B-cell precursor acute lymphoblastic leukemia. *Blood* **121**, 1165-1174, doi:10.1182/blood-2012-06-438002 (2013).

291 Schmidt, P. *et al.* Novel DNA vectors encoding a chimeric antigen receptor mediate long term expression without genomic integration. *Cancer Research* **78**, doi:10.1158/1538-7445.Am2018-3573 (2018).

292 Kwaks, T. H. J. *et al.* Identification of anti-repressor elements that confer high and stable protein production in mammalian cells (vol 21, pg 553, 2003). *Nat Biotechnol* **21**, 822-822, doi:10.1038/nbt0703-822a (2003).

293 Darquet, A. M. *et al.* Minicircle: an improved DNA molecule for in vitro and in vivo gene transfer. *Gene Therapy* **6**, 209-218, doi:DOI 10.1038/sj.gt.3300816 (1999).

294 Maniar, L. E. G. *et al.* Minicircle DNA Vectors Achieve Sustained Expression Reflected by Active Chromatin and Transcriptional Level. *Molecular Therapy* **21**, 131-138, doi:10.1038/mt.2012.244 (2013).

295 Munye, M. M. *et al.* Minicircle DNA Provides Enhanced and Prolonged Transgene Expression Following Airway Gene Transfer. *Sci Rep-Uk* **6**, doi:ARTN 2312510.1038/srep23125 (2016).

296 Sun, S., Zhang, X., Tough, D. F. & Sprent, J. Type I interferon-mediated stimulation of T cells by CpG DNA. *J Exp Med* **188**, 2335-2342, doi:10.1084/jem.188.12.2335 (1998).

297 Bessis, N., GarciaCozar, F. J. & Boissier, M. C. Immune responses to gene therapy vectors: influence on vector function and effector mechanisms. *Gene Ther* **11 Suppl 1**, S10-17, doi:10.1038/sj.gt.3302364 (2004).

298 Takeshita, F. *et al.* Cutting edge: Role of Toll-like receptor 9 in CpG DNA-induced activation of human cells. *J Immunol* **167**, 3555-3558, doi:10.4049/jimmunol.167.7.3555 (2001).

299 Pandey, S., Kawai, T. & Akira, S. Microbial sensing by Toll-like receptors and intracellular nucleic acid sensors. *Cold Spring Harb Perspect Biol* **7**, a016246, doi:10.1101/cshperspect.a016246 (2014).

300 Ahn, J. & Barber, G. N. STING signaling and host defense against microbial infection. *Exp Mol Med* **51**, 1-10, doi:10.1038/s12276-019-0333-0 (2019).

301 Sun, L. J., Wu, J. X., Du, F. H., Chen, X. & Chen, Z. J. J. Cyclic GMP-AMP Synthase Is a Cytosolic DNA Sensor That Activates the Type I Interferon Pathway. *Science* **339**, 786-791, doi:10.1126/science.1232458 (2013).

302 Wu, J. X. *et al.* Cyclic GMP-AMP Is an Endogenous Second Messenger in Innate Immune Signaling by Cytosolic DNA. *Science* **339**, 826-830, doi:10.1126/science.1229963 (2013).

303 Welsh, R. M., Bahl, K., Marshall, H. D. & Urban, S. L. Type 1 interferons and antiviral CD8 T-cell responses. *Plos Pathog* **8**, e1002352, doi:10.1371/journal.ppat.1002352 (2012).

304 Fraietta, J. A. *et al.* Type I interferon upregulates Bak and contributes to T cell loss during human immunodeficiency virus (HIV) infection. *Plos Pathog* **9**, e1003658, doi:10.1371/journal.ppat.1003658 (2013).

305 Hornstein, B. D., Roman, D., Arevalo-Soliz, L. M., Engevik, M. A. & Zechiedrich, L. Effects of Circular DNA Length on Transfection Efficiency by Electroporation into HeLa Cells. *Plos One* **11**, doi:ARTN e016753710.1371/journal.pone.0167537 (2016).

306 Lesueur, L. L., Mir, L. M. & Andre, F. M. Overcoming the Specific Toxicity of Large Plasmids Electrotransfer in Primary Cells In Vitro. *Mol Ther-Nucl Acids* **5**, doi:ARTN e29110.1038/mtna.2016.4 (2016).

307 Dietz, W. M. *et al.* Minicircle DNA is Superior to Plasmid DNA in Eliciting Antigen-specific CD8(+) T-cell Responses. *Molecular Therapy* **21**, 1526-1535, doi:10.1038/mt.2013.85 (2013).

308 Molnar, M. J. *et al.* Factors influencing the efficacy, longevity, and safety of electroporation-assisted plasmid-based gene transfer into mouse muscles. *Molecular Therapy* **10**, 447-455, doi:10.1016/j.ymthe.2004.06.642 (2004).

309 Sukharev, S. I., Klenchin, V. A., Serov, S. M., Chernomordik, L. V. & Chizmadzhev, Y. A. Electroporation and Electrophoretic DNA Transfer into Cells - the Effect of DNA Interaction with Electropores. *Biophys J* **63**, 1320-1327, doi:Doi 10.1016/S0006-3495(92)81709-5 (1992).

310 Wu, M. N. & Yuan, F. Membrane Binding of Plasmid DNA and Endocytic Pathways Are Involved in Electrotransfection of Mammalian Cells. *Plos One* **6**, doi:ARTN e2092310.1371/journal.pone.0020923 (2011).

311 Delville, M. *et al.* A Nontoxic Transduction Enhancer Enables Highly Efficient Lentiviral Transduction of Primary Murine T Cells and Hematopoietic Stem Cells. *Mol Ther-Meth Clin D* **10**, 341-347, doi:10.1016/j.omtm.2018.08.002 (2018).

312 Tervo, H. M., Goffinet, C. & Keppler, O. T. Mouse T-cells restrict replication of human immunodeficiency virus at the level of integration. *Retrovirology* **5**, doi:Artn 5810.1186/1742-4690-5-58 (2008).

313 Tsurutani, N. *et al.* Nuclear import of the preintegration complex is blocked upon infection by human immunodeficiency virus type 1 in mouse cells. *Journal of Virology* **81**, 677-688, doi:10.1128/Jvi.00870-06 (2007).

314 Baumann, J. G. *et al.* Murine T cells potently restrict human immunodeficiency virus infection. *Journal of Virology* **78**, 12537-12547, doi:Doi 10.1128/Jvi.78.22.12537-12547.2004 (2004).

315 Kerkar, S. P. *et al.* Genetic Engineering of Murine CD8(+) and CD4(+) T Cells for Preclinical Adoptive Immunotherapy Studies. *J Immunother* **34**, 343-352, doi:10.1097/CJI.0b013e3182187600 (2011).

316 Chicaybam, L., Sodre, A. L., Curzio, B. A. & Bonamino, M. H. An Efficient Low Cost Method for Gene Transfer to T Lymphocytes. *Plos One* **8**, doi:ARTN e6029810.1371/journal.pone.0060298 (2013).

317 Kotnik, T., Rems, L., Tarek, M. & Miklavcic, D. Membrane Electroporation and Electropermeabilization: Mechanisms and Models. *Annu Rev Biophys* **48**, 63-91, doi:10.1146/annurev-biophys-052118-115451 (2019).

318 Gehl, J. Electroporation: theory and methods, perspectives for drug delivery, gene therapy and research. *Acta Physiol Scand* **177**, 437-447, doi:DOI 10.1046/j.1365-201X.2003.01093.x (2003).

319 Teague, T. K., Munn, L., Zygourakis, K. & McIntyre, B. W. Analysis of lymphocyte activation and proliferation by video microscopy and digital imaging. *Cytometry* **14**, 772-782, doi:10.1002/cyto.990140710 (1993).

320 Bohmer, R. M., Bandala-Sanchez, E. & Harrison, L. C. Forward Light Scatter Is a Simple Measure of T-Cell Activation and Proliferation but Is Not Universally Suited for Doublet Discrimination. *Cytom Part A* **79a**, 646-652, doi:10.1002/cyto.a.21096 (2011).

321 Zhang, Z., Qiu, S. F., Zhang, X. P. & Chen, W. Optimized DNA electroporation for primary human T cell engineering. *Bmc Biotechnology* **18**, doi:ARTN 410.1186/s12896-018-0419-0 (2018).

322 Weaver, J. C., Smith, K. C., Esser, A. T., Son, R. S. & Gowrishankar, T. R. A brief overview of electroporation pulse strength-duration space: A region where additional intracellular effects are expected. *Bioelectrochemistry* **87**, 236-243, doi:10.1016/j.bioelechem.2012.02.007 (2012).

323 Saulis, G. & Saule, R. Size of the pores created by an electric pulse: Microsecond vs millisecond pulses. *Bba-Biomembranes* **1818**, 3032-3039, doi:10.1016/j.bbamem.2012.06.018 (2012).

324 Wolf, H., Rols, M. P., Boldt, E., Neumann, E. & Teissie, J. Control by Pulse Parameters of Electric Field-Mediated Gene-Transfer in Mammalian-Cells. *Biophys J* **66**, 524-531, doi:Doi 10.1016/S0006-3495(94)80805-7 (1994).

325 Rols, M. P. & Teissie, J. Electropermeabilization of mammalian cells to macromolecules: Control by pulse duration. *Biophys J* **75**, 1415-1423, doi:Doi 10.1016/S0006-3495(98)74060-3 (1998).

326 Escoffre, J. M. *et al.* Gene electrotransfer: from biophysical mechanisms to in vivo applications : Part 1- Biophysical mechanisms. *Biophys Rev* **1**, 177, doi:10.1007/s12551-009-0022-7 (2009).

327 Demiryurek, Y. *et al.* Transport, resealing, and re-poration dynamics of two-pulse electroporation-mediated molecular delivery. *Bba-Biomembranes* **1848**, 1706-1714, doi:10.1016/j.bbamem.2015.04.007 (2015).

328 Sadik, M. M. *et al.* Scaling relationship and optimization of double-pulse electroporation. *Biophys J* **106**, 801-812, doi:10.1016/j.bpj.2013.12.045 (2014).

329 Stroh, T., Erben, U., Kuhl, A. A., Zeitz, M. & Siegmund, B. Combined pulse electroporation--a novel strategy for highly efficient transfection of human and mouse cells. *PLoS One* **5**, e9488, doi:10.1371/journal.pone.0009488 (2010).

330 Andre, F. M. *et al.* Efficiency of high- and low-voltage pulse combinations for gene electrotransfer in muscle, liver, tumor, and skin. *Hum Gene Ther* **19**, 1261-1271, doi:10.1089/hgt.2008.060 (2008).

331 Kanduser, M., Miklavcic, D. & Pavlin, M. Mechanisms involved in gene electrotransfer using high- and low-voltage pulses - An in vitro study. *Bioelectrochemistry* **74**, 265-271, doi:10.1016/j.bioelechem.2008.09.002 (2009).

332 Cepurniene, K., Ruzgys, P., Treinys, R., Satkauskiene, I. & Satkauskas, S. Influence of Plasmid Concentration on DNA Electrotransfer In Vitro Using High-Voltage and Low-Voltage Pulses. *J Membrane Biol* **236**, 81-85, doi:10.1007/s00232-010-9270-5 (2010).

333 Chmielewski, M., Hombach, A., Heuser, C., Adams, G. P. & Abken, H. T cell activation by antibody-like immunoreceptors: Increase in affinity of the single-chain fragment domain above threshold does not increase T cell activation against antigen-positive target cells but decreases selectivity. *Journal of Immunology* **173**, 7647-7653, doi:DOI 10.4049/jimmunol.173.12.7647 (2004).

334 Hudecek, M. *et al.* Receptor Affinity and Extracellular Domain Modifications Affect Tumor Recognition by ROR1-Specific Chimeric Antigen Receptor T Cells. *Clinical Cancer Research* **19**, 3153-3164, doi:10.1158/1078-0432.Ccr-13-0330 (2013).

335 Liu, X. J. *et al.* Affinity-Tuned ErbB2 or EGFR Chimeric Antigen Receptor T Cells Exhibit an Increased Therapeutic Index against Tumors in Mice. *Cancer Research* **75**, 3596-3607, doi:10.1158/0008-5472.Can-15-0159 (2015).

336 Watanabe, K., Kuramitsu, S., Posey, A. D. & June, C. H. Expanding the Therapeutic Window for CAR T Cell Therapy in Solid Tumors: The Knowns and Unknowns of CAR T Cell Biology. *Frontiers in Immunology* **9**, doi:ARTN 248610.3389/fimmu.2018.02486 (2018).

337 Engelhardt, B. T cell migration into the central nervous system during health and disease: Different molecular keys allow access to different central nervous system compartments. *Clinical and Experimental Neuroimmunology* **1**, 79-93, doi:10.1111/j.1759-1961.2010.009.x (2010).

338 Gust, J. *et al.* Endothelial Activation and Blood-Brain Barrier Disruption in Neurotoxicity after Adoptive Immunotherapy with CD19 CAR-T Cells. *Cancer Discov* **7**, 1404-1419, doi:10.1158/2159-8290.Cd-17-0698 (2017).

339 Akhavan, D. *et al.* CAR T cells for brain tumors: Lessons learned and road ahead. *Immunological Reviews* **290**, 60-84, doi:10.1111/imr.12773 (2019).

340 Pieren, D. K. J., Smits, N. A. M., van de Garde, M. D. B. & Guichelaar, T. Response kinetics reveal novel features of ageing in murine T cells. *Sci Rep-Uk* **9**, doi:ARTN 558710.1038/s41598-019-42120-1 (2019).

341 Hacker, G., Redecke, V. & Hacker, H. Activation of the immune system by bacterial CpG-DNA. *Immunology* **105**, 245-251 (2002).

342 Bendigs, S., Salzer, U., Lipford, G. B., Wagner, H. & Heeg, K. CpG-oligodeoxynucleotides co-stimulate primary T cells in the absence of antigen-presenting cells. *Eur J Immunol* **29**, 1209-1218, doi:Doi 10.1002/(Sici)1521-4141(199904)29:04<1209::Aid-Immu1209>3.0.Co;2-J (1999).

343 Chuang, T. H., Lee, J., Kline, L., Mathison, J. C. & Ulevitch, R. J. Toll-like receptor 9 mediates CpG-DNA signaling. *J Leukocyte Biol* **71**, 538-544 (2002).

344 Trinchieri, G. Type I interferon: friend or foe? *J Exp Med* **207**, 2053-2063, doi:10.1084/jem.20101664 (2010).

345 Ivashkiv, L. B. & Donlin, L. T. Regulation of type I interferon responses. *Nat Rev Immunol* **14**, 36-49, doi:10.1038/nri3581 (2014).

346 Lakkis, F. G. & Lechler, R. I. Origin and Biology of the Allogeneic Response. *Csh Perspect Med* **3**, doi:ARTN a01499310.1101/cshperspect.a014993 (2013).

347 Martin, P. J. *et al.* Genome-wide minor histocompatibility matching as related to the risk of graft-versus-host disease. *Blood* **129**, 791-798, doi:10.1182/blood-2016-09-737700 (2017).

348 Hong, L. K. *et al.* CD30-Redirected Chimeric Antigen Receptor T Cells Target CD30(+) and CD30(-) Embryonal Carcinoma via Antigen-Dependent and Fas/FasL Interactions. *Cancer Immunol Res* **6**, 1274-1287, doi:10.1158/2326-6066.Cir-18-0065 (2018).

349 Lanitis, E. *et al.* Redirected Antitumor Activity of Primary Human Lymphocytes Transduced With a Fully Human Anti-mesothelin Chimeric Receptor. *Molecular Therapy* **20**, 633-643, doi:10.1038/mt.2011.256 (2012).

350 Walker, A. J. *et al.* Tumor Antigen and Receptor Densities Regulate Efficacy of a Chimeric Antigen Receptor Targeting Anaplastic Lymphoma Kinase. *Mol Ther* **25**, 2189-2201, doi:10.1016/j.ymthe.2017.06.008 (2017).

351 Dikopoulos, N. *et al.* Type I IFN negatively regulates CD8+ T cell responses through IL-10-producing CD4+ T regulatory 1 cells. *J Immunol* **174**, 99-109, doi:10.4049/jimmunol.174.1.99 (2005).

352 Caruso, H. G. *et al.* Tuning Sensitivity of CAR to EGFR Density Limits Recognition of Normal Tissue While Maintaining Potent Antitumor Activity. *Cancer Research* **75**, 3505-3518, doi:10.1158/0008-5472.Can-15-0139 (2015).

353 Bonifant, C. L., Jackson, H. J., Brentjens, R. J. & Curran, K. J. Toxicity and management in CAR T-cell therapy. *Mol Ther-Oncolytics* **3**, doi:UNSP 1601110.1038/mto.2016.11 (2016).

354 Choi, Y. W., Henrard, D., Lee, I. C. & Ross, S. R. The Mouse Mammary-Tumor Virus Long Terminal Repeat Directs Expression in Epithelial and Lymphoid-Cells of Different Tissues in Transgenic Mice. *Journal of Virology* **61**, 3013-3019, doi:Doi 10.1128/Jvi.61.10.3013-3019.1987 (1987).

355 Henrard, D. & Ross, S. R. Endogenous Mouse Mammary-Tumor Virus Is Expressed in Several Organs in Addition to the Lactating Mammary-Gland. *Journal of Virology* **62**, 3046-3049, doi:Doi 10.1128/Jvi.62.8.3046-3049.1988 (1988).

356 Rahman, M. A., Hwang, G. L., Razak, S. A., Sohm, F. & Maclean, N. Copy number related transgene expression and mosaic somatic expression in hemizygous and homozygous transgenic tilapia (Oreochromis niloticus). *Transgenic Res* **9**, 417-427, doi:Doi 10.1023/A:1026517212807 (2000).

357 Chang, S. P., Opsahl, M. L., Whitelaw, C. B. A., Morley, S. D. & West, J. D. Relative transgene expression frequencies in homozygous versus hemizygous transgenic mice. *Transgenic Res* **22**, 1143-1154, doi:10.1007/s11248-013-9732-5 (2013).

358 Garrels, W. *Transgene Expression durch zytoplasmatische Injektion von Plasmiden und Transposon-basierten Konstrukten in Säugerembryonen*, Tierärztliche Hochschule Hannover, (2010).

359 Fink, D., Yau, T. Y., Kolbe, T. & Rulicke, T. Non-invasive Instant Genotyping of Fluorescently Labeled Transgenic Mice. *Altex-Altern Anim Ex* **32**, 222-227 (2015).

360 Lareyre, J. J. *et al.* A 5-kilobase pair promoter fragment of the murine epididymal retinoic acid-binding protein gene drives the tissue-specific, cell-specific, and androgen-regulated expression of a foreign gene in the epididymis of transgenic mice. *Journal of Biological Chemistry* **274**, 8282-8290, doi:DOI 10.1074/jbc.274.12.8282 (1999).

361 Yan, B. W., Li, D. F. & Gou, K. M. Homologous illegitimate random integration of foreign DNA into the X chromosome of a transgenic mouse line. *Bmc Mol Biol* **11**, doi:Artn 5810.1186/1471-2199-11-58 (2010).

362 Yun, J. S. *et al.* The Human Growth-Hormone Transgene - Expression in Hemizygous and Homozygous Mice. *P Soc Exp Biol Med* **194**, 308-313 (1990).

363 Dobie, K. W. *et al.* Variegated transgene expression in mouse mammary gland is determined by the transgene integration locus. *P Natl Acad Sci USA* **93**, 6659-6664, doi:DOI 10.1073/pnas.93.13.6659 (1996).

364 Haruyama, N., Cho, A. & Kulkarni, A. B. Overview: engineering transgenic constructs and mice. *Curr Protoc Cell Biol* **Chapter 19**, Unit 19 10, doi:10.1002/0471143030.cb1910s42 (2009).

365 Garrick, D., Fiering, S., Martin, D. I. K. & Whitelaw, E. Repeat-induced gene silencing in mammals. *Nat Genet* **18**, 56-59, doi:DOI 10.1038/ng0198-56 (1998).

366 Song, D. G. *et al.* In vivo persistence, tumor localization, and antitumor activity of CAR-engineered T cells is enhanced by costimulatory signaling through CD137 (4-1BB). *Cancer Res* **71**, 4617-4627, doi:10.1158/0008-5472.CAN-11-0422 (2011).

367 Gardner, R. A. *et al.* Intent-to-treat leukemia remission by CD19 CAR T cells of defined formulation and dose in children and young adults. *Blood* **129**, 3322-3331, doi:10.1182/blood-2017-02-769208 (2017).

368 Ramakrishna, S. *et al.* Modulation of Target Antigen Density Improves CAR T-cell Functionality and Persistence. *Clin Cancer Res* **25**, 5329-5341, doi:10.1158/1078-0432.CCR-18-3784 (2019).

369 Golubovskaya, V. & Wu, L. J. Different Subsets of T Cells, Memory, Effector Functions, and CAR-T Immunotherapy. *Cancers* **8**, doi:ARTN 3610.3390/cancers8030036 (2016).

370 Ross, S. H. & Cantrell, D. A. Signaling and Function of Interleukin-2 in T Lymphocytes. *Annu Rev Immunol* **36**, 411-433, doi:10.1146/annurev-immunol-042617-053352 (2018).

371 Brehm, M. A., Daniels, K. A. & Welsh, R. M. Rapid production of TNF-alpha following TCR engagement of naive CD8 T cells. *J Immunol* **175**, 5043-5049, doi:10.4049/jimmunol.175.8.5043 (2005).

372 Bhat, P., Leggatt, G., Waterhouse, N. & Frazer, I. H. Interferon-gamma derived from cytotoxic lymphocytes directly enhances their motility and cytotoxicity. *Cell Death Dis* **8**, e2836, doi:10.1038/cddis.2017.67 (2017).

373 Hamza, T., Barnett, J. B. & Li, B. Y. Interleukin 12 a Key Immunoregulatory Cytokine in Infection Applications. *Int J Mol Sci* **11**, 789-806, doi:10.3390/ijms11030789 (2010).

374 Lopez-Castejon, G. & Brough, D. Understanding the mechanism of IL-1 beta secretion. *Cytokine Growth F R* **22**, 189-195, doi:10.1016/j.cytogfr.2011.10.001 (2011).

375 Magram, J. *et al.* IL-12-deficient mice are defective in IFN gamma production and type 1 cytokine responses. *Immunity* **4**, 471-481, doi:10.1016/s1074-7613(00)80413-6 (1996).

376 Bao, K. & Reinhardt, R. L. The differential expression of IL-4 and IL-13 and its impact on type-2 immunity. *Cytokine* **75**, 25-37, doi:10.1016/j.cyto.2015.05.008 (2015).

377 Wynn, T. A. IL-13 effector functions. *Annu Rev Immunol* **21**, 425-456, doi:10.1146/annurev.immunol.21.120601.141142 (2003).

378 Wong, C. K. *et al.* Proinflammatory cytokines (IL-17, IL-6, IL-18 and IL-12) and Th cytokines (IFN-gamma, IL-4, IL-10 and IL-13) in patients with allergic asthma. *Clin Exp Immunol* **125**, 177-183, doi:10.1046/j.1365-2249.2001.01602.x (2001).

379 Iyer, S. S. & Cheng, G. H. Role of Interleukin 10 Transcriptional Regulation in Inflammation and Autoimmune Disease. *Crit Rev Immunol* **32**, 23-63, doi:DOI 10.1615/CritRevImmunol.v32.i1.30 (2012).

380 Sharma, S. *et al.* T cell-derived IL-10 promotes lung cancer growth by suppressing both T cell and APC function. *Journal of Immunology* **163**, 5020-5028 (1999).

381 Lee, D. W. *et al.* Current concepts in the diagnosis and management of cytokine release syndrome. *Blood* **124**, 188-195, doi:10.1182/blood-2014-05-552729 (2014).

382 Wang, Z. & Han, W. Biomarkers of cytokine release syndrome and neurotoxicity related to CAR-T cell therapy. *Biomark Res* **6**, 4, doi:10.1186/s40364-018-0116-0 (2018).

383 Scheller, J., Chalaris, A., Schmidt-Arras, D. & Rose-John, S. The pro- and anti-inflammatory properties of the cytokine interleukin-6. *Biochim Biophys Acta* **1813**, 878-888, doi:10.1016/j.bbamcr.2011.01.034 (2011).

384 Giavridis, T. *et al.* CAR T cell-induced cytokine release syndrome is mediated by macrophages and abated by IL-1 blockade. *Nat Med* **24**, 731-738, doi:10.1038/s41591-018-0041-7 (2018).

385 van der Stegen, S. J. *et al.* Preclinical in vivo modeling of cytokine release syndrome induced by ErbB-retargeted human T cells: identifying a window of therapeutic opportunity? *J Immunol* **191**, 4589-4598, doi:10.4049/jimmunol.1301523 (2013).

386 Wang, L. X. J. *et al.* Tumor Ablation by Gene-Modified T Cells in the Absence of Autoimmunity. *Cancer Research* **70**, 9591-9598, doi:10.1158/0008-5472.Can-10-2884 (2010).

387 Boivin, W. A., Cooper, D. M., Hiebert, P. R. & Granville, D. J. Intracellular versus extracellular granzyme B in immunity and disease: challenging the dogma. *Lab Invest* **89**, 1195-1220, doi:10.1038/labinvest.2009.91 (2009).

388 Workman, A. M., Jacobs, A. K., Vogel, A. J., Condon, S. & Brown, D. M. Inflammation Enhances IL-2 Driven Differentiation of Cytolytic CD4 T Cells. *Plos One* **9**, doi:ARTN e8901010.1371/journal.pone.0089010 (2014).

389 Wang, D. R. *et al.* Glioblastoma-targeted CD4(+) CAR T cells mediate superior antitumor activity. *Jci Insight* **3**, doi:ARTN e9904810.1172/jci.insight.99048 (2018).

390 Devadas, S. *et al.* Granzyme B is critical for T cell receptor-induced cell death of type 2 helper T cells. *Immunity* **25**, 237-247, doi:10.1016/j.immuni.2006.06.011 (2006).

391 Zhao, D. M., Thornton, A. M., DiPaolo, R. J. & Shevach, E. M. Activated CD4+CD25+ T cells selectively kill B lymphocytes. *Blood* **107**, 3925-3932, doi:10.1182/blood-2005-11-4502 (2006).

392 Cao, X. F. *et al.* Granzyme B and perforin are important for regulatory T cell-mediated suppression of tumor clearance. *Immunity* **27**, 635-646, doi:10.1016/j.immuni.2007.08.014 (2007).

393 Stalder, T., Hahn, S. H. & Erb, P. Fas Antigen Is the Major Target Molecule for Cd4+ T-Cell-Mediated Cytotoxicity. *Journal of Immunology* **152**, 1127-1133 (1994).

394 Bi, E. G. *et al.* Novel function of perforin in negatively regulating CD4(+) T cell activation by affecting calcium signaling. *Cell Res* **19**, 816-827, doi:10.1038/cr.2009.32 (2009).

395 Fang, M. *et al.* Perforin-dependent CD4(+) T-cell cytotoxicity contributes to control a murine poxvirus infection. *P Natl Acad Sci USA* **109**, 9983-9988, doi:10.1073/pnas.1202143109 (2012).

396 Wherry, E. J. T cell exhaustion. *Nature Immunology* **12**, 492-499, doi:10.1038/ni.2035 (2011).

397 Zhang, Z. *et al.* T Cell Dysfunction and Exhaustion in Cancer. *Front Cell Dev Biol* **8**, doi:ARTN 1710.3389/fcell.2020.00017 (2020).

398 Cheng, J. *et al.* Understanding the Mechanisms of Resistance to CAR T-Cell Therapy in Malignancies. *Front Oncol* **9**, 1237, doi:10.3389/fonc.2019.01237 (2019).

399 Johnstone, C. N. *et al.* Functional and molecular characterisation of EO771.LMB tumours, a new C57BL/6-mouse-derived model of spontaneously metastatic mammary cancer. *Dis Model Mech* **8**, 237-251, doi:10.1242/dmm.017830 (2015).

400 Iwanowycz, S. *et al.* Emodin Inhibits Breast Cancer Growth by Blocking the Tumor-Promoting Feedforward Loop between Cancer Cells and Macrophages. *Mol Cancer Ther* **15**, 1931-1942, doi:10.1158/1535-7163.Mct-15-0987 (2016).

401 Takaba, H. & Takayanagi, H. The Mechanisms of T Cell Selection in the Thymus. *Trends Immunol* **38**, 805-816, doi:10.1016/j.it.2017.07.010 (2017).

402 Huang, C. Y. & Kanagawa, O. Ordered and coordinated rearrangement of the TCR alpha locus: Role of secondary rearrangement in thymic selection. *Journal of Immunology* **166**, 2597-2601, doi:DOI 10.4049/jimmunol.166.4.2597 (2001).

403 Maggi, E. *et al.* Thymic regulatory T cells. *Autoimmun Rev* **4**, 579-586, doi:10.1016/j.autrev.2005.04.010 (2005).

404 Nemazee, D. Mechanisms of central tolerance for B cells. *Nat Rev Immunol* **17**, 281-294, doi:10.1038/nri.2017.19 (2017).

405 Melchers, F. Checkpoints that control B cell development. *Journal of Clinical Investigation* **125**, 2203-2210, doi:10.1172/Jci78083 (2015).

406 Haynes, B. F., Verkoczy, L. & Kelsoe, G. Redemption of autoreactive B cells. *P Natl Acad Sci USA* **111**, 9022-9023, doi:10.1073/pnas.1407877111 (2014).

407 Ham, D. I. *et al.* Central immunotolerance in transgenic mice expressing a foreign antigen under control of the rhodopsin promoter. *Invest Ophth Vis Sci* **45**, 857-862, doi:10.1167/iovs.03-1028 (2004).

408 Clarke, P., Mann, J., Simpson, J. F., Rickard-Dickson, K. & Primus, F. J. Mice transgenic for human carcinoembryonic antigen as a model for immunotherapy. *Cancer Research* **58**, 1469-1477 (1998).

409 Piechocki, M. P., Ho, Y. S., Pilon, S. & Wei, W. Z. Human ErbB-2 (Her-2) transgenic mice: A model system for testing Her-2 based vaccines. *Journal of Immunology* **171**, 5787-5794, doi:DOI 10.4049/jimmunol.171.11.5787 (2003).

410 Rowse, G. J., Tempero, R. M., VanLith, M. L., Hollingsworth, M. A. & Gendler, S. J. Tolerance and immunity to MUC1 in a human MUC1 transgenic murine model. *Cancer Res* **58**, 315-321 (1998).

411 Derbinski, J., Schulte, A., Kyewski, B. & Klein, L. Promiscuous gene expression in medullary thymic epithelial cells mirrors the peripheral self. *Nature Immunology* **2**, 1032-1039, doi:DOI 10.1038/ni723 (2001).

412 de Vos, A. F. *et al.* Breakdown of tolerance to a neo-self antigen in double transgenic mice in which B cells present the antigen. *Journal of Immunology* **164**, 4594-4600, doi:DOI 10.4049/jimmunol.164.9.4594 (2000).

413 Delovitch, T. L. & Singh, B. The nonobese diabetic mouse as a model of autoimmune diabetes: Immune dysregulation gets the NOD. *Immunity* **7**, 727-738, doi:Doi 10.1016/S1074-7613(00)80392-1 (1997).
414 Brodnicki, T. C., Quirk, F. & Morahan, G. A susceptibility allele from a non-diabetes-prone mouse strain accelerates diabetes in NOD congenic mice. *Diabetes* **52**, 218-222, doi:DOI 10.2337/diabetes.52.1.218 (2003).
415 Greiner, D. L., Hesselton, R. A. & Shultz, L. D. SCID mouse models of human stem cell engraftment. *Stem Cells* **16**, 166-177, doi:DOI 10.1002/stem.160166 (1998).
416 Malynn, B. A. *et al.* The scid defect affects the final step of the immunoglobulin VDJ recombinase mechanism. *Cell* **54**, 453-460, doi:10.1016/0092-8674(88)90066-9 (1988).
417 Woodbine, L. *et al.* PRKDC mutations in a SCID patient with profound neurological abnormalities. *Journal of Clinical Investigation* **123**, 2969-2980, doi:10.1172/Jci67349 (2013).
418 Lieber, M. R. *et al.* The Defect in Murine Severe Combined Immune-Deficiency - Joining of Signal Sequences but Not Coding Segments in V(D)J Recombination. *Cell* **55**, 7-16, doi:Doi 10.1016/0092-8674(88)90004-9 (1988).
419 Tong, J. C., Tan, T. W. & Ranganathan, S. Methods and protocols for prediction of immunogenic epitopes. *Brief Bioinform* **8**, 96-108, doi:10.1093/bib/bbl038 (2007).
420 Shultz, L. D. *et al.* Human lymphoid and myeloid cell development in NOD/LtSz-scid IL2R gamma(null) mice engrafted with mobilized human hemopoietic stem cells. *Journal of Immunology* **174**, 6477-6489, doi:DOI 10.4049/jimmunol.174.10.6477 (2005).
421 Koo, G. C., Hasan, A. & O'Reilly, R. J. Use of humanized severe combined immunodeficient mice for human vaccine development. *Expert Rev Vaccines* **8**, 113-120, doi:10.1586/14760584.8.1.113 (2009).
422 Uribe, L. & Weinberg, K. I. X-linked SCID and other defects of cytokine pathways. *Semin Hematol* **35**, 299-309 (1998).
423 Sugamura, K. *et al.* The interleukin-2 receptor gamma chain: its role in the multiple cytokine receptor complexes and T cell development in XSCID. *Annu Rev Immunol* **14**, 179-205, doi:10.1146/annurev.immunol.14.1.179 (1996).
424 Asao, H. *et al.* Cutting edge: The common gamma-chain is an indispensable subunit of the IL-21 receptor complex. *Journal of Immunology* **167**, 1-5, doi:DOI 10.4049/jimmunol.167.1.1 (2001).
425 Zhou, Q. J., Facciponte, J., Jin, M., Shen, Q. & Lin, Q. Humanized NOD-SCID IL2rg(-/-) mice as a preclinical model for cancer research and its potential use for individualized cancer therapies. *Cancer Lett* **344**, 13-19, doi:10.1016/j.canlet.2013.10.015 (2014).
426 Kavsan, V. M., Iershov, A. V. & Balynska, O. V. Immortalized cells and one oncogene in malignant transformation: old insights on new explanation. *Bmc Cell Biol* **12**, doi:Artn 2310.1186/1471-2121-12-23 (2011).
427 Lin, Y. C. *et al.* Genome dynamics of the human embryonic kidney 293 lineage in response to cell biology manipulations. *Nat Commun* **5**, doi:ARTN 476710.1038/ncomms5767 (2014).
428 Stepanenko, A. A. & Dmitrenko, V. V. HEK293 in cell biology and cancer research: phenotype, karyotype, tumorigenicity, and stress-induced genome-phenotype evolution. *Gene* **569**, 182-190, doi:10.1016/j.gene.2015.05.065 (2015).
429 Debeb, B. G. *et al.* Characterizing cancer cells with cancer stem cell-like features in 293T human embryonic kidney cells. *Mol Cancer* **9**, doi:Artn 18010.1186/1476-4598-9-180 (2010).
430 Lanitis, E., Dangaj, D., Irving, M. & Coukos, G. Mechanisms regulating T-cell infiltration and activity in solid tumors. *Annals of Oncology* **28**, 18-32, doi:10.1093/annonc/mdx238 (2017).
431 Ansari, A. M. *et al.* Cellular GFP Toxicity and Immunogenicity: Potential Confounders in in Vivo Cell Tracking Experiments. *Stem Cell Rev Rep* **12**, 553-559, doi:10.1007/s12015-016-9670-8 (2016).

432 Stripecke, R. *et al.* Immune response to green fluorescent protein: implications for gene therapy. *Gene Ther* **6**, 1305-1312, doi:10.1038/sj.gt.3300951 (1999).

433 Skelton, D., Satake, N. & Kohn, D. B. The enhanced green fluorescent protein (eGFP) is minimally immunogenic in C57BL/6 mice. *Gene Ther* **8**, 1813-1814, doi:10.1038/sj.gt.3301586 (2001).

434 Cheng, Y.-S. *et al.* Autonomous combinatorial color barcoding for multiplexing single molecule RNA visualization. *bioRxiv* (2017).

435 Schmidts, A. & Maus, M. V. Making CAR T Cells a Solid Option for Solid Tumors. *Front Immunol* **9**, 2593, doi:10.3389/fimmu.2018.02593 (2018).

436 Harlin, H. *et al.* Chemokine Expression in Melanoma Metastases Associated with CD8(+) T-Cell Recruitment. *Cancer Research* **69**, 3077-3085, doi:10.1158/0008-5472.Can-08-2281 (2009).

437 Mulligan, A. M. *et al.* Tumoral Lymphocytic Infiltration and Expression of the Chemokine CXCL10 in Breast Cancers from the Ontario Familial Breast Cancer Registry. *Clinical Cancer Research* **19**, 336-346, doi:10.1158/1078-0432.Ccr-11-3314 (2013).

438 Slaney, C. Y., Kershaw, M. H. & Darcy, P. K. Trafficking of T Cells into Tumors. *Cancer Research* **74**, 7168-7174, doi:10.1158/0008-5472.Can-14-2458 (2014).

439 Guirnalda, P., Wood, L., Goenka, R., Crespo, J. & Paterson, Y. Interferon gamma-induced intratumoral expression of CXCL9 alters the local distribution of T cells following immunotherapy with Listeria monocytogenes. *Oncoimmunology* **2**, doi:ARTN e2575210.4161/onci.25752 (2013).

440 David, J. M., Dominguez, C., Hamilton, D. H. & Palena, C. The IL-8/IL-8R Axis: A Double Agent in Tumor Immune Resistance. *Vaccines-Basel* **4**, doi:UNSP 2210.3390/vaccines4030022 (2016).

441 Lin, Y. *et al.* Identification of interleukin-8 as estrogen receptor-regulated factor involved in breast cancer invasion and angiogenesis by protein arrays. *International Journal of Cancer* **109**, 507-515, doi:10.1002/ijc.11724 (2004).

442 Gesser, B. *et al.* IL-8 induces T cell chemotaxis, suppresses IL-4, and up-regulates IL-8 production by CD4(+) T cells. *J Leukocyte Biol* **59**, 407-411 (1996).

443 Santarlasci, V., Cosmi, L., Maggi, L., Liotta, F. & Annunziato, F. IL-1 and T Helper Immune Responses. *Front Immunol* **4**, 182, doi:10.3389/fimmu.2013.00182 (2013).

444 Tugues, S. *et al.* New insights into IL-12-mediated tumor suppression. *Cell Death Differ* **22**, 237-246, doi:10.1038/cdd.2014.134 (2015).

445 Damo, M. & Joshi, N. S. Treg cell IL-10 and IL-35 exhaust CD8(+) T cells in tumors. *Nat Immunol* **20**, 674-675, doi:10.1038/s41590-019-0389-y (2019).

446 Hombach, A. A., Heiders, J., Foppe, M., Chmielewski, M. & Abken, H. OX40 costimulation by a chimeric antigen receptor abrogates CD28 and IL-2 induced IL-10 secretion by redirected CD4(+) T cells. *Oncoimmunology* **1**, doi:10.4161/onci.19855 (2012).

447 Kundu, N., Beaty, T. L., Jackson, M. J. & Fulton, A. M. Antimetastatic and antitumor activities of interleukin 10 in a murine model of breast cancer. *J Natl Cancer Inst* **88**, 536-541, doi:10.1093/jnci/88.8.536 (1996).

448 Hamidullah, Changkija, B. & Konwar, R. Role of interleukin-10 in breast cancer. *Breast Cancer Res Treat* **133**, 11-21, doi:10.1007/s10549-011-1855-x (2012).

449 Dennis, K. L., Blatner, N. R., Gounari, F. & Khazaie, K. Current status of interleukin-10 and regulatory T-cells in cancer. *Curr Opin Oncol* **25**, 637-645, doi:10.1097/CCO.0000000000000006 (2013).

450 Khong, H. T. & Restifo, N. P. Natural selection of tumor variants in the generation of "tumor escape" phenotypes. *Nature Immunology* **3**, 999-1005, doi:DOI 10.1038/ni1102-999 (2002).

451 Rabinovich, G. A., Gabrilovich, D. & Sotomayor, E. M. Immunosuppressive strategies that are mediated by tumor cells. *Annual Review of Immunology* **25**, 267-296, doi:10.1146/annurev.immunol.25.022106.141609 (2007).

452 Monjazeb, A. M. *et al.* Immunoediting and antigen loss: overcoming the achilles heel of immunotherapy with antigen non-specific therapies. *Front Oncol* **3**, 197, doi:10.3389/fonc.2013.00197 (2013).

453 O'Rourke, D. M. *et al.* A single dose of peripherally infused EGFRvIII-directed CAR T cells mediates antigen loss and induces adaptive resistance in patients with recurrent glioblastoma. *Sci Transl Med* **9**, doi:10.1126/scitranslmed.aaa0984 (2017).
454 Hegde, M. *et al.* Tandem CAR T cells targeting HER2 and IL13Ralpha2 mitigate tumor antigen escape. *J Clin Invest* **126**, 3036-3052, doi:10.1172/JCI83416 (2016).
455 Hamieh, M. *et al.* CAR T cell trogocytosis and cooperative killing regulate tumour antigen escape. *Nature* **568**, 112-+, doi:10.1038/s41586-019-1054-1 (2019).
456 Beyersdorf, N., Kerkau, T. & Hunig, T. CD28 co-stimulation in T-cell homeostasis: a recent perspective. *Immunotargets Ther* **4**, 111-122, doi:10.2147/ITT.S61647 (2015).
457 Hombach, A. *et al.* T-cell activation by recombinant receptors: CD28 costimulation is required for interleukin 2 secretion and receptor-mediated T-cell proliferation but does not affect receptor-mediated target cell lysis. *Cancer Res* **61**, 1976-1982 (2001).
458 Gulati, P. *et al.* Aberrant Lck Signal via CD28 Costimulation Augments Antigen-Specific Functionality and Tumor Control by Redirected T Cells with PD-1 Blockade in Humanized Mice. *Clin Cancer Res* **24**, 3981-3993, doi:10.1158/1078-0432.CCR-17-1788 (2018).
459 Long, A. H. *et al.* 4-1BB costimulation ameliorates T cell exhaustion induced by tonic signaling of chimeric antigen receptors. *Nat Med* **21**, 581-590, doi:10.1038/nm.3838 (2015).
460 Suryadevara, C. M. *et al.* Preventing Lck Activation in CAR T Cells Confers Treg Resistance but Requires 4-1BB Signaling for Them to Persist and Treat Solid Tumors in Nonlymphodepleted Hosts. *Clin Cancer Res* **25**, 358-368, doi:10.1158/1078-0432.CCR-18-1211 (2019).
461 Cheuk, A. T., Mufti, G. J. & Guinn, B. A. Role of 4-1BB:4-1BB ligand in cancer immunotherapy. *Cancer Gene Ther* **11**, 215-226, doi:10.1038/sj.cgt.7700670 (2004).
462 Quintarelli, C. *et al.* Choice of costimulatory domains and of cytokines determines CAR T-cell activity in neuroblastoma. *Oncoimmunology* **7**, doi:ARTN e143351810.1080/2162402X.2018.1433518 (2018).
463 Drent, E. *et al.* Combined CD28 and 4-1BB Costimulation Potentiates Affinity-tuned Chimeric Antigen Receptor-engineered T Cells. *Clin Cancer Res* **25**, 4014-4025, doi:10.1158/1078-0432.CCR-18-2559 (2019).
464 Redmond, W. L., Ruby, C. E. & Weinberg, A. D. The role of OX40-mediated co-stimulation in T-cell activation and survival. *Crit Rev Immunol* **29**, 187-201, doi:10.1615/critrevimmunol.v29.i3.10 (2009).
465 Konstorum, A., Vella, A. T., Adler, A. J. & Laubenbacher, R. C. A mathematical model of combined CD8 T cell costimulation by 4-1BB (CD137) and OX40 (CD134) receptors. *Sci Rep-Uk* **9**, doi:ARTN 1086210.1038/s41598-019-47333-y (2019).
466 Watts, T. H. Tnf/tnfr family members in costimulation of T cell responses. *Annual Review of Immunology* **23**, 23-68, doi:10.1146/annurev.immunol.23.021704.115839 (2005).
467 Dawicki, W., Bertram, E. M., Sharpe, A. H. & Watts, T. H. 4-1BB and OX40 act independently to facilitate robust CD8 and CD4 recall responses. *Journal of Immunology* **173**, 5944-5951, doi:DOI 10.4049/jimmunol.173.10.5944 (2004).
468 Taraban, V. Y. *et al.* Expression and costimulatory effects of the TNF receptor superfamily members CD134 (OX40) and CD137 (4-1BB), and their role in the generation of anti-tumor immune responses. *Eur J Immunol* **32**, 3617-3627, doi:10.1002/1521-4141(200212)32:12<3617::AID-IMMU3617>3.0.CO;2-M (2002).
469 Bancroft, G. J., Schreiber, R. D. & Unanue, E. R. Natural Immunity - a T-Cell-Independent Pathway of Macrophage Activation, Defined in the Scid Mouse. *Immunological Reviews* **124**, 5-24, doi:DOI 10.1111/j.1600-065X.1991.tb00613.x (1991).
470 Bosma, G. C. *et al.* Evidence of functional lymphocytes in some (leaky) scid mice. *J Exp Med* **167**, 1016-1033, doi:10.1084/jem.167.3.1016 (1988).
471 Katano, I., Ito, R., Eto, T., Aiso, S. & Ito, M. Immunodeficient NOD-scid IL-2Rgamma(null) mice do not display T and B cell leakiness. *Exp Anim* **60**, 181-186, doi:10.1538/expanim.60.181 (2011).

472 Chen, Y. *et al.* Tumor-associated macrophages: an accomplice in solid tumor progression. *J Biomed Sci* **26**, 78, doi:10.1186/s12929-019-0568-z (2019).

473 Hu, Y. *et al.* Tumor-associated macrophages correlate with the clinicopathological features and poor outcomes via inducing epithelial to mesenchymal transition in oral squamous cell carcinoma. *J Exp Clin Cancer Res* **35**, 12, doi:10.1186/s13046-015-0281-z (2016).

474 Zhang, Y. *et al.* High-infiltration of tumor-associated macrophages predicts unfavorable clinical outcome for node-negative breast cancer. *PLoS One* **8**, e76147, doi:10.1371/journal.pone.0076147 (2013).

475 Medrek, C., Ponten, F., Jirstrom, K. & Leandersson, K. The presence of tumor associated macrophages in tumor stroma as a prognostic marker for breast cancer patients. *Bmc Cancer* **12**, doi:Artn 30610.1186/1471-2407-12-306 (2012).

476 Shiao, S. L. *et al.* TH2-Polarized CD4(+) T Cells and Macrophages Limit Efficacy of Radiotherapy. *Cancer Immunol Res* **3**, 518-525, doi:10.1158/2326-6066.CIR-14-0232 (2015).

477 Qiu, S. Q. *et al.* Tumor-associated macrophages in breast cancer: Innocent bystander or important player? *Cancer Treat Rev* **70**, 178-189, doi:10.1016/j.ctrv.2018.08.010 (2018).

478 Kelly, B. L. & Locksley, R. M. Coordinate regulation of the IL-4, IL-13, and IL-5 cytokine cluster in Th2 clones revealed by allelic expression patterns. *J Immunol* **165**, 2982-2986, doi:10.4049/jimmunol.165.6.2982 (2000).

479 Luzina, I. G. *et al.* Regulation of inflammation by interleukin-4: a review of "alternatives". *J Leukoc Biol* **92**, 753-764, doi:10.1189/jlb.0412214 (2012).

480 Yang, W. C. *et al.* Interleukin-4 Supports the Suppressive Immune Response Elicited by Regulatory T Cells. *Frontiers in Immunology* **8**, doi:ARTN 150810.3389/fimmu.2017.01508 (2017).

481 Fasoulakis, Z., Kolios, G., Papamanolis, V. & Kontomanolis, E. N. Interleukins Associated with Breast Cancer. *Cureus* **10**, e3549, doi:10.7759/cureus.3549 (2018).

482 DeNardo, D. G. *et al.* CD4(+) T cells regulate pulmonary metastasis of mammary carcinomas by enhancing protumor properties of macrophages. *Cancer Cell* **16**, 91-102, doi:10.1016/j.ccr.2009.06.018 (2009).

483 Tanaka, T., Narazaki, M. & Kishimoto, T. IL-6 in inflammation, immunity, and disease. *Cold Spring Harb Perspect Biol* **6**, a016295, doi:10.1101/cshperspect.a016295 (2014).

484 Kofler, D. M. *et al.* CD28 Costimulation Impairs the Efficacy of a Redirected T-cell Antitumor Attack in the Presence of Regulatory T cells Which Can Be Overcome by Preventing Lck Activation. *Molecular Therapy* **19**, 760-767, doi:10.1038/mt.2011.9 (2011).

485 Flynn, J. P., O'Hara, M. H. & Gandhi, S. J. Preclinical rationale for combining radiation therapy and immunotherapy beyond checkpoint inhibitors (i.e., CART). *Transl Lung Cancer R* **6**, 159-168, doi:10.21037/tlcr.2017.03.07 (2017).

486 Xu, J. *et al.* Combination therapy: A feasibility strategy for CAR-T cell therapy in the treatment of solid tumors. *Oncol Lett* **16**, 2063-2070, doi:10.3892/ol.2018.8946 (2018).

487 Rupp, L. J. *et al.* CRISPR/Cas9-mediated PD-1 disruption enhances anti-tumor efficacy of human chimeric antigen receptor T cells. *Sci Rep* **7**, 737, doi:10.1038/s41598-017-00462-8 (2017).

488 McGowan, E. *et al.* PD-1 disrupted CAR-T cells in the treatment of solid tumors: Promises and challenges. *Biomed Pharmacother* **121**, doi:ARTN 10962510.1016/j.biopha.2019.109625 (2020).

489 Liu, G. N. *et al.* CXCR2-modified CAR-T cells have enhanced trafficking ability that improves treatment of hepatocellular carcinoma. *Eur J Immunol*, doi:10.1002/eji.201948457 (2020).

490 Craddock, J. A. *et al.* Enhanced Tumor Trafficking of GD2 Chimeric Antigen Receptor T Cells by Expression of the Chemokine Receptor CCR2b. *J Immunother* **33**, 780-788, doi:10.1097/CJI.0b013e3181ee6675 (2010).

491 Flynn, J. K. & Gorry, P. R. T cell therapies-are T memory stem cells the answer? *Ann Transl Med* **3**, 251, doi:10.3978/j.issn.2305-5839.2015.08.13 (2015).

492 Gattinoni, L., Speiser, D. E., Lichterfeld, M. & Bonini, C. T memory stem cells in health and disease. *Nat Med* **23**, 18-27, doi:10.1038/nm.4241 (2017).

Figures

Figures 1.1.1, 1.1.2, 1.2.1, 1.2.2, 1.2.4, 1.2.6 and 1.2.7 were created with BioRender.com.

Figure 1.2.5 derived from Wong et. al. (2015).

Statistical analyses and illustrations were done with GraphPad prism 8.

Acknowledgements

At this point I would like to thank all the people who supported me to make this Dissertation possible.

First, I would like to give my special thanks to Prof. Dr. Dirk Jäger for giving me the opportunity to work on this interesting project. I am very grateful for his support and scientific advice. In addition, I would like to thank him for the review of this dissertation.

My special thanks for the academic supervision, valuable advice and interesting TAC meetings go to Prof. Dr. Viktor Umansky.

I have deep gratitude for my supervisor Dr. Patrick Schmidt for all his support and patience throughout my PhD time. I thank him for all the new ideas, advice, feedback and helpful discussions.

I would also like to thank Dr. Inka Zörnig for her constant support with any problems. I thank her for all the scientific input and guidance.

I am extremely grateful to Dr. Richard Harbottle and Dr. Matthias Bozza for the great cooperation and provision of the pS/MARter and NanoCMARter vectors.

A special thanks goes to Prof. Dr. Claus Peter Heußel and Prof. Dr. Frederik Marmé for the cooperation and provision of the primary patient material.

I would like to acknowledge the entire lab team and our group in the Bioquandt. My special thanks go to PD Dr. Niels Halama, PD Dr. Frank Momburg, Iris, Isabella, Silke, Claudia Z., Jutta, Meggy, Nek, Jana and Marten for your support. I am very thankful to Rosa for all her support in the preparation of tissue stainings.

I especially want to thank Lasse, Sarah and Clemens for all these funny and crazy days together inside and outside of the lab.

I am extremely thankful to Alex for her willingness to help me with everything. I thank her for the daily moral and scientific support in dealing, for example, with many “monster” mouse experiments. I thank her for the great time together in the lab, all the jokes, the distractions from all these problems and, most of all, for the great friendship.

I would like to thank Claudia for all her help with any problems since the first day of my PhD. I thank her for the daily support and encouragement during all these ups and downs.

I would also like to thank Krysten for the great time together. I am glad that our friendship remains even beyond continents.

A very special thanks goes to my family, who have always stood behind me and believed in me, especially during my PhD time. I am thankful that I can always rely on you. I would not be here without you.